Toward dipolar physics with ultracold molecules:

Mixing of atomic species under confinement

Dissertation by

DEBORAH CAPECCHI

submitted to the Faculty of Mathematics, Computer Science, and Physics of the
University of Innsbruck in partial fulfillment of the requirements for the degree of:
Doctor of Philosophy (Ph.D.)

ADVISOR:
Univ.-Prof. Dr. Hanns-Christoph Nägerl,
Institute for Experimental Physics, University of Innsbruck

CO-ADVISOR:
Univ.-Prof. Dr. Tracy E. Northup
Institute for Experimental Physics, University of Innsbruck

universität
innsbruck

Abstract

Ultracold heteronuclear molecules distinguish themselves for the presence of long-range tunable dipolar interactions. These are of interest for the investigation of exotic phases of matter as well as for quantum simulation, quantum computation, and precision measurements. A successful pathway to enter the quantum regime with molecules consists in forming the molecules by associating their atomic components in the ultracold regime and successively transferring the molecules to their absolute ground state. The introduction of an optical lattice prior to the formation of the molecules helps in the creation of low entropy samples of molecules that are ideal for studying the effects of dipolar interactions. However, the role of the lattice itself, and more generally the role of confinement, is often non-trivial.

In this thesis, I focus on the role of the confinement from the optical lattice on the degenerate atomic gases in the steps leading to the formation of ultracold RbCs molecules. First, I investigate the interplay of the confinement from the lattice and the interatomic interactions in a Mott insulator of Cs, and I show the emergence of scattering resonances that can be predicted and interpreted within the framework of inelastic confinement-induced resonances. These results constitute the first systematic observation of such resonances under three-dimensional confinement. Then, I investigate superfluid transport of Rb atoms through the lattice by the translation of an underlying harmonic trap, and I show how the criterion for transport depends on the interplay between the confinement of the trap and that of the optical lattice. I show the presence of a lower and upper critical frequency of the trap, and through theoretical modeling, I identify some of the experimental conditions that could lead to the appearance of the lower critical trap frequency. Finally, I show a series of targeted interventions on the experimental RbCs apparatus, sequence, and data analysis that simplify the experimental setup, improve the stability of the experimental conditions, and speed up the processing of the experimental data. In particular, the interventions allow for the removal of six lasing devices with the relative electronics and extend significantly live data analysis capabilities. This, together with the improved understanding of the confinement effects, provides a solid and stable basis for the next generation of RbCs experiments aimed at studying the RbCs dipolar physics.

Contents

Chapter 1

Introduction

Everyday experience teaches us that water at low temperatures solidifies into ice, while at high temperatures it evaporates becoming gaseous. Solid, liquid, and gas are three different phases of matter with well-distinct properties. Entering the quantum regime, where the wave nature of matter can not be neglected anymore, new astonishing phases of matter are possible. Superconductors, which transport electrical current without dissipation, and supersolids, which have the properties of a liquid and a solid at the same time, are just two examples of the vastness of quantum physics marvels.

Water also teaches us that the effective dimensions achieved through external confinement will modify the behavior: one such example is the capillary effect when one immerses a thin straw in a glass of water, the level that the water reaches inside the straw is higher than in the glass, and the thinner the straw the higher the level. This is due to the interplay between the adhesive forces that make the water molecules stick to the straw and the cohesive forces with which the molecules stick to each other. Similarly, the way that interactions between atoms rearrange themselves at the edge of a material to accommodate for the interaction with the external environment (or lack thereof) leads to spectacular effects that are dominated by quantum physics, especially when the sample is reduced to a single layer or single line of atoms, These properties could lead to significant technological advancement for industries, which are constantly in search of materials with new exotic properties and which have a drive for miniaturization.

1.1 Cold atoms

Gases of ultracold atoms or ultracold molecules provide an excellent entry point to the quantum regime. At extremely low temperatures, the de Broglie wavelength of these particles becomes so large that even in dilute gases it is comparable to or larger than the inter-particle distance, giving rise to a regime dominated by quantum effects. These very cold gases led, e.g., to the observation of the Bose-Einstein condensate (BEC) in 1995 [1, 2], which was awarded the Nobel prize in 2001. The BEC is a new phase of matter arising in the quantum regime where all the particles behave as one. It is realized when a macroscopic fraction of the atoms is in the lower energetic state of the system. In the presence of even weak interactions between its components, a BEC becomes superfluid [3], which means that it can flow without internal friction. Since the first observation of the BEC with Rb atoms, the field of ultracold atoms expanded with the development of many more tools and by bringing to quantum degeneracy many more atomic species, enabling the exploration of many new exciting avenues as discussed below.

By now, atomic physicists can control atomic interactions almost at will and engineer arbitrary potential landscapes. Through external potentials, it is possible to implement strong confinements that effectively reduce the system's dimensionality, making it behave like a single layer or a single line of atoms, or even isolate the atoms in individual wells in analogy with crystalline lattices in condensed matter.

Control over the interactions and engineering of external potentials has led to the observation of even more spectacular effects long sought in other fields of physics. Control over the interactions by means of Feshbach resonances [4] led to the condensation of Fermion pairs and a paring mechanism at strong interaction [5] analogous to the Cooper pairs, which are expected to be at the base of superconductivity in metals [6]. Control over an external crystalline potential can lead the atoms to acquire a phase coherence in the superfluid phase or localize at the crystal cell and distribute uniformly in the Mott-Insulator phase [7]. Experimentally, such potential can be realized through optical lattices [8]. The phase transition between the two quantum states in the optical lattice can be driven back and forth by tuning the external parameters [7]. Optical lattices can also be used to investigate quasi-one-dimensional and quasi-two-dimensional systems. In both cases, the confinement leads to a drastic change in the properties of the atomic cloud. For example in one-dimensional systems, it is possible to achieve a stable gas even in the presence of strong repulsive [9] or attractive interactions [10].

However, the interactions between ultracold neutral atoms are in most cases contact interactions and manifest themselves only at very short distances. Also, single-species cold-atoms experiments can realize almost perfect systems. On the contrary, solid-state systems that cold-atom experiments aim to simulate are often characterized by different elements with different competing interactions and often the presence of defects. To account for these effects, the cold-atoms field expanded exploring new avenues with systems of increased complexity, e.g. with mixtures of two atomic species and the introduction of additional interactions, in particular long-range interactions. Long-range interactions have been achieved in optical cavities with strong light-atom couplings [11], via atomic excitation to Rydberg states, which strongly enhances the natural electric dipole of the atoms [12], with the choice of peculiar atomic species that have strong magnetic properties [13] (magnetic atoms), and by the employment of heteronuclear molecules [14]. The last one is the path chosen in my thesis.

1.2 Molecules

Heteronuclear molecules inherit controllability from the techniques used for ultracold atoms and they have electric dipole interactions that can be tuned in intensity and direction. The dipolar interaction strength can be much higher than for magnetic atoms and the internal states of the molecules can be used to store information and enable systems with synthetic dimensions. Heteronuclear molecules are expected to allow access to new quantum phases: in the bulk, theory predicts, e.g, the spontaneous formation of superfluid and crystalline phases, with new phases emerging depending on the value of the dipolar interaction [15], or the formation of self-bound dipolar droplets and supersolids, analogous to what has recently been observed with magnetic atoms [16, 17, 18], but with much stronger and tunable dipolar interactions [19]; In optical lattices, insulating phases with fractional fillings [20] and occupation-dependent tunneling induced by dipolar-interaction and pair superfluid phases [21] are expected. All these nice properties come with a price: The rich internal structure makes direct cooling extremely difficult, and the collisional dynamics between molecules feature dense and complex, if not even chaotic, spectra of intermediate states [22, 23].

Direct laser cooling of molecules has been applied so far mainly for alkaline Earth fluorides and oxides [24]. Recently, significant progress towards direct cooling of molecules [25, 26] led to spectacular results in benchmarking standard model extensions with ThO [27, 28]. Nevertheless, the temperatures achieved with direct cooling are still far from quantum degeneracy. While more progress on direct cooling is definitely on the horizon, for bi-alkali and alkali-alkaline earth molecules a different approach has been applied successfully. For these molecules, their component atoms can be cooled down individually to or near the quantum regime and successively associated to form the molecule. With this second technique, Fermi degeneracy has been achieved in gases of KRb [29] and NaK [30] molecules.

The other major obstacle of ultracold molecules is the collisional dynamics. First, there are exothermic chemical reactions, for example, it is energetically favorable for two KRb molecules upon collision to react and form a K_2 and a Rb_2 molecule. As the investigation of ultracold molecules advanced, it was discovered that this is not the only process to take into account. Even for species that would undergo endothermic reactions, the lifetime of the molecules has been observed to be much shorter than the expectation [31]. It is now widely accepted for molecules formed by two bosonic atoms or one boson and one fermion, that the lifetime is limited by the formation of four-atom bound state complexes, which populate the short-range interaction potential of two molecules, whether the chemical reactions are endothermic or exothermic. The scattering process that leads to the formation of complexes takes the name of 'sticky collisions' and has been recently reviewed in Ref. [32]. For endothermic reactions, such a complex eventually decays in the original molecules, but it does so via a progressive relaxation over numerous internal states which takes a long time. Before the complex breaks, different loss channels might enter and affect the sample lifetime, like light-assisted losses and three-body losses. Direct observation of a complex has been performed for KRb molecules colliding with K atoms [33], which is an exothermic reaction. Indirect observation of the complex, and especially the measurement of its lifetime, has been tried on several molecules with contrasting results. For RbCs molecules, the complex lifetime measured in Ref. [34, 35] was found to agree with the predictions of the Rice-Ramsperger-Kassel-Marcus theory [22, 23]. On the contrary, bosonic [30] and fermionic NaK [36] and NaRb [36] showed complex lifetimes much longer than the expected ones [37], according to the same theory. Although there is not yet a full answer to this discrepancy, a fairly accredited hypothesis is that the lifetime of the complexes does depend on the initial hyperfine state of the colliding components. This hypothesis is supported by studies conducted on molecule-molecule and molecule-atom collisions in RbCs [38] and bosonic NaK [39]. Sticky collisions open new fascinating perspectives on chemistry at ultracold temperature and deserve to be investigated more in detail, but they also highlight the necessity to prevent inelastic processes altogether if the molecules are to be used for different purposes like the investigation of dipolar physics.

1.2.1 Molecule dipole moment and shielding techniques

The techniques used to prevent molecular collisions at short range go under the name of shielding. They are based on engineering repulsive dipolar interactions and exploiting their long-range character to prevent the molecules from entering the short-range part of the potential and forming complexes.

To understand these techniques it is necessary to go a bit more into detail on the nature of the dipolar interaction in molecules. The intrinsic electric dipole moment of the molecule in the roto-vibrational ground state is well-defined only in the molecule frame. The spherical symmetry of the lower state implies that, in the laboratory frame, the dipole moment averages zero. To induce a dipole moment in the laboratory frame, it is necessary to break the rotational symmetry. This can be achieved by creating a superposition of the ground state with higher excited states with a different symmetry via electric or microwave fields. The state superposition also determines the effective strength of the dipolar moment in the laboratory frame.

The most immediate shielding technique consists of confining the molecules to a single plane, i.e. a quasi-two-dimensional system, and aligning the dipoles perpendicular to it by means of a DC electric field or microwave radiation. In this case, dipolar interactions are always side-by-side, thus repulsive, and they prevent the molecules from getting sufficiently close to each other to suffer from collisional losses. In 2020, Valtolina *et al.* [29] used this principle to evaporatively cool KRb molecules below the Fermi temperature and obtained the first degenerate gas of fermionic molecules.

In the three-dimensional case, the shielding becomes more complicated, but it was suggested [40, 41, 42, 43] that it can be achieved with special admixtures of rotational states. Such mixtures bring the higher rotationally excited states to be degenerate with the initial collisional channel and lead to a resonant effect in dipolar interactions that alters the interaction strength. This effect can lead either to an enhancement or a suppression of the losses. An enhancement of the losses has been observed by Yan *et al.* [44]. The shielding via this method was first implemented with the employment of electric fields by Matsuda *et al.* [45] for a two-dimensional Fermi gas and successively by Li *et al.* in 3D [46].

The same shielding effect has been observed with blue-detuned microwave dressing on CaF by Anderegg *et al.* [47], and harnessed by Schindewolf *et al.* [48] to evaporate NaK molecules and achieve a degenerate Fermi gas, and to stabilize bosonic gas of NaCs [49] and NaRb [50].

Shielding via electric fields and microwave fields is quite effective and it allowed the achievement of the degenerate regime for a three-dimensional gas, which represents a milestone of the research on ultracold molecules. At the same time, the shielding in free space partly limits the effective tunability of the dipole moment of the molecules near the shielding resonance (with some flexibility available at the cost of larger molecular losses) and forces the choice of the excited state. A different option to shield molecules from contact interactions and achieve long lifetimes consists of confining the molecules into optical lattices. In this case, the dipole moment can be chosen at will, but evaporation is not possible.

1.2.2 Molecules in optical lattices

Optical lattices are periodic light patterns, that act on atoms and molecules as periodic potentials. The shape of optical lattices can mimic the potential experienced by electrons in a solid-state crystal.

Distributing the molecules within an optical lattice with an average occupation equal to or lower than one molecule per lattice site can prevent contact interactions. Shielding of contact interactions by the optical lattices has proven effective in increasing the lifetime of the molecular sample for both homonuclear [51] and heteronuclear [52] molecules. In particular, for the latter, lifetimes of $\sim 20-30\,\mathrm{s}$ have been achieved, despite the molecules being chemically reactive [52]. The long lifetime also allows for a long coherence time of the nuclear spin states [53]. Differently from the electric field and microwave shielding, the optical lattice does not rely on special mixtures of the rotational states, therefore the molecules in the lattice preserve the possibility to access an almost arbitrary number of rotational states. With it, it preserves the tunability of the effective dipole moment in the laboratory frame, the freedom in the choice of the excited rotational state, and the possibility of using it to map other quantities. This gives molecules a strong advantage with respect to Rydberg atoms where the interactions are mainly on-off type and a limited tunability is achieved by changing the Rydberg state, which also changes other properties of the sample. At the same time, the strong dipole-dipole interaction can dominate the dynamics for typical lattice spacings, even when the molecules are a few lattice sites apart, this does not happen for magnetic atoms at typical lattice spacings. As a consequence, the lattice framework is the basis for many theoretical proposals with ultracold molecules, just to give a few examples: spin-models with topological order [54], superfluid phases [55], spin liquids [56], spin–orbital dynamics [57], ordered phases and supersolidity [20], and quantum magnetism [58]. Preliminary experimental results in this direction have been obtained regarding the observation of dipolar spin-exchange on a three-dimensional optical lattice [59], the observation of interlayer interaction between atoms in two-dimensional optical lattices [60], and itinerant spin dynamics [61].

For many of the aforementioned proposals, it is important to be able to produce samples of molecules in the lattice with low entropy, i.e., to reach high lattice fillings. A huge step forward in this direction was achieved around 2015 when Moses *et al.* [62] developed a protocol for mixing one fermionic and one bosonic species in a three-dimensional optical lattice. The protocol is based on the overlap of two insulating phases, respectively the Mott-Insulator for the bosons and the band-insulator for the fermions. Thanks to this protocol, the molecules are created directly in the optical lattice from quantum degenerate gases, leading to extremely low entropies. Shortly after, Reichsöllner and Schindewolf *et al.* [63] developed a similar quantum engineer protocol for the RbCs project in which the work presented in my thesis has been carried out. Similar to Moses's, the protocol by Reichsöllner and Schindewolf culminates with the formation of two insulating states, specifically two Mott-insulators of bosons, but it also accounts for an additional preliminary step to overlap the two immiscible species at separate locations. This additional step is realized by transporting one species across the optical lattice while the other is strongly localized. Both protocols [62, 63] lead to an overall entropy per molecule of $\sim 2\,k_\mathrm{B}$, where k_B is the Boltzmann constant, a good condition to start studying dipolar physics with the molecules. The protocol by Reichsöllner and Schindewolf is at the core of many of the results I present in this thesis.

1.3 Confinement

The formation and storage of molecules in controlled conditions lead back to the topic of confinement. In the course of my thesis, I will focus on two specific instances of confinement that enter the protocol for the formation of RbCs molecules sketched above: the role of the confinement from the optical lattice on the strongly interacting atoms, and the interplay between the confinement from the optical lattice and that of a trap used to transport the atoms across the lattice. In general, strong external confinement is receiving higher and higher attention as it leads to the emergence of special properties in quantum systems. Quantum gases have been and are exploited to explore such properties [64, 65]. For example, in the presence of strong confinement along one direction, which reduces the motion of the atoms to two dimensions, the formation of a topological order at finite temperature was observed: the BKT transition [66]. In the presence of strong confinement along two directions, which limits the system to be one-dimensional, strong repulsive interactions between bosons can mimic the Pauli blocking effect, and the bosons will start to behave like fermions [67, 9, 10]. In particular, it has been observed that scattering properties can also be resonantly modified by the confinement for quasi-two-dimensional [68, 69] or quasi-one-dimensional quantum gas [70, 71]. Similar effects have been proposed also for strong confinement along all three directions [72] which gives a quasi-zero-dimensional system, in analogy with the confinement experienced by an atom or a molecule when confined to a single lattice site or that of an electron in a quantum dot [73]. These resonances are known as confinement-induced resonances.

In cold atoms experiments, not only a strong confinement can modify the dimensionality and the properties of the quantum system, but a weak confinement can be used to realize trapping potential. These play a crucial role in the cooling steps that bring a gas from above room temperature to the ultralow temperatures needed for achieving quantum degeneracy. For example, in evaporative cooling, one of the most common strategies toward quantum degeneracy, the temperature of a trapped gas is reduced by changing the depth of the trapping confinement, and the speed of the dynamics is partially controlled by the geometry of the confinement.

1.4 Thesis outline

My thesis investigates the emergence of confinement effects in the protocol that leads to the formation of low entropy samples of RbCs molecules in the optical lattice. In this context, the main result is the first observation of confinement-induced resonances in a three-dimensional lattice, which is part of Ref. [74]. In the same context, a preliminary study of the interplay between a trap and the optical lattice during the transport of the atoms is also presented. A large part of the thesis work has been dedicated to changing and improving the experimental apparatus, the experimental sequence, and the data analysis. In particular, the paradigm was shifted from many weak light sources to a few high-power lasers, and live data analysis has been introduced.

The first two Chapters of the thesis constitute the background information for the work presented here:

- In **Chapter 2** I give an overview of the forms of confinement used in this thesis for the creation of the degenerate gas and the formation of the molecules, emphasizing their role within the cooling steps. Contextually, I discuss the dynamics that can take place in the presence of the confinement and the formation of a BEC. Next, I discuss the effect of the confinement on atomic interactions. The content of this Chapter is very generic and applies to most cold-atom experiments.

- In **Chapter 3** I show how the elements of Chapter 2 come together to allow the simultaneous cooling of Rb and Cs, and describe the protocol followed in the RbCs project for the formation of the molecules in the optical lattice.

Chapters 4 to 6 contain the original contributions:

- In **Chapter 4** I discuss the role of the confinement from the optical lattice on the stability of the Mott-Insulator state, which is one of the intermediate states in the mixing protocol reviewed in Chapter 3. In particular, I discuss the modification of the scattering properties in the presence of such confinement and report the first observation of inelastic confinement-induced resonances in a three-dimensional lattice, that led to the work of Ref. [74].
- In **Chapter 5** I discuss the interplay between the optical lattice and the presence of an additional trap while moving the atoms across the lattice, showing, through data and theoretical modeling, that the trap stiffness and experimental conditions limit the superfluid transport.
- In **Chapter 6** I report technical upgrades to the experimental setup and the detailed characterization of the experimental sequence, which enhances the control over the setup and improves the stability of the samples. In particular, two high-power lasers have been introduced for the initial steps of cooling, responsible for reducing the temperature of the room-temperature gas by about nine orders of magnitude. The full experimental sequence has been optimized to better profit from the new sources. The data analysis has been significantly sped up with the introduction of open-source tools that allow live analysis as opposed to the previous post-processing strategy. Chapter 6 is complemented by Appendix A listing the final values of the optimization and Appendix B reporting details of the scripts for the live data analysis. Appendix C contains the function definition for the fit used across the thesis and incorporated in the data analysis.

To help the reader keep track of the two species, across the thesis I use cold colors for measurement and theory concerning Rb and warm colors for measurement and theory concerning Cs, consistently with the color code used for the project documentation.

Chapter 2

Confinement as a tool for cooling and controlling the atoms

2.1 Introduction

One of the most important tools in the research field of ultracold atoms is the possibility to implement almost arbitrary external confinements via either magnetic or optical means. The confinement could be providing a weak or moderate trapping to a three-dimensional cloud or be so tight in one or more directions as to limit effectively the dimensionality of the cloud. Across the next Chapters, I will show different implementations of confinement: To control the external degrees of freedom of the atoms during cooling, to realize different quantum phases, to transport atoms around, and even to control interactions between atoms. The variety of applications derives from how the atoms interact with light, magnetic fields, and other atoms. But in the end, the confinement presented in my thesis comes in two shapes, a 'trap' with a well-defined minimum of the potential energy along one or more directions, and the slightly special case of a lattice, which can be regarded as a periodic arrangement of traps. Just to anticipate some names that will be explained in the next pages, the magnetic trap, the reservoir trap, and the dimples, belong to the first case, while degenerate Raman sideband cooling and the experiments with BECs shown in this thesis make use of optical lattices.

Before entering into the topic of confinement, I will provide a quick description of how the atoms interact with their environment Sec. 2.2, as this is the basis of all the cooling mechanisms. In Sec. 2.3–Sec. 2.8 I will briefly introduce a number of textbook-standard cooling techniques, found, e.g., in Refs. [75, 76], and on the formation of a BEC in a trap 2.5. The cooling techniques are combined during the experimental sequence of the RbCs project as presented in Chapter 3, and partly characterized anew in Chapter 6. Some of these concepts also find application in the discussion of Chapter 5. In Sec. 2.9–Sec. 2.10 I will introduce the problem of scattering in confined systems, this is a set of more specialized notions that is the basis for the results of Chapter 4.

2.2 Atoms interacting with...

2.2.1 ...light

In the field of ultracold atoms, the main tool to control neutral atoms is light. Through the application of light from a laser, the internal and external degrees of freedom of the atoms can be manipulated almost at will. The interaction between the laser and an atom can be described, as is well known, by three fundamental processes: absorption of a photon from the laser which excites the atom, relaxation of the atom through spontaneous emission of a photon, or relaxation through stimulated emission of a photon in the field mode of the laser, see e.g. Ref. [75]. In free space, all processes transfer momentum between the photon and the atom. For absorption and stimulated emission, the transferred momentum matches the momentum of the photons in the field mode of the laser and it keeps adding over multiple processes. On the contrary, the momentum transferred from spontaneous emission is in a random direction and it averages to zero over multiple photon-atom scattering events.

Following the treatment in, e.g., Ref. [75], the force can be derived explicitly for a two-level system in an electric field described. Indicating by $\vec{r}$ the position and t the time, the field $\vec{E}$ is described by $\vec{E}_\mathrm{L}(\vec{r},t) = \vec{e}_\mathrm{L}(\vec{r})\mathcal{E}_\mathrm{L}(\vec{r})\cos\left[\omega_\mathrm{L} t + \phi(\vec{r})\right]$ of amplitude $\mathcal{E}_\mathrm{L}(\vec{r})$ and polarization $\vec{e}_\mathrm{L}(\vec{r})$, with frequency ω_L and phase $\phi(\vec{r})$. The coupling between the two levels is given by the Rabi frequency $\hbar\Omega = -\mathcal{E}_\mathrm{L}(\vec{r})\vec{d}_\mathrm{eg}\cdot\vec{e}_\mathrm{L}$, where $\vec{d}_\mathrm{eg}$ is the dipole transition matrix element. In the steady state, in the rotating wave approximation [77], the total radiative force exerted on the atoms can be expressed as [75]:

$$\mathcal{F} = -\hbar\frac{s}{1+s}\left(\frac{\Gamma}{2}\vec{\nabla}\phi + \delta\frac{\vec{\nabla}\Omega}{\Omega}\right) \tag{2.1}$$

where $s = \Omega^2/2/(\delta^2 + \Gamma^2/4)$ is the saturation parameter and Γ the transition linewidth. The first term is the dissipative force and it is proportional to the phase gradient of the laser field. The second term is called reactive or dipole force. It is a conservative force proportional to the amplitude gradient of the electric field. The potential energy associated with the dipolar force is negative for light that is red-detuned with respect to the atomic transition and positive for light that is blue-detuned with respect to the atomic transition. Taking into account the dependence of s on the detuning for the two forces, it can be seen that the dissipative force decreases quadratically with the detuning, while the dipolar force decreases linearly. Therefore, at large detuning, the radiative force is mainly due to the dipolar force. As reviewed in Sec. 2.3, the dissipative force is the driving force to slow down the atoms in the Zeeman slower and in the magneto-optical trap (MOT). The reactive force, in the RbCs project, is exploited in two typical configurations, both using red-detuned light. One configuration is known as optical dipole trap ODT [78] and its properties are discussed in Sec. 2.4 and Sec. 2.6. This trap is the result of a beam with a transversal gaussian intensity profile (gaussian beam [77]). As the intensity of the light increases toward the center of the beam, the radiative force gives rise to a transversal potential that has its minimum at the center of the beam. The other configuration is a particular kind of ODT, achieved when pairs of beams interfere with each other. This configuration gives rise to a periodic light pattern, which generates a periodic potential known as optical lattice OL [8] as presented in Sec. 2.7 and Sec. 2.8. ODT and OL are instrumental to the experiments with the quantum gas presented in Chapter 4 and Chapter 5.

2.2.2 ...magnetic fields

When one atom in a given hyperfine level F is placed in an external magnetic field, the energy levels of the atoms are shifted. In particular, the field acts on the magnetic sublevels m_F removing their degeneracy. For weak static fields, the shift is well-described by the anomalous Zeeman effect Ref. [79]:

$$\Delta E_{|F m_F\rangle} \simeq -\mu_B g_F m_F B_z \tag{2.2}$$

where μ_B is the Bohr magneton and g_F is the Landé g-factor, and B_z is the projection of the magnetic field along the quantization axis.

A free atom in a given m_F sublevel in a magnetic field gradient moves along the gradient to minimize its energy. In the presence of a spin mixture, the different response to the magnetic field allows separation of the different spin states with the Stern-Gerlach technique [80], as used, e.g., to isolate spatially the desired m_{F} from the other states after degenerate Raman side-band cooling (dRSC) (Sec. 3.9). In the presence of a polarized sample where all the atoms occupy the same m_F state, a magnetic field gradient can be used to compensate gravity or other external forces. Drifts of the position of the atomic cloud due to uncompensated magnetic field gradient are responsible for effects in Chapter 5. Quadrupole magnetic fields can give rise to magnetic trapping along one direction, this is the magnetic trap. While many experiments working with Rb make large use of magnetic trapping, in this thesis magnetic trapping has been used only marginally to detect vacuum conditions as briefly mentioned in Sec. 6.4.5.

2.2.3 ...other atoms

Under most circumstances, the atoms also interact with other atoms. In general, to evaluate the interaction between two atoms it would be necessary to consider the interactions between all the subatomic components for all possible collisional channels between the two atoms. In an ultracold gas of bosonic atoms, the low kinetic energy of the atoms allows for two simplifications of the scattering problem: only s-wave collisions are taken into account; the interaction potential at large interatomic distances can be replaced by means of an effective potential, which neglects the details of the short-range potential while reproducing well the contributions of the valence electrons at larger distances. This translates to a single universal parameter a_{s} describing the scattering process.

As mentioned in Chapter 1, a_{s} can be tuned experimentally. This is possible thanks to Feshbach resonances FR [4]. A FR can be described (with some simplification [4]) in a model with two molecular channels, a closed channel V_{c}, supporting a bound state, and an open channel V_{bg}, degenerate with the energy of the two scattering atoms at large separation. As shown in Fig. 2.1, the bound state supported by V_{c} can couple resonantly to V_{bg}. The differential energy between the open and closed channels can be engineered to tune the system in and out of resonance. In the experiments, this is typically done by using the magnetic field to tune the differential Zeeman shift, a_{s} reads [4]:

$$a_{\mathrm{s}} = a_{\mathrm{bg}} \left(1 - \frac{\Delta}{B - B_0}\right), \tag{2.3}$$

where a_{bg} is the background scattering length, away from resonance. B_0 is the pole of the resonance, at which a_{s} diverges, and Δ is the width of the resonance, which depends on the coupling strength between the two channels, a_{bg}, and the differential magnetic moment [4]. Near the resonance, the

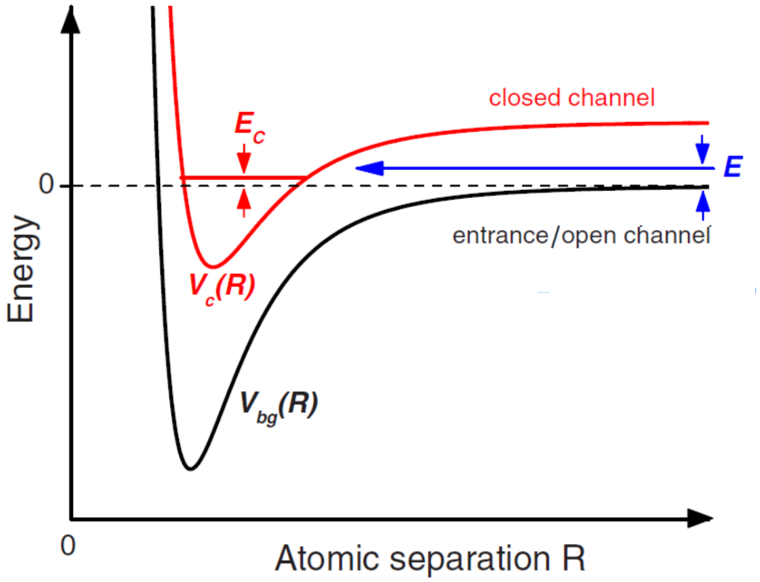

Figure 2.1: Schematic picture of a Feshbach resonance. The curves show the energy as a function of the interparticle distance. The open channel $V_{\text{bg}} \rightarrow 0$ and becomes degenerate with the two separate atoms. The closed channel V_{c} supports a bound state. The figure has been adapted from Ref. [4].

scattering and bound state property depend only on a_{s} and the atomic mass, this region is defined as the universality domain [4]. On the contrary, the position of the resonances is strongly dependent on the species and the details of the real atomic scattering potential [4].

The main loss channel in ultracold bosonic alkali is due to three-body losses [81, 82, 83, 84] (see Sec. 2.4.3), these losses at zero temperature scale as $\sim {a_{\text{s}}}^4$. It is then imperative to keep a_{s} sufficiently low, such that the losses are negligible over the timescale of the dynamics of interest, the latter in many cases corresponds to the timescale of the elastic scattering processes. In the presence of two species, this is not straightforward, as a variation of the field might change simultaneously the intraspecies scattering length for each species and the interspecies scattering length. The 'good conditions' for the experiment are realized when the rate of intraspecies elastic scattering processes (Γ^1_{el}) for e.g., species one is much larger than the rate of intra and inter-species three-body inelastic processes and, at the same time, the interspecies elastic scattering rate is sufficiently small to allow the species to coexist at the same position, i.e., the two species are miscible. For many atomic combinations, such conditions only apply in very narrow magnetic field ranges. In the Rb and Cs mixture described in this thesis, there is no such window, and different tricks are applied (see Sec. 3.11).

In view of this problem, it is interesting to explore different ways of tuning a_{s}. One particular case is what happens in the presence of external confinement. In this case, the confinement provides a closed channel that supports virtual and real discrete excited molecular states, and the role of the open channel is played by the trap state that is degenerate with the non-bound atoms. A detailed review of this case is given in Sec. 2.9, and Sec. 2.10 as it closely relates to the results of Chapter 4.

2.3 Confining the thermal gas

This section deals with how a hot gas in the oven chamber is slowed down sufficiently by the Zeeman slower to be successively confined in the magneto-optical trap MOT by a combination of magnetic field and laser beams. Both processes, the cooling in the Zeeman slower and the cooling and trapping in the MOT, make use of laser cooling [75], which relies on the anomalous Zeeman effect and exploits the dissipative term of the light-atom interaction, seen respectively in Sec. 2.2.2 and Sec. 2.2.1. The use of these cooling processes is so well-established in the field (details on the working principles can be found, e. g., in Ref. [76]), that at first glance it might seem surprising to find it reported in a Ph.D. thesis. The choice to give here a quick overview of the processes is motivated by the upgrade of the experimental setup presented in Chapter 6. During the upgrade both Zeeman slower and MOT have been characterized almost anew, following the laser replacement.

2.3.1 Zeeman slower

The Zeeman slower [85] consists of a region of tapered magnetic field, typically with a length of a few to several tens of centimeters, which connects directly to the oven section. The field in the RbCs project is realized by a combination of solenoids. The laser light, which in this thesis I refer to as Zeeman light, travels along the axis of the solenoid. It is off-resonance with respect to the atomic transition in the laboratory frame. In the atomic frame, the light becomes resonant for atoms moving toward the source thanks to the Doppler shift. As the atoms propagate along the solenoid and slow down, the magnetic field compensates for the change in the Doppler shift for a given velocity class and keeps the light-atom scattering resonant. In the ideal case, the transition addressed by laser cooling is closed. In reality, off-resonant excitation, and spontaneous decay can bring the atoms out of the cooling transition, for this reason, an additional 'repumper' beam is used to address atoms that escape in different levels and bring them back to the cooling transition. The velocity of Rb and Cs atoms in the Zeeman slower is typically reduced from a few hundred m/s to about 10 m/s. At the final velocity, it is possible to capture the gas in the MOT.

2.3.2 Magneto-optical trap

After the Zeeman slower, the atoms are stopped and trapped in the MOT. Here polarized counter-propagating beams in conjunction with a quadrupole magnetic field, which linearly shifts the hyperfine sublevels, allow for spatially selective scattering of the light, and gives rise to cooling and trapping of the atoms. More in detail, the optical part of the MOT consists of three pairs of mutually orthogonal beams applying a dissipative force on the atomic cloud along all six directions, in the thesis I refer to these beams as MOT beams and, respectively, MOT light. The result of the MOT beams is that the velocity of the atoms experiences a viscous damping, which gives this step the name of optical molasses [76]. The beams alone do not provide trapping. A set of coils in the anti-Helmhotz configuration generates a quadrupole field, that splits the hyperfine substates m_F anti-symmetrically with respect to the zero of the field. Using counter-propagating beams with opposite polarization it is possible to address mainly the lower spin state, which differs between the two regions separated by the center of the field, and apply a radiative force that, on average, slows down only the atoms moving away from the center of the trap [76]. This mechanism effectively traps the atoms near the center of the field.

Similar to the Zeeman slower, the MOT requires repumper light to keep restoring the atoms in the cooling transition. In alkali atoms, for the most common transitions, one repumper is generally sufficient.

Alkali-atom MOT can be loaded in a MOT at around $10^6 - 10^{10}$ atoms/s depending on the characteristics of the atomic flow and capture range. The total atom number depends greatly on the scope of the experiment, the maximum atom number recorded reaches 10^{11} atoms [86]. Typical temperatures in a MOT are between a few μK and 1 mK, depending on the atomic species and the parameters of the MOT [77], the final temperature is typically slightly below the doppler limit.

In molecules, the internal structure comprehends many more levels due to the rotational and vibration states, so it is generally hard to keep track of all possible transitions needed for cooling and mostly repumping, except for a few specific classes of molecules for which cooling had been achieved in recent times [87, 88, 89] as reviewed in Ref. [90]. A detailed description of the working principles for the magneto-optical trap for atoms can be found, e.g., in Ref. [76].

2.4 Confining an ultracold gas

ODTs play an important role at low temperatures, near the quantum regime. ODTs are based on the reactive force while the dissipative term is strongly suppressed by introducing a large detuning of the laser frequency with respect to the atomic transition. If the atoms are at equilibrium, i.e. they have thermalized in the trap, the properties of the cloud depend on the geometry of the trap and the atomic scattering properties. These properties and the timescales needed for equilibrium are instrumental to understanding the cooling mechanisms taking place in the ODT, such mechanisms are implicitly used in Chapter 4 and Chapter 5, while they are briefly discussed from an experimental point of view in Chapter 3 and Chapter 6.

For brevity, I will limit here to provide the main results and the formulas that are used daily in the lab. ODTs are explained in several sources, the following discussion follows mostly Ref. [78] for the trap properties. A derivation of such properties is found, e.g., in Ref. [3]. The dynamical processes in the ODT are instead treated here according to Ref. [91].

2.4.1 ODT parameters

An ODT is typically formed by a gaussian beam with waist w_0, red-detuned with respect to the atomic transition. In this case, the dissipative term of the light-atom interaction is negligible and the dipolar term gives rise to a trapping energy potential proportional to the intensity I of the beam

$$V_{\mathrm{t}} = \frac{1}{2\epsilon_0} Re(\alpha) I, \tag{2.4}$$

where ϵ_0 is the vacuum dielectric constant and α the atom's polarizability. If $V_{\mathrm{t}}/k_{\mathrm{B}}$ is much higher than the average temperature of the trapped atoms, as it happens at equilibrium, the atoms sit near the center of the ODT. In this case, the potential can be approximated by that of a harmonic confinement, deriving from the Taylor expansion of the potential at the center position to the second order in the position. Along the transversal direction r, the potential takes the form

$$V_{\mathrm{t}}(r) = V_{\mathrm{t}0}\left[1 - 2\left(\frac{r^2}{w_0^2}\right)\right], \tag{2.5}$$

where $V_{\mathrm{t}0}$ denotes the trap depth and the trap frequency is given by

$$\omega_t = \left(\frac{4V_{\mathrm{t}0}}{mw_0^2}\right)^{\frac{1}{2}}. \tag{2.6}$$

The energies of the excitation modes in the ODT are proportional to the trap frequency. Therefore the trap frequency is typically measured by exciting either the quadrupole mode for a thermal gas, which happens at $2\omega_{\mathrm{t}}$, or the dipole mode at ω_{t}. The density of the atomic cloud, the temperature, and the collisional rate, at equilibrium, depend entirely on the trap depth, trap frequency, total atom number, and a_s.

2.4.2 Cloud properties in a harmonic trap

At equilibrium, a trapped cloud is characterized by its temperature, peak density, and phase-space density. Here, I review how in the approximation of the harmonic trap these properties depend on the trap parameters.

Temperature

The temperature T of the gas in the trap is such that $k_{\mathrm{B}}T \ll V_{\mathrm{t}}$ [91]. The rule of thumb [92] for a harmonic trap is $k_{\mathrm{B}}T \sim V_{\mathrm{t}}/10$. If the atoms initially loaded in the trap are hotter, the most energetic atoms can escape the trap, and the kinetic energy redistributes between the remaining atoms. This process is the basic step of evaporative cooling and it is known as plain evaporation, another instance of evaporative cooling, namely forced evaporation, is reviewed in Sec. 2.6.2

Peak density

The peak density corresponds to the maximum density of the cloud in the trap. For a thermal gas in a harmonic trap, the peak density for an ideal Boltzmann gas is defined as [78]

$$n_0 = N\bar{\omega}^3\left(\frac{m\lambda_{\mathrm{dB}}(T)}{2\pi\hbar}\right)^3. \tag{2.7}$$

Here N is the total atom number, and the effective volume occupied by the atoms is proportional to the geometric mean of the trap frequencies along the three directions $\bar{\omega}^3 = \omega_x\omega_y\omega_z$ and to the cube of the de Broglie wavelength [75]

$$\lambda_{\mathrm{dB}}(T) = \frac{\hbar}{\sqrt{2\pi m k_{\mathrm{B}}T}}. \tag{2.8}$$

Phase-space density

The quantum regime is entered when the extension of the wave function becomes larger than the interparticle distance. For this reason, the main parameter to evaluate the progress in cooling is provided by the phase-space density PSD, which relates to both length scales

$$PSD = \lambda_{\mathrm{dB}}(T) n_0 \tag{2.9}$$

2.4.3 Scattering and dynamics rates

Elastic scattering

The rule of thumb for atoms in a trap is that thermalization takes on average three elastic scattering events [91]. The elastic scattering rate depends on n, the scattering cross section σ, and the relative velocity of the atoms v_{rel}. The scattering rate can be written in the simple form

$$\Gamma_{\mathrm{el}} = n \left\langle v_{\mathrm{rel}} \sigma \right\rangle . \tag{2.10}$$

For identical bosons, in the s-wave scattering regime, σ is

$$\sigma \simeq \frac{8\pi {a_{\mathrm{s}}}^2}{1 + (k_{\mathrm{rel}} a_{\mathrm{s}})^2}, \tag{2.11}$$

where k_{rel} is the relative momentum between the two particles.

In the case of two species A and B, the scattering rates become slightly more complicated. Firstly, the scattering rate of A with B is different from the scattering rate of B with A. Secondly, the volume occupied by each species in the trap is not the same as the volume that it would occupy by itself.

The total scattering rate for one species in the presence of two species is then given by the sum of the intra- and inter-species scattering rates. For species A, it reads [91]

$$\Gamma_{\mathrm{el}}^{\mathrm{A}} = \frac{1}{2} n_A \left\langle v_{AA} \sigma_{AA} \right\rangle \frac{\mathcal{V}_{2\mathrm{e}}}{\mathcal{V}_{\mathrm{e}}} + n_B \left\langle v_{AB} \sigma_{AB} \right\rangle \frac{\mathcal{V}_{2\mathrm{e}}}{\mathcal{V}_{\mathrm{e}}} \tag{2.12}$$

where $v_{AA}(v_{AB})$ denotes the relative velocity between two particles of A (one particle of A with one particle of B), analogously for the scattering cross-section σ_{AA} and σ_{AB}. The average is done over the relative velocity. In the presence of two species, the rate takes into account the distribution of pairs, and scales by $\mathcal{V}_{2\mathrm{e}}/\mathcal{V}_{\mathrm{e}}$ with the total volume

$$\mathcal{V}_{\mathrm{e}} = \int \exp\left(-\left[V_{\mathrm{t}}(r)/(k_{\mathrm{B}}T)\right]\right) dr, \tag{2.13}$$

and the volume given by the distribution of pairs [91]

$$\mathcal{V}_{2\mathrm{e}} = \int \exp\left(-2\left[V_{\mathrm{t}}(r)/(k_{\mathrm{B}}T)\right]\right) dr. \tag{2.14}$$

Three-body losses

Three-body recombination processes lead to major losses and they are by far the dominating loss channel for ground state bosons in the ODT [81, 82, 83, 84]. They are due to processes in which two atoms enter the last bound state upon collision with a third atom that ensures momentum and energy conservation, the binding energy (of the order of $\hbar^2/(m{a_\mathrm{s}}^2)$ [93]) is then released in the form of kinetic energy, which is typically sufficient to expel all three atoms from the trap. In the low energy limit, where the scattering properties are well described by a_s, and such that for $a_\mathrm{s} \gg a_\mathrm{vdW}$, with a_vdW van der Waals length, and $a_\mathrm{s} \ll \lambda_\mathrm{dB}$, the three-body loss rate coefficient L_3 scales as [91]

$$L_3 = 3C\frac{\hbar}{m}{a_\mathrm{s}}^4. \tag{2.15}$$

Here, the factor of 3 comes from the fact that the three atoms are lost, C is a constant whose value is typically C=0–70 depending on the details of the short-range three-body interaction and it oscillates near a FR [84]. The losses are given by

$$\frac{\dot{N}}{N} = L_3\left\langle n^2\right\rangle. \tag{2.16}$$

The released energy leads also to heating processes proportional to the ${a_\mathrm{s}}^4\left\langle n^2\right\rangle$. Cs, thanks to the large tunability of a_s, has been instrumental in confirming this scaling law [94]. In the experiments shown in this thesis $a^\mathrm{Rb}_\mathrm{vdW} = 82.5\,a_0$ $a^\mathrm{Cs}_\mathrm{vdW} = 101.0\,a_0$ for Rb and Cs [4], respectively. The scattering lengths are $a_\mathrm{Rb} = 110\,a_0$ and $a_\mathrm{Cs} = 200\text{–}2400\,a_0$. Note that for the trapped gas, as n depends on the temperature as discussed above, the three-body losses implicitly depend on the temperature ($\propto T^2$). This trend is valid only for low a_s. For $a_\mathrm{s} \gg \lambda_\mathrm{dB}$ the unitarity limit is entered and the dependence of L_3 on a_s is lost, while a dependence on λ^4_{dB} emerges [95, 96, 97].

2.5 Bose-Einstein condensation in a harmonic trap

In 1924, Satyendra Nath Bose *et al.*[98] and Albert Einstein [99] predicted that below a critical temperature T_c, the quantum statistic gives rise to a macroscopic occupation of the lower energy state. This macroscopic occupation constitutes an entirely new state of matter known as Bose-Einstein condensate, BEC. In particular, the condition for condensation is given by [3]

$$\lambda_\mathrm{dB}(T_c)^3 n = g_{3/2}(1) \sim 2.61 \tag{2.17}$$

where n is the atomic density and $g_n(z) = \sum_{l=1}^{\infty}(z^l/l^n)$. The first experimental evidence of condensation of dilute alkali gases was shown in 1995 experimentally in two seminal works in the group of Eric Cornell and Carl Wieman [1] and in the group of Wolfgang Ketterle [2]. In both cases a magnetic trap was used to confine and cool the atoms, this trap could be approximated with a harmonic potential. Similar to the quantities seen in the previous section, the condensation criteria in a harmonic trap can be derived from the atom number, temperature, and trap parameters. The critical temperature is defined as [3]

$$k_\mathrm{B}T_\mathrm{c} = \hbar\bar{\omega}\left(\frac{N}{g_3(1)}\right)^{1/3} \simeq 0.94\,\hbar\bar{\omega}N^{1/3} \tag{2.18}$$

where $g_3(1) \sim 1.202$. This means that for a cloud of $N = 10^4$–10^7 atoms and $\bar{\omega} \sim 2\pi\,100\,\mathrm{Hz}$ condensation happens between 10^2–$10^3\,\mathrm{nK}$ [3]. The condensate fraction N_0/N depends on the temperature and is [3]

$$\frac{N_0}{N} = 1 - \left(\frac{T}{T_c}\right)^3 \tag{2.19}$$

In the non-interacting case, a BEC is extremely fragile. In the presence of interactions, this is not true anymore. This case was explored by Nikolay Bogoliubov [100], who showed that for a dilute gas (i.e., the interatomic distance is much larger than the particle size) with weak interactions, emerges a critical velocity. Anything moving slower than the critical velocity does not create excitations in the condensate. This phenomenon was already known from Helium experiments as superfluidity [101, 102].

The BEC in this thesis constitutes the endpoint of the cooling sequence as described in Chapter 3 and revised in Chapter 6 and it is the starting point for the formation of the molecules and the results presented in Chapter 4 and Chapter 5. The conditions for superfluidity in the optical lattice are at the base of Chapter 5 and are discussed therein.

2.6 Achieving quantum degeneracy through confinement manipulation

Since many parameters of the cloud depend on the properties of the confinement, as seen above, it should come as no surprise that it is possible to engineer a series of manipulations on the trap geometry to vary the cloud parameters and in particular to increase the PSD to reach condensation. In the RbCs project, we use two kinds of manipulations, we modify the shape of the ODT with the dimple trick (Sec. 2.6.1) and we modify the depth and trap frequency of the ODT during forced evaporation (Sec. 2.6.2).

2.6.1 The dimple trick

The dimple trick creates a trap with a geometry that allows a local sharp increase of n_0, thus of the PSD, by thermalization processes [103, 104]. The trick consists in superimposing two optical dipole traps with very different volumes: the reservoir with a large volume $\mathcal{V}_1$, and the dimple with a small volume $\mathcal{V}_2$. In this paragraph, I indicate with 1, and 2 the parameters respectively of the reservoir and of the dimple. Collisions lead to populating both volumes. As the potential depth V_t of the dimple increases, the atoms will populate more and more the dimple, leading to a compression of the gas and an increase in the spatial density with respect to the reservoir. At the same time the atoms that are left in the reservoir act as a thermal reservoir, hence the name. The final temperature of the gas will be T_f and is mainly dominated by the reservoir characteristics. When $V_\mathrm{t}/T_\mathrm{f}$ is of a similar order to $\ln(\mathcal{V}_1/\mathcal{V}_2)$, the final PSD_2 in the dimple increases with respect to the initial PSD_1 in the reservoir as

$$\ln\left(\frac{PSD_2}{PSD_1}\right) = \frac{V_{\mathrm{t}0}/(k_B T_f)}{1 + (\mathcal{V}_2/\mathcal{V}_1)e^{V_{\mathrm{t}0}/(k_B T_f)}} \tag{2.20}$$

The dimple trick has two critical steps, first trapping, i.e., loading, the atoms in the reservoir trap, second transferring the atoms from the reservoir to the dimple. Especially in the second step, it is fundamental to find a good ratio between the elastic and inelastic collisions: a high elastic collision rate is necessary to populate the dimple but the increase in density in the dimple leads to a stark increase of three-body losses, this becomes more and more a problem as the volume ratio increases. On the other hand for a small volume ratio, the increase in phase-space density remains small. A way to address the problem and improve the efficiency of the trick is to decrease the a_s dynamically during the loading of the dimple to ensure the three-body recombination rate is always smaller than the elastic collision rate in the dimple as the density in the dimples increases.

When using large volume ratios the dimple trick is effective enough to directly reach the BEC [104], but as the reservoir volume increases (at a constant number of atoms), the density decreases and consequently the scattering rate. Thermalization in this regime is slow and the time needed to load the dimple increases accordingly. In the RbCs project, in the interest of keeping the entire sequence short, to avoid incurring other problems (of the more disparate natures raging from one-body losses due to background collisions, to buffer memory overflow for the control program), and to keep a high repetition rate for the experiment, the volume ratio is kept around 1000. The dimple trick is used as an intermediate step, followed by the removal of the reservoir trap, and continuing toward quantum degeneracy with forced evaporative cooling as described in the next section. In Chapter 3, I discuss how to apply the trick simultaneously for Rb and Cs and the effect of the cross-talk of the two species in the reservoir trap. In Chapter 6, I discuss the latest characterization of the dimple trick in the RbCs experiment.

2.6.2 Evaporative cooling in the ODT

In the RbCs experiment, the dimple trick seen in the previous paragraph helps to increase the local PSD but it is used only as an intermediate step. Once the reservoir is removed, further cooling is done via forced evaporative cooling [105]. This technique is probably the most common strategy to reach BEC and Fermi gases for cold atoms. It can be applied both in magnetic traps or optical traps with some variations. A review can be found, e.g., in Refs. [106, 78]. In short in Sec. 2.4, I discussed how the final temperature of the atomic cloud T_f relates directly to $V_{\mathrm{t}0}$ of the ODT, since hotter atoms escape the trap and the remaining atoms rethermalize until an equilibrium is reached. By reducing $V_{\mathrm{t}0}$, e.g., with the laser intensity, or less commonly by tilting the potential with an external gradient [107], it is possible to introduce a cut-off in energy of the ODT. Through thermalization, the cut-off in energy of the ODT enforces a reduction of the temperature for the atomic sample. The cooling comes at the cost of losing the high-energetic atoms which are expelled from the trap during thermalization. This process takes the name of forced evaporative cooling as opposed to the plain evaporation seen in Sec. 2.4.

The efficiency of the forced evaporative cooling is typically characterized by the gain in PSD against the loss in the atom number N

$$\gamma = -\frac{\log\left(PSD_\mathrm{f}/PSD_0\right)}{\log\left(N_\mathrm{f}/N_0\right)}. \tag{2.21}$$

Here, I used the subscript 0(f) for the parameters of the initial(final) V_t. The efficiency depends on the cut-off of $V_{\mathrm{t}0}$ and on the losses. In forced evaporative cooling, there is an incremental cut-off applied by using ramps for the trap depth that are sufficiently slow compared to thermalization rates, such that the properties of the atomic cloud follow almost adiabatically the changes in the trap,

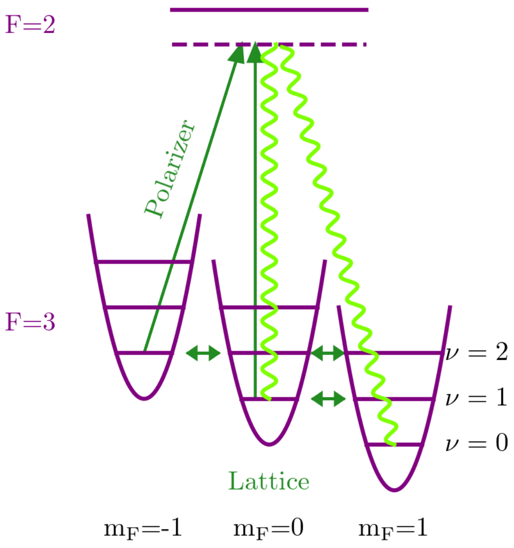

Figure 2.2: Schematic of the dRSC process. The OL drives the resonant transitions between the state with $|m_F + 1, \nu\rangle$ to $|m_F, \nu - 1\rangle$. The polarizer optically pumps the atoms to the m_F with the lower energy while preserving ν. To drive both transitions from $m_F = 0$ and $m_F = -1$, the polarizer needs mixed σ^+, and π polarization.

and/or using multiple steps for the ramps. Good evaporation ramps, for single species, generally yield $\gamma \sim 2.5 - 3$.

In evaporative cooling, either plain or forced, the evaporative losses due to the elastic collisions should be the dominant loss process, with respect to the inelastic three-body losses, which generate heating. It is needless to say that great attention should be given also to having a clean experimental setup that reduces unwanted one-body losses, no resonant light leakages, good vacuum conditions, etc.

2.7 Raman sideband cooling in the lattice

In some experimental sequences, there is a gap in temperature between the lower temperature achievable with the MOT and the typical initial conditions for loading the ODT. In the RbCs project, this gap is about two orders of magnitude. How to bridge such a gap, when present, is a step that varies a lot between cold-atom experiments as a number of techniques are available. In the RbCs project, the choice is to use dRSC [108, 109], as this step has the double advantage of cooling the atoms at constant density and polarizing the cloud at the same time. This cooling step takes place in a deep OL which provides well-resolved vibrational states. It is based on a stimulated Raman process driven by the OL that reduces the vibrational state of the atoms, followed by optical pumping driven by a polarizer beam that transfers the atoms in the higher spin state, as shown in Fig. 2.2. A homogeneous magnetic field shifts the hyperfine states according to Eq. 2.2, bringing into resonance the ν vibrational level in the lattice for a given m_{F} state with the $\nu-1$ level of a different state, typically the $m_{\mathrm{F}}-1$. This way the lattice, not only provides the separation of the vibrational levels but also drives the transition between said levels. The polarizer beam excites the atoms from the lowest m_{F} to an excited state. To address multiple initial hyperfine states it is necessary that the polarizer has a σ^+ mixed with a small π polarization component. The spontaneous emission typically preserves the original ν, when the recoil energy from the photon is smaller than the separation of the vibrational levels [108]. Therefore the atoms end up in the initial m_F state but with a lower ν due to a decrease in ν induced by the Raman lattice. The lower vibrational state in the lowest spin state is dark with respect to both processes, therefore the atoms will accumulate there. Due to the presence of the lattice, the spatial density is unchanged, but the removal of the vibrational energy leads to cooling, therefore the overall PSD increases. The lower achievable temperature is due to off-resonant absorption of lattice photons, for far detuned optical lattices dRSC has been used in combination with the manipulation of the confinement strength to cool Cs atoms directly in a strongly correlated quantum gas [110].

DRSC is a well-established technique for a single species, however simultaneous optimization of dRSC for two species proved a tricky part in the optimization shown in Chapter 6. Starting from the requirement of independent beams for the OL and polarizer of the two species. The atoms of the two species are also subjected to the same magnetic field, but due to the different magnetic moments, the energy shifts between the hyperfine levels are different. The resonance condition is different for the two species and the trap frequencies need to be matched individually. A conceptual approach to the dual-species dRSC is provided in Chapter 3.

2.8 Quantum gas in the lattice

The other regime in which the OL is used in the RbCs project is in conjunction with the BEC. Once the BEC is formed after evaporative cooling in the ODT, the atoms can be transferred to a far-detuned OL. If the lattice depth is ramped up adiabatically, the atoms follow the new ground state of the system, and the quantum character is preserved.

In the regime of a few atoms per lattice site, the structure of the lattice takes a predominant role. In this regime, the system can be described by the Bose-Hubbard model [111]. The Hamiltonian is expressed in the basis of Wannier functions $w_l(\mathbf{x})$, which are localized on the individual lattice sites with index l. The Hamiltonian, expressed in the second quantization formalism, reads

$$\hat{H} = J\sum_{\langle ll'\rangle} \hat{b}_l^\dagger \hat{b}_{l'} + \frac{U}{2}\sum_l \hat{n}_l\left(\hat{n}_l-1\right) + \sum_l \epsilon_l \hat{n}_l. \tag{2.22}$$

The first term describes the tunneling between neighboring sites l, l'. Here J denotes the tunneling energy:

$$J = -\int d^3x\; w^*(\mathbf{x}-\mathbf{x}_l)\left(-\frac{\hbar^2\nabla^2}{2m} + V^{\mathrm{lat}}(x)\right) w(\mathbf{x}-\mathbf{x}_{l'}), \tag{2.23}$$

and $\hat{b}_l^\dagger$, $\hat{b}_l$ are the creation and annihilation operators for a particle at site l. $V^{\mathrm{lat}}(x)$ is the depth of the optical lattice, this is often expressed in units of the recoil energy $\mathrm{E}_{\mathrm{rec}}$ as $V^{\mathrm{lat}} = s\mathrm{E}_{\mathrm{rec}}$. In the lowest lattice band, for large s, $J \sim 4\mathrm{E}_{\mathrm{rec}}/\sqrt{\pi}(s)^{3/4}\exp(-2\sqrt{s})$. The second term of Eq. 2.22 is the on-site interaction with energy

$$U = \frac{4\pi\hbar a_{\mathrm{s}}}{m}\int |w(\mathbf{x})|^4 d^3x, \tag{2.24}$$

typically the prefactor is denoted as the coupling term $g = \frac{4\pi\hbar a_{\mathrm{s}}}{m}$. Finally, in the last term of Eq. 2.22, $\hat{n}_l$ is the particle number operator at site l. This term is the energy associated with the presence of the trap at the individual sites, with slowly varying onsite energy ϵ_{l}. Even at zero temperature, the Bose-Hubbard model supports a quantum phase transition between two different ground states [112, 111], first observed in Ref. [7]. One of these states is the Mott-insulator state (MI), which is characterized by the atomic wavefunctions being strongly localized, while tunneling is inhibited. In a MI, the atoms distribute homogeneously across the OL with a finite number of particles per site, which depends on the initial density and the onsite interaction energy. The other state is a superfluid state (SF), in which the atomic wavefunctions are delocalized thanks to the resonant tunneling. The phase diagram at zero temperature is shown in Fig. 2.3. In the interval shown by the figure, there are several Mott-insulator lobes, with an increasing occupation of the lattice with increasing chemical potential μ, from $n = 1$ up to $n = 5$ atoms per lattice site. Outside the lobes the cloud is superfluid.

In the regime of a large number of atoms and weak interactions ($J \gg U$), i.e. when there is a BEC and the atoms are delocalized in the OL, a mean-field description is appropriate and given by the time-dependent Gross-Pitaevskii equation (GPE)

$$i\hbar\frac{\partial}{\partial t}\psi(\mathbf{x},t) = \left(-\frac{\hbar^2\nabla^2}{2m} + V^{\mathrm{lat}}(\mathbf{x}) + g|\psi(\mathbf{x},t)|^2\right)\psi(\mathbf{x},t), \tag{2.25}$$

where g measures the atomic interaction and $|\psi(\mathbf{x},t)|^2$ is the atomic density.

2.8.1 External forces in lattices

Sometimes, in experimental conditions, the atoms in the lattice are not at equilibrium, but they are in the presence of external forces, like, e.g., gravity. Under the action of a constant force $\mathcal{F}$, the atomic quasi-momentum increases up to the edge of the band [114]. At this point two phenomena might take place: If the speed at which the atom approaches the edge of the band, the atom can tunnel to the higher band, this effect is called Landau-Zener tunneling [115, 116]. Instead at low speed, the atom is reflected at the edge of the band, giving rise to an oscillatory behavior known as Bloch oscillations [117, 118, 119, 120, 121]. The oscillation period is given by:

$$\tau = \frac{\hbar}{|\mathcal{F}d|}, \tag{2.26}$$

with d the lattice spacing. Bloch oscillations are an important part of the discussion in Chapter 5.

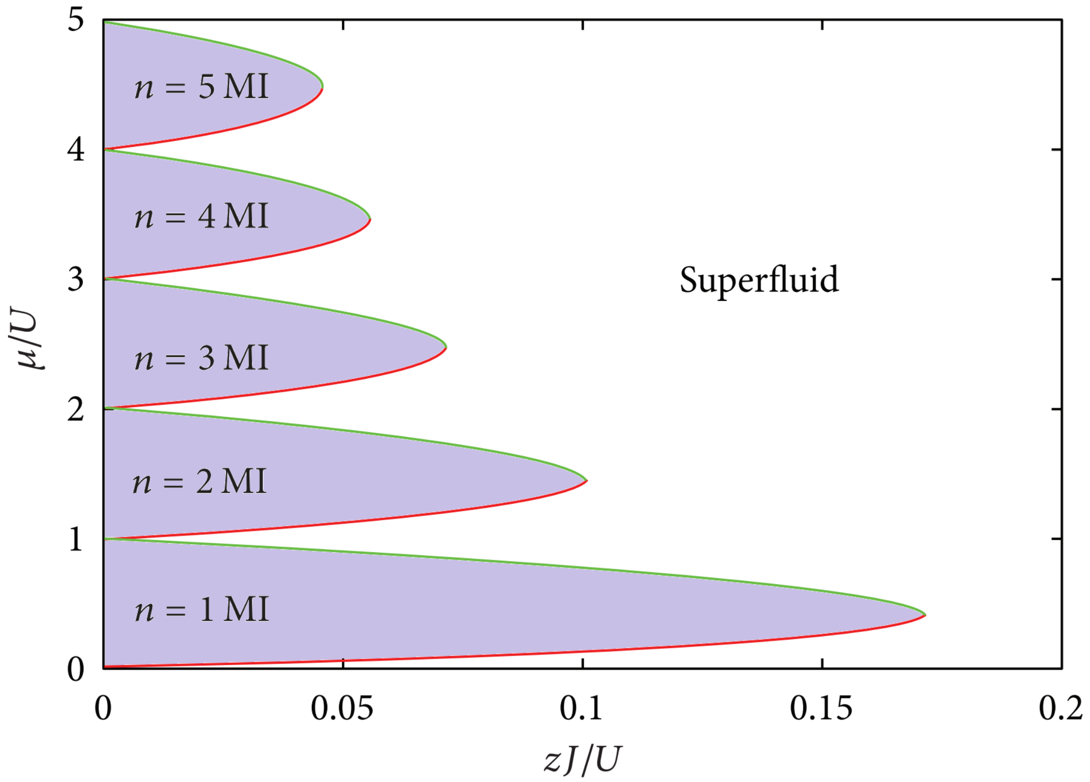

Figure 2.3: Mean-field phase diagram at zero temperature for the first five lobes of the single-band Bose-Hubbard model as a function of the chemical potential μ and the tunneling energy J per tunneling direction z. Both axes have been scaled with the on-site interaction energy. The purple area represents the insulating state with the number of atoms per lattice site indicated in the figure. The white area is superfluid. This figure has been adapted from Ref. [113].

2.8.2 Transporting atoms in the lattice

The GPE formalism is convenient for describing the dynamics of the atoms in the lattice, in the case that the atoms are moving with respect to the lattice. This case can be realized experimentally by either moving the lattice through the atomic sample, typically by shifting in frequency the retroreflected beam, e.g. [122], or by shifting the atoms through the lattice by means of a tight external magnetic [123] or optical [63] trap. In principle, a superfluid can be transported through the lattice without dissipation as long as its velocity is below a certain critical velocity v_c, typically corresponding to the speed of sound in the medium. Once the critical velocity is exceeded the condensate can reduce its energy through the formation of phononic modes [3]. These excitations, known as energetic instabilities, are analogous to the Landau instabilities for a superfluid BEC without the lattice. The critical velocity is given by

$$v_c = \frac{p_c}{m^*} = \min_q \frac{\epsilon(q)}{q} \tag{2.27}$$

with $\epsilon(q)$ the change in energy due to the excitation and m^* is the effective mass of the atoms in the lattice.

In Chapter 5, I will address the critical transport velocity. In this context, it will be initially compared to the atom group velocity, which varies significantly between the two realizations of transport mentioned above. When the lattice moves through the atoms the atoms are almost at rest with respect to the lab frame, and their group velocity is provided by [3]

$$v_{\mathrm{g}}^{\mathrm{lat}} = \frac{\partial E(q)}{\partial q} \tag{2.28}$$

where E(q) is the dispersion relation of the populated energy band. When instead a tight trap is applied and moved through the lattice, the group velocity corresponds roughly to the trap velocity $v_{\mathrm{g}}^{\mathrm{trap}} \sim v_{\mathrm{trap}}$ [124]

2.8.3 Lattice with dipolar particles

For dipolar molecules and dipolar atoms in the OL, both the Bose-Hubbard model and the GPE formalism can be used but, in both formalisms, it is necessary to add a term for the long-range dipole-dipole interactions. In the presence of competing contact and dipolar interaction, beyond mean-field effects can become visible. The new phase diagrams become richer with the emergence of new phases of matter like the supersolid [125], ordered insulating phases with partial filling [20], and interesting topological phases [126].

2.9 Scattering in confined dimensions

In this section and the next, I will describe the problem of scattering in tight external confinement, which ties in directly to the results reported in Chapter 4. Therefore I will provide a broader historical perspective as well as a general view of the main theoretical results. Some of the results presented in this section can be found in Ref. [127].

In the previous sections, the description of the two-body scattering problem for the atoms in a three-dimensional (3D) space was reduced to a single parameter, the s-wave scattering length a_{s} (Sec. 2.2.3). In 1998, Olshanii predicted that in the presence of a strong transversal confinement, the description of the scattering changes drastically [70] and a_{s} alone is not a good representation of the scattering properties of the system. He considered two atoms in a one-dimensional system with harmonic confinement along two directions, while the atoms are free to move and scatter along the third direction. For all three directions, he assumed that the energy associated with the motion is lower than the energy of the first trap state $\hbar\omega_\perp$. Finally, he approximated the interactions with Huang's regularized pseudo-potential [128]. The resulting system can be treated by splitting center-of-mass (CM) and relative motion (RM), giving rise to the Schrödinger equation for the relative motion:

$$\left\{ \frac{\hbar}{2\overline{m}} \frac{\partial^2}{\partial z^2} + g\delta\left(\vec{r}\right) \frac{\partial}{\partial r}\left(r\cdot\right) + H_\perp(p_x, p_y, x, y) \right\} \Psi(r) = E\Psi(r), \tag{2.29}$$

where z is the relative position along the longitudinal direction of the trap, which, in this description, is the only direction in which scattering is allowed, and x and y are the transversal directions,

$\overline{m} = m/2$ is the reduced mass, for two scattering atoms of mass m, $H_\perp$ is the 2D harmonic oscillator Hamiltonian operator describing the motion perpendicular to the trap axis, and $g = 2\pi\hbar^2 a_\mathrm{s}/\overline{m}$ is the coupling parameter.

The asymptotic one-dimensional scattering wave function along z can be written as a linear combination of plane waves, whose amplitude depends on the different angular momentum of the scattering atoms along the z-axis. The amplitude depends on the parity of the angular momenta. For odd angular momentum states, the amplitude is zero, for even angular momentum states the amplitude is [70]

$$f_\mathrm{even}\left(k_z\right) \simeq -\frac{a_\mathrm{1D}}{1 + ik_z a_\mathrm{1D}} \tag{2.30}$$

Therefore the scattering cross-section for these events

$$\sigma_\mathrm{even} = |f_{even}(k_z)|^2 = \frac{a_\mathrm{1D}^2}{1 - (k_z^2 a_\mathrm{1D})^2} \tag{2.31}$$

has the same aspect of the three-dimensional cross-section, except for the fact that the s-wave scattering length a_s has been replaced by an effective one-dimensional scattering parameter a_1D, known as the 1D scattering length, which is related to a_s as follows [70]:

$$a_\mathrm{1D} = \frac{a_\perp^2}{2a_\mathrm{s}}\left(1 - C\frac{a_\mathrm{s}}{a_\perp}\right). \tag{2.32}$$

Here $a_\perp$ is the oscillator length in the confined directions and C is a numerical factor of the form

$$C = \lim_{s\to\infty}\left(\int_0^s \frac{ds'}{\sqrt{s'}} - \sum_{s'=1}^{s}\frac{1}{\sqrt{s'}}\right) = 1.4603. \tag{2.33}$$

It can be shown [70], that the 1D coupling parameter, in this picture, has the form

$$g_\mathrm{1D} = -\frac{\hbar}{\overline{m}a_{1D}} \propto g\left(1 - C\frac{a_\mathrm{s}}{a_\perp}\right) \tag{2.34}$$

The coupling diverges when $a_\perp/a_s = C$, giving rise to a single resonance in the scattering properties that does not exist without the confinement. In the proximity of this resonance, it is possible to change a_1D by changing $a_\perp$ as well as by changing a_s.

The scattering process could be described similarly to a FR [129]. The main difference is that the bound state involved was, as described by Olshanii, a “virtual excitation of the high-energy axially symmetric modes". Such a state cannot be populated, therefore, at the resonance, it is possible to tune the scattering length but not to coherently form molecules. As a consequence, losses are also unlikely to take place at resonance [130]. Another important aspect of Olshanii’s prediction is that it avails itself only of parameters like a_s and $a_\perp$ and does not depend explicitly on the specifics of the systems, like atomic masses, or the details of how the harmonic potential is created. Hence the prediction inherits the universality property of a_s.

The resonance described by Olshanii is what in the years following his publication was dubbed elastic confinement-induced resonance (ECIR). Similar theoretical investigations have been extended to the case of a two-dimensional system [68]. An important difference in the occurrence of resonances in these two cases is represented by the resonance condition: While the 1D resonance predicted by Olshanii happens at $a_\mathrm{s} > 0$, the ECIR in 2D is predicted at $a_s < 0$.

There is nowadays general agreement on the theory of ECIR. In the 1D and 2D cases ECIR have found first experimental realization in Ref. [10] and Ref. [69], respectively. In particular, the 1D case is now routinely exploited in experiments, for example, for achieving strongly interacting regimes like the super Tonks-Girardeau regime with bosons [10] or fermions [131], for the investigation of super-orbital spin exchange in OL [132], or to avoid thermalization in the realization of scar states [133].

However, the early experiments generated some confusion across the community.

In 2005 Moritz *et al.* [134] showed the formation of molecules on a confinement-induced resonance in a 1D guide. A few years later, Haller *et al.*, after using a confinement-induced resonance to study quantum phases in a 1D systems [10], did the first systematic study of the resonance in a 1D system and at the 1D–2D crossover [71] .

In Haller's experiment [71], a BEC of Cs atoms was prepared in a crossed ODT and subsequently loaded into a 2D OL, which traps the atoms in 1D tubes. They tune a_s on a FR at 48 G, which is 164 mG wide [135]. They observed an atom loss congruent with the prediction of the ECIR theory, and they showed the relation between the lattice confinement $a_\perp$ and a_s, confirming experimentally the value of C.

In the same work, they gradually lowered the confinement in one of the directions and observed the crossover from a 1D to a 2D system. At small differences between the strength of the confinement along the two directions, it is observed that the resonance peak splits as a consequence of the different excitation energy along the two directions, and furthermore, a structure emerged on one of the peaks, in obvious disagreement with the single resonance picture from Olshanii [70]. An even more striking result was that even in the 2D limit, the resonance was found at $a_\mathrm{s} > 0$, contrary to the prediction of a resonance at negative scattering length from Ref. [68]. On the contrary, Frölich *et al.* [69] observed the resonance in the 2D case at attractive interactions as expected.

The discrepancy between the two experiments, and between theory and experiments, made it evident that the theoretical picture surrounding elastic confinement-induced resonances was either incomplete or incorrect with respect to the experimental conditions.

2.10 Inelastic confinement-induced resonances

In the following, I will show that the experiment of Ref. [71] did not map exactly to the theoretical derivation proposed by Olshanii (Sec. 2.9). The perfectly harmonic trap used in the treatment of the ECIR is actually a poor representation of the conditions of the experiment in Ref. [71], where the trapping potential is generated by an OL and only at the very bottom of the individual wells the potential can be approximated by a harmonic potential, as shown in Fig. 2.4. Parallel studies by Peng [136] and Sala [72] introduced perturbatively the anharmonicity in the treatment of the scattering problem. They found that the anharmonicity couples CM and RM motion and that this coupling allows an additional kind of resonance. They have called it, respectively, anharmonic confinement-induced resonance and inelastic confinement-induced resonance (ICIR). An ICIR emerges when the energy of two scattering atoms becomes equal to the energy of a bound state with transversal CM

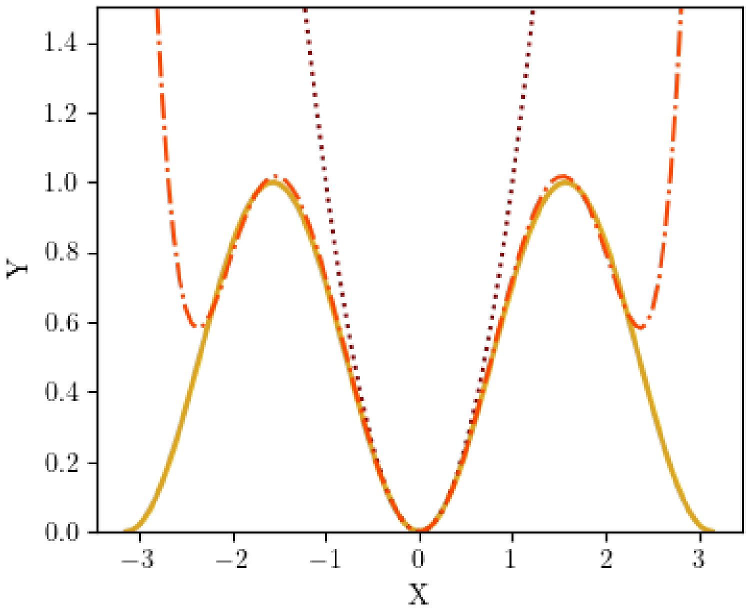

Figure 2.4: Schematic representation of different lattice models: the continuous line in yellow represents the intensity of the optical lattice in arbitrary units and it is obtained by $y = sin^2(x)$, the maroon dotted line is the harmonic approximation as used for modeling the ECIR $y = x^2$, the orange dashed-dotted is a sextic potential as used for modeling ICIR and is obtained here as $y = x^2 - 0.3x^4 + 0.025x^6$.

excitation (Sec. 2.11). In the presence of the CM-RM coupling, whose origin I will discuss below, the energy can be traded between the two motions, leading to the formation of a bound state in addition to the coupling due to the a magnetic FRs.

In the ICIR theory

- there are multiple ICIRs, the exact number is given by how many CM excited states the confinement can support
- the bound states involved in the ICIRs are real, therefore molecule formation is allowed and three-body losses are likely to take place.

The differences between ECIR and ICIR are summarized in Tab. 2.1. It is now commonly agreed that the resonances observed in Ref. [71] are ICIRs, while the resonances observed in Ref. [10] and Ref. [69] were ECIRs. The coherent formation and dissociation of molecules on an ICIR in 1D were further confirmed in Ref. [137].

The coupling term between RM and CM can have different origins. Despite the nomenclature, an ICIR not only can originate from the anharmonicity of the trapping potential, but it also appears in the presence of scattering atoms with different masses or different polarizabilities. For example, it has been shown [138] that a mass imbalance between the scattering atoms leads to the emergence

	ECIR	ICIR
Bound state	Virtual bound state	Real bound state
Number of resonances	One resonance	Multiple resonances
Other conditions	None	RM-CM coupling

Table 2.1: Summary of the main differences between elastic and inelastic confinement-induced resonances.

of ICIRs also in the regime of $a_s \ll a_h$. Additionally, the possibility to extend ICIRs also to dipolar systems [139] and to excitons in quantum dots [73] broadens the interest in the topic.

2.11 ICIRs in a lattice

After the initial demonstration in the 1D case, ICIRs were extended to different geometries of the confinement. Among them, in the following, I want to review the case of two atoms in a potential well, which is used as a starting point for the modeling of the experimental data in Chap. 4. The behavior of the atoms in the well uses a full 3D description, but the confinement along the three directions limits the motion to effectively a quasi-0D system.

For simplicity, and consistency with the experiment, the analysis is limited to the case where the CM-RM coupling is due to the anharmonicity of the potential and follows the treatment used in Ref. [130]. Such an approach consists in first deriving the states for the harmonic wells and then adding perturbatively the anharmonic corrections and the RM-CM coupling.

The Hamiltonian for two interacting atoms, at positions $\vec{r_1}$, $\vec{r_2}$, can be written in center-of-mass and relative coordinates. Using the substitution

$$\vec{R} = \frac{\vec{r_1} + \vec{r_2}}{2}, \qquad \vec{r} = \vec{r_2} - \vec{r_1}, \tag{2.35}$$

the Hamiltonian is

$$H\left(\vec{r}, \vec{R}\right) = T_{\mathrm{RM}}\left(\vec{r}\right) + T_{\mathrm{CM}}\left(\vec{R}\right) + V_{\mathrm{RM}}\left(\vec{r}\right) + V_{\mathrm{CM}}\left(\vec{R}\right) + U_{\mathrm{RM}}\left(\vec{r}\right) + W\left(\vec{r}, \vec{R}\right). \tag{2.36}$$

Here, $T_{\mathrm{RM(CM)}}$ represents the kinetic-energy operator for the RM(CM) motion, V_{RM} and V_{CM} are the separable parts of the external potential. Assuming that the lattice is centered at the origin of the axes, they take the form $V_{\mathrm{RM}}(\mathbf{r}) = 2sE_{\mathrm{R}} \sum_i \sin^2\left(kr_i/\sqrt{2}\right)$ and $V_{\mathrm{CM}}(\mathbf{R}) = 2sE_{\mathrm{R}} \sum_i \sin^2(kR_i/\sqrt{2})$. W is the inseparable part of the potential and gives rise to the CM–RM coupling. It is given by $W(\mathbf{r}, \mathbf{R}) = -4sE_{\mathrm{R}} \sum_i \sin^2\left(kr_i/\sqrt{2}\right) \sin^2(kR_i/\sqrt{2})$. U_{RM} represents the inter-particle interaction, which acts only on the RM part of the system [130].

All the terms in the Hamiltonian allow for different approximations. I will review here a basic case, assuming a simple interaction potential and an expansion to the sixth order for the lattice site. More elaborate alternatives have been elaborated to explain the data of Chapter 4, respectively Ref. [74], these elaboration are presented in the next sections.

2.11.1 A simple case

The interaction potential can be approximated by a regularized $\delta-$pseudopotential of the form [140]

$$U_{\mathrm{RM}}(\vec{r}) = \frac{8\pi\hbar^2 a_{\mathrm{s}}}{m}\delta(\vec{r})\frac{d}{d(\vec{r})}. \tag{2.37}$$

This is a typical approximation for contact interaction, the pointlike interaction given by the δ-function assumes the two atoms to be at the same position, hence it implies they are on the same lattice site. The eigenstates for the RM motion and CM motion can be initially found by approximating the lattice site as a harmonic trap. For the RM motion the solution was first derived by Busch *et al.* [141]. In order to do so, in Ref. [141] they expand the wavefunction on the base of the 3D isotropic harmonic oscillator, i.e. for the case where the trap frequency $\omega = \omega_x = \omega_y = \omega_z$. The states with $l \neq 0$ are not perturbed from the pointlike interaction, therefore only the states with $l = 0$ contribute to the total wavefunction [141]. With this basis, the eigenvalues E^{RM} of the RM harmonic Hamiltonian are given implicitly by

$$\sqrt{2}\frac{\Gamma\left(-\frac{E^{\mathrm{RM}}}{2}+\frac{3}{4}\right)}{\Gamma\left(-\frac{E^{\mathrm{RM}}}{2}+\frac{1}{4}\right)} = \frac{1}{a_{\mathrm{s}}}, \tag{2.38}$$

where $\Gamma()$ is the well-known gamma function. The eigenstates are schematically reproduced in Fig. 2.5. Among the various states, it is possible to recognize the bound state of energy E_{b}, which goes to negative infinite energy when a_{s} goes to 0^+, and several unbound states, whose energies in the following are denoted by E_i^{RM} with i=1, 2,... . In the course of this thesis, I will always work with $a_{\mathrm{s}} > 0$. Further generalization of the energy of the bound state in the case of anisotropy can be found in Ref. [138].

Using again the approximation of a harmonic well, the CM states are simply given by the harmonic oscillator states of energies:

$$E^{\mathrm{CM}} = n\hbar\omega \tag{2.39}$$

Since the CM-RM coupling is fairly weak for typical anharmonicity of the OL, in first approximation the position of an ICIR can be found using only CM and RM states (the coupling is still necessary to obtain the avoided crossing). The energy of the lowest trap (unbound) state can be written as

$$E_1^{\mathrm{RM}} = E_0 + \hbar\omega. \tag{2.40}$$

The resonance condition is met when the energy of the least bound state E_b^{RM} plus the energy Δ_n due to the CM excitation to the $n-$th state matches the energy of the lowest bound state

$$E_b^{\mathrm{RM}} + \Delta_n = E_1^{\mathrm{RM}}. \tag{2.41}$$

In the harmonic approximation, Δ_n is given by the energy of the center-of-mass excitation: $\Delta_n = E_n^{\mathrm{CM}} - E_{(0,0,0)}^{\mathrm{CM}}$, where E_n^{CM} denotes an arbitrary CM excitation and $E_{(0,0,0)}^{\mathrm{CM}}$ the lower CM state. Fig. 2.6 is a slightly more complicated case, reporting the RM states as described in Ref. [141] and reported in Fig. 2.5 and a slightly more advanced version of the CM states explained in Sec. 2.12.

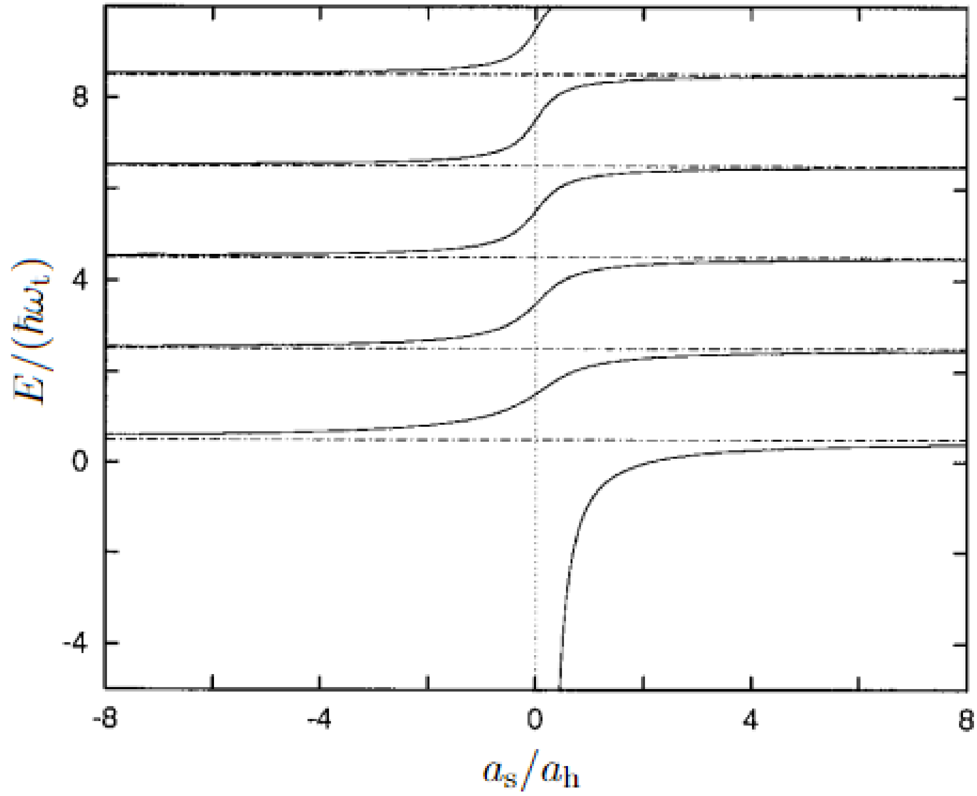

Figure 2.5: Energy of the relative motion eigenstates in a 3D harmonic trap in units of $\hbar\omega$ as a function of $a_0 = a_\mathrm{s}/a_\perp$. This figure has been adapted from Ref. [141].

To account for the coupling between CM and RM motion, it is necessary to consider the anharmonicity of the lattice site. For the case of a well derived from an optical lattice, a good way to approximate the lattice potential is to use a sextic potential as shown in Fig. 2.4. This allows calculating the coupling W but at the same time, it also introduces some higher-order corrections to the separable part of the potential. Again using a single well, implies that the two atoms are on the same site. For an isotropic lattice, i.e., with equal depth along the three spatial directions, the potential along the three directions can be separated and the total potential can be obtained as the sum over the different lattice directions $j = x, y, z$. The optical lattice potential for two particles can be written as

$$V = V_j^\mathrm{lat} \sin^2(k_j(r_1)) + V_j^\mathrm{lat} \sin^2(k_j(r_2)) = V_j^\mathrm{lat} \sin(k_j R) \sin(k_j r) \tag{2.42}$$

where k_j indicates the lattice wavevector in the j direction and V_j^lat the lattice depth in the j direction. The Taylor expansion of the potential to the sixth order around the center of a well gives the three following terms [130]

$$\begin{aligned}
V_{\mathrm{RM}}(\vec{r}) &= \sum_{j=x,y,z} V_j^{\mathrm{lat}} \left[\frac{1}{2}k_j^2 r_j^2 - \frac{1}{24}k_j^4 r_j^4 + \frac{1}{720}k_j^6 r_j^6\right], \\
V_{\mathrm{CM}}(\vec{R}) &= \sum_{j=x,y,z} V_j^{\mathrm{lat}} \left[2k_j^2 R_j^2 - \frac{2}{3}k_j^4 R_j^4 + \frac{4}{45}k_j^6 R_j^6\right], \\
W(\vec{r},\vec{R}) &= \sum_{j=x,y,z} V_j^{\mathrm{lat}} \left[-k_j^4 r_j^2 R_j^2 + \frac{1}{3}k_j^6 r_j^2 R_j^4 + \frac{1}{12}k_j^6 r_j^4 R_j^2\right].
\end{aligned} \tag{2.43}$$

It is important to remark that the coupling term W, obtained in this approximation, can only couple states with the same parity of the center-of-mass and relative motion excitation [130].

The anharmonicity also leads to small corrections for both the CM excitation and the trap state energy, those become more and more relevant with increasing excitation energy of the CM [130]

$$\Delta_{(n_x,n_y,n_z)} = \sum_{j=x,y,z} \hbar\omega_j \left[n_j - \frac{\hbar\omega_j}{16V_{1,j}}\left(n_j^2 + n_j\right) + \frac{\hbar^2\omega_j^2}{576V_{1,j}^2}\left(2n_j^3 + 3n_j^2 + 4n_j\right)\right], \tag{2.44}$$

$$E_1^{\mathrm{RM}} = \hbar\omega_z + \sum_{j=x,y,z} \frac{1}{2}\hbar\omega_j - \frac{\hbar\omega_j^2}{32V_{1,j}} + \frac{\hbar\omega_j^3}{384V_{1,j}^2}. \tag{2.45}$$

Therefore, with increasing anharmonicity, small deviations of the resonance position are to be expected. Nevertheless, for an optical lattice generated by the interference of counterpropagating beams, the depth of the lattice that gives the energy separation of the state and the anharmonicity are correlated, making this deviation difficult to identify experimentally. The presence of the coupling gives rise to an avoided crossing that transfers the energy from the RM to the CM motion. Similarly to the FR seen in Sec. 2.2, ICIR can provide tuning of the effective scattering parameter.

2.12 Different models for ICIRs in the lattice

The detection of ICIRs in the 3D lattice, reported in Chapter 4 of this thesis, triggered the refining of the theoretical derivation of ICIRs seen in the previous section. This resulted in two independent and complementary models for the Hamiltonian of two atoms in a OL (Eq. 2.36). The first model, M1 uses a fully analytical treatment, while the second M2 uses a numerical approach. M1 and M2 differ for the treatment of the CM motion and of the interatomic interaction. While both models are able to predict the resonances in the isotropic lattice, only M2 can be further extended to the anisotropic lattice. In the discussion, I will use ψ to refer to the RM motion states, with the subfix ψ_b^{RM} for the bound state and ψ_i^{RM} for the i-th RM trap state ($i = 1, ...$). The CM states are instead referred to by ϕ^{CM}, their excitation along the three directions is represented with the notation $\phi^{\mathrm{CM}}(n_x, n_y, n_z)$.

2.12.1 Model M1

So far, I reported a generic derivation of ICIR where both RM and CM are treated in a sextic-potential, and the interaction is described by a δ-pseudopotential. M1 differs from this generic description, by accounting for the full lattice potential for the CM. M1 was derived for us by Manuele Landini, it is based on Ref. [130] and it has many similarities with the modelling done in Ref. [142]. I worked with this model for a while and the finer and final details on the calculations are owed to Camilo Cantillano. In the isotropic lattice the potential can be factorized along the three directions of motion x, y, z. For each direction of motion $i = x, y, z$, the CM component of Eq. 2.36, the eigenvectors ϕ_i^{CM} and eigenenergies E_i^{CM} can be found as

$$\left(-\frac{\hbar^2}{2m}\left(\frac{d}{dR_i}\right)^2 + 2s\mathrm{E}_{\mathrm{rec}}\sin^2\left(k_{\mathrm{l}}R_i\sqrt{2})\right)\right)\phi_i^{\mathrm{CM}} = E_i^{\mathrm{CM}}\phi_i^{\mathrm{CM}}, \tag{2.46}$$

where s indicates the depth of the OL in units of $\mathrm{E}_{\mathrm{rec}}$, and R_i is the CM position of the atoms along the direction i, and k_{l} is the lattice wave vector. Using the substitutions $x = k_{\mathrm{l}}R_i/\sqrt{2}$, $q = -s$ and $a_i = 2E_{i,\mathrm{CM}}$, Eq. 2.46 can be written as:

$$\left(-\frac{d^2}{dx^2} + 2q\cos(2x) + a_i\right)\phi_i^{\mathrm{CM}} = 0, \tag{2.47}$$

which has the form of the Mathieu equation [143]. Its eigenvalues can be computed analytically and they give the energy of the CM:

$$E_{\mathrm{CM}} = \frac{1}{2}\left(3s + \sum_i a_i\right). \tag{2.48}$$

The eigenfunctions ϕ_i^{CM} are periodic and correspond to the Bloch functions.

For the RM component of Eq. 2.36, the energy is computed by using the δ-pseudopotential as discussed for the generic case in Sec. 2.11. Its eigenenergies are the same as Eq. 2.38 and the wavefunctions ψ^{RM} are described by:

$$\begin{aligned}\psi^{\mathrm{RM}}(\mathbf{r}) =& \frac{1}{2\pi^{3/2}}Ae^{-\frac{r^2}{2a_h^2}}\Gamma\left(\frac{3}{4} - \frac{E^{\mathrm{RM}}}{2\hbar\omega}\right)\\ &\times\mathcal{U}\left(\frac{3}{4} - \frac{E^{\mathrm{RM}}}{2\hbar\omega}, \frac{3}{2}, \frac{r^2}{a_h^2}\right),\end{aligned} \tag{2.49}$$

where $\mathcal{U}$ denotes the confluent hypergeometric function [144]. The crossings of the RM states with the CM states give the ICIR positions. The states $\psi_b^{\mathrm{RM}}\phi^{\mathrm{CM}}(n_x, n_y, n_z)$, respectively $\psi_i^{\mathrm{RM}}\phi^{\mathrm{CM}}(n_x, n_y, n_z)$ obtained by M1 are shown in Fig. 2.6. The bound states go to negative energy for $a_{\mathrm{s}} \to 0$, and their energy changes significantly similarly to the states of two atoms in a trap. The widths of the excited bound states depend on the width of the relative lattice band. The trap states being identified via the sextic potential are instead discrete states and are the same as derived by Busch [141] and shown in Fig. 2.5. The coupling term, not shown in Fig. 2.6, is calculated from the sextic expansion analogously to Sec. 2.11. The crossing positions are evaluated numerically.

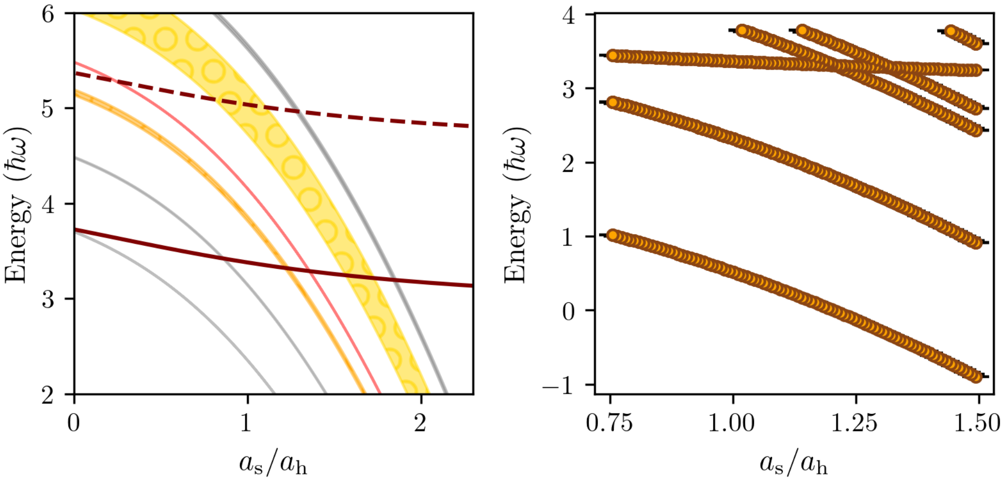

Figure 2.6: Theoretical crossing for ECIRS. Left eigenstates from M1. The shaded area is due to the width of the OL bands for the CM states. In colors the ψ_b^{RM} with CM excitation that are responsible for the resonance shown in this thesis: orange $\phi^{\mathrm{CM}}(2,2,0)$, red $\phi^{\mathrm{CM}}(4,0,0)$, yellow with pattern $\phi^{\mathrm{CM}}(6,0,0)$. In grey other states from lower to higher energy at $0\,a_{\mathrm{s}}$, $\phi^{\mathrm{CM}}(2,0,0)$, $\phi^{\mathrm{CM}}(3,0,0)$, $\phi^{\mathrm{CM}}(4,2,0)$. In brown the trap states: solid line ψ_0^{RM}, dashed ψ_2^{RM}. Right: configurations according to M2.

2.12.2 Model M2

M2 has been developed by the collaboration between Fabio Revuelta[1] and Alejandro Saenz[2] and, similarly to M1, it stems from the derivation in Ref. [130].

Here, the CM motion is treated in the sextic potential, as described in Sec. 2.11. The interaction between the two atoms is modeled by taking into account the Born-Oppenheimer potential, following the approach in Ref. [145], contrary to the δ-pseudopotential which was used in the generic case and in M1. These *ab-initio* calculations based on Cs would require an incredibly large amount of computational capabilities, due to the large number of molecular states. Assuming that ICIRs depend only on a_{s} and a_{h}, it is possible to calculate their position on any other atomic species. In particular, M2 computes ICIRs for two Li atoms, which have only 11 bound states. This substitution has already been successful in representing the 1D confinement-induced resonance for Cs [72]. For each direction the potential is expanded to the sixth order similar to what has been shown in Eq. 2.43. The wavefunctions are calculated in what is called configuration interaction or full diagonalization method [145], for both RM and CM. The basis was built using B-splines [146] for the radial part, and spherical harmonics for the angular part. The eigenstates of the Hamiltonian with this choice are described by configuration $\Phi_{i,j} = \psi_i^{\mathrm{RM}}\phi^{\mathrm{CM}}\,(n_x, n_y, n_z)$ as above. The depth of the potential for Li in the simulations $V_i^{\mathrm{Li}} = s^{\mathrm{Li}}\mathrm{E}_{\mathrm{rec}}^{\mathrm{Li}}$ in comparison to the potential for Cs in the experiment $V_i^{\mathrm{Cs}} = s^{\mathrm{Cs}}\mathrm{E}_{\mathrm{rec}}^{\mathrm{Cs}}$ was chosen such that the depth of the OL is the same when expressed in

---

[1] Grupo de Sistemas Complejos, Escuela Técnica Superior de Ingeniería Alimentaria y de Biosistemas, Universidad Politécnica de Madrid, Av. Puerta de Hierro, 2, 28040 Madrid, Spain.

[2] Institut für Physik, Humboldt-Universität zu Berlin, Newtonstraße, 15, 12489 Berlin, Germany

units of the respective $\mathrm{E}_{\mathrm{rec}}$, i.e. $s^{Li} = s^{Cs}$. This choice implies $V_i^{\mathrm{Li}} \neq V_i^{\mathrm{Cs}}$. The results obtained by modelling a single isotropic well with M2 are reported in Fig. 2.6. Qualitative and quantitatively these results are consistent with M1.

Chapter 3

Mixing Rb and Cs

3.1 Introduction

The formation of a BEC, and more in general of a degenerate gas, is now achieved routinely in laboratories for a number of species. The procedure uses mostly the techniques described in Chapter 2, with few variations. Nevertheless, when mixing two species, bringing them to be in the degenerate state at the same time is not as simple as repeating the same procedure twice. On one end, the problem of which steps are suited for each species is still central, but now for each step and for each species, it is necessary to question also what will happen to the other species in the meantime, e.g., can it survive in the experimental conditions required to cool the other species? Can it coexist with the other species at the same location? Does mixing it with the other species help to cool it down or does it heat it up? *etc.* In the end, the combination of techniques used becomes almost unique for each two-species experiment.

In this Chapter, I describe the pathway to the simultaneous condensation of Rb and Cs in the RbCs project in Innsbruck, the formation of molecules, and their transfer to the ground state. In Sec. 3.2, I first justify the choice of the two species and introduce the properties of Rb and Cs. In Sec. 3.3–Sec. 3.5, respectively, I provide a qualitative overview of the experimental sequence, the coil system for the magnetic field, and the main light sources and their handling. The individual steps of the experimental sequence that lead to the cooling and trapping of the atomic species are detailed according to their order in Sec. 3.6–Sec. 3.11. In Sec. 3.12, I give a quick overview of the pathway from the association of the atoms into molecules to the transfer of the molecules to the ground state. The experimental sequence described in Sec. 3.6–Sec. 3.11 is the one used for the results shown in Chapter 4 and Chapter 5. The changes to the experimental setup and the optimization of the experimental sequence described in Chapter 6 affect mainly the content of Sec. 3.6–Sec. 3.10. The topics presented in this Chapter are scattered on a number of Ph.D. theses authored by the people preceding me on the project, more details can be found in Refs. [147, 148, 149, 150, 151, 124].

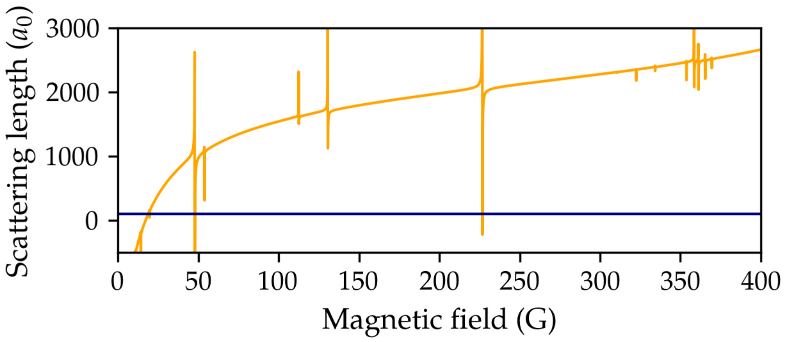

Figure 3.1: Intraspecies scattering length as a function of the magnetic field, for Rb in blue and for Cs in orange [155]

3.2 Why Rb and Cs

In the experiment, we use ^{87}Rb and ^{133}Cs to form molecules via magneto-association. At the time when the RbCs project started, the other main molecule under examination to be formed by magneto-association of ultracold atoms was KRb [152, 153]. The main difference between the two combinations is that RbCs are bosons, while the investigation with KRb used the fermionic isotope of K, resulting in fermionic molecules. RbCs molecules have a larger electric dipole moment 1.22 D [31, 154], with respect to the 0.76 D of KRb [62], and, contrary to KRb, RbCs molecules are chemically stable. With little knowledge of molecular collisions and no knowledge of sticky collision, chemical stability was considered relevant to the long lifetime of the molecules. Actually, the RbCs project was the first to report the experimental observation of anomalous losses of molecules in the absolute ground state [31] and played an important role in stimulating the discussion on sticky collision.

From a technical point of view, the simultaneous manipulation of the two species is made relatively easy by similar magnetic-moment-to-mass ratios between the two species. At low magnetic field, the ratios differ only by $\sim 4\%$. This means that the effect of the magnetic fields on the two species can be considered the same for many purposes, as it will be better described in the following sections.

In the magnetic field region discussed in this thesis, which, as will be seen in the course of this Chapter and the next, ranges 20–360 G, scattering properties are also quite favorable. Rb and Cs scattering lengths are shown in Fig. 3.1. Rb scattering length a_{Rb} is constant at about $\sim 110\,\mathrm{a}_0$, as there are no FRs in this region. This makes Rb scattering insensitive to the magnetic field. On the contrary, Cs scattering length has a high tunability, thanks to a large combination of broad and narrow FRs. This implies that, during the early stages of the experimental sequence, Cs scattering length can be tuned by changing the magnetic field between $\sim 21-50$ G, e.g., to optimize evaporative cooling, without the field affecting Rb scattering properties. The background interspecies scattering length a_{RbCs} is large ($\sim 650\,a_0$) and there are no interspecies FRs up to ~ 190 G, therefore, it will also not change when tuning the a_{Cs} as described above. On the other hand, at high density and low field, as in the case of the BECs, the large a_{RbCs} gives rise to a strong repulsive interaction that prevents the two species from mixing [124]. This immiscibility, combined with the fact that a_{Cs} is extremely high at the location of the interspecies FRs, is one of the main technical difficulties to overcome with the experimental sequence when aiming to overlap the two species adiabatically. The solution to this problem, presented in Ref. [63], is discussed in Sec. 3.10–Sec. 3.12, as it constitutes the starting point for part of the original contributions presented in this thesis. Finally, it is worth remarking that when the project started Rb and Cs had already been widely studied in the ultracold-atom community, and the Innsbruck group had an extensive experience with Cs, having been the first group to condense it [156].

3.3 Sequence overview

The possibility to simultaneously levitate both species, mentioned in the previous section, allows Rb and Cs to be cooled simultaneously and almost at the same position, by applying the same cooling steps until the beginning of the evaporative cooling, when the densities become sufficiently high that the interspecies scattering rate becomes relevant. I give below an overview of the experimental sequence, starting from the atoms still in solid form and ending with the formation of the molecules and their transfer to their rovibrational ground state. The details on the individual steps are found in Sec. 3.6–Sec. 3.12.

Rb and Cs metal samples are evaporated in the ovens and the Rb and Cs gas are mixed (Sec. 3.6). At the exit of the oven section, the atoms cross the Zeeman slower and reach the cell (Sec. 3.7). The small difference in the magnetic-moment-to-mass ratio and the use of dedicated laser beams for each species allow the Zeeman slower to work simultaneously for both species. The Zeeman slower is attached directly to the main chamber: An uncoated quartz cell where all successive steps take place [148], in jargon, the cell serves both as a cooling and as a science chamber. The flow entering the cell is first trapped by the MOT (Sec. 3.8). MOT beams for both species are overlapped giving rise to overlapped MOT clouds. Following the MOT, after a short compression achieved with the magnetic field (Sec. 3.8), the atoms are transferred in a OL a few tens of GHz detuned from the main transition for dRSC (Sec. 3.9). Similarly to the MOT the lattice beams are overlapped. dRSC takes place during three pulses. In between the pulses, the atoms relax in a large shallow ODT, which serves next as a reservoir for the dimple trick (Sec. 3.10). While the reservoir is the same for both species, the dimple trick is implemented by applying two crossed dimples, one for each species, effectively spatially separating the two species for the first time since they left the ovens (Sec. 3.10). After the dimples are loaded the reservoir is gradually removed and forced evaporative cooling is performed in the dimples until condensation is achieved. Next, the BECs, still at separated locations, are loaded in a shared far detuned OL (Sec. 3.11). At the initial intensity of the OL, Rb is in the SF phase, while Cs is in the MI phase with predominant occupation of one atom per lattice site. At this point, the OL shields greatly the interaction between Cs atoms (with the exceptions and limitations discussed in Chapter 4), and the magnetic field can be adjusted to tune a_{RbCs} to the interspecies FR to allow the overlap of the two species, regardless of the value assumed by a_{Cs} at the new magnetic field. To perform the overlap, Rb atoms are transported at Cs location (Sec. 3.12), the overlap velocity is crucial in the efficiency of the molecule formation, too fast and Rb atoms are excited out of the ground state, to slow and the losses in both species become important. Some elements affecting the transport velocity are discussed in Chapter 5. After the overlap, the intensity of the OL beams is increased until both species are localized in a MI phase. On the OL sites where one atom of each species is present, molecules can be formed via Feshbach association (Sec. 3.12). Although this has not been implemented yet with the overlap scheme in the lattice described here. The plan is to continue the sequence with STImulated Raman Adiabatic Passage (STIRAP) to transfer the molecules to the absolute ground state (Sec. 3.12). The detection is done via absorption imaging on the atoms [106]. If molecules are present they are first separated from the unbound atoms via Stern-Gerlach or by the application of resonant pulses that remove the unbound atoms without affecting the molecules, then they are dissociated in order to image the constituent atoms. In the next sections, I will provide typical atom numbers achieved for each step, while a more detailed characterization including temperatures is presented for the optimization of Chapter 6.

3.4 Lasers for cooling and trapping light

Laser cooling, relying on the dissipative force of the light-atom interaction(2.3), needs near-resonant light. Near resonant light is also used for imaging. For these purposes, each species uses dedicated lasers emitting at 780 nm and 852 nm, respectively addressing the D2 line of Rb [157] and Cs [158]. As the scattering rate near resonance is high, the power required never exceeds a few hundred mW. I will refer to this as cooling light. On the contrary, trapping in the ODT and OL exploits the dipolar forces of the light-atom interaction and they require far off-resonance light. In this case, the experiment makes use of light around 1064 nm, which is sufficiently red-detuned from both atomic transitions, and the lasers can be shared between the two species. The difference in polarizability between the two species is responsible for a difference of ~ 1.7 in the trapping potential, which helps with the mixing (Sec. 3.12). The power of the trapping light ranges between several hundred mW and 100 W. An in-between case is represented by the OL for dRSC, due to the initial relatively high temperature of the atoms, the lattice needs to be fairly deep to provide trapping. This is achieved with light that is only about 10–20 GHz detuned with respect to the atomic transition. In this case, dedicated lasers for each species are necessary.

Cooling light is obtained via a large use of the master slave-configuration [159] and seeded tapered amplifiers (TA) [160]. The first is a configuration of two lasers, which relies on injection locking [161] to synchronize the emission of the so-called slave laser, a broadband laser with relatively high power, to that of a narrow band laser with low power, the master. In the second configuration, the TA is a chip with a tapered profile of the gain region that enables cascade emission. The emission is seeded externally from a laser diode that features the desired spectral characteristics. In detail, the near-resonant light, for cooling, dRSC and imaging is obtained as follows, a schematic picture is provided in Fig. 3.2

- Both Rb and Cs Zeeman light are produced by laser systems in master-slave configuration, Rb repumper light also uses a master-slave configuration, while Cs repumper light is generated by a distribute-feedback diode laser. All four systems are locked to the respective atomic transitions via modulation transfer spectroscopy [162].

- The light for Rb MOT is produced by a home-built diode laser, beatnote-locked to the Zeeman

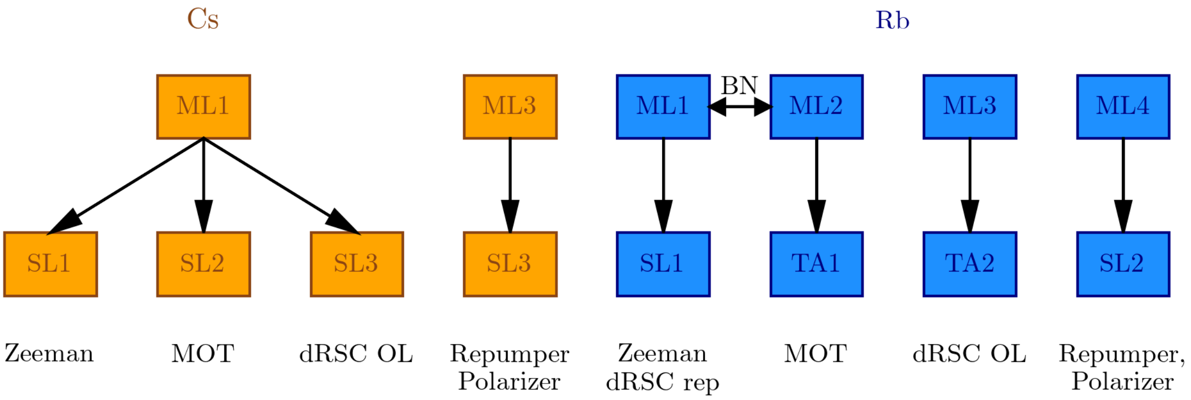

Figure 3.2: Schematic view of the laser system for near-resonant light. On the left Cs, on the right Rb. For Cs one master laser (ML1) is used to injection-lock three slave lasers, SL1 for Zeeman cooling light, SL2 for MOT light, and SL3 for the light for the dRSC OL. A second master laser (ML3) is used for Zeeman and MOT repumper light, as well as for dRSC polarizer. For Rb there are two master lasers ML1 and ML4 used to injection-lock the slave laser SL1 for Zeeman light and dRSC repumper, and SL4 for Zeeman and MOT repumper light and dRSC polarizer, respectively. Two seed lasers ML2 is locked via beatnote (BN) to ML1 and ML3 are used to seed the tapered-amplifiers TA1 for MOT light and T2 for the light for dRSC OL, respectively.

master laser. The light is then amplified with a TA[1]. The repumper light for MOT is the same one used for the Zeeman slower. The light for Cs MOT is produced in a master-slave configuration with home-built diode lasers. Analogously to Rb, the light for the repumper is the same as the one used for the Zeeman slower.

- The light for Rb dRSC OL is generated by a home-built laser diode amplified by means of a TA[2]. Rb polarizer is provided by the same lasers as the Rb Zeeman's and MOT's repumper. Repumper light for dRSC is from the Zeeman laser setup. The light for Cs dRSC OL is obtained by a laser in a master-slave configuration, where the master is common to the Zeeman and MOT light. Polarizer light is obtained from the Zeeman's and MOT's rempumper setup.

More details on the laser setup and transitions that use near-resonant light can be found in Ref. [150].

The trapping light is obtained from three lasers. A fiber laser at 1070 nm with single transversal mode and multiple longitudinal modes emits up to 100 W dedicated to the reservoir ODT. All three dimples and the far-detuned OL are obtained with light at 1064 nm, generated from a home-built fiber amplifier[3] which has been tested up to ~ 30 W emission. The Rb dimple, in addition, has a

---

[1] Toptica BoosTA

[2] Toptica BoosTA

[3] Nufern: PLMA-YDF-20/400-VIII, PLMA Yb doped DC fiber, seeded by Innolight MOPA at 1064.45 nm and

component at 830 nm from a titanium-sapphire (Ti:Sapph)[4]. This component is red-detuned with respect to Rb but it is blue-detuned with respect to Cs. Therefore it can compensate the potential due to the 1064 nm-component for Cs atoms at Rb location, while it makes the potential deeper for Rb atoms.

For both cooling and trapping light, individual frequencies are fine-tuned with the help of acousto-optic modulators AOMs. On-off of the signals and stabilization of the intensity for all beams are controlled via the amplitude of the RF input on the AOMs.

3.5 Magnetic field and coil setup

The experimental setup contains four sets of coils. The 'gradient coils' are a pair of coils in an anti-Helmholtz configuration, they provide a quadrupole field with a gradient along the vertical direction that can reach up to $\nabla B = 40\,\mathrm{G/cm}$ at the center of the cell. The quadrupole field is used for the MOT, and in combination with a bias field for the levitation of the atoms against gravity. For diagnosis purposes, the field can be used as a weak magnetic trap, that can be loaded after MOT and compression. For special applications, the direction of the quadrupole field can be changed dynamically in the sequence thanks to an H-bridge.

Concentric to the gradient coils, the 'homogeneous field coils' are a pair of coils in a Helmholtz configuration. They provide a strong bias field used to control interactions via FRs. These coils can be driven by a power supply[5] or with batteries for better stability [151], in both cases the field reaches over 400 G.

Two additional sets of coils in a Helmholtz configuration, called historically 'tracking coils', provide a bias field in the horizontal plane up to 25 G. They are now used to fine-tune the position of the center of the quadrupole field during levitation and to adjust the quantization axis during dRSC to have the right projections for the polarizer polarisation.

Fig. 3.3 reports a sketch of the coils closer to the cell. A detailed description of the coils and their geometry can be found in Ref. [151], in particular, it is known from Ref. [151], that the center of the homogeneous field coils and the quadrupole coils are slightly misaligned in the horizontal plane.

Away from the cell, there are three pairs of coils (the 'compensation coils', one along each spatial direction), which can provide a weak homogeneous field for compensation of the Earth's magnetic field and stray fields from the room. The vertical pair is also used during the dRSC, to achieve the degeneracy of the hyperfine substates.

In addition to the aforementioned coils, the Zeeman coils, between the ovens and the cell, provide the field for the Zeeman slower and are described in Sec. 3.7.

---

pumped by a DILAS diode array centered at 975nm. The design of the amplifier itself is similar to the one reported in Ref. [163].

[4] Coherent 699, converting green light from Coherent Verdi V10.

[5] Delta Elektronika SM6000 series 60-100

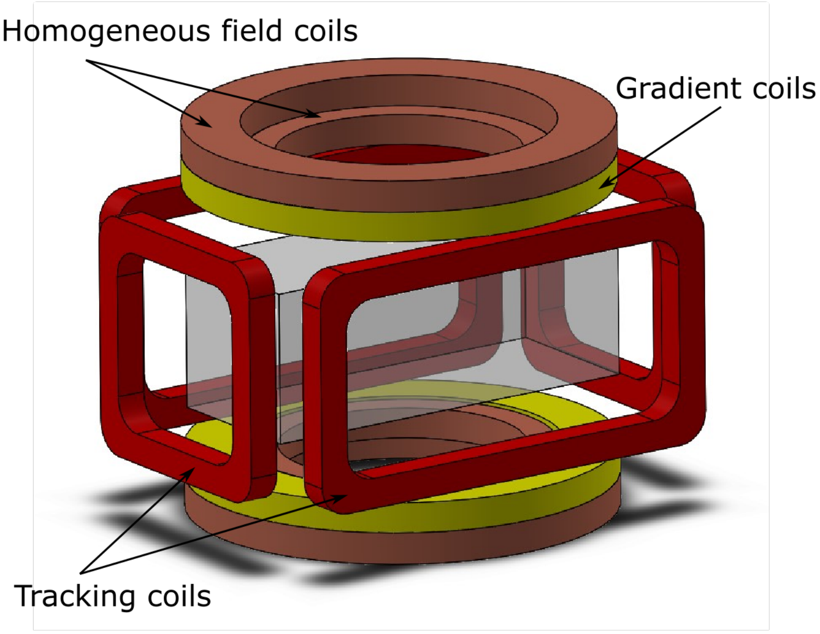

Figure 3.3: Schematics drawing of the coils closer to the cell. The figure shows the relative position of gradient coils (yellow), homogeneous field coils (copper), and tracking coils (red) with respect to the cell. The compensation coils and Zeeman coils are not included in the figure.

3.6 Ovens

The design of the oven chambers shown in Fig. 3.4 is inspired by a three-species oven design [164], where each oven chamber has an internal tripartition. The use of a tripartition helps to prevent reactions between the species and cross-contamination of the reservoirs. The adaptations from the three-species design to the two-species design are described in Ref. [147]. Each atomic gas is obtained from an ampule containing approximately 1 g. Each ampule is contained in a half nipple, called reservoir, that connects to an oven chamber dedicated to loading that species via a flux valve. The reservoirs are heated up to 60 °C for Rb, and 50 °C for Cs, with upfront melting points of 39.3 °C and 28.44 °C, respectively. This ensures a vapor pressure at the entrance of the respective oven chamber of $\sim 2.1 \times 10^{-5}$ mbar for both species. Working with two species, the design is composed of two sequential oven chambers one for Rb and one for Cs, as shown schematically in Fig. 3.4

The first oven chamber, i.e. the one farther from the glass cell, is the Rb oven chamber. In this chamber, two out of the three partitions are closed, and the third one connects to the reservoir containing Rb atoms. Rb atoms can leave the Rb oven chamber only through an array of microchannel tubes as they enter the Cs oven chamber. In the Cs oven chamber, Rb atoms propagate freely through one of the partitions. A second partition connects to the reservoir containing Cs atoms. Cs atoms can leave this oven chamber only through an array of microchannel tubes and only in the

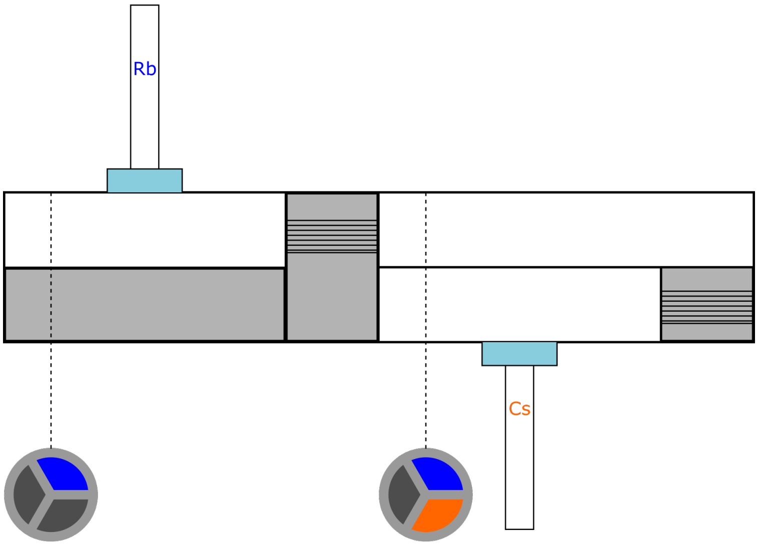

Figure 3.4: Schematic representation of the two oven chambers. Each chamber is internally divided into three sections as shown in the projection in the lower part of the drawing. The Rb, respectively Cs, atoms are loaded in one of the partitions from a half nipple where the metal samples are located. The oven chamber can be left only through an array of microchannel tubes.

direction of the cell, similar to Rb atoms leaving the Rb oven chamber. The third partition in the Cs oven chamber is closed. The use of microchannel tubes at the exit of each oven chamber has the advantage that the atomic beams are roughly collimated before they leave the ovens.

When the atomic flow leaves the oven chambers, two differential pumping stages guide it toward the Zeeman slower. The stages are characterized by two sequential apertures with conductance respectively $C_1 = 43\,\mathrm{ml/s}$ and $C_2 = 290\,\mathrm{ml/s}$. An ion pump with a $20\,\mathrm{l/s}$ flow is connected between the two apertures and helps to keep the differential pressure. Following, a gate valve and a servo-shutter control the flow into the Zeeman slower.

The design presented in this section has been used for the results reported in Chapter 4 and in Chapter 5. A new design of the oven section has been introduced prior to the results of Chapter 6, when Rb and Cs reservoirs have been replenished. This design is briefly described in that Chapter. Further problems with the vacuum that emerged during the editing of this thesis triggered a revisitation of the vacuum setup.

3.7 Zeeman slower

The RbCs project uses a single Zeeman slower for both species. This means that the coils of the Zeeman slower are common to both species, while the light for cooling and repumping is instead specific for Rb and Cs. This combination allows simultaneous cooling and slowing of the two species from the Zeeman slower, permitting simultaneous loading of the two MOTs. The coil system is composed of 6 coils, with decreasing sizes. Coils C1-C5 are before the cell, coil C6 is after the cell and it is winded in the opposite direction. This configuration gives an inversion of the field at the center of the cell, grants a fast decrease of the field after C5, and allows for a reduction of the distance between the coils and the loading position of the MOT. A description of the Zeeman design can be found in Ref. [148]. During operation, the coils can be driven in two blocks, a power supply controls the current for C1 and C6, while a second power supply controls C2-C5. In typical experimental operations, I first find the optimal set of currents for each species. For Rb, this is located at slightly higher currents than for Cs. Then, I select an intermediate set of values that balances the number of atoms of the two species when loading the MOTs and scan the detuning and intensity of the beams. An example of the optimization for the Zeeman coils is provided in Sec. 6.4.2.

The Zeeman light and Zeeman repumping light propagate coaxially to the Zeeman slower coils, in the direction opposite the atomic flow. The power of the Zeeman beam is about $P_Z = 5\,\mathrm{mW}$ for both species. The Rb beam is detuned by $-22\,\mathrm{MHz}$ with respect to the $F = 2 \to F' = 3$ transition and has σ^+ polarization. Cs beam is detuned by $-20\,\mathrm{MHz}$ with respect to the $F = 4 \to F' = 5$ transition and has σ^+ polarization, this value disagrees with the theoretical prediction that for the same coil current and oven temperature would fix the optimum around 35 MHz The repumper light instead is about 1.5 mW in power and is resonant with the $F = 1 \to F' = 2$ transition for Rb, while for Cs it is detuned by $-20\,\mathrm{MHz}$ with respect to the $F = 3 \to F' = 3$ transition. The size of Zeeman and Zeeman repumper beams changes across the cell and the Zeeman slower, it has a diameter of $\sim 1\,\mathrm{cm}$ at the entrance to the cell and it focuses at the aperture of the ovens.

3.8 Magneto-optical trap and compression

The MOTs for the two species are loaded simultaneously at roughly the same position in space. The quadrupole magnetic field is controlled by the gradient coils for both species, typical magnetic field gradients are around $\nabla B = 6\,\mathrm{G/cm}$. The light comes in a standard 6-beam configuration [76]. The light for the two species is overlapped in an optical fiber, then it is split into six beams by a combination of polarizing beam splitters (PBSs) and $\lambda/2-$waveplates, as shown in Fig. 3.5. No retroreflection is used. The individual polarizations of the beams are controlled by a combination of achromatic $\lambda/2-$waveplates and $\lambda/4-$waveplates, and waveplates with phase retardation $\lambda/2$ and $\lambda/4$ at 852 nm, however these are not dichroic and affect the polarization of Rb beams. Through a small unbalancing of pairs of counter-propagating beams, it is possible to adjust slightly the relative position of the two clouds. The initial configuration for the MOT, splits the beam pairs in a ratio 1:1:2, where the last one is the vertical direction, and each pair of counterpropagating beams is set to have roughly the same power. As shown in Fig. 3.5, the repumper light for Rb and Cs is overlapped on the main table and subsequently, it is overlapped on a PBS with the MOT light, before the six beams are split. Therefore, the MOT and repumper beams have orthogonal polarizations. This gives rise to a very inhomogeneous power distribution of the repumper beam. In fact, the first beam pair to be split is a horizontal beam pair, in order to respect the intensity ratios described above for the MOT, it contains only about 1/4 of the total intensity. Due to the fact that the MOT and repumper have opposite polarization at this PBS, it follows that most of the repumper light is overlapped with the first beam pair. The detuning of the MOT beams is 10 MHz with respect to the $F = 2 \to F' = 3$ transition for Rb, which corresponds to $1.7\,\Gamma^{\mathrm{Rb}}_{\mathrm{MOT}}$, and 14 MHz with respect to the $F = 4 \to F' = 5$ transition for Cs, which corresponds to $2.6\,\Gamma^{\mathrm{Cs}}_{\mathrm{MOT}}$. Typical powers are about

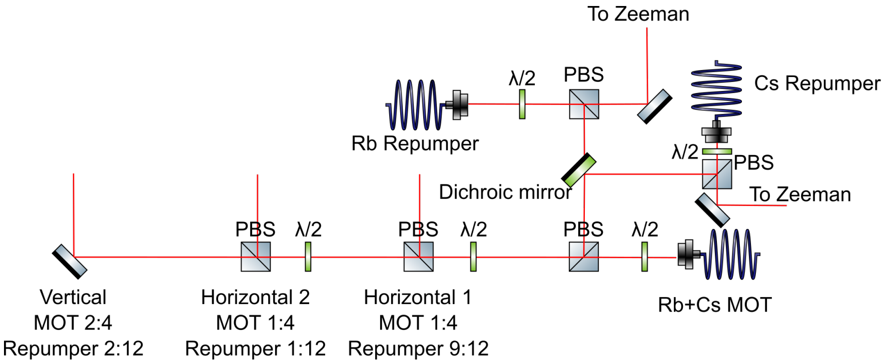

Figure 3.5: Simplified scheme for the splitting of the MOT beams and the repumper beam for MOT and Zeeman. The MOT beams are splitted by means of PBSs and $\lambda/2$-waveplates in three beam pairs Horizontal 1, Horizontal 2, Vertical, where the vertical has twice the power as the horizontal beams. The repumper splits first between Zeeman and MOT repumper. The MOT part overlaps with the MOT beams on a PBS but it has orthogonal polarization at the first PBS, therefore most of the power of the repumper is in Horizontal 1.

$5-10\,\mathrm{mW}$ for each of the horizontal beams for both species. The waist size is one inch and the transversal profile of each MOT beam is flattened by taking only the central part of a Gaussian beam and clipping its wings on an iris with a diameter of one inch.

The loading of the MOTs ends when the atomic beam shutter is closed and the Zeeman light and Zeeman repumper light are switched off. Typical loading times range between 4 s and 7 s. The size of the cloud at this point is larger than the field of view of the camera, therefore the number of loaded atoms is counted after a short compression phase which is assumed to take place without significant losses. For the compression stage, the quadrupole field is strengthened to 22 G/cm and the light is further detuned up to 100 MHz in 100 ms. The compressed MOTs are imaged in situ with light that is red-detuned by 12 MHz with respect to the $F = 2 \to F' = 3$ transition for Rb and the $F = 4 \to F' = 5$ transition for Cs, to avoid saturating the cloud. After loading the MOTs for 7 s and compressing them, I measure a typical number of $\sim 2\text{–}3 \times 10^7$ atoms for Rb and $\sim 1.5\text{–}2.5 \times 10^7$ atoms for Cs. These numbers have been improved upon the change of the laser system and the optimization of the sequence as discussed in Chapter 6.

3.9 Degenerate Raman sideband cooling

After compression, the sequence continues with dRSC. The OLs for dRSC of Rb and Cs have a four-beam configuration similar to the setup of Ref. [109], two beams enter the cell from the top at a $\sim 45°$ angle, and the other two are obtained by retroreflecting a beam that crosses the cell in the horizontal plane and perpendicularly to the atomic flow. The beam configuration is shown in Fig. 3.6. For each species, the interference between the four beams gives rise to a 3D OL. The light for the two species is overlapped in an optical fiber and successively it splits on the main table to create three beams with a combination of waveplates and PBSs. The spatial separation between the two OL is limited to the small difference in the diffraction angle at the exit of the fiber due to the fiber termination being at an angle. The lattice sites are displaced between the two species due

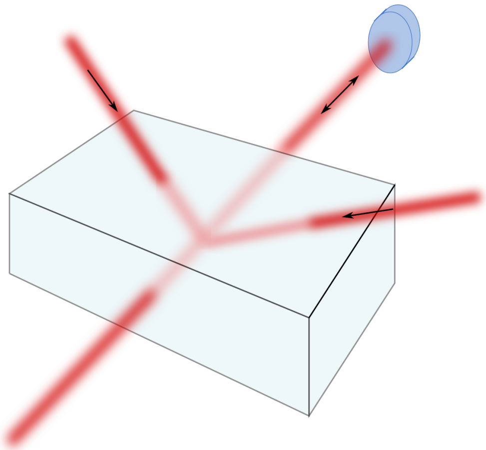

Figure 3.6: Beam orientation for dRSC. One beam enters the cell horizontally and it is retroreflected, the other two beams enter the cell at a 45° angle with respect to the vertical.

to the different wavelengths, but due to the large detuning, and relatively low power, Rb beams are not affecting Cs significantly and vice versa.

The light for the OL is about 20 GHz detuned with respect to the $F = 1 \rightarrow F' = 0$ transition. The total light at the experiment is about 150 mW and it splits equally in three beams of about 1 mm diameter. For Cs, dRSC works on the $F = 3$ state, therefore the cooling light addressing the $F = 4 \rightarrow F' = 5$ state is sufficiently red-detuned from $F = 3 \rightarrow F' = 2$ to obtain a lattice with reasonably low dissipation. The total power available for the Cs lattice is about 120 mW Quantitatively, this detuning corresponds to the natural splitting of Cs $6^2S_{1/2}$, which is about 9 GHz.

The polarizer light for both species enters the cell from the bottom, at a small angle with respect to the vertical direction. As the magnetic field is oriented along the vertical direction, the angle between the polarizer beam and the magnetic field allows for the proper mixing of σ^+ and π components, when using a light that is circularly polarized. The polarizer is resonant with the $F = 1 \rightarrow F' = 0$ transition for Rb and the $F = 3 \rightarrow F' = 2$ transition for Cs. The light for the two species reaches the main table through independent paths and, there, it is overlapped in free space. Rb dRSC, in addition to the OL and the polarizer, requires a third beam that acts as a repumper on the $F = 2 \rightarrow F' = 2$ transition.

To achieve the resonance between the $|m_F, \nu + 1\rangle$ and the $|m_F + 1, \nu\rangle$ states, a magnetic offset is applied along the vertical direction. The field is generated by the compensation coils. To optimize for the two species, I initially scan the magnetic field to match the resonance condition for Cs. Then I adjust the intensity of Rb OL to adjust the trap frequencies and level separation. An important technical aspect in the implementation of dRSC in the RbCs project is that the initial size of the cloud after compressing the MOT is still fairly large when compared with the curvature of the gaussian beams composing the Raman lattice. As the intensity of the OL beams decreases toward the fringes of the beam, hence of the MOT, the resonance condition changes across the sample. To account for this effect, the intensity of the magnetic field is ramped slightly during the pulses.

In the sequence, dRSC is achieved via three pulses with a duration of 3 ms and rest time in

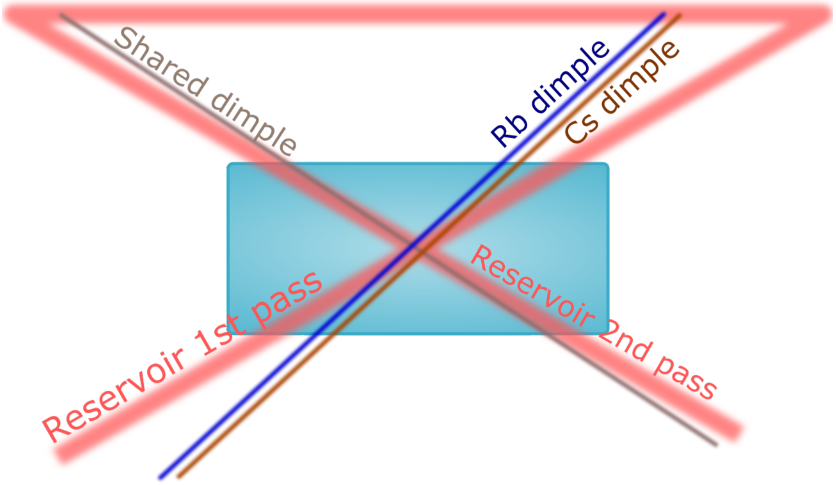

Figure 3.7: Schematic representation of the ODTs from top view. The reservoir beam in red is 'folded' to obtain a crossed trap. Rb dimple (blue) and Cs dimple (brown) cross the shared dimple (gray) at independent locations.

between of 3 ms. The reservoir ODT is kept on during the dRSC, therefore the atoms are expected to relax in the potential of the reservoir during the rest time (Sec. 3.10). This helps to compress the cloud and increases the spatial density, while the dRSC itself cools the atoms at constant spatial density. Proper switching on and off of the levitation fields is not possible over this time scale, therefore the levitating field is constantly off, as required by dRSC, resulting in a tilt of the potential of the reservoir ODT under gravity.

To benchmark the cloud after dRSC the beams are switched off and 50 ms expansion are used during which the fields are set to levitate the atoms in the dark states of the dRSC. The atoms that have not been transferred to the dark state are either under-levitated or over-levitated (Stern-Gerlach separation [75]) and they will leave the field of view of the camera. At the end of the 50 ms the absorption pictures are acquired. Typical atom numbers for this step are $N^{\text{Rb}}_{\text{dRSC}} \sim 1 \times 10^7$, $N^{\text{Cs}}_{\text{dRSC}} \sim 6.5 \times 10^6$. Many technical aspects of dRSC have been characterized extensively during the new optimization of the experimental sequence and part of the results is reported in Sec. 6.4.4.

3.10 Dipole traps and evaporative cooling

The evaporative cooling is fully optical and it makes use of the dimple trick shown in Sec. 2.6.1. This technique entails the overlap of a large ODT, the reservoir, and of a combination of tighter ODTs, the dimples, which get populated by thermalization collisions. The geometrical configuration of the reservoir and the dimples for the experimental setup of the RbCs project can be seen in Fig. 3.7. The volume ratio between the reservoir and each crossing is about 1000.

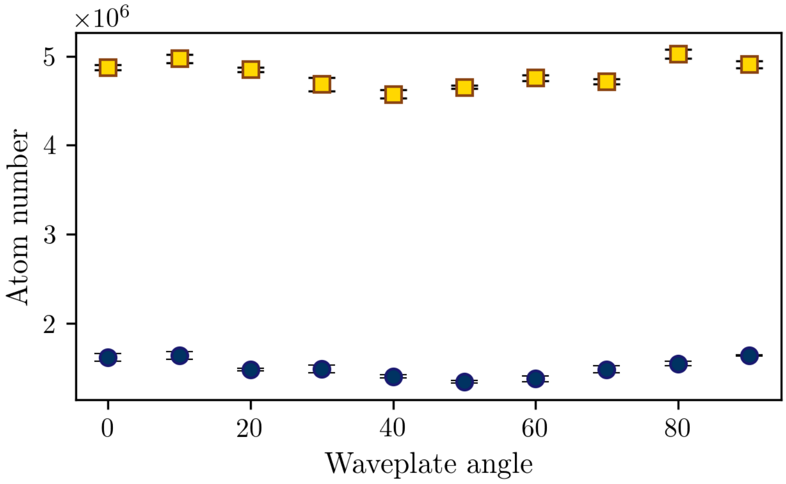

Figure 3.8: Polarization of the reservoir second pass. The figure shows the atom number in the reservoir after 900 ms of hold time in the reservoir as a function of the angle of a $\lambda/2$ waveplate installed in the second pass of the reservoir beam. 0° is the Brewster angle and parallel polarization of the two beams, 45° is crossed polarization.

3.10.1 Reservoir

The reservoir is composed of two beams that cross at the center of the trap. The second beam is obtained by reflecting and 'folding' the first beam after it crosses the cell as shown in Fig. 3.7. Both beams enter the cell at the Brewster angle $\Theta_B \sim 60°$ from opposite sides and they have polarizations parallel to the table to maximize transmission through the cell. The polarization of the second pass has been varied to check the effects of polarization on the atomic losses, by adding an additional $\lambda/2$ waveplate in the second pass of the reservoir. In Fig. 3.8, I show the number of atoms left in the reservoir after holding a thermal cloud of atoms in the ODT for 900 ms as a function of the waveplate angle. 0° corresponds to the initial polarization at the Brewster angle. At 45° the two beams are orthogonal and the interference is minimum, but the reflection at the cell is higher. From the data, there is only a very shallow dip, centered around 45°, which is expected due to the drop in power of the second pass (due to the increased reflection) and therefore of the total trap depth. There is no significant decrease in the atom number due to the interference between the two beams. Overall switching between parallel and crossed polarization of the two beams did not change significantly the performance of the reservoir. The total power at the cell for the first pass is about $\sim 60\,\mathrm{W}$, due to the folded configuration, the power of the second pass is about 16% lower than the first pass. The width, expressed by the $1/e$-waist, is about $500\,\mu\mathrm{m}$ with collimated beams. The size is chosen to be larger than the size of the Raman clouds, which is $\sim 300\,\mu\mathrm{m}$ for both species. At the crossing the depth is $V_{\mathrm{Res}}^{\mathrm{Cs}} \sim 20 - 30\,\mu\mathrm{K}$ for Cs, which corresponds to $V_{\mathrm{Res}}^{\mathrm{Rb}} \sim 12 - 17\,\mu\mathrm{K}$ for Rb.

The reservoir ODT is switched on during dRSC. Thanks to the pulsed scheme explained in the previous section, the atoms relax in the potential from the reservoir in between pulses, 'rolling' toward the center of the trap, in a fashion similar to delta-kick cooling [165]. This scheme removes *de facto* the mode-matching conditions between the reservoir parameters and the free-expanding cloud after dRSC.

3.10.2 Dimples

From the reservoir, the atoms are transferred to the dimples. When this happens, the density in the dimples increases significantly and the large repulsive a_{RbCs} discussed in Sec. 3.2 becomes relevant. To reduce losses and be able to perform evaporative cooling in the dimples, it is necessary to separate the cloud of the two atomic species in space by using separate crossed ODTs. The crossings are created via the intersection of three focused beams as shown in Fig. 3.7: Rb dimple, Cs dimple, and shared dimple.

The three dimples are switched on at the same time as the reservoir, before dRSC, and are loaded from the latter through collisions during and after dRSC. The reservoir beam is switched off 500 ms after dRSC and, successively, the dimple intensities are decreased in four exponential ramps of forced evaporative cooling. The ramps are designed to have a fixed duration in time, which goes from 0.5 to 4 s, while the power cut is optimized to achieve condensation of both species. The details of the evaporative cooling sequence can be found in Ref. [151]. Four piezoelectric stages allow changing the horizontal and vertical position of the Rb dimple and the vertical position and the focus position of the Cs dimple dynamically during the experimental sequence. The distance between the dimples allows the coupling and decoupling of the evaporative cooling of the two species, and, in later stages, the overlap of the samples for the formation of molecules in the OL.

The technical difficulties of applying the dimple trick to two species simultaneously, do not limit to preventing cross-talking between the dimples. The question might arise why not use also two entirely separate ODT as reservoirs? The combination of the two species in a single reservoir has a few advantages. For example, when loading the dimples, the Rb-Rb scattering rate is low and Rb-Cs scattering helps to have a more efficient thermalization of Rb and, consequently, loading of the Rb dimple. Rb atoms are lighter and, in the state of interest, they experience a shallower trapping potential, with respect to Cs. Therefore Rb atoms in the Cs dimple help to cool down Cs, by carrying away large fractions of the kinetic energy upon collisions. The optimization of the evaporative cooling is normally performed with the two species to account for this kind of cross-talking. Single-species operation can be achieved by switching on resonant light to blow away the undesired species, after the second ramp of the evaporative cooling when the dimples are far enough that the evaporative cooling is fully decoupled.

The waist of the Cs dimple is $w_{\mathrm{CsD}} = 122\,\mu\mathrm{m}$ and the one of the shared dimple is $w_{\mathrm{ShD}} = 39\,\mu\mathrm{m}$. The two light components for the Rb dimples are overlapped in the fiber delivering the light to the experiment, due to the different diffraction index of the optics, the two waists are slightly different, and the waist of the combined Rb dimple is $w_{\mathrm{RbD}} = 55\,\mu\mathrm{m}$ (obtained from trap frequency measurement). Typical numbers at the end of the evaporative cooling are 1.5–3×10^4 atoms for Rb and 1.5–2.5×10^4 atoms for Cs, with BEC fractions above 80% for both species. Smaller BECs clouds are shown in Fig. 3.9, the absorption pictures have been taken after 52 ms levitated TOF with $a_{\mathrm{Cs}} = 0$

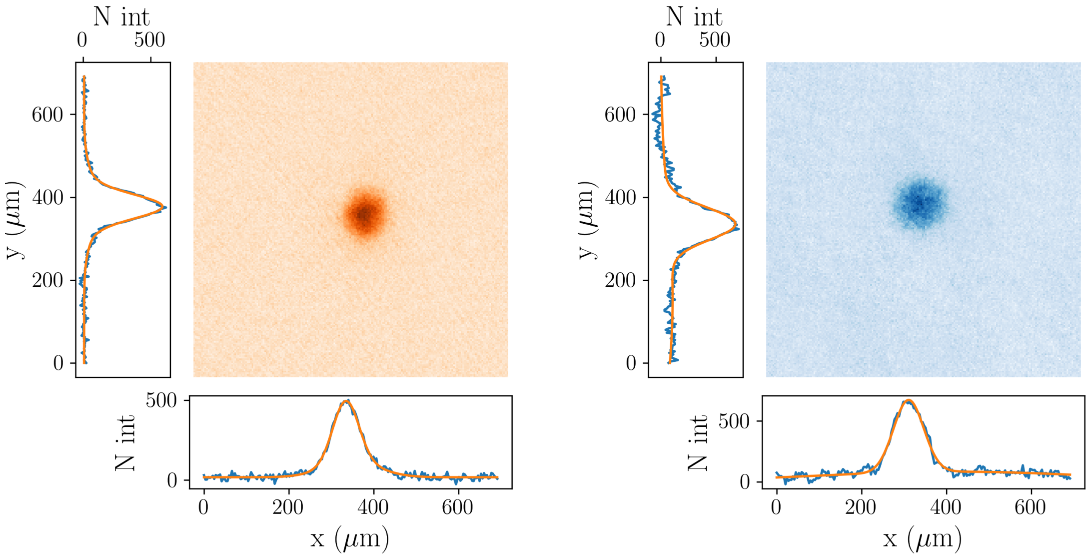

Figure 3.9 (a). a

Figure 3.9 (b). b

Figure 3.9: BEC absorption picture. Optical density for partially condensed clouds of Cs (a) and Rb (b) acquired via absorption imaging after 52 ms of levitated TOF. In the bottom and on the side, the integrated profile in blue thin lines, respectively over the y- and over the x-axis of the image. The solid lines are fits of the sum of two gaussians in orange- The fits yields for Cs a BEC fraction of 62% and for Rb 54%.

3.11 Optical lattice

The formation of the molecules requires overlapping the samples after the evaporative cooling. The overlap of Rb and Cs is problematic due to the immiscibility of the two BECs. In fact, as mentioned in Sec. 3.2, around 21 G, where the conditions are favorable for the simultaneous evaporation of Rb and Cs, the interspecies scattering length $a_{\mathrm{RbCs}} \sim 650\, a_0$ is strongly repulsive and prevents the adiabatic mixing of the two species. The magnetic field can be used to tune a_{RbCs} in the proximity of a FR, but the interspecies FR are localized at values where the Cs intraspecies scattering length has the background value of $a_{\mathrm{Cs}} \sim 2470\, a_0$. In this regime, three-body recombination rates are extremely large and limit the lifetime of Cs BEC by inducing losses and heating [94].

To circumvent this problem, the two species are mixed in a far-detuned OL. The lattice light for this OL is generated by the same fiber amplifier that provides the light for the dimples, and the power is transferred dynamically between the dimples and the OL beams at the end of the evaporative cooling, by means of a motorized waveplate in front of a PBS. The OL is formed by three-retroreflected beams. The beam pairs originated by the retroreflections are friendly called 'Heimat', 'Klamm', and 'Zeus'. Klamm is almost parallel to the small dimple. Zeus is making a 6° angle with the vertical direction. Heimat is orthogonal to Klamm and Zeus. The beams are detuned with respect to each other by 16 MHz to avoid interference, more details about the polarization and frequencies are provided in Ref. [151]. Given the geometry of the beams and the fact that they only interfere with their retroreflection, the OL is a cubic lattice with a spacing of 532.27 nm, formed by three mutually-orthogonal retro-reflected beams.

The intensity of the beams of the OL is ramped up adiabatically after the evaporative cooling, while the samples are still $\sim 100\,\mu$m apart. The depth of the OL in the RbCs project is calibrated, typically, with parametric heating [8]. It is worth reminding once more of the different atomic polarizabilities and different masses of Rb and Cs, which lead to different lattice depths for the two species when hosted in the same OL. In particular, the loading conditions, at 21 G and at a depth of $V_l = 20\,\mathrm{E}_{\mathrm{rec}}^{\mathrm{Cs}}$ give for Cs $U/J = 318$ almost a factor of ten above the SF-MI transition seen in Sec. 2.8. Therefore, Cs is in a Mott insulator state. The initial density of the BEC is chosen such that there is predominantly one atom per site of the OL. The presence of only one atom per lattice site helps to reduce contact interactions when tuning the field to tune the interspecies scattering length. A more detailed discussion on the topic follows in Chapter 4. For Rb the same OL has $V_l = 7.7\,\mathrm{E}_{\mathrm{rec}}^{\mathrm{Rb}}$ and $U/J = 5$ leading to the formation of a superfluid, which allows transport through resonant tunneling. The conditions for SF transport are discussed in Chapter 5.

The MI state can be probed with different techniques, including dimer association or density-induced tunneling [151]. The SF is typically probed in the RbCs project through interference measurements in TOF [124].

3.12 Formation of molecules and transfer to the ground state

When the atoms are loaded into the OL with $V^{\mathrm{lat}} = 20\,\mathrm{E}_{\mathrm{rec}}^{\mathrm{Cs}}$, it is possible to tune the magnetic field to reach an interspecies FRs. The optimal condition for the overlap is achieved if $a_{\mathrm{RbCs}} = 0$ as shown in Ref. [63]. This can be achieved on a broad interspecies FR located at ~ 352.7 G that has a width of 2 G. Ramping the field to the FR values implies increasing a_{Cs} to $2470\,\mathrm{a}_0$ and naively one could expect driving the Cs atoms deeper in the MI phase[6]. To overlap the two samples, Rb atoms are moved to Cs location, by shifting the position of the Rb dimple[7]. After the overlap, V^{lat} is further increased to drive the SF-MI transition for Rb. Once the atoms of both species are localized, Feshbach association is used to create weakly bound molecules, commonly known as Feshbach molecules [4], i.e., the magnetic field is swept across the pole of the FR to associate the atoms. Up to 6000 Feshbach molecules were created, with a lattice filling[8] of roughly 30% and an average entropy per molecule of $2k_{\mathrm{B}}$. These numbers are at the edge of the percolation threshold for a 3D cubic lattice (31% [166]), which means large clusters of molecules can be found inside the lattice.

The protocol has two main advantages. In the beginning, the localization of Cs atoms reduces significantly the losses with respect to free space, increasing the lifetime of the Cs sample sufficiently to perform Rb transport. After Rb is transported at Cs location, increasing the depth of the OL at the end of the overlap, localizes Rb atoms. The presence of Rb and Cs atoms localized on the same site of the OL maximizes the overlap of the atomic wave functions at the lattice sites

---

[6] Through the Bose-Hubbard model in a tight-binding approximation, I estimated $U/J = 3817$, but the value of U calculated for $a_{\mathrm{Cs}} = 2470\,a_0$ in this approximation exceeds the bandgap, making the model not valid. See the discussion at Sec. 4.7

[7] Technically this step is realized by using a piezo-electric element to shift the position of the optical fiber delivering the light for the Rb dimple and overlapping Rb and Cs dimples on a PBS, details of the setup can be found in Ref. [151]

[8] The percentage is obtained by normalizing the number of molecules to the number of Cs atoms that is the limiting species.

and increases the association efficiency to almost 100% when performing Feshbach association, i.e. associating the molecules by ramping across the FR. The losses that reduce the lattice filling to only 30% for molecules happen mainly during the mixing: losses of Cs atoms from the MI, three-body recombination of two Rb atoms and one Cs atom when the atoms start to localize. More details on the protocol are provided in Refs. [151, 63, 124]. Molecules formed this way need to be transferred to the roto-vibrational ground state. From Feshbach association, molecules are formed in the $a^3\Sigma^+$ state and are transferred to the ground state $X^1\Sigma^+$ via STImulated Raman Adiabatic Passage (STIRAP) [167, 168], a two-photon coherent transfer. The intermediate state of STIRAP is the $b^3\Pi_1$ with vibrational state $\nu' = 29$. This state mixes with the state $A^1\Sigma^+$ giving the excited state both a singlet and triplet character [31, 169]. The pump beam addressing the $a^3\Sigma^+ \to b^3\Pi_1$ transition has a wavelength of 1557 nm, while the Stokes beam addressing the $b^3\Pi_1 \to X^1\Sigma^+$ is at 977 nm. The STIRAP transition had been previously tested in our experiment for molecules created on a narrow FR at 197.1 G, showing up to 90% efficiency for the one-way transfer, as reported in Ref. [31]. However, this FR is not suitable for the overlap in the OL. STIRAP on molecules formed at the FR at 352 G has been reported from a separate RbCs project in Ref. [169]. STIRAP has been previously tested on the RbCs project with molecules formed with a different association protocol, in that case, the single-way transfer efficiency was $\sim 90\%$ [31]. STIRAP has not yet been tested in combination with the molecules formed in the lattice.

In light of the previously observed high efficiency of STIRAP, the major constraint limiting the efficiency of the molecule formation is so far expected to be the losses during the overlap of the two samples. During the overlap, atoms are constantly lost from the Cs sample, due to the limited stability of the MI. The lifetime of the Cs sample does not scale as expected for increasing interactions, contrary to the naive expectation of a more localized MI phase discussed above. This problem is explored in the measurement of Chapter 4. On the other hand, the overlap time is limited by the velocity at which Rb atoms can be transported without triggering instabilities. During the overlap and prior to Rb localization, three-body recombination processes involving two Rb atoms and one Cs atom can take place and are one of the main loss channels [124]. Increasing the overlap speed, thus reducing the time before the localization of Rb, would help to limit these losses. The critical transport speed for Rb atoms in the RbCs project has a much more peculiar behavior than expected for superfluid atoms tunneling resonantly through the lattice. As shown in Chapter 5 some aspects of this behavior can be traced back to the interplay between the confinement from the dimple and that of the OL.

Chapter 4

Inelastic confinement-induced resonances

4.1 Introduction

As seen in Chapter 3, one of the bottlenecks in the formation of the molecules is the overlap of the two species in the OL, which relies on the transport of SF Rb on top of a MI of Cs. In this Chapter, and the next, I characterize and discuss some effects of the confinement on the two species during the overlap. In particular, in this Chapter, I focus on the MI of Cs and the role of the confinement from the OL. For a 3D MI with on average one atom per lattice site, as aimed for to overlap Rb and Cs, the SF to MI transition happens when $U/J > 6 \times 5.8$ [7]. Since our MI is formed at $a_{\mathrm{Cs}} \sim 200\, a_0$, for an OL of depth $V^{\mathrm{lat}} = 20\, \mathrm{E}_{\mathrm{rec}}^{\mathrm{Cs}}$ we have $U/J = 318$, according to Eq. 2.22. According to the diagram of Fig. 2.3 a further increase of U at constant and J should bring the system deeper into the MI phase. Nevertheless, in Ref. [63] it was brought to light that, in the experimental conditions, an increase in U at constant J does not always lead to an increase of the stability of the MI. I start my work on the topic by confirming and extending these results in Sec. 4.2.

Next, this Chapter takes a different direction, starting from Sec. 4.3 I focus on the role of the lattice as an array of (almost) individual traps and discuss the stability of the Cs sample in terms of CIRs, as introduced in Sec. 2.9 and Sec. 2.10. In Sec. 4.3–Sec. 4.5.2 I show and characterize resonant loss and heating features in a MI with predominant single occupancy and I provide a description of such resonances in the framework of ICIRs. Sec. 2.12 and Sec. 4.6 compare the results with ad-hoc theoretical modeling and similar experimental results. Sec. 4.7 discusses some possible implications in the context of the RbCs project.

The relevance of ICIRs in zero-dimensional systems under three-dimensional confinement goes beyond the purpose of the RbCs project. In cold atom systems, ICIRs can be used to engineer the position and the strength of scattering resonances at will, also for magnetic fields where there are no magnetic FR and are likely to play a major role in the formation of molecules in tweezers via mergo-association [170]. ICIRs have been predicted also for non-cold atom systems like excitons in semi-conductors [73].

4.2 Stability of the Mott Insulator

In Chapter 3, I discussed the formation of molecules. In the protocol, one of the major problems that affect the final number of molecules and the entropy of the sample consisted of losses from the Cs MI. In particular, in Ref. [63] it was shown that the measured lifetime of the MI does not increase when increasing the scattering length contrary to the expectation. This observation constitutes the starting point of this Chapter. I start by reproducing those results and I investigate the stability of the sample in the OL when forming a Mott insulator.

The stability is evaluated as losses of atoms from the sample over time. Such losses can be fitted with a single exponential decay whose characteristic timescale is defined as the lifetime of the Mott insulator, in agreement with the definition of Ref. [63]. Here, and in the course of this Chapter, I always work with a Mott insulator with predominantly single occupancy.

Experimentally, I start by preparing $10-20\times10^3$ Cs atoms in a BEC with a condensate fraction $\sim$ 80%. The sequence follows the protocol outlined in Chapter 3, Rb atoms are blown away by means of a short resonant pulse during the evaporative cooling in the dimples, in order to work with a clean Cs sample. V^{lat} is increased up to a final value V_i in 500 ms, reproducing the loading sequence used in the protocol for the formation of the molecules. The depth of the OL along the three perpendicular directions is kept equal at any given time[1] such that $V^{\text{lat}}(t) = V_x(t) = V_y(t) = V_z(t)$. The ramp shape follows $V^{\text{lat}}(t) = e^{\gamma_l t}$ with $\gamma_l = 7\,\text{ms}^-1$, as it has been shown previously that this shape gives the best adiabaticity when loading the lattice [151]. Similar to Ref. [63], the initial density in the dimple is chosen to achieve predominant single occupancy. Once V^{lat} reaches V_i, the magnetic field is increased linearly in 3 ms from $B = 21\,\text{G}$ at which the BEC was created, up to a final value B_i The atoms are held at the final B_i, in the lattice for a variable time τ_{h}. Afterward, the field is ramped down to the initial value. Then the depth of the OL is decreased down to zero. The down-ramps are symmetric to the up-ramps for both the field and the depth of the OL. The atoms released by the OL are transferred back to the dipole trap, which is left on for the entire duration of the experiment. If the process is perfectly adiabatic the atoms will form again the initial condensate. In the experiment, there is typically a decrease of the BEC fraction from the initial 80% to 55%. The detection is performed with absorption imaging, after 52 ms of levitated time-of-flight. The cloud size after the end of the time of flight is dominated by the expansion of the thermal part of the cloud, an increase in temperature of the cloud can then be detected as an increase of the cloud size for a fixed time.

In Fig. 4.1 I show afew sample measurements for $B_i = 30.00\,\text{G}$, $B_i = 60.00\,\text{G}$, $B_i = 80.00\,\text{G}$, and $B_i = 100.00\,\text{G}$, the uncertainty on the field is dominated by the resolution of our control software and is 0.04 G on all values of the magnetic field reported in this Chapter. The chosen values of B_i gives $a_{\text{Cs}} = 586(2)\,\text{a0}$, $a_{\text{Cs}} = 1169.9(6)\,\text{a0}$, $a_{\text{Cs}} = 1388.2(4)\,\text{a0}$, $a_{\text{Cs}} = 1536.2(3)\,\text{a0}$, respectively, according to Ref. [171]. The ramp duration is kept fixed for all the cases, changing the rate to adjust to the final value.

A single exponential decay C is fitted to the data, the time constant of the fit is assumed to be the lifetime of the sample. The lifetime at $a_{Cs} = 586\,\text{a0}$ is longer than at the other fields, it is estimated in the regime of several tens of seconds and for a better estimation the measurement has been done on a long timescale. For the lowest band single-occupancy Mott-insulator as seen from

---

[1] this property will become relevant in Sec. 4.5.2

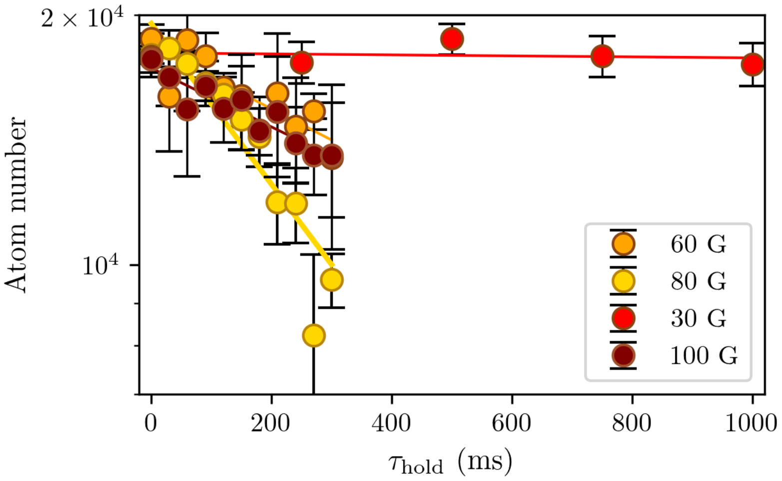

Figure 4.1: Lifetime measurement of Cs Mott insulator for 16 $\mathrm{E}_{\mathrm{rec}}^{\mathrm{Cs}}$ lattice. Remaining atom numbers for Cs after holding the atoms in a predominantly single-shell MI for a time τ_{h} at $a_{Cs} = 586\,\mathrm{a0}$ (red), $a_{Cs} = 1169\,\mathrm{a0}$ (orange), $a_{Cs} = 1388\,\mathrm{a0}$ (yellow), $a_{Cs} = 1536\,\mathrm{a0}$ (brown). The errorbars represent the standard deviation over three repetitions. The solid lines are fits to the data with exponential decays, the lifetimes are $7(6) \times 10^4$ ms, $1.1(2) \times 10^3$ ms, $4.5(6) \times 10^2$ ms, $1.2(2) \times 10^3$ ms, respectively.

the plot of Fig. 2.3, an increase in U at constant J and μ should bring the system deeper in the MI regime. This increases the localization of the atomic wave functions and reduces their overlap between adjacent lattice sites, hence inhibiting tunneling events and the scattering of particles in neighboring sites. However, the lifetimes of the sample at higher scattering lengths are much shorter, with significant losses already on the first 300 ms. The fact that the losses increase with an increase of a_{s}, indicates a non-trivial behavior of the system for large values of a_{s}. In particular, the fact that $a_{\mathrm{Cs}} = 1388\,\mathrm{a0}$ the lifetime $4.5(5) \times 10^{-1}$ s, is shorter than for $a_{\mathrm{Cs}} = 1169\,\mathrm{a0}$, and $a_{\mathrm{Cs}} = 1536\,\mathrm{a0}$ suggests the possibility of a modulated behavior. In the next sections, it will be shown that there are indeed two loss resonances in between those values. I expanded the investigation to a larger interval of depths of the OL V_i =14(3)–18(3) $\mathrm{E}_{\mathrm{rec}}^{\mathrm{Cs}}$ and obtained qualitatively similar results.

4.3 From losses to confinement-induced resonances

Here, I explore the possibility that the losses from Sec. 4.2 can be interpreted in the framework of CIRs in 0D due to the three-dimensional confinement of the OL on each lattice site. The distinct aspect of confinement-induced resonances is their dependence on both the length scale of the confinement and the scattering properties in free space (Sec. 2.9). In the laboratory, scattering properties are determined by a_{s}, which is controlled through B. For the OL, the potential on the individual lattice sites can be approximated with that of a harmonic oscillator. The harmonic oscillator length a_{h} deriving from this approximation is taken as the length scale for the confinement as used in 1D

ECIR [71]. This quantity can be controlled through V^{lat} as follows

$$a_{\mathrm{h}}(\omega_{\mathrm{h}}) = \sqrt{\frac{\hbar}{m\omega_{\mathrm{h}}}}, \tag{4.1}$$

where $\omega_{\mathrm{h}} = (2\pi/\lambda_{\mathrm{l}})\sqrt{2V^{lat}/m}$ is the harmonic oscillator angular frequency for a cubic lattice of spacing $\lambda_{\mathrm{l}}/2$.

I chose a set of parameters where the lifetime of the MI is particularly short and I systematically scan the surrounding region in two complementary experiments: in one I scan V_i and keep B_i constant, in the other I scan B_i and keep V_i constant. In both cases, the experimental sequence is the same as the one described in Sec. 4.2 and culminates in a MI with predominantly single-occupancy. In the first experiment, whose results are reported in Fig. 4.2 (a), B_i, hence a_{s}, is fixed, while I scan V_i. From this data, it is possible to identify the presence of a loss feature, represented by a dip in the atom number as a function of V_i. Most importantly, the loss feature occurs at different V_i by repeating the measurement at different B_i. In the second experiment, I repeat the measurement, this time keeping fixed V_i and scanning the magnetic field, the results are shown in Fig. 4.2 (b). Similarly to the previous experiment, there is a clear dip in the atom number as a function of B_i. Repeating the experiment for different V_i, there is a clear shift in the position of the resonance. Fig. 4.2(a) and Fig. 4.2(b) side-by-side confirm that there is indeed at least one resonance, which gives rise to losses in the OL and whose position has a dependence on both a_{s} and a_{h} in agreement with CIRs properties.

4.4 Elastic or inelastic confinement-induced resonances?

After detecting the presence of a CIR the question arises whether the resonance is an ECIR or an ICIR. From what discussed so far, the presence of the losses is already a strong indication of an ICIR, since the molecular state in ECIR can not be populated (Sec. 2.9). Additional evidence can be obtained considering that there are multiple ICIRs, due to the possibility of coupling to bound states with different CM excitation, while there is only a single ECIR. One way to proceed is to extend the investigation to a wider range of B_i, respectively a_{s}, and see if it is possible to detect multiple resonances. In a new set of measurements, I tuned the magnetic field in the region between 40 G and 100 G, which allows the tuning of a_{s} by almost $1000\,\mathrm{a}_0$ as shown in Fig. 3.1. As in the previous measurements, the atoms are first loaded into the OL with $V_i = 20(3)\,\mathrm{E}_{\mathrm{rec}}^{\mathrm{Cs}}$, then the magnetic field is ramped up from 21 G to B_i, and the atoms are held for $\tau_{\mathrm{h}} = 20\,\mathrm{ms}$ before the procedure is reversed. After the lattice is removed the cloud is levitated and expands for 52 ms. In this configuration, the cloud size has a better signal-to-noise ratio than the atom number and can provide a clear signature of resonance features. The results for the cloud size are reported in Fig. 4.3. There are four resonant peaks. To extract the positions and widths of the peaks, I fit the sum of four gaussian curves to the data, I forced a constant offset common to all four gaussians. The results from the fits are reported in Table 4.1.

From the comparison between Fig. 4.3 and Fig. 3.1, it emerges that P_0 is compatible with the FR at 48 G. The FR at 53 G is not evident from the scan, probably because it is much narrower than the 48-G resonance. The tuning of a_{s} on the side of the 48-G resonance has not enough

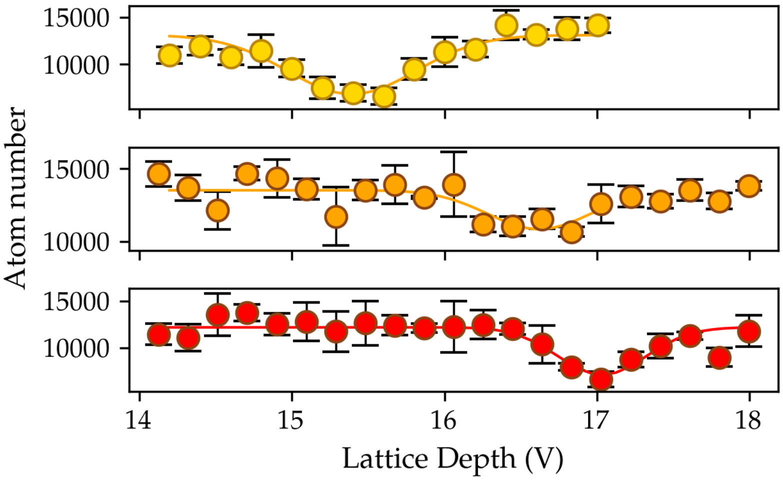

Figure 4.2 (a).

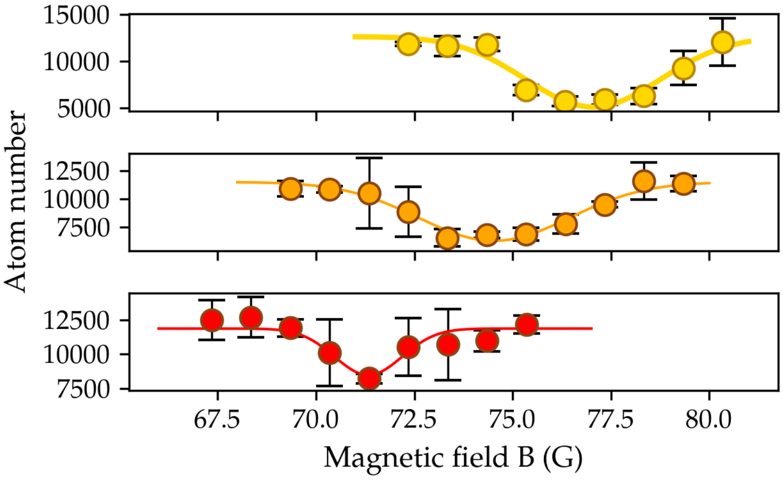

Figure 4.2 (b).

Figure 4.2: Observation of an ICIR. (a) Shift of the loss feature as the magnetic field is varied. Number of atoms released from the OL as a function of V_i for several values of the magnetic field: top $B_i = 77\,\mathrm{G}$, center $B_i = 65\,\mathrm{G}$, bottom $B_i = 62\,\mathrm{G}$. The lattice depth is equal in the three directions. The solid lines are gaussian fits to the data. (b) Shift of the loss feature as the lattice depth is varied. Number of atoms released from the OL as a function of B_i, for several V^{lat} of the OL: top $V_i = 14\,\mathrm{E}_{\mathrm{rec}}^{\mathrm{Cs}}$, center $V_i = 15.5\,\mathrm{E}_{\mathrm{rec}}^{\mathrm{Cs}}$, bottom $V_i = 16\,\mathrm{E}_{\mathrm{rec}}^{\mathrm{Cs}}$. The lattice depth is equal in the three directions. The errorbars in all plots are the standard deviation over three repetitions. The solid lines are gaussian fits to the data.

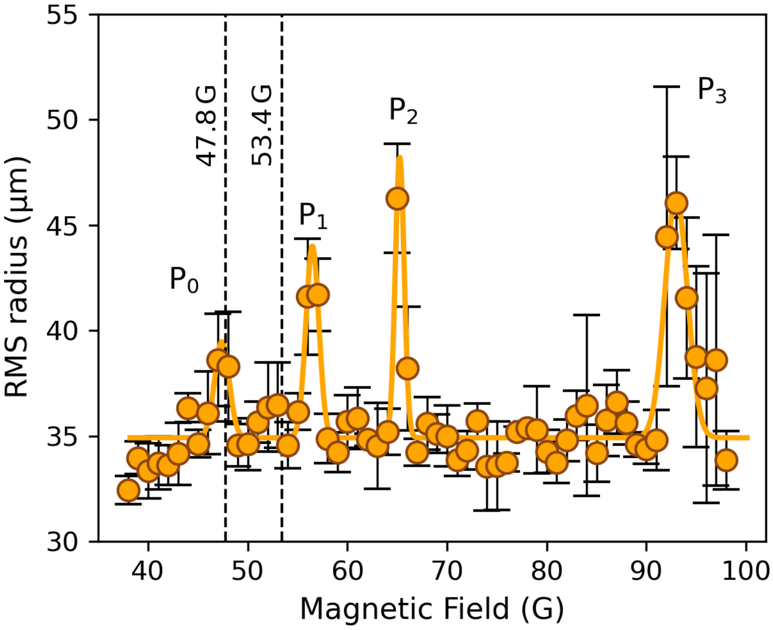

Figure 4.3: Observation of multiple heating features due to ICIRs. Cloud size along z-direction after 52 ms TOF as a function of B_i. The increase in radius at fixed TOF is used as an indicator of heating in the atomic sample. There are four resonant peaks labeled as P_0, P_1, P_2, P_3. The solid line is a fit based on four gaussian curves. The dashed lines mark the position of known FRs in the interval according to Ref.[171].

Resonance	Center G	Center $a_\mathrm{s}(a_0)$
P0	47.4(3)	
P1	56.5(2)	1116 (4)
P2	65.2(3)	1237 (4)
P3	93.0(2)	1489 (1)

Table 4.1: Summary of the resonance positions from the fit of Fig. 4.3

resolution to show any substructure (see Sec. 4.6). The resonances P_1, P_2, P_3 do not correspond to any FR calculated or measured in Ref. [171], which included up to the g-molecular channel. Since the coupling to higher molecular channels is usually considered negligible, P_1, P_2, P_3 are most likely ICIRs.

4.5 Resonance shift

4.5.1 Isotropic lattice

As a final check to confirm that all three resonances observed in the previous section are indeed ICIRs, I characterize systematically the position of the resonances as a function of a_{s} and a_{h}. The experimental sequence is performed similarly to the one already presented in Sec. 4.2. I scan B_i, for different V_i: $V_i = 15.5(3)\,\mathrm{E}_{\mathrm{rec}}^{\mathrm{Cs}}$, $V_i = 16.5(3)\,\mathrm{E}_{\mathrm{rec}}^{\mathrm{Cs}}$, $V_i = 17.5(3)\,\mathrm{E}_{\mathrm{rec}}^{\mathrm{Cs}}$, $V_i = 18.5(3)\,\mathrm{E}_{\mathrm{rec}}^{\mathrm{Cs}}$ and $V_i = 20.0(3)\,\mathrm{E}_{\mathrm{rec}}^{\mathrm{Cs}}$, respectively, $a_{\mathrm{h}} = 1613(8)\,a_0$, $a_{\mathrm{h}} = 1588(7)\,a_0$, $a_{\mathrm{h}} = 1565(7)\,a_0$, $a_{\mathrm{h}} = 1543(6)\,a_0$, and $a_{\mathrm{h}} = 1513(6)\,a_0$. In view of the next section (Sec. 4.5.2), I would like to stress again that here the ramps for all three beams of the OL are identical. This ensures that the OL is completely symmetric along the three axes at all times during the ramps. As discussed previously, the OL is loaded initially at $B = 21\,\mathrm{G}$, which gives U/J ratios between 150.7 and 345, depending on V^{lat}, this is well in the Mott-insulating regime. Similarly to the previous experiments, the initial peak density of the BEC determines predominant single occupancy [151]. Analogously to what was done in Fig. 4.3, the sum of three gaussian curves with a common offset is fitted to the data, and the resulting center positions are reported as closed circles in Fig. 4.4 as a function of a_{h}. The three data sets correspond to the three peaks P1, P2, P3 of Fig. 4.4. The width of the peaks from the fit are reported as errorbars, this choice accounts for systematic uncertainties that might be due to a possible shift between the pole of the ICIR and the maximum of the heating. These systematic uncertainties are much larger than the uncertainties from the fits. There is a well-defined trend of the resonance positions with a_{h}, where for larger a_{h} the resonance is found at larger a_{s}. The exact relation between a_{h} and a_{s} is unique to each resonance and is determined by the CM and RM state involved as discussed in Sec. 2.12.

4.5.2 Anisotropic lattice

Next, I investigate the effect of the anisotropy on the resonances. In order to do so, I introduce a controlled anisotropy by ramping up the depth of the OL such that $V_x(t) = V_y(t) \neq V_z$. The intensity ramps for the three OL beams along the three directions have the same duration even though the final value is different, therefore the anisotropy is introduced from the very beginning of the ramps. The anisotropy lifts the degeneracy of the resonances and a second resonance at a different a_{s} appears.

I ramp two lattice beams to $V_x = V_y = 18.5(3)\,\mathrm{E}_{\mathrm{rec}}^{\mathrm{Cs}}$, the corresponding harmonic oscillator lengths along the two directions are $a_{\mathrm{h,x}} = a_{\mathrm{h,y}} = 1543(6)\,\mathrm{a}_0$ [171], and I use $V_z = 16.5(3)\,\mathrm{E}_{\mathrm{rec}}^{\mathrm{Cs}}$ or $V_z = 17.5(3)\,\mathrm{E}_{\mathrm{rec}}^{\mathrm{Cs}}$, respectively $a_{\mathrm{h,z}} = 1588(7)\,\mathrm{a}_0$ and $a_{\mathrm{h,z}} = 1565(7)\,\mathrm{a}_0$ [171]. As shown in Fig. 4.5, an individual resonance splits in two peaks whose separation depends on the difference in energy of the different lattice directions. Gaussian curves are used to fit the two peaks. The center positions and the widths from the fits are reported in Fig. 4.4, as a function of V_z. In Fig. 4.5 the splitting gives rise to two well-defined resonances. Qualitatively one resonance takes place for CM excitations along the z-axis of the OL and it is approximatively at the same a_{s} at which I found the resonance in the isotropic lattice of $V_l = V_z$. The other resonance takes place for atoms with CM excitations along the x- and y- axis and it is approximatively at the same a_{s} at which I found the resonance in the isotropic lattice of $V_l = V_x = V_y$. Quantitatively the system deviates slightly from these values

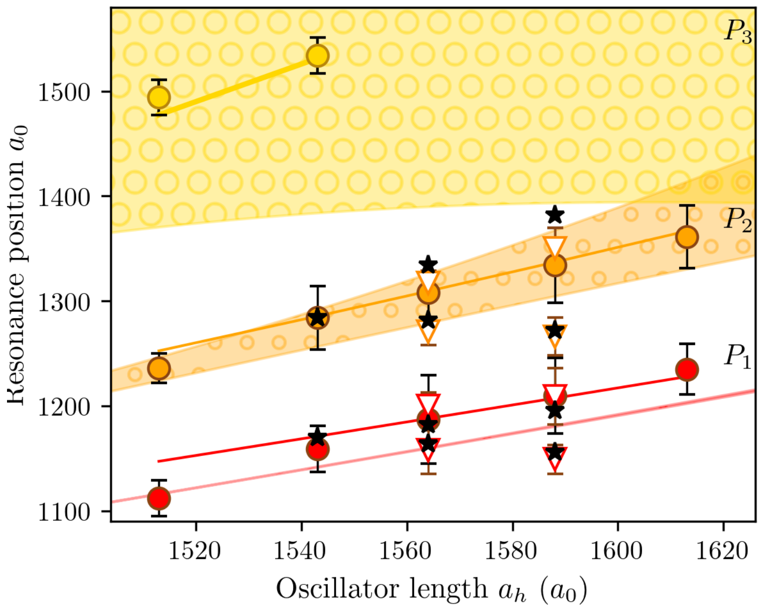

Figure 4.4: Comparison of the shifts of the three ICIRs with the theoretical prediction. Resonance position for the isotropic case, for different V_i, respectively a_h, as full circles, for the resonances P1 (red), P2 (orange), P3 (yellow). Experimental data for the anisotropic lattice as empty triangles, for the resonances P1 (red), P2 (orange), plotted as a function of a_h along the z-direction. The errorbars represent the width of the resonances. Theory predictions from M1 (Sec. 2.12) for the isotropic case as shaded areas with circle patterns, for the resonances P1 (red), P2 (orange), P3 (yellow). Theory predictions from M2 (Sec. 2.12) for the isotropic case as solid lines, for the resonances P1 (red), P2 (orange), P3 (yellow). Theory predictions from M2 (Sec. 2.12) for the anisotropic case as black stars.

due to the corrections to the energy of the trap state due to the anisotropy, and the anharmonicity (Sec. 2.12).

4.5.3 Comparing the data to the model

I report in Fig. 4.4 the position of the crossings from the two theoretical models M1 and M2 described in Sec. 2.12 for each oscillator length, obtained from plots analogous to Fig. 2.6, together with the data for the isotropic and anisotropic lattice. There is no fitting parameter used in the representation of M1 or M2. It can be observed that despite the differences between the two models, both models are in good qualitative and quantitative agreement with the data. From the comparison between the data and the theoretical models, it is possible to clearly identify the trap and excited states involved for the resonances P1 and P2. P1 is in good quantitative agreement with the crossing of the $\psi_1^{\mathrm{RM}}\phi^{\mathrm{CM}}(0,0,0)$ with $\psi_b^{\mathrm{RM}}\phi^{\mathrm{CM}}(2,2,0)$. While P2 is in good quantitative agreement with the crossing of $\psi_1^{\mathrm{RM}}\phi^{\mathrm{CM}}(0,0,0)$ with $\psi_b^{\mathrm{RM}}\phi^{\mathrm{CM}}(4,0,0)$. The identification of P3 is more demanding. In Fig. 4.4 I report the crossing of the state $\psi_1^{\mathrm{RM}}\phi^{\mathrm{CM}}(2,0,0)$ with $\psi_1^{\mathrm{RM}}\phi^{\mathrm{CM}}(6,0,0)$. However, the

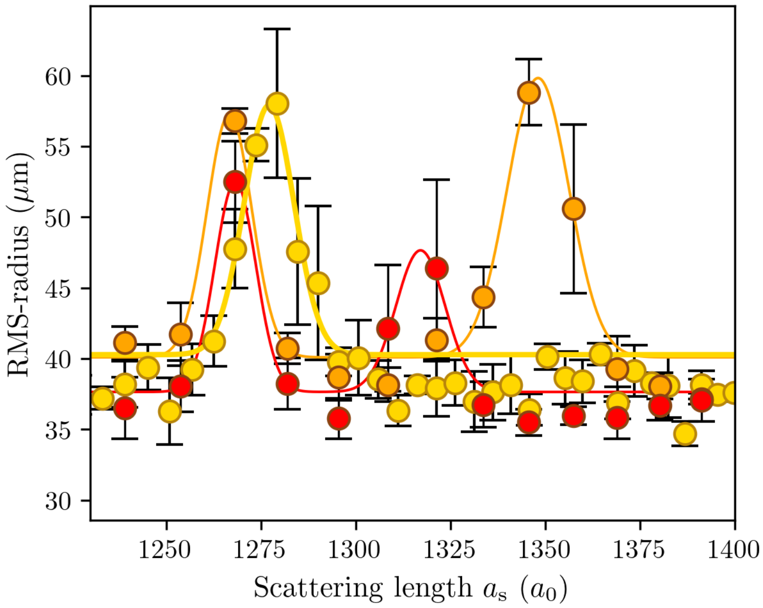

Figure 4.5: Splitting of the resonance in the presence of a controlled anisotropy. Cloud size after holding the atoms in an anisotropic OL as a function of the a_s for Cs imaged after 52 ms TOF. For the three data sets $V_x = V_y = 18.5\,\mathrm{E}_{\mathrm{rec}}^{\mathrm{Cs}}$, the third direction has $V_z = 18.5\,\mathrm{E}_{\mathrm{rec}}^{\mathrm{Cs}}$ (yellow), $V_z = 17.5\,\mathrm{E}_{\mathrm{rec}}^{\mathrm{Cs}}$ (red),$V_z = 16.5\,\mathrm{E}_{\mathrm{rec}}^{\mathrm{Cs}}$ (orange). The errorbar are the standard deviation over three repetitions. The solid lines are fit based on gaussian curves.https://www.overleaf.com/project/613776e400a2e51d6e74ffd3

approximation at the core of the Hubbard model as presented in this thesis neglects the possibility of atoms in the excited bands of the lattice as discussed more in detail in Sec. 4.7.

The good qualitative and quantitative agreement between theory and data should come as a surprise. Firstly, the localization of the atoms at the lattice sites is not only due to the confining potential but it is largely due to the strong interatomic interaction. Secondly, both models assume for the treatment of the RM motion that both atoms are on the same lattice site, and in M2 this hypothesis extends also to the treatment of the CM. On the contrary, in the experiment doubly-occupied sites should be limited to a small number of defects in the experiment and not be the dominant case. Before discussing this later point I want to compare the data with related experimental results.

4.6 Comparing the data with related experiments

In this section, I discuss two experimental results, E2 and E3, from different projects, that closely relate to the discussion presented so far which I will refer to as E1. E2 is a dataset from Innsbruck, of which I became aware during the analysis of the data above and that has been incorporated in Ref. [74]. E3 is a recent work by Lee *et al.* [172] in parallel to Ref. [74]. E2 shows scattering resonances in a three-dimensional OL starting from a predominantly single-shell MI, E3 shows the analogous effect for a quasi-one-dimensional lattice.

Data for E2 have been acquired by Manfred Mark[2] with the collaboration of Florian Meinert[3], during the investigation that led to the results reported in Ref. [173]. This dataset was taken in a three-dimensional OL with a magnetic gradient compensating the effect of gravity, similar to the conditions I used in my experiments. They also worked on Cs atoms at a lattice depth of $20\,\mathrm{E}_{\mathrm{rec}}^{\mathrm{Cs}}$. The main differences of E2 with respect to E1 are: a_{s} is varied on the side of the 48-G resonance, rather than on the broad background; the hold time $\tau_{\mathrm{h}} = 50\,\mathrm{ms}$ is longer; the data report the loss feature in the atom number instead of the cloud size as I used for most results. In Fig. 4.6, I plot the data from E2 together with the data from Fig. 4.3, as a function of a_{s}. For reference, I also report in Fig. 4.6 the theory for both M1 and M2. Despite the different FR involved, the ICIR positions match well between the two data sets, for all three resonances. This is a further indication that the position does not depend on the molecular state involved in the bound state, in agreement with the expected universality of ICIRs. The data from E2 shows in general broader resonances, I found the broadening to be compatible with the presence of the levitating field $\nabla B \sim 30$ G/cm, which shifts the resonance condition across the cloud. This effect is much bigger in E2 with respect to E1, due to the drastic change of a_{s} with B close to the pole of the FR with respect to changing a_{s} on the background.

The first peak in E2 splits into two peaks $\mathrm{P}'_{1\mathrm{A}}$ and $\mathrm{P}'_{1\mathrm{B}}$. The separation between $\mathrm{P}'_{1\mathrm{A}}$ and $\mathrm{P}'_{1\mathrm{B}}$ is $\sim 30\ a_0$. When compared to the investigation of a controlled anisotropy, in Sec. 4.5.2, it is evident that this splitting is comparable with the systematic uncertainty of $5\%(\sim 1\,\mathrm{E}_{\mathrm{rec}}^{\mathrm{Cs}})$ declared by the authors for the calibration of V^{lat} [74]. This leads to interpreting both $\mathrm{P}'_{1\mathrm{A}}$ and $\mathrm{P}'_{1\mathrm{B}}$ as corresponding to P_1 in E1, with a splitting due to an unwanted anisotropy (Sec. 4.5.2).

E3 reports on the observation of scattering resonances from a single-shell MI of Li atoms in a quasi one-dimensional OL. The resonances were detected as a tuning of the effective interaction strength by measuring super-exchange spin dynamics [174]. Tunneling was explicitly reported with the formation of doubly-occupied sites. Despite the similarities of the experimental conditions, the resonances detected in E3 do not match the ICIRs reported in this thesis. A further extension of M2 which includes two atomic wells[4][175] is able to predict both the ICIRs presented in this thesis and the resonances of E3[5]. However, the coupling predicted for the resonances of E3 is much smaller and it relies on the presence of the tunneling.

4.7 Outlook

So far the emergence of resonances in a 3D OL was presented and the resonances have been identified as ICIRs, leading in some cases to the identification of the states involved. This phenomenon has not been previously observed in a 3D confinement.

---

[2] Now at Institut für Quantenoptik und Quanteninformation, Österreichische Akademie der Wissenschaften, Technikerstraße 21a, 6020 Innsbruck, Austria.
Institut für Experimentalphysik, Universität Innsbruck, Technikerstraße 25, 6020 Innsbruck, Austria

[3] Now at 5. Physikalisches Institut, Universität Stuttgart, Pfaffenwaldring 57, 70569 Stuttgart, Germany

[4] This is realized by expanding the trapping potential to the twelfth order [74].

[5] Fabio Revuelta, private communication.

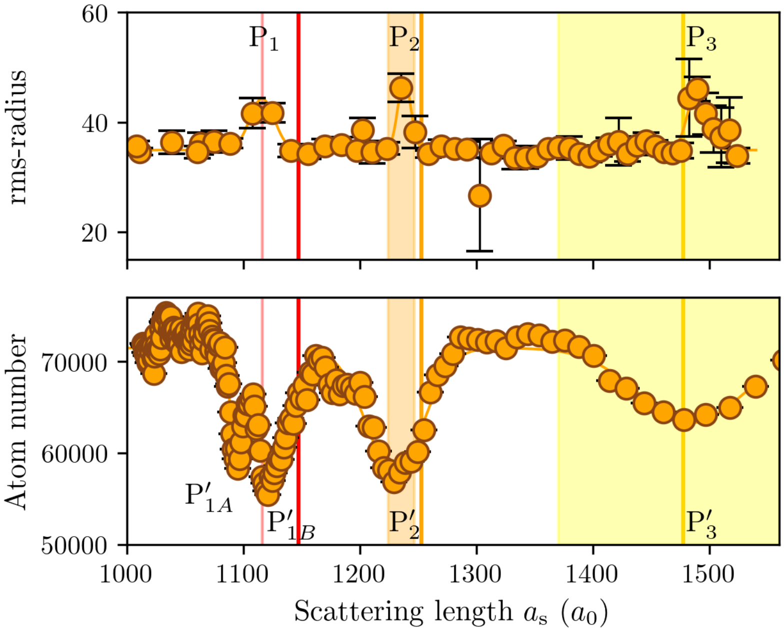

Figure 4.6: Comparison of part of the data presented in this thesis with E2. Top: E1, cloud size as a function of a_s for $B_i \simeq 60{-}100$ G, $\tau_h = 20$ ms, the erorrbars represent the standard deviation over three repetitions. Bottom: E2, atom number as a function of a_s for $B_i \simeq 46 - 47.6$ G, $\tau_h = 50$ ms, single repetition. Both datasets have been acquired for $V^{\mathrm{lat}} = 20\,\mathrm{E}_{\mathrm{rec}}^{\mathrm{Cs}}$. In both plots, the shaded areas correspond to the results from M1, the solid vertical lines correspond to the results from M2. A fit based on three (four inverted) gaussian curves has been applied to the data in the top (bottom) plot.

Like any investigation, a few open questions remain. In the following, I want to discuss the possible dynamics of the underlying ICIRs in a MI with predominant single occupancy, in view also of the energy discrepancy between the theory and experiment, and add a few considerations on the identification of P3 in the context of the RbCs project.

4.7.1 The dynamics of ICIRs

The difference in the initial conditions between the experiment and the theory is the major question that remains after the characterization of the ICIRs. This question relates directly to the dynamics underlying the process. The fact that matching ICIRs have been found completely independently in E1 and E2 makes major systematic errors in the sample preparation unlikely. Nevertheless, small imperfections are bound to emerge in the experimental system: a small percentage of doubly-occupied sites (E2 claims less than 10%), a small percentage of holes that lead to the formation of SF-pockets, and the finite size of the sample implies the presence of a SF shell at the edge of the cloud. Approximating the cloud as a perfect sphere, in E1 the outer shell involves about 20% of the total number of atoms. It is possible that the coupling due to ICIRs is extremely sensitive to the presence of such defects. Doubly-occupied sites realize exactly the conditions of our modelling and it is then clear they would be affected by ICIR. If this were the only process, the dynamics would be limited to the initial number of doubly-occupied sites. If the molecule is lost, upon collision with a third atom, it would leave behind a hole and create a small shell in which the atoms are mobile. If the atoms in such superfluid shells would not be subjected to ICIRs, the loss dynamic would stop when all doubly-occupied sites have been depleted from the system. On the contrary, if SF shells within the sample or at the edge are susceptible to ICIR, it could lead to a chain reaction. When the atoms in the initial shell are lost, the boundary of the shell moves to the next occupied lattice site. This process could propagate through the sample until its full depletion, independently of the initial size of the SF shell. Scattering in the SF shells also accounts for the additional energy due to onsite interaction. Extension to multiple wells of the ICIRs theory is expected to work also in the presence of delocalized atoms [175] and the results of E3, which use a much weaker lattice, are compatible with such approximation. Ref. [176] also predicts some similar effects for two atoms delocalized on a OL, but similarly to the modeling presented in this Chapter, it does not include the many-body character of the system. A detailed characterization of the dynamical rate at which the losses and heating take place, in relation to the initial conditions, would be interesting to determine the role of the different kinds of defects. In this mindset, a comparison between the dynamical loss and heating rates starting from a MI with predominant doubly-occupied sites or from a SF regime and the losses from a MI with predominant single-occupancy can help to obtain more information on the dynamics underlying the ICIRs. I conducted preliminary studies on the decay rate and molecule formation at the resonance, in the case of a MI with predominant single occupancy, but due to large shot-to-shot fluctuation of the atom number and cloud size, these measurements were inconclusive. The stability of the experimental setup and the reproducibility of the experimental conditions have been addressed with a series of targeted interventions reported in Chapter 6, but due to technical failures of the experimental apparatus, I did not have the opportunity to continue the measurements on the dynamics of ICIRs afterward.

4.7.2 Considerations on P_3 and its role in the context of RbCs

The other big open question remaining in this chapter concerns the identification of P_3, and it might have some deeper ramifications in the context of the RbCs project. During the comparison of Sec. 4.3, several combinations of CM and RM states have been taken into consideration for the resonance and all combinations lead to the conclusion that the trap state responsible for P3 has some CM excitation, i.e. the atoms are in an excited lattice band. Typically when loading a singly-occupied MI from a BEC these lattice bands are not expected to be occupied. It must be noted, that for E1 loading and unloading the atoms in the OL away from resonance already reduces the BEC fraction, indicating the introduction of excitations in the system, but this might not be the case for E2. Another possibility is that band mixing occurs due to the increase of a_s. To the best of my knowledge, I could not find an experimental investigation of the behavior of the atoms in the OL at high a_s when starting from singly-occupied sites, except for the work of Ref. [172]. Nevertheless, it is possible to do some energetic considerations in a simplified picture. Starting from the Bose-Hubbard model [6] in the tight-binding approximation, it is possible to calculate the band structure and the

---

[6] I used the script developed in the context of Ref. [173]

band gap of the OL for non-interacting atoms.

From them, it is possible to compare the interaction energy U and the bandgaps 0^{th} to 1^{st} ($\mathrm{bg}_{0,1}$), and 0^{th} to 2^{nd} band ($\mathrm{bg}_{0,2}$) as a function of a_s for $V^\mathrm{lat} = 20\,\mathrm{E}^\mathrm{Cs}_\mathrm{rec}$. It can be seen that already for $a_\mathrm{s} = 1000$–$1500\,a_0$ as used in the ICIRs measurements, the naïve calculation returns $U = 3.9$–$5.9\,\mathrm{E}_\mathrm{rec}$ which cannot be considered negligible with respect to the two bandgaps, $\mathrm{bg}_{0,1} = 7.6\,\mathrm{E}_\mathrm{rec}$ and $\mathrm{bg}_{0,2} = 13.2\,\mathrm{E}_\mathrm{rec}$. In this regime, the approximation done for the evaluation of the Bose-Hubbard model that the bandgap is the dominating energy scale clearly fails, and the model can not be considered quantitatively accurate. However, given the approaching energy scales and the experimental evidence of occupation of the excited band, in the future it would be interesting to probe the initial state with bandmapping as a function of a_s, to verify experimentally if the atoms are found in the lower Brillouin zone or can also be found at higher quasi-momentum. This study can be extended up to reach $a_\mathrm{s}\sim 2400\ a_0$, the scattering length assumed by Cs near the 355-G interspecies FR, where the RbCs project aims at forming the molecules. In this case the onsite interaction energy calculated in the same way exceeds the bandgap, making the model unreliable. The possibility of atoms in excited bands questions significantly the timescales for the dynamics due also to the increase of the tunneling energy in the higher lattice bands. For reference, the tunneling rates for non-interacting atoms for the three lower bands of a $20\,\mathrm{E}_\mathrm{rec}$lattice are $J_0 \sim 3 \times h\,\mathrm{Hz}$, $J_1 \sim 80 \times h\,\mathrm{Hz}$, and $J_2 \sim 590 \times h\,\mathrm{Hz}$. Faster tunneling timescales would clearly challenge the stability of the atoms in the OL and the assumption of working with an insulating state such as the MI.

4.8 Conclusion

This chapter has shown the effect of the confinement from the OL on the collisional stability of the atoms in a MI with predominant single occupancy. In particular, it establishes the presence of ICIRs in the three-dimensional OL. This phenomenon has not been previously documented in any kind of 3D confinement.

The investigation was performed using a Cs MI with predominant single occupancy and showed the emergence of resonant loss and heating features at positions depending on both the confinement length and the three-dimensional s-wave scattering length. The positions of the resonances were found to be tunable as predicted by ICIR theory. The position of the resonances is found to be in good agreement with the two theoretical models M1 and M2, which assume the presence of two atoms on the same lattice site, despite the MI in the experiment having predominant single occupancy. A controlled anisotropy was introduced to remove the degeneracy of the resonances, the splitting was found in agreement with M2.

The presence of a resonance that is in agreement with the occupation of the 1^{st} or 2^{nd} band of the lattice raises reasonable doubts over the possibility of band mixing. Energetic considerations stemming from this observation show that band mixing could also be affecting the initial conditions at which RbCs molecules are created, further limiting the MI stability, hence, the efficiency of the molecule formation.

The detection of ICIRs in the lattice might be of crucial importance in systems with numerous FR like lanthanides atoms in the lattice [177, 178] or in the presence of very deep lattices like in the case of single site imaging [179, 180]. ICIRs can also prove to be a useful tool in lattices when the anharmonicity of the sites themselves can be tuned [181]. In this case, ICIRs have a strong advantage with respect to magnetic FRs and ECIRs because not only their position is tunable but also their coupling strength. This can be done, e.g., for identical atoms by changing the anharmonicity of the confinement, which modifies the CM- coupling as seen in M1 and M2. For distinguishable atoms, the CM-RM coupling is also enhanced by a difference in the masses and the polarizabilities of the atoms. Due to this ICIRs can pose a new way for the association of dimers. Dipolar interactions are also expected to provide an extra 'knob' to tune the position of ICIRs [139]. A three-dimensional confinement, similar to the confinement on the individual sites of the OL is also realized in optical tweezers. In this framework, ICIRs are expected to play a major role in mergo-association of heteronuclear dimers [170]. The observation of ICIRs in OL lays also the foundation for a better understanding of ICIRs in other systems like dipolar gases [139] and excitons in semi-conductor cavities [73].

Chapter 5

Transport

5.1 Introduction

The mixing of Rb and Cs in the OL, as seen in Chapter 3, relies on two different processes, on one hand, the transport of the Rb atoms in a ODT across the OL to overlap it with Cs, on the other hand, storing Cs atoms in a MI. In this Chapter, I will focus on the transport of Rb, and investigate the role of the confinement from the OL, with respect to the confinement from the ODTand in the presence of spurious experimental conditions.

Transport is a very general term in cold atoms experiments that covers, just to give a few examples, lattice instabilities [8], conductivity in atomtronics [182], and relativistic analogs like the Lieb-Robinson bound [183]. In this Chapter, I will limit the description to the specific case of transporting a degenerate cloud of Rb atoms in the superfluid state in the OL, from point A, its original position, to point B, where Cs atoms are expected to be, through the OL, with the help of an optical harmonic trap, the Rb dimple. This transport should be fast for two reasons: first, as seen in the previous Chapter (Chapter 4), Cs atoms necessary to the molecule formation are lost over time even when storing them in a predominantly single-occupancy MI; second three-body recombination processes involving two Rb atoms and one Cs atom can take place from the time the two clouds start to overlap up to the time the SF-MI transition (Sec. 2.8) is induced for Rb after the overlap is completed. Several variations of this transport instance have been realized over the years covering different ingredients of the problem presented in the next sections. Transport of atoms without the optical lattice has been realized for example in Ref. [184]. In quasi-1D systems, the instantaneous displacement of a magnetic trap has been used to study the onset of localization [185, 123], in 3D systems transport over a few to tens of lattice sites has been tested with weak and tight traps, moving either the atoms through the lattice [186] or keeping atoms at a fixed position while moving the lattice [122].

The RbCs project combines a longer-distance transport, more than 200 lattice sites, with a tight trap. Here, I address the interplay between the lattice depth and the dimple and discuss the role of experimental imperfections. In Sec. 5.2, I show previous experimental results of the RbCs project from Ref. [63] and Ref. [124]. In Sec. 5.3, I report the investigation of transport as a function of the ODT parameters. In Sec. 5.4 I propose a simpler description of the data of Sec. 5.3. In Sec. 5.5, I investigate the need for a minimum trap frequency of the dimple to achieve transport by means of numerical simulations of experimental imperfections within the framework of a time-dependent GPE.

The transport described in this Chapter remains within the adiabatic constraints, therefore the discussion neglects short-cut-to-adiabaticity techniques [187].

5.2 Previous results

Reichsöllner and Schindewolf observed for the RbCs project [151, 124] that critical transport velocities at which transport is not suitable for the formation of molecules are much lower than the ones expected by energetic instabilities (Sec. 2.8) as, e.g., contrary to what observed in other experiments like the one by Mun *et al.* in Ref. [122]. The results from Ref. [124] are reported in Fig. 5.1.

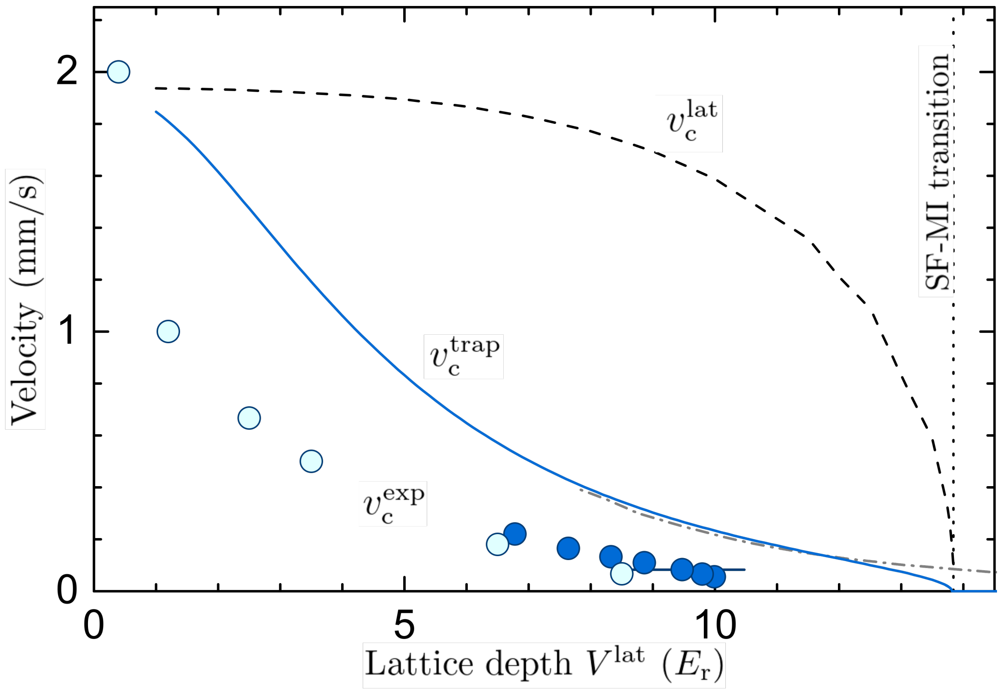

Figure 5.1: Critical velocities as a function of $V^{\rm lat}$ for a trap with $\omega_{Rb} = 20\,\rm Hz$. The light blue circles are critical transport velocities detected by measuring directly the number of Rb atoms, the dark blue circles have been measured indirectly as the velocities that induced a sharp drop in the number of associated RbCs molecules. The dashed line represents the theoretical $v_{\rm c}^{\rm lat}$. The solid line represents the theoretical $v_{\rm c}^{\rm trap}$. The figure has been adapted from Ref. [124].

The experimental critical velocity $v_{\rm c}^{\rm exp}$ from Ref. [151] has been estimated as the transport velocity for which the formation of RbCs molecules, at the end of the sequence described in Chapter 3, drops below 15%. In Ref. [124] additional data have been taken using only the Rb condensate (without Cs), in this case, the critical velocity has been estimated as the velocity for which the BEC fraction of the transported atoms drops below 15%. As seen in Fig. 5.1 the two criteria are compatible in the region where the datasets overlap. The data were compared with two mean-field approaches, one derives the critical velocity comparing the critical quasi-momentum q_c for energetic instabilities according to the Landau theory [102], with the lattice group velocity $v_\mathrm{g}^\mathrm{lat}$, this velocity is indicated with $v_\mathrm{c}^\mathrm{lat}$, in the second approach q_c is compared to the trap group velocity $v_\mathrm{g}^\mathrm{trap}$ (Sec. 2.8) obtaining $v_\mathrm{c}^\mathrm{trap}$.

It can be easily seen that the data differ significantly both quantitatively and qualitatively from the $v_\mathrm{c}^\mathrm{lat}$, and that the data differ quantitatively from $v_\mathrm{c}^\mathrm{trap}$. On the contrary, the critical velocities reported in Ref. [122] agree with the expected critical quasi-momentum.

The deviation of the critical velocity from both theoretical and experimental results triggered a new analysis of the experimental procedure and its results. Our experiments and the ones reported in Ref. [122] differ on two important aspects: The first is the stiffness of the confinement due to the dimple [124], which is much tighter in the RbCs experiments, and the second is the transport distance that in the case of RbCs is much larger, making the process sensitive to spatial inhomogeneity of the experimental conditions.

5.3 The experiment

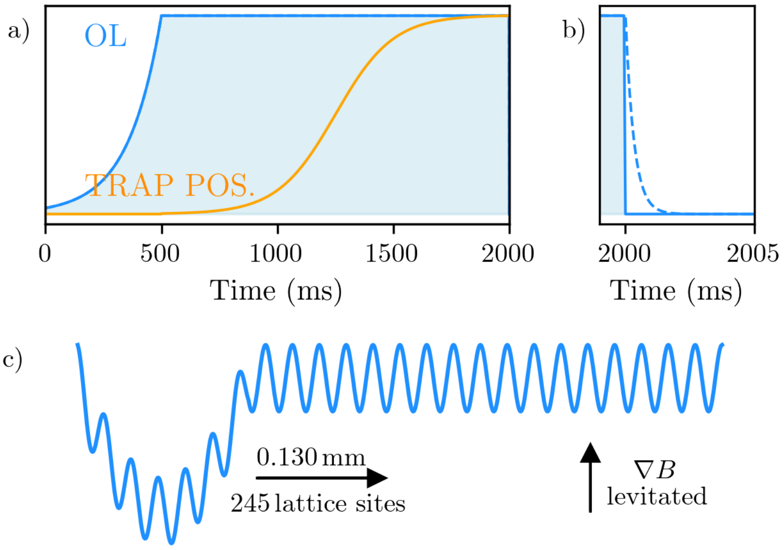

Figure 5.2: Schematic representation of the sequence for coherent transport. a) Depth of the optical lattice and trap position as a function of time. b) Zoom on the switch-off sequence. The solid and dashed blue lines are the switch-off, respectively for projecting on the spatial distribution the momentum or quasimomentum of the atoms (see text). c) Cartoon picture of the system (simplified to 1D). The dimple modifies locally the potential. During transport the dimple is shifted by 130 μm in 1.5 seconds. The atoms are levitated against gravity.

At the beginning of my Ph.D. work, we investigated the role of the trap frequency of the dimple on the efficiency of the transport. The experimental sequence follows the footsteps of the mixing of

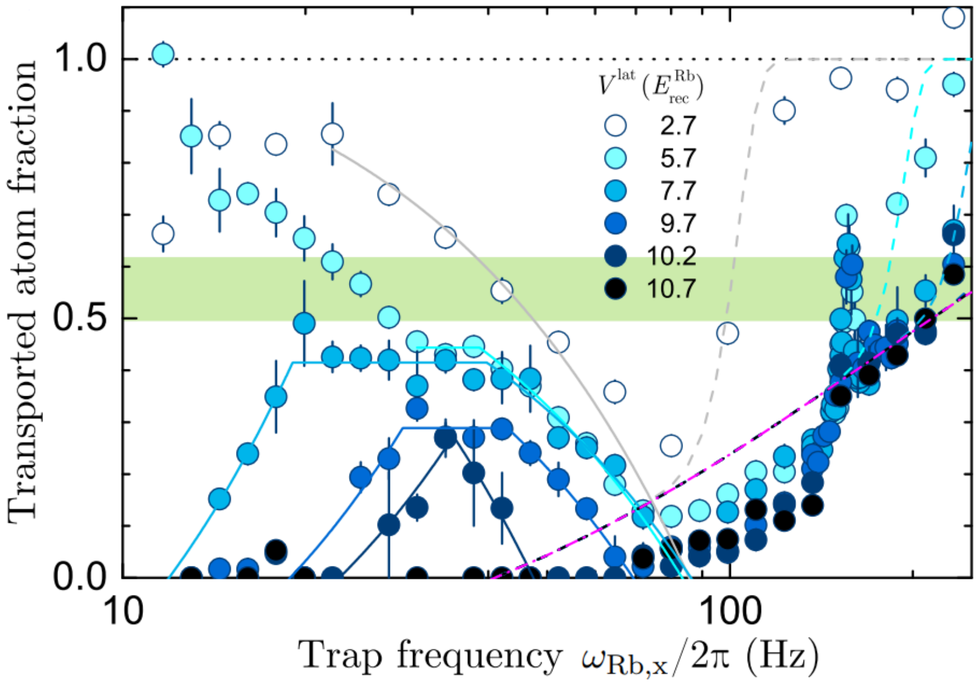

Figure 5.3: Fraction of transported atoms and transport regimes. Fraction of transported atoms as a function of $\omega_{\mathrm{Rb,x}}$, for different V^{lat}. The atoms are transported over a distance of 130 μm at a speed of 87 μm/s. The green area represents the typical BEC fraction for the measurements and is here reported for reference. The solid lines are piece-wise linear fits to the data. The dashed lines show the estimated total fraction of atoms transported in excited lattice bands and it includes the calculations for atoms that undergo a Landau–Zener transition into excited bands during the transport process. The figure is taken from Ref. [124]

Rb and Cs described in Chapter 3. Cs atoms are blown away during evaporative cooling (Sec. 3.10), to work with a pure Rb sample. The successive steps of the sequence are sketched in Fig. 5.2.

At the end of the evaporative cooling, the Rb condensate, held by the dimple, is loaded in the OL, by ramping the OL adiabatically to $V^{\mathrm{lat}} = 2.7$–$10.7\,\mathrm{E}_{\mathrm{rec}}^{\mathrm{Rb}}$ in 500 ms. The magnetic field gradient is set to levitate Rb. Next, the position of the Rb dimple is moved in 1.5 s by about $\sim 130\,\mu$m, which gives a speed of 87 μm/s and a distance in lattice units of about 245 lattice sites. For the measurements, two different protocols have been used to release the atoms from the OL. In the first, after the transport, the OL and the dimple are switched off. The cloud expands for 52 ms of TOF before imaging. Alternatively, it is possible to map on the spatial distribution the quasi momentum of the atoms [188] and image the occupation of the Brillouin zones. This process, known as band mapping, is achieved by ramping down the depth of the OL sufficiently slow that atoms are not excited to higher bands, but faster than the timescale at which the atoms can redistribute to preserve the chemical potential [188]. In our case, for typical lattice depths, this is realized with an exponential ramp ($e^{-\gamma t}$ with $\gamma = 3\,\mathrm{ms}^{-1}$) of 2 ms. Following the ramp, a levitated TOF of 12 ms is applied.

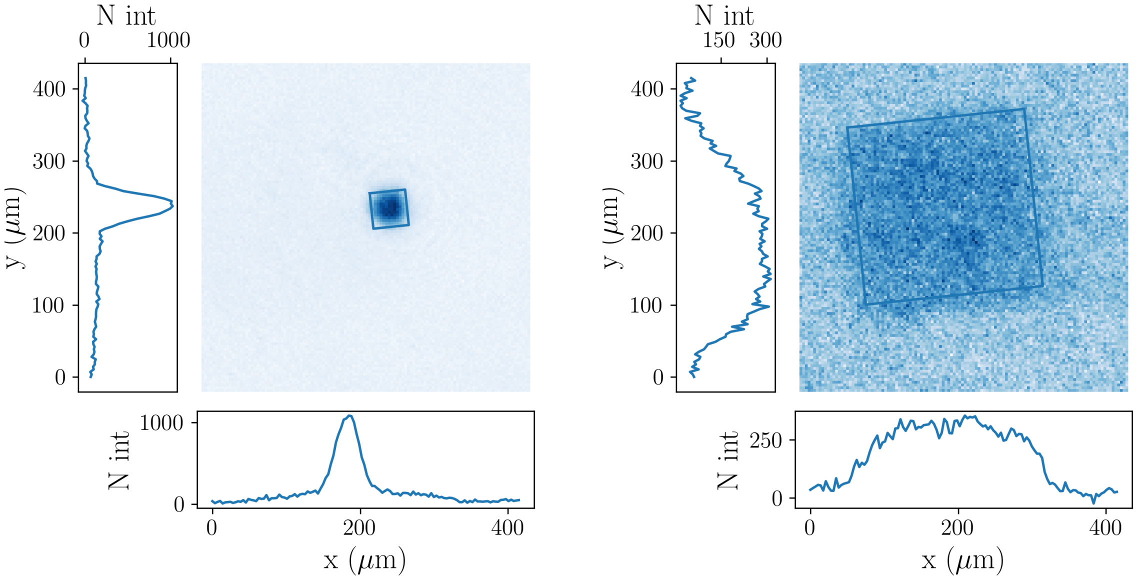

Figure 5.4: Band mapping after superfluid transport in a OL at 7.7 Erec. The trap frequencies are $\omega_{\mathrm{Rb,x}}/(2\pi) = 101.3(6)\,\mathrm{Hz}$ (left) and $\omega_{\mathrm{Rb,x}}/(2\pi) = 59.97(6)\,\mathrm{Hz}$ (right). The squares are guides to the eye, the length of side of the square on the right figure is 5 times larger than the square on the left figure.

Fig. 5.3, shows the fraction of atoms transported to the final location, for different values of V^{lat}, as a function of the trap frequency $\omega_{\mathrm{Rb,x}}$ of the Rb dimple along the transport axis. According to Ref. [124], four main regions can be identified. Toward small values of $\omega_{\mathrm{Rb,x}}$, the fraction of atoms transported increases gradually, at intermediate values of $\omega_{\mathrm{Rb,x}}$ there is a plateau corresponding to optimal transport conditions, and for higher $\omega_{\mathrm{Rb,x}}$ the transported fraction decreases. Above $\omega_{\mathrm{Rb,x}}/(2\pi) \sim 100\,\mathrm{Hz}$ the transported fraction rises again. Band mapping shows that when $\omega_{\mathrm{Rb,x}}/(2\pi) \lesssim 100\,\mathrm{Hz}$, the transported atoms are found in the lowest lattice band [124]. In the same conditions, momentum imaging shows the interference pattern typical of superfluidity 3.11. Under these conditions, the SF-MI transition for the Rb sample leads to a high-quality Rb MI, a prerequisite for the formation of the molecules (Sec. 3.12). On the contrary, the revival of transport above 100 Hz is characterized by the presence of atoms in excited lattice bands, detected through band mapping, due to either thermal excitations or Landau-Zener tunneling [124].

Fig. 5.4, shows the band mapping picture taken for an OL of $7.7\,\mathrm{E}_{\mathrm{rec}}^{\mathrm{Rb}}$, respectively at $\omega_{\mathrm{Rb,x}}/(2\pi) = 59.97(6)\,\mathrm{Hz}$ and at $\omega_{\mathrm{Rb,x}}/(2\pi) = 101.3(6)\,\mathrm{Hz}$. In both cases, the cloud is in good approximation squared with a flat density distribution at the center. This profile is what is expected for a cubic lattice. The squares in Fig. 5.4 are drawn as a guide to the eye and their sides are in a ratio 1:5. Assuming that at small $\omega_{\mathrm{Rb,x}}$the square has a side of length $\propto \hbar k_{\mathrm{l}}$ as expected for the first Brillouin zone after the expansion, at the higher $\omega_{\mathrm{Rb,x}}$the length of the side is consistent with an increment of the quasi momentum of $2\hbar k_{\mathrm{l}}$ in all directions, i.e. an atom in the second excited band.

The excitation of the atoms in the lattice for $\omega_{\mathrm{Rb,x}}/(2\pi) \gtrsim 100\,\mathrm{Hz}$ increases the entropy of the system and consequently of the final molecular sample. For these reasons, the regime of $\omega_{\mathrm{Rb,x}}/(2\pi) \gtrsim$

100 Hz is not of interest for the formation of the molecules, and since it has already been detailed in Ref. [124], it will not be addressed in the following discussion. The region below $\omega_{\mathrm{Rb,x}}/(2\pi) = 100\,\mathrm{Hz}$ is instead treated with a new description in the following. In particular, I will show that the presence of a plateau for optimal transport might be an artifact of the analysis, and I will extract the trend for the maximum and minimum frequencies for transport.

5.4 Critical trap frequencies

In the new description of the data presented in Sec. 5.3, I focus on the number of transported atoms for $\omega_{Rb} = 80\,\mathrm{Hz}$, to extract the critical velocities. A sample of the data from Fig. 5.3 is shown in Fig. 5.5, on a lin-lin plot. When displaying the data on this scale, as opposed to the plot of Fig. 5.3 that used a log-lin axis scale to fit the larger frequency range, the presence of a plateau is not easily detectable by the eye. For the physics, this would imply that there is not an optimal transport regime, but rather a single maximum. On the basis of this observation, I try to further simplify the description of the data, by applying a two-piece piece-wise linear fit:

$$\begin{cases} N(x) = \frac{N}{b-a}(\omega - a) \quad \text{for} \quad a < \omega < b, \\ N(x) = -\frac{N}{c-b}(\omega - c) \quad \text{for} \quad b < \omega < c. \end{cases} \tag{5.1}$$

The fit has four free parameters: two frequencies a and c, which are respectively the zero crossing of the ascending part and descending part with the origin of the y-axis, and the coordinates of the intermediate point, b and N, which corresponds to optimal $\omega_{\mathrm{Rb,x}}$ for transporting the atoms and the maximum number of transported atoms. Fits of Eq. 5.1 to the data are reported in Fig. 5.5. The three frequencies a, b, and c are shown also on the plot for one of the fits. I tested the validity of the fitting model of Eq. 5.1, with the R-squared test. The test returned $\mathrm{R}^2 = 0.9$–0.99 for the curves with $V^{\mathrm{lat}} < 10.7\,\mathrm{E}_{\mathrm{rec}}^{\mathrm{Rb}}$, confirming the validity of this description[1].

For comparison, I also tried to fit a three-piece piece-wise function to reproduce the plateau of Fig. 5.3. The fitting model has the form:

$$\begin{cases} N(x) = \frac{N}{b'-a'}(\omega - a') \quad \text{for} \quad a' < \omega < b', \\ N(x) = N \quad \text{for} \quad b' < \omega < c', \\ N(x) = -\frac{N}{d'-c'}(\omega - d) \quad \text{for} \quad c' < \omega < d'. \end{cases} \tag{5.2}$$

In this case, the quantity $c' - b'$ returns the width of the plateau. This second model equivalently returned $\mathrm{R}^2 = 0.9$–0.95, but for one measurement the fit returned a parameter c' smaller than b', for one measurement $c' - b'$ was compatible with zero within the fit uncertainties, and in two more cases, the plateau was smaller than 10 Hz. The absence of a plateau or the small size of the plateau when fitting the model of Eq. 5.2 indicates that the simpler model described by Eq. 5.1 is a good description for the data.

The maximum number of atoms N obtained from the fits with Eq. 5.1 over a larger sample of data is shown in Fig. 5.6(a) as a function of V^{lat}. As expected this number decreases with increasing lattice depth since the system approaches the SF-MI transition.

---

[1] Eq. 5.1 is a very drastic model, physically there is no reason to expect a sharp transition with a discontinuity of the first derivative at point b of the model. Therefore some small deviation from the model is expected due to a

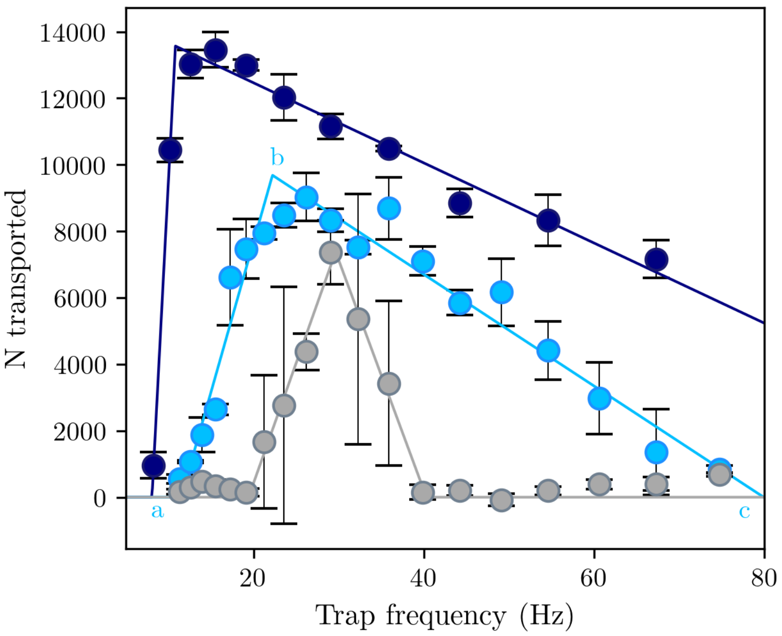

Figure 5.5: Critical transport frequencies. Two-piece piece-wise fits (Eq. 5.1) for part of the data of Fig. 5.3. The different colors represent different depths of the OL: $V^{\text{lat}} = 2.7\,\mathrm{E}_{\text{rec}}^{\text{Rb}}$ in navy,$V^{\text{lat}} = 8.7\,\mathrm{E}_{\text{rec}}^{\text{Rb}}$ in light blue, and $V^{\text{lat}} = 10.2\,\mathrm{E}_{\text{rec}}^{\text{Rb}}$ in gray. The fit uses two linear ramps up and down with four fitting parameters: the crossing of the ascending and descending part with the origin of the y-axis a, c respectively. The maximum number of transported atoms N and the frequency at which it takes place b.

The parameters a, b, and c obtained from the fits of Eq. 5.1 are reported in Fig. 5.6(b) as a function of V^{lat}. All three parameters have well-defined trends. As a consequence of the trends of a and c, the region where transport could be performed shrinks as the depth of the OL approaches the SF-MI transition. This makes sense since SF transport does not take place above the SF-MI transition. In particular, parameter c, which provides the maximum trapping frequency at which the transport is possible, decreases for increasing lattice depths, with a slope that becomes steeper above $V^{\text{lat}} = 7.7\,\mathrm{E}_{\text{rec}}^{\text{Rb}}$. This trend is qualitatively similar to what was observed for the atom number. As mentioned earlier for $\omega_{\text{Rb,x}} \gtrsim 100\,\text{Hz}$, the transport enters a different regime, this explains the saturation of c around $\omega_{\text{Rb,x}} \sim 110\,\text{Hz}$. Nevertheless, it could be interesting to do further experiments at low lattice depth to characterize this region better.

On the other side, the trend of the parameter a highlights the existence of a minimum finite $\omega_{\text{Rb,x}}$ required to enable transport in the system. The parameter a varies very little for $V^{\text{lat}} = 2.7$–$7.7\,\mathrm{E}_{\text{rec}}^{\text{Rb}}$, and it increases for larger V^{lat}. Interestingly, parameter b has a very similar trend to a. In general, the frequency b of the maximum transport is found at low $\omega_{\text{Rb,x}}$.

---

smoothing of the transition in that region.

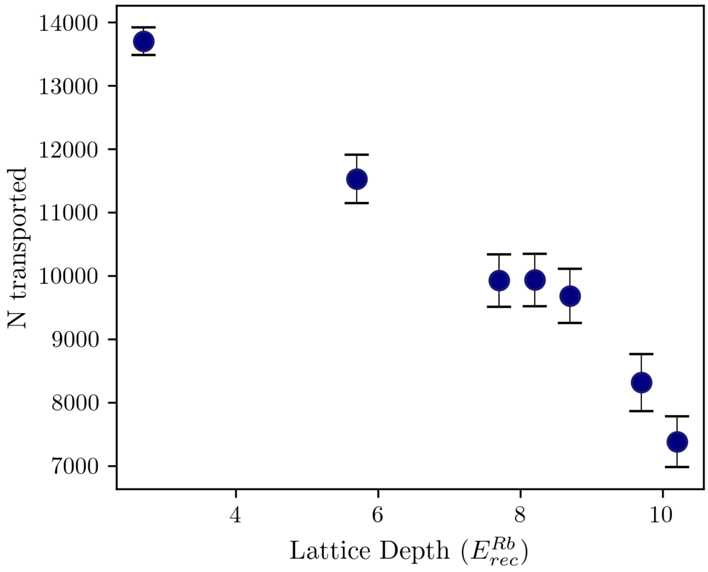

Figure 5.6 (a).

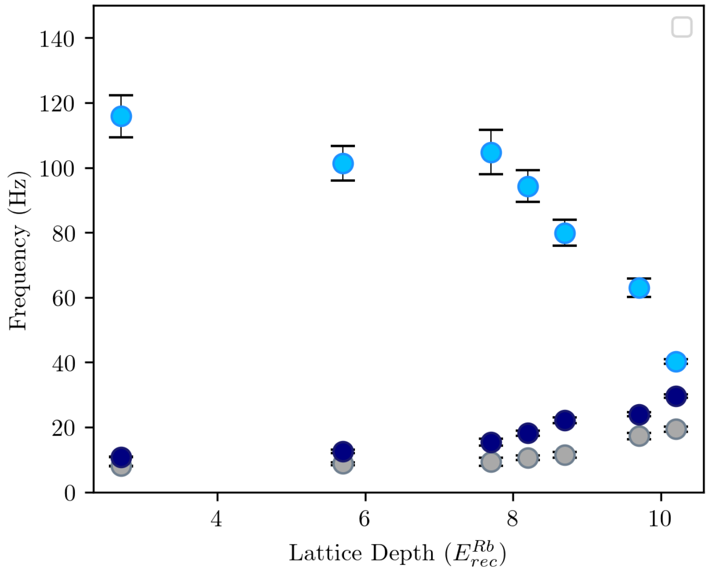

Figure 5.6 (b).

Figure 5.6: (a) Maximum number of transported atoms. Optimized parameter N of the fitting function as a function of V^{lat}. The errorbars represent the uncertainty of the fit. (b) Critical and optimal frequencies for the transport. Optimized parameters a (grey), b (navy), and c (light blue) from the fits with Eq. 5.1 as a function of V^{lat}.

5.5 Gross-Pitaevskii simulation

To further investigate the problem, I built on a code for the simulation of a one-dimensional GPE, written for the RbCs lab by Zekai Chen. The code is written in MATLAB and uses the split-step method [189]. This method is quite robust and also allowed me to modify the GPE. In particular, I added energy terms that represent possible experimental conditions to explore their effects.

In the ideal case of atoms transported through a OL with identical wells, by means of a harmonic trap, the GPE reads [3]:

$$\left[-\frac{h^2}{2m}\nabla^2 + V(x) + g|\Psi(x,t)|^2\right]\Psi(x,t) = i\hbar\frac{\partial\Psi(x,t)}{\partial t}, \tag{5.3}$$

where $V(\vec{r})$ is now the external potential, which contains contributions from both the OL, indicated with superscript lat, and the dimple, with superscript trap:

$$V(\vec{r}) = V^{\text{lat}}\sin^2(k_{\text{l}}x) + V^{\text{trap}}\left(-\exp\left(-\frac{2(x-x_0(t))^2}{w_0^2}\right)\right). \tag{5.4}$$

Here $x_0(t)$ is the center position of the trap at time t and w_0 is the trap waist, while k_{l} is the lattice wavevector. Contrary to what was observed in the experiment, the solution of Eq. 5.3 does not present a critical minimum trap frequency for transport, and the number of transported atoms keeps increasing at low frequencies. Understanding the origin of this feature can provide an immediate 'knob' to improve the efficiency of our transport.

The main candidates to explain the discrepancy are the experimental conditions that are not those of the idealized model. In the following, I will take into account two experimental aspects: the levitation field used to hold atoms against gravity, and a modulation of the depth of the OL.

5.5.1 Magnetic levitation

In experimental conditions, the atoms are under the effect of gravity. Gravity tilts the potential of the OL in the vertical direction. To compensate for this, the RbCs project uses the widespread strategy of applying a magnetic field gradient along the vertical direction. For Rb, this gradient is $\nabla B = 30.2\,\text{G/cm}$. In the experiment, it is produced by the gradient coils, as explained in Sec. 3.5. The homogeneous field at this point is $B = 355\,\text{G}$ from the homogeneous field coils. This neat and well-established trick comes at the price of an anti-trapping potential in the horizontal plane. Near the center of the quadrupole field in the xy-plane, the anti-trapping potential is quadratic. In addition to this unavoidable gradient, other gradients can emerge due to the simultaneous presence of fields from at least 5 pairs of coils during transport, as said coils can have cross-talking and their centers might be slightly misaligned. Since the atoms in our experiment are transported across a relatively large portion of space without changing the magnetic field, gradients are one of the main differences between our experiment and experiments that use short transport distances [186], experiments that move the lattice across the atoms [122], and experiments that shift the atoms by means of magnetic traps [123].

A measurement of the average value of the anti-trapping potential for the experimental apparatus of the RbCs project will be reported in Sec. 6.4.6. The tilt of the potential induced by the anti-trapping can give a difference in energy between adjacent lattice sites of up to $\Delta V^{\text{lat}}(V^{\text{tilt}}) =$

$0.01\,\mathrm{E}_{\mathrm{rec}}^{\mathrm{Rb}}$, which appears fairly negligible compared to the total lattice depth. However Rb atoms, move across a region of $\sim$ 245 lattice sites, and over this region, the overall difference in energy between the starting and final point becomes of the order of $2.5\,\mathrm{E}_{\mathrm{rec}}^{\mathrm{Rb}}$ that is not negligible with respect to the values of V^{lat} used here. The shift per lattice site can also be compared to the local tilt induced by the potential of the dimple trap. For a dimple obtained from a gaussian beam, the maximum slope of the potential is found at a distance σ from the center of the trap and it is $1/\sqrt{\pi}\exp\left(1/\sqrt{2}\pi\right)$. This slope equals the expected lattice tilt due to the estimated anti-trapping for a dimple with trap frequency $\omega_{\mathrm{Rb,x}}/(2\pi) = 30\,\mathrm{Hz}$, which is quite close to the minimum trap frequency found in the experiment. For reference for $\omega_{\mathrm{Rb,x}}/(2\pi) = 10\,\mathrm{Hz}$ and $\omega_{\mathrm{Rb,x}}/(2\pi) = 100\,\mathrm{Hz}$ the tilt is respectively $\Delta V_{\mathrm{t}}(V_{\mathrm{l},10}) = 0.001\,\mathrm{E}_{\mathrm{rec}}^{\mathrm{Rb}}$ and $\Delta V_{\mathrm{t}}(V_{\mathrm{l},100}) = 0.1\,\mathrm{E}_{\mathrm{rec}}^{\mathrm{Rb}}$.

To simulate the anti-trapping potential, in the GPE of Eq. 5.3, I approximate it with a linear tilt that changes signs at the center of the field, similar to the way it has been estimated in Sec. 6.4.6. The modified potential reads:

$$V(r) = V^{\mathrm{lat}}\sin^2(k_{\mathrm{l}}x) + V^{\mathrm{trap}}\left(1 - \exp\left(-\frac{2(x - x_0(t))^2}{w_0^2}\right)\right) + V^{\mathrm{tilt}}(x - x_f) \tag{5.5}$$

The numerical results of the simulation of Eq. 5.3 with the potential of Eq. 5.4 and with the potential of Eq. 5.3 are shown in Fig. 5.7. In both cases, I used the same parameters for the lattice $V^{\mathrm{lat}} = 5.7\,\mathrm{E}_{\mathrm{rec}}^{\mathrm{Rb}}$ and a dimple with trap frequency $\omega_{\mathrm{Rb,x}}/(2\pi) = 11\,\mathrm{Hz}$ for transport, such that the tilt provided by the trap is smaller than that of the anti-trapping potential. The transport velocity is $v = 80\mu\mathrm{m/s}$, and the total transport time 1.5 s is also the same for the two cases. At the end of the transport, the depth of the OL is ramped down in 2 ms, to reproduce the experimental procedure for band mapping. For simulation without the tilt, the transport time is divided into steps of $1\,\mu\mathrm{s}$, while for the simulation with the tilt, the transport time is divided into steps of $5\times10^{-8}\,\mathrm{s}$ to increase the precision by 20 times. Smaller time steps, i.e. higher numerical precision, provide results consistent with the results shown here, confirming there are no numerical instabilities in the calculation. The resulting data have been treated with the Python Matplotlib built-in bilinear interpolation method to remove the aliasing due to the finite sampling [190]. This is a four-point interpolation method [191].

Fig. 5.7 shows the amplitude of the wave function in real space and momentum space. For the case without the tilt, the wave function in real space has a peak around the position of the trap, and this peak follows the movement of the trap from the original position at $\tilde{\mathrm{x}}(0) = 0$ to the final position $\tilde{\mathrm{x}}(\mathrm{t}) = 120\,\mu\mathrm{m}$. There is a small sloshing motion of the atoms around the center of the trap, whose frequency is consistent with a dipole mode at $\omega_{\mathrm{Rb,x}}$. In momentum space, the wavefunction has a peak close to zero momentum $\vec{k} = 0$, in agreement with the atoms being always at equilibrium at the bottom of the trap. Around $\vec{k} = 0$, there is a small oscillation that reproduces the sloshing mode observed in the spatial distribution. In conclusion, even at the low $\omega_{\mathrm{Rb,x}}$ the atoms are following the trap and transport takes place with extremely high efficiency.

In the case of a tilt Fig. 5.7, the atoms stay at the original position and do not move with the trap. In momentum space, they are completely delocalized, and the wavefunction is spread so much that its amplitude can not be seen on the color scale of the plot. Further sets of data at $\omega_{\mathrm{Rb,x}}/(2\pi) = 60\,\mathrm{Hz}$ and $\omega_{\mathrm{Rb,x}}/(2\pi) = 100\,\mathrm{Hz}$, not shown here, show that at higher trap frequency transport is recovered. The atoms are transported to the final position without any significative

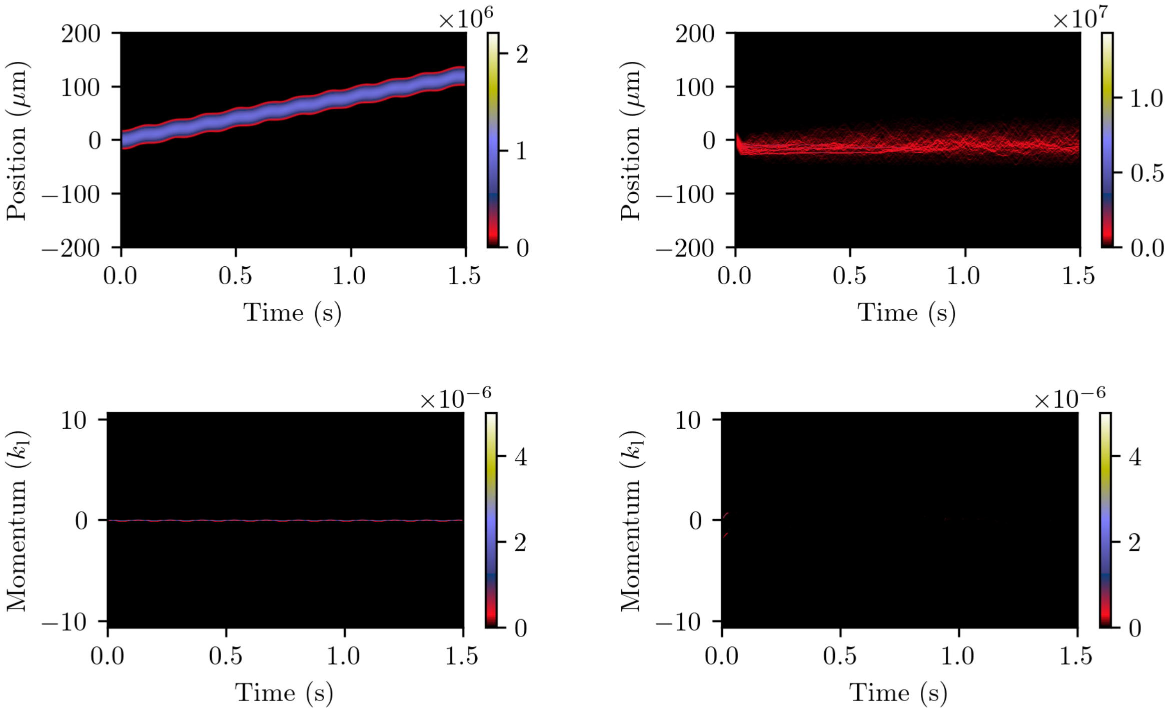

Figure 5.7: Left transport in a non-tilted lattice, right transport with a tilt. Top: amplitude of the atomic wave function in real space along the transport direction x, as a function of time. Bottom: amplitude of the atomic wave function in momentum space. and momentum space as a function of time during transport. The tilt is dimple trap frequency is 11 Hz. In the case of the tilt, the atoms localize and the wave function in momentum time spread and is not visible on this color map.

effect of the tilting. The failure of transport at low $\omega_{\mathrm{Rb,x}}$ is consistent with the experimental results. Even if the tilt is able to reproduce the presence of a minimum trap frequency, the results obtained with this modeling do not show the plateau for the optimum transport regime described in Fig. 5.3.

One early interpretation for the lower critical $\omega_{\mathrm{Rb,x}}$ was that the tilt compensates the potential of the dimple along one direction, such that the atoms spill out of the dimple when the dimple moves toward higher energy in the anti-trapping potential. This hypothesis was further supported by the fact that the tilt of the anti-trapping was comparable to the maximum tilt due to the local dimple-trap potential, as mentioned above. Interestingly the simulation shows that a tilt with the opposite sign, i.e. atoms moving toward lower energy in the anti-trapping potential, also leads to a localization of the atoms at the initial position. The fact that the atoms localize independently of the direction of the tilt stirs the interpretation in a completely different direction.

A likely scenario that can explain the symmetry with respect to the sign of the anti-trapping tilt is the presence of Bloch oscillations (Sec. 2.8). The energy gradient due to the linear tilt, gives rise to a constant force. Such force is expected to induce Bloch oscillation in the OL, independently of the direction of the tilt. It is possible that if $\omega_{\mathrm{Rb,x}}/(2\pi)$ is lower than the frequency of the

Bloch oscillations, the atoms undergo Bloch oscillations around their original position rather than following the trap. Viceversa, if $\omega_{\mathrm{Rb,x}}/(2\pi)$ is larger than the frequency of the Bloch oscillations the transport is diabatic with respect to the Bloch oscillations and the atoms follow the trap. This hypothesis leaves two main open points.

- Bloch oscillations are not observed in k-space, it is possible that the shift in energy across the OL due to the tilt and the initial presence of the dimple lead to a fast decoherence in the phase of the oscillations.
- Diabatic transport with respect to the Bloch oscillation is expected to excite the atoms to higher energy bands in the lattice via Landau-Zener tunneling. It is unclear how the atoms decay coherently in the lower band.

Further measurements in this regime should be performed to confirm the hypothesis.

5.5.2 Amplitude modulation

The ideal OL has perfect periodic modulation with wells of all equal depth. In the actual experiment, there are a number of effects that can slightly modify it, e.g., for a one-dimensional OL mechanical noise on the retroreflection mirror or fast fluctuations of the light intensity. In the experiment, a three-dimensional OL is used, in this case, a residual interference between two orthogonal lattice beams or forcing the atoms to move along an ideal straight line, not aligned with the OL axes, leads to the emergence of an additional variation of the potential between wells. Here, I try to simulate such effects, by adding to Eq. 5.3 a modulated potential, referred to in the following as super-modulation. The total potential has the form:

$$V(r) = V^{\mathrm{lat}} \sin^2(k_{\mathrm{l}} x) + V^{\mathrm{trap}} \left(1 - \exp\left(-\frac{2(x - x_0(t))^2}{w_0^2}\right)\right) + V^{\mathrm{mod}} \sin^2(k_{\mathrm{mod}} x). \tag{5.6}$$

where k_{mod} and V^{mod} are, respectively, the wavevector and the amplitude of the modulation. To better appreciate its effects, the supermodulation term is added to Eq. 5.4 independently of the tilt.

These simulations require higher precision, i.e shorter time steps of 1×10^{-9} s, with respect to the simulation performed using the potential introduced in Eq. 5.5, and therefore they were run on a shorter transport sequence, with only 100 ms transport time at a transport velocity of 40 μm/s, which correspond to a transport distance of 4 μm (only about 8 lattice sites). Fig. 5.8 shows the results for Eq. 5.3 with the potential of Eq. 5.6 with $k_{\mathrm{mod}} = 1.25 \times 10^5$, and $V^{\mathrm{mod}} = 0.15\,\mathrm{E}_{\mathrm{rec}}^{\mathrm{Rb}}$, while all the other parameters for the OL are left the same as in the previous cases. The three plots of Fig. 5.8 show the results obtained for three different $\omega_{\mathrm{Rb,x}}/(2\pi)$: 30 Hz, 60 Hz, and 120 Hz, in the absence of excitation the transport is expected at $k_{\mathrm{l}} = 0$

Despite the short transport time and distance the effects of the supermodulation are clearly visible on the momentum distribution. It can be seen from Fig. 5.8 that the momentum dispersion increases at low trap frequencies with some sort of periodic dephasing. On the contrary, increasing the trap frequency can stabilize the transport again. The increase of the momentum dispersion is symptomatic of the localization of the atoms. This effect would be hard to appreciate in the spatial distribution on such a transport distance, which is short compared to the size of the dimple.

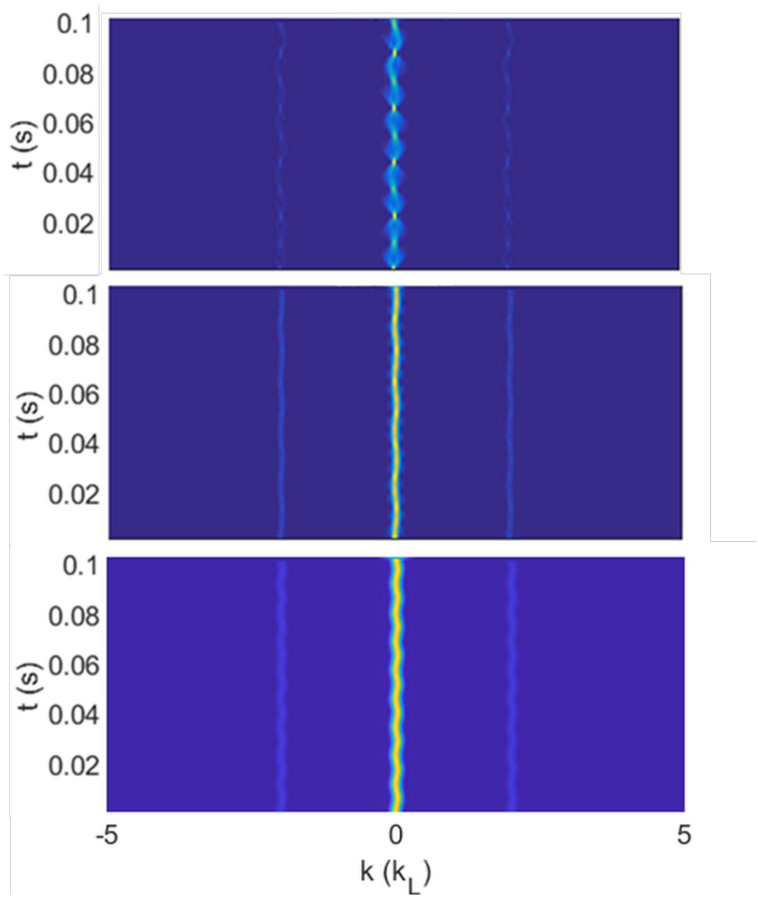

Figure 5.8: Transport with super-modulation of the OL depth. Time evolution of the distribution of the atoms in momentum space in the presence of a super-modulation with $k_{\mathrm{mod}} = 1.25e5$, $V^{\mathrm{mod}} = 0.15$. The color map is set such that the atom number increases going from blue to yellow. The depth of the OL is $V^{\mathrm{lat}} = 5.7\,\mathrm{E}_{\mathrm{rec}}^{\mathrm{Rb}}$. The three plots correspond to different $\omega_{\mathrm{Rb,x}}$, from top to bottom: 30 Hz, 60 Hz, and 120 Hz. The color map is set such that the atom number increases going from blue to yellow.

The localization of the atoms at low trap frequencies is then qualitatively analogous to what was observed with the tilt in the previous section, and it further justifies the emergence of a lower critical $\omega_{\mathrm{Rb,x}}$ for transport.

The approach used here is qualitatively similar to the techniques used to simulate disorder, specifically to the Aubry-André model [192], which uses incommensurate lattices, i.e., lattices with an irrational $k_{\mathrm{l}}/k_{\mathrm{mod}}$ ratio. The Aubry-André theory predicts localization for $V^{\mathrm{mod}} > 2\mathrm{J}$. The two lattices used in this simulation are not perfectly incommensurate, $k_{\mathrm{l}}/k_{\mathrm{mod}} = 47.241994790$, but $J = 0.05\,\mathrm{E}_{\mathrm{rec}} \ll V^{\mathrm{mod}}$ which falls under the conditions for localization.

From an experimental point of view, it could be interesting to introduce an incommensurate lattice and study how the harmonic trap affects localization. On the other hand, the effects that could give rise to the super-modulation can be addressed individually, e.g., mechanical stability can be improved, the interference between orthogonal beams can be reduced by a better cleaning of the polarizations, and by a larger detuning between the beams, etc.

5.6 Conclusion

This chapter discusses the effects of the confinement from the dimple on the efficiency of transport in the OL. The discussion starts by revisiting the data of Ref.[124], to which I contributed, with an independent analysis. The new analysis highlights a lower and an upper critical $\omega_{\mathrm{Rb,x}}$. The main difference with respect to the interpretation of Ref. [124] is the identification of an optimal $\omega_{\mathrm{Rb,x}}$ for transport rather than an optimal transport region, the new description is supported by the coefficient of determination R^2. The analysis is then strengthened by the use of a numerical model to simulate the time-dependent 1D GPE both in ideal conditions and in more realistic experimental conditions.

In the ideal case, they reproduce qualitatively (but not quantitatively) the trend of the critical upper $\omega_{\mathrm{Rb,x}}$ as a function of the depth of the OL. However, the numerical model in the ideal conditions does not reproduce the lower critical $\omega_{\mathrm{Rb,x}}$. The experimental conditions could be plagued among other effects by the presence of small magnetic field gradients and the inhomogeneity of the potential of the OL. The two effects have been simulated independently by modifying the external potential in the GPE. For the first, I introduced a tilt of the OL along the transport direction, for the second, a super-modulation of the OL intensity (similar to disordered system approaches). Both the tilt and the super-modulation reproduce the presence of a minimum trap frequency for transport. None of them account for an optimal transport regime.

The possible causes identified in this Chapter for a lower critical $\omega_{\mathrm{Rb,x}}$ originate in the experimental details and spurious experimental conditions and as such they can be addressed specifically in the experimental setup and in the experimental sequence to further improve the efficiency of SF transport. For example, an anti-trapping potential can be compensated by means of an optical potential. Alternatively, it can be compensated by using the tracking coils (Sec. 3.5) to move the center of the quadrupole field in the horizontal plane consistently with the center of the Rb dimple. The latest technique shifts the tilt at the location of Cs atoms and can have consequences on the stability of the Cs MI. The anti-trapping potential due to levitation can also be avoided entirely by displacing Rb and Cs clouds vertically rather than horizontally, exploiting that Rb a_{s} does not depend significantly on the field. However, when mixing the two species the Feshbach resonance should be sufficiently broad resonance that the interspecies scattering length changes little during the overlap. To compensate specifically the supermodulation, it would be first needed to identify the causes. In this case, addressing the causes individually could be an easier solution, e.g., improving the mechanical stability by replacing optomechanics components, reducing interference between the beams of the OL by increasing the detuning between the beams and by using higher-quality polarizer, *etc.*

There is no indication that the effects added in the simulation are affecting the upper critical $\omega_{\mathrm{Rb,x}}$. What could modify the upper $\omega_{\mathrm{Rb,x}}$ and has not been investigated so far in our experiment is the dimensionality of the system and the condensate fraction. During transport, the atoms are moving at a small but finite angle with respect to the axis of the 3D OL. An investigation of transport as a function of the angle between the transport direction and the OL axes could help to clarify this aspect. Alternatively, the same question can be addressed by adding a controlled anisotropy to the OL to control the tunneling rate in one direction. This should highlight the role of second-order processes that allow the atoms to move diagonally in the lattice via two consecutive tunneling processes along orthogonal axes of the OL. The condensate fraction could be taken into account by starting with a good condensate and artificially worsening it, e.g. by changing the evaporation sequence. Atomic interactions were present in the simulations and they did not reproduce the quantitative upper critical $\omega_{\mathrm{Rb,x}}$. Nevertheless, it can be interesting to confirm it experimentally, for this purpose the experiments could be repeated with Cs, such that the broad tunability of Cs a_{s} can be used.

An alternative route to improve significantly the efficiency of the transport is to break adiabaticity and implement shortcuts-to-adiabaticity schemes as reviewed for example in Ref. [193]. Such schemes could be greatly beneficial to the formation of molecules, because, on one hand, they could improve the number of transported atoms, on the other they can significantly reduce the transport time curbing Cs losses. These methods require a precise description of the potential landscape and will benefit a lot from the understanding of the experimental conditions and the role of the different confinements presented in this Chapter.

Chapter 6

RbCs next generation

6.1 Introduction

This Chapter presents several upgrades I contributed to on the RbCs project during my Ph.D. work. These changes followed from several motivations: The stability of the experimental conditions was limited with large shot-to-shot fluctuations as mentioned in the previous Chapters; the experimental apparatus had high ordinary maintenance requirements on a day-to-day basis; the data analysis was done mostly on post-processing; the necessity of extraordinary maintenance acted as a catalyst to revisit the full experiment.

The leading idea is to have a machine that is simpler and easier to handle on a day-to-day basis, which in turn improves the reliability of the experimental apparatus and the reproducibility of the experimental conditions. This is a large team effort that addresses different aspects of the daily operations in the lab. In Sec. 6.2, I discuss the introduction of a new oven design meant to improve the atomic flow. Sec. 6.3 shows the dramatic changes undergone by the laser systems used for laser cooling and dRSC, in particular, two high-power sources have been installed to replace a large fraction of slave lasers (Sec. 3.4) and a TA(Sec. 3.4). In Sec. 6.4, the experimental sequence is optimized anew to take into account the different initial conditions provided by the new laser system. This Section provides a qualitative interpretation of the data, and it is complemented by Appendix A, which lists the final values of the optimized parameters. The optimization of the sequence has benefited a lot from the introduction of real-time data analysis, based on open-source tools presented in Sec. 6.5. Extended information about part of this work is given in Appendix B. The full process took a large amount of time, Sec. 6.6 discusses some of the difficulties that cost more time and the lessons learnt from that.

6.2 Ovens

One of the earliest improvements concerns the replacement of part of the oven section. The old design as reviewed in Sec. 3.6 consisted of two separate chambers for Rb and Cs. The two species mix only after leaving the ovens and microchannel tubes partially collimate the Rb and Cs atomic

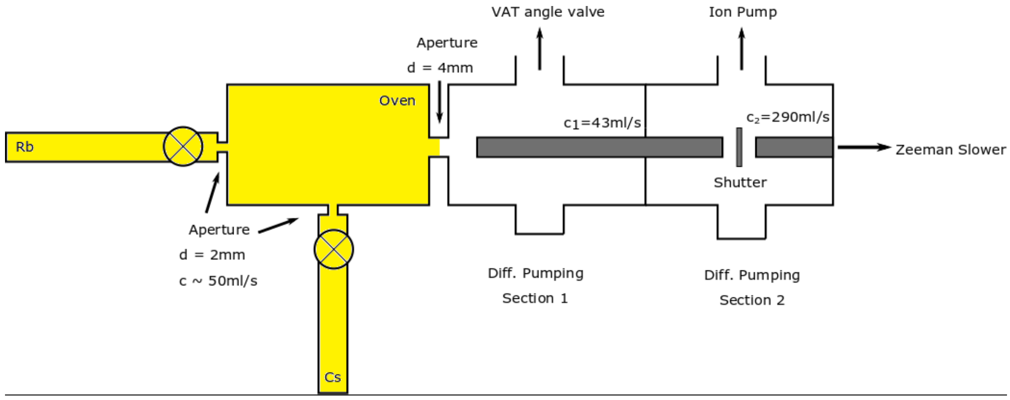

Figure 6.1: Schematics of the new oven design and how it merges with the previous parts. A T-shaped three-way crossing where the two species mix connects the two reservoirs (labeled with the respective species in the drawing) and the differential pumping section. Each reservoir is a half-nipple sealed off from the crossing by a CF16 angle valve.

beams before they exit their respective chambers, hence the hot section of the vacuum. At the same time, the reduced size of the microchannel tubes limits the flow and increases the possibility of clogging. The new design is greatly simplified in comparison to the previous version as shown in Fig. 6.1. The oven chamber is composed of a single T-shaped three-way crossing connecting the two reservoirs. Each reservoir is formed by a blind pipe, containing the ampules, respectively with Rb or Cs, and a CF16 angle valve seals it off. Rb reservoir is on a straight line with respect to the atomic beam, while Cs is at an angle of 90° with respect to it. To reduce the flux from the reservoirs into the oven, each reservoir has a CF16 blind flange with a 2 mm aperture cut-out. The new oven is expected to increase the overall flow of atoms by almost a factor of 8 with respect to the old oven, due to the larger aperture and larger conductance between the oven and the beginning of the differential pumping[1].

Similarly, the outlet of the ovens is constituted by a CF40 blind flange with a 4 mm aperture. The differential pumping section was left almost unchanged in comparison to what has been discussed in Sec. 3.6 and shown in Fig. 6.1. The only difference is that the ion pump in the second chamber had been replaced with a new one of the same model. The new ion pump reached saturation within about three years of working. The initial pressure was $\sim 5 \times 10^{-6}$ and progressively increased, possibly due to the progressive deterioration of the ion pump. The manual reported an expected lifetime of 80000 hours ($\sim$ 9 years) for a pressure of 1×10^{-6} mbar [194], which is much longer than what we have observed. After six additional months of working with this ion pump switched off, the lifetime of the atomic sample in the main cell due to collisions with the background gas has been estimated to be about 2.5 s for both species[2]. This is too short when compared for example to the old evaporation sequence that lasted 6 s. The optimization of the sequence described in the next sections was interrupted due to this problem.

---

[1] Erich Dobler, University of Innsbruck and Institut für Quantenoptik und Quanteninformation (IQOQI), *private communication*

[2] This value has been measured as the lifetime of the atoms in a purely magnetic trap, loaded after MOT and compression.

6.3 Cooling light

To improve the day-to-day stability and reduce the maintenance time, a large part of the laser infrastructure used for the Zeeman slower, the MOT, and the dRSC has been replaced. The experimental setup used in the laboratory when I started the Ph.D. work and presented in Sec 3.4 made large use of slave lasers and TAs and had several drawbacks. Injection-locked slave lasers and seeded TAs require their controlling electronic and dedicated beam paths for injection and seeding, respectively, which increase the complexity of the experimental setup. Even though these systems can certainly do the job and have been the workhorse of laser cooling for many years, in our specific case having a two-species experiment with all optical cooling steps meant having so many parts that 'statistically' something would not work optimally or fail, resulting in fluctuations and down-time. Daily, we observed that despite the fact that slave lasers and TAs are meant to amplify the power, the overall power achieved for the optical beams was in most cases barely enough for the sequence given the consolidated optical setup. As a consequence, the numerous optical paths needed frequent optimization to keep the overall power delivered to the atoms on the edge of the requirements for cooling. Using a higher overall power is not the only possible answer to this problem, reducing the beam size or retroreflecting the beams when possible are also viable solutions. However, the latter two options are not without disadvantages, reducing the beam size reduces the capture range for the MOT and increases the change of depth across the OL for dRSC. About retroreflecting the beams, it must be said that in the presence of two species like Rb and Cs with transition frequencies fairly close to each other, handling the polarization beam is definitely not trivial. Achromatic or custom dichroic phase-retardation waveplates can be applied, but these are intrinsically multi-order phase retarders and therefore are more susceptible to thermal effects [195, 196].

Sometimes, the complexity also manifested itself as 'rogue' electronic signals, which led to hours of debugging. Much less frequently, but not less aggravating, one of the laser diodes stopped working and needed replacement, for example, the diode of the master laser for the Rb Zeeman beam has been replaced at least three times in the last two and a half years that was in use, of which one time it required to swap several diodes during the course of the same week. In practical terms, the time spent on maintenance on the old setup was often comparable to or larger than the time dedicated to the experimental investigation of cold atoms and cold molecules properties.

The growing awareness of the waste of time and resources represented by maintenance led to a complete revisitation of the laser system. The new concept is based on a few high-power laser sources combined with the use of AOMs, rather than a large ensemble of scattered lasing devices as described in Sec. 3.4. Thanks to the high power of the new laser systems it is possible to decouple the optical paths relative to the different cooling steps by splitting the initial laser beam in a number of optical fibers, before the frequency adjustments and on/off of the beams are performed, rather than do it in free space. This also decouples the sensitive parts of the beam path from the laser itself, which can be useful if the laser at any point needs to be sent in for repairs or refurbishing. As typical of ultracold-atom experiments, optical fibers are also used to deliver the light to the experiment. Therefore all beam paths have at least two optical fibers.

In addition to these lasers, during the course of my Ph.D. work, in the laboratory, the fiber laser for the reservoir trap was replaced with the same model, and the fiber amplifier used for the dimples needed to be refurbished (polishing of the fiber) a few times. As mentioned above, several diode lasers have been replaced. These changes are standard and are not discussed in the following.

6.3.1 New design

The new light sources at the core of the design are a fiber laser with doubling stage[3] for Rb and a Titanium-Sapphire laser (Ti:Sapph) [4] pumped with green light from an LBO-based technology[5] for Cs. The two laser systems can provide respectively 7 W and 6 W of light resonant with the D2 lines of the two species, respectively a factor of ~ 5 and ~ 8 more with respect to the old setups if we sum up the individual contribution of the replaced slave lasers and the TA. Part of this additional power is lost in the optical path, however I will show in Sec. 6.4.7 that a factor of two more power is already sufficient for saturating the MOT in the current conditions. The linewidth of the light output by the Cs laser system has been measured in the lab to be ~ 57 kHz (measured by Camilo Cantillano over ~ 3 s after locking), while for the light output by the Rb laser system, the linewidth is too small to be measured, the nominal linewidth is < 0.1 kHz.

The locking point of the laser systems is the main variation with respect to the previous design. Especially in the case of Rb, where one master laser had been removed, the new laser needed to be locked at a frequency where all atomic transitions for cooling are within reach with AOMs or AODs. In the following, I provide the details of the new setup and frequency shifts. Initially, the detuning for the individual cooling steps have been scanned, as shown in the optimization of Sec. 6.4.3 and Sec. 6.4.4, after fixing the optimal values or ranges, tuning capability (namely, feeding VCOs or DDSs signals to the AOMs, through an amplifier) are then left only for the beams that need them actively during the sequence, like the MOT beams whose frequency is reduced during compression, or day-to-day operation, like the beams for absorption imaging that are detuned for imaging the compressed MOTand resonant when imaging atoms in the dimples.

The Rb laser system is locked at -220 MHz from the $F = 2 \rightarrow F' = 3$ transition, thanks to an AOM shifting the beam used for the modulation transfer spectroscopy lock. The final frequencies are listed below, while the powers are provided in Appendix A. All the detunings, with the exception of the repumper for dRSC, are expressed with respect to the $F = 2 \rightarrow F' = 3$ transition.

- MOT beams, with a double pass through an AOD, which allows tunability between $-10... - 110$ MHz.

- Absorption imaging beams, with a double pass through an AOM, which allows tunability of 12 MHz, typically the window is set as $0... - 12$ MHz but can be shifted with the alignment of the AOM to find the atomic resonance.

- Zeeman beams, with a single pass through an AOM that brings the light at -22 MHz (see discussion in Sec. 6.4.2)

- dRSC repumper beam, from the zero order of the AOM used for the Zeeman beam, with an additional AOM that brings the light at -4 MHz with respect to the $F = 2 \rightarrow F' = 2$

---

[3] NKT Koheras Harmonik

[4] Msquared SolSTiS

[5] Coherent Verdi V20

The Cs laser system is locked at -194 MHz from the $F = 4 \rightarrow F' = 5$ transition, thanks to an AOM shifting the beam used for the modulation transfer spectroscopy lock. The light is then used to generate: All the detunings are here expressed with respect to the $F = 4 \rightarrow F' = 5$ transition.

- MOT beams, with a double pass through an AOD, which allows tunability between $-4... -64$ MHz.
- Absorption imaging beams, with a double pass through an AOM, which allows tunability of 12 MHz, typically the window is set as $0... -12$ MHz, but can be shifted with the alignment of the AOM to find the atomic resonance.
- Zeeman beams, with a single pass through an AOM that brings the light at -20 MHz (see discussion in Sec. 6.4.2)
- Beams of the dRSC OL, with an AOM that brings the light close to resonance with the $F = 4 \rightarrow F' = 5$ which implies -9 GHz with respect to the transition $F = 3 \rightarrow F' = 2$.

For both species, the AOMs and AODs also serve as on/off switches for the beams. When tunability is needed, the RF frequency to the AOMs and AODs can be changed dynamically through VCO [197] or DDS [198] technology. Feedback on the RF amplitude is used to control the intensity of the beams.

Although it would in principle be possible to obtain repumping light as well from the new lasers, this would require additional frequency-shifting mechanisms. The choice was made here to keep a system based on home-built laser diodes. In the case of Rb, the setup described in Sec. 3.4 is used. A new laser system for Rb repumper based on an interference filter design [199] which requires no amplification is also available, but not yet in use. The Cs setup for the repumper light uses a new home-built laser, also, based on an interference filter design and amplified with a home-built TA that I assembled and tested. The slave and the TA for the repumper light are used not just to amplify the power to meet the experiment requirements but to boost the output powers to a level that is significantly above the experimental requirements, in these conditions frequent optimization of the alignment of the beam path is not required.

6.3.2 Old vs new design

The introduction of the new Rb laser system allowed for the removal of the master laser for the Rb MOT light, which was almost on the same frequency as the Zeeman laser, and in addition, it allowed for the removal of the slave laser of the Zeeman light, and the TA for the MOT light. The introduction of the new Cs laser system allowed the removal of the slave lasers used for Zeeman light, MOT, and the OL for dRSC. These changes, which sum up to one master laser, four slave lasers, and one TA, are summarized in Table 6.1.

The removal of slave lasers and TAs reduces the number of electronic devices, by allowing the removal of the related temperature stabilization devices and current drivers. At the same time, not needing any more seeding and injection beams, allowed the removal of the dedicated optics, hence it simplified the optical setups. The removal of electronic and optical items reduces the possible sources of malfunctions in the experiment and therefore increases the chances of the experimental apparatus being in its best condition on a daily basis. In addition, the new setups present themselves

Task	OLD **Lasers**	**Amplifiers**	NEW **Lasers**	**Amplifiers**
Zeeman	2	2		
Repumper	2	1	2	1
MOT	1	2	2	
Sideband cooling	1	2	1	1
Dipole Traps/Far-detuned OL	3	1	3	1
STIRAP	2		2	
Total	11	8	**10**	**3**

Table 6.1: Total count of lasers and amplifiers in the experiment for the old and new setup. Under amplifiers, I am here counting, slave-lasers, tapered amplifiers, and fiber amplifiers. For the Rb laser system, as the fiber amplifier at 1550 nm is built-in in the commercial product it is not counted explicitly.

as much more compact, while the previous systems occupied two optical tables one for each species, the new system fits almost entirely on a single optical table.

The transversal mode of both the frequency-doubled fiber laser for Rb and the Ti:Sapph laser for Cs have in good approximation a gaussian intensity profile. This reduces power losses, since this shape is the optimal one to propagate through optical fibers and AOMs with efficiencies typically around 70% and 80%, respectively. On the contrary, in the old setup, TAs had a three-lobe emission profile for which typically more than 30% of the total power is in the side-lobes and it is lost for applications. A smaller simplification comes also in the beam shaping, the new lasers only require adjustment of the beam size, but not of the shape itself, like it was instead necessary for diode lasers which typically are characterized by an elliptical emission pattern and often a moderate astigmatism [159].

The ring cavity used in the Ti:Sapph laser and the doubling stage of the fiber laser strongly suppress multimode emission. This implies also that the two laser systems are insensitive to back-reflections, according to the respective manufacturers. On the contrary, in the old setup, diode lasers, slave lasers, and TAs are notoriously sensitive to back-reflections and could be damaged irreparably by them. In the old setup, the presence of multimode emission was also tricky in the case of slave lasers where it could emerge due to a number of reasons: a multimode feature of the master laser, too little power in the injection lock, and the natural emission profile of the slave being too far away from the lock point. This effect was in many cases large and easy to detect, but in some cases, when the injection lock was working just at the edge, multimode behavior could be subtle and it could be detected only through the use of scanning cavities or beatnote measurements. Such effect is still quite detrimental for dRSC of Rb, the laser that is used for both dRSC polarizer and MOT repumper laser is still in a master-slave configuration. It has been observed on multiple occasions that small problems with the injection lock give rise to large fluctuations in the efficiency of dRSC, even if the MOT is not sensitive to it. Similar to other effects listed here, this is well addressable with a bit of time, but with many such devices to keep track of, the time consumption becomes considerable.

The new setup has also a few drawbacks. One is that the use of only one light source for several applications introduces the necessity of splitting the beam a lot for the different applications. The alignment of such a complex optical path can be decoupled into several sub-parts thanks to the use of optical fibers, which also helps to keep a clean transverse mode of the beam. This trick has the price of the insertion loss into the fibers which leads to a reduction of at least 10-15% on the overall signal and therefore it needs to be applied with some consideration. In this regard the use of numerous separate amplifiers, as done in the previous setups, naturally decoupled the optical paths. Any misalignment in the new setup converts directly to a drop in the power that reaches the experiment and it is therefore easy to detect. Instead, in case of misalignments of the beam for the injection lock of slave lasers, the power output of the slave is constant but the emission is multimode, a feature, as discussed above, that could be sometime harder to detect.

Another drawback of the new design, with respect to the old one, concerns the use of double passes through AOMs to achieve large frequency sweeps during the sequence. This leads to power losses that are close to 30% at the optimum frequency and increase when changing the frequency by means of the RF due to the unavoidable increasing mismatch for the Bragg diffraction condition. In the old setup, tuning was done between the master laser and the slave laser, therefore such losses were compensated by the slave laser. An attempt to mitigate such losses in the new setup has been made by replacing the AOMs with acousto-optic deflectors (AODs), which have a flatter gain profile as a function of the RF input, this change helped to recover tunability capabilities comparable to the previous design where needed.

6.4 Sequence revisitation

In addition to greatly simplifying the setup, the introduction of the new laser system allowed for a small improvement in the power of the beams dedicated to the individual cooling steps. The integration of the new laser systems into the experiment then called for a reoptimization of the experimental sequence, exploring new regions of the parameter space.

The optimization was done in a cyclic way: after optimizing each step individually, the parameters were finely tuned by benchmarking the cloud after the next cooling step in the sequence and optimizing for it. The results are presented here in a qualitative fashion with emphasis mainly on the achieved cloud properties, while the numerical value of the main parameters in the sequence is listed in Appendix A.

6.4.1 Benchmarking: absorption vs fluorescence.

The first two steps in the sequence are Zeeman slowing and MOT. As discussed in Sec. 3.8, in the RbCs experimental setup the efficiency of the Zeeman slower can only be probed indirectly via the loading rate of the MOT, which already depends on the MOT parameters. With the current imaging capabilities of the experiment, absorption imaging cannot be applied directly at the MOT because of the cloud size and position. In a day-to-day operation, it is usually sufficient to apply absorption imaging after the compression of the MOT. This is realized with two pulses with duration $150\,\mu$s, one with the atoms and one without, for each species. The order in which the two species are imaged can be varied. The pulses are stabilized in intensity. The beam size is about $\sim 3.3\,$mm in diameter.

Here, when characterizing the performance of the new laser system on the atoms, we wanted to

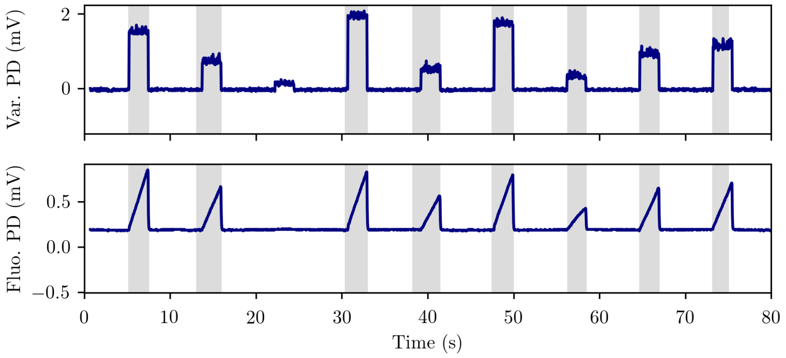

Figure 6.2: Sample of traces from a short run benchmarked with fluorescence photodiode. Top: light intensity recorded on the photodiode for the laser beam scanned during the measurement. Bottom: fluorescence signal from the MOT fluorescence photodiode, the slope up corresponds to the loading of the MOT. For this particular trace, the loading time 2 s is below MOT saturation and the relative atom number is proportional to the loading rate. The grey areas correspond to the individual repetitions of the sequence.

decouple the steps as much as possible. As an alternative to absorption imaging, we reintroduced the detection based on photodiodes capturing the light from the fluorescence of the MOT atoms that I will refer to in the following as fluorescence detection. An example of such a trace is given in Fig. 6.2, for a short sequence scanning one parameter. Both the photodiode voltage and the parameter value can be read directly from the oscilloscope. The fluorescence signal grows from zero proportionally to the number of atoms in the MOT for each repetition of the sequence. For each repetition, the maximum voltage output from the fluorescence photodiode is proportional to the number of atoms loaded in the MOT, during the allowed loading time. For long loading time, the MOT saturates and this number corresponds to the maximum atom number, for times much shorter than what is needed for saturation the number is proportional to the loading rate. In the following, this number is referred to as the relative atom number and expressed in Volts. During each repetition, there is a small variable delay of the signals with respect to the gray areas, this is due to the finite precision with which the repetitions are selected automatically and could be improved if necessary. The value of the parameter scanned during the sequence is taken as the average over the repetition of the relative analog signal. This is typically a photodiode when scanning an intensity, or a current sensor monitoring the current to the coil when scanning a magnetic field.

6.4.2 Zeeman slower

In the experimental setup of the RbCs project, there is no direct detection of the atomic flow through the Zeeman slower and into the cell. The optimization of the Zeeman slower is then benchmarked by looking at the rate at which the atoms are loaded in the MOT. The optimization of the Zeeman slower involves the magnetic field in the Zeeman slower, the Zeeman light detuning and intensity. The light for the Zeeman repumper is shared with the MOT repumper as it was shown in Fig.3.5, and its optimization is addressed in the next section (Sec. 6.4.3). For the optimization of the magnetic field, we span the current of the two channels controlling respectively coils C1 and C6 (channel 2), and coils C2-C5 (channel 1) of the Zeeman slower, described in Sec. 3.7. In Fig. 6.3, I show the relative atom number from fluorescence detection on the MOT after a fixed loading time for the MOT. The loading time is 2 s and it is shorter than the time taken to saturate the MOT, the recorded value is proportional to the loading rate. The measurement shows that there is a dependence between the two channels. It is clear that optimized current values for Rb (channel 1 = 2(0.5) A, channel2 = 3.5(0.5) A) differ from the optimized value for Cs (channel 1 = 1(0.5) A, channel2 = 3(0.5) A) as expected since they have different magnetic moments and different initial velocity distributions. In particular, Cs MOT loading rate is higher for lower currents of the Zeeman coils. The choice is to compromise between the optimum values relative to the two species.

Qualitatively the Zeeman slowing efficiency for the two species shows a similar dependency on the frequency and detuning of the cooling light. The number of atoms captured after the Zeeman slower has only a small dependence on the light frequency detuning for the Zeeman light of both species. Historically the detuning of the Zeeman beam in this project has been documented as $-50\,\mathrm{MHz}$ [148] and $-25\,\mathrm{MHz}$[147], contrary to the typical values of $1–2 \times 10^2\,\mathrm{MHz}$, while for the measurements reported in, e.g., Ref [63] this detuning was set at $-22\,\mathrm{MHz}$. The discrepancy between typical values and the values used in the experiment was highlighted during the editing of this thesis and it is currently under further examination. Originally the optimization started from the most recent value $-22\,\mathrm{MHz}$ and gave the results reported in this section. A wrong setting of the initial point of the optimization could explain both the small dependence of the loading rate on the detuning of the Zeeman beam in the explored parameter range. It could also explain why it was not possible to compensate the large discrepancy between the fields for the two species by means of the light. On the contrary, both species showed a strong dependence on the light intensity with a well-defined maximum, as shown for Cs in Fig. 6.4. Experience showed that the atom number in the next steps, and mostly its stability, is very sensitive to the alignment of the Zeeman beams.

6.4.3 Magneto-optical trap and compression

After optimizing the Zeeman slower, I use fluorescence detection to optimize the MOT. In this case, an improvement in the relative atom number was mostly obtained by optimizing the light parameters. While the MOT was quite insensitive to changes in the magnetic field gradient within $10 - 20\,\mathrm{G/cm}$. The intensity of the MOT beams is the most notable difference with respect to the previous setup. The new laser systems allow the use of slightly higher intensities and access a saturated regime where the relative atom number does not depend on the beam intensities anymore and only has a weak dependence on the frequency of the beams. An example of such regime is shown, e.g., for Rb in Fig. 6.4, where the fluorescence signal of the Rb MOT is plotted as a function of the combined intensity of the MOT beams and their detuning. The MOT repumper for each species is split out on the table from the Zeeman repumper and there is no independent control over the power nor the frequency of the beams dedicated to the two cooling processes. The combined effect shows that the atom number in the MOT saturates quickly as a function of the repumper beam power, in this regime the dependence on the frequency also reduces, while at smaller intensity smaller detunings are favored, as shown in Fig. 6.4 for Cs. As there is no independent control for the characteristics of the MOT and Zeeman repumper beams, and there is no monitoring of the atomic flow independent of the MOT loading, it is impossible to distinguish which of the two steps is more

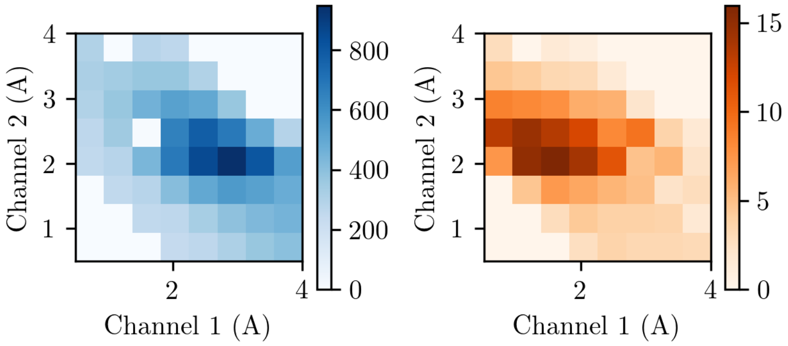

Figure 6.3: Fluorescence signal as a function of the current to the two sets of coils that compose the Zeeman slower. Left: signal from Rb MOT fluorescence photodiode with $-22\,MHz$ detuning with respect to the $F = 2 \rightarrow F' = 3$ transition. Right: signal from Cs MOT fluorescence photodiode with light with $-20\,MHz$ detuning with respect to the $F = 4 \rightarrow F' = 5$ transition. Channel 1 controls the current to coils C2–C5, channel 2 to coils C1, and C6.

sensitive to the repumper characteristics. A further upgrade that splits the repumper is currently in the plans for the project.

Further optimization of the MOT parameters is performed by benchmarking the cloud with absorption imaging after compression of the MOT. This method confirms the trends in the atom numbers and the optimal parameter values observed with fluorescence detection. In addition, benchmarks of the MOT clouds with absorption imaging showed that the optimal values for the atom numbers also correspond to low temperatures of the MOT cloud. In multiple instances, we experienced that the MOT position, shape, and stability are very susceptible to the polarization of the beams. The latter can be efficiently optimized near the maximum by looking at the fluorescence signal from the MOT. On the contrary, the alignment doesn't seem to hold major effects. This is probably due to the fact that the beams are fairly large and with a reasonably flat intensity profile (Sec. 3.8).

The compression is first optimized for atom number and temperature, but we later found out that the cloud after dRSC is much more sensitive to the compression parameters. In particular, a hotter but more compressed cloud improves dRSC. After compression, when loading both species together, there are about 3×10^7 atoms for both species at temperatures of $50\,\mu$K for Cs and $30\,\mu$K for Rb. This configuration was initially chosen as it gives similar properties for Rb and Cs clouds after MOT and compression. Later Cs loading is improved by increasing the oven temperature, this leads to up to 1.1×10^8 Cs atoms in the MOT after compression. These numbers, in particular Rb's, are lower than other similar experiments [200] and it was not possible to increase them significantly even after careful optimization. However, they are comparable to or higher than previous benchmarks in our laboratory and in particular they have been proved sufficient to achieve molecules. The detuning of

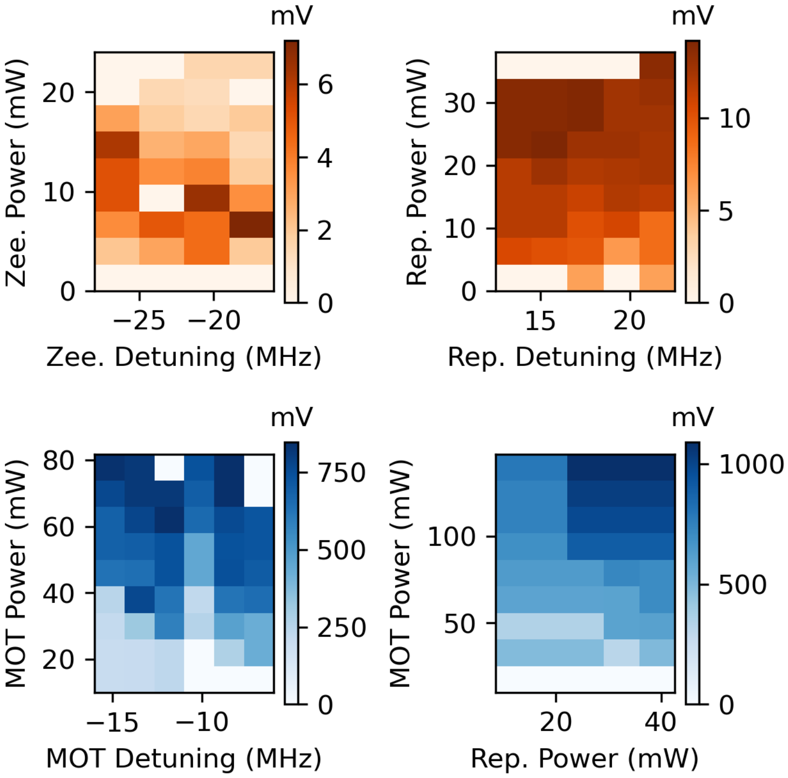

Figure 6.4: Samples of two-dimensional optimization scans with the signal from the fluorescence photodiodes. Top row: signal from Cs MOT fluorescence photodiode. Left: as a function of the intensity and frequency of the Zeeman beam. Right: as a function of MOT repumper power and MOT repumper detuning for Cs. Bottom row: signal from Rb MOT fluorescence photodiode. Left: as a function of MOT detuning and MOT Intensity. Right: as a function of MOT repumper intensity and MOT intensity for Rb.

the Zeeman cooling and repumper light is currently the main candidate to explain the low numbers, however during the time I worked on the experiment there has not been concrete evidence that it is the sole responsible. The loading rates for the configuration with Cs at the higher oven temperature are 4.5×10^7 atoms/s for Cs and 1.7×10^7 atoms/s for Rb. In conclusion, in the case of the MOT, the new lasers not only allowed for a more compact and more robust setup as it was initially intended but also provided a small improvement in the atom number.

6.4.4 Degenerate Raman sideband cooling

The next step in the sequence is dRSC. As discussed in Sec. 2.7, this step has the double purpose of cooling down the atoms while keeping a constant density, and polarizing the cloud in the dark state, the latter corresponds in the specific case of Rb and Cs to the lowest energy spin state. To image only the atoms in the dark state, 50 ms of Stern-Gerlach separation are applied to remove the atoms in the other spin states. This time comes from a compromise. For a time of Stern-Gerlach separation shorter than $25 - 30\,\text{ms}$ (depending on the cloud size) the atoms in different states are not well resolved, the upper limit of Stern-Gerlach depends on the temperature and is set by when the cloud expands outside of the imaging beam. For a temperature of about $1\,\mu\text{K}$ and typical cloud sizes, this happens around $55 - 60\,\text{ms}$ (since the initial size of the cloud is fairly large, the expansion is accelerated by the anti-trapping potential while the atoms are levitated). In Sec. 3.9, I discussed the parameters that play a role in dRSC and how they are interconnected. Here, we start optimizing this cooling step with two-dimensional scans in the parameter space and aim to increase the number of atoms that reach the dark state and decrease the temperature. Once these scans have excluded the presence of local maxima, the strategy that proves more effective is to keep optimizing the parameters in a loop.

Typically, the optimization loop begins with the Z-offset field, first because the cloud parameters strongly depend on it and there is a well-defined resonance even before fine-tuning the other parameters, second and most importantly because this parameter is shared by dRSC of both species. Given the presence of inhomogeneity of the OL, it works better to immediately set up a small ramp of the Z-offset field of a few hundred mG, as already discussed in Sec. 3.9. First, the initial value of the Z-offset field is addressed while keeping the ramp amplitude and duration fixed, then, the final value of the ramp for the Z-offset field ramp is addressed successively. These values together with the pulse length define also the slope of the magnetic field ramp. The X- and Y-offset fields are not addressed at this point, but they are scanned later when optimizing the polarizer beam. In Fig. 6.5, I show the effect of such a scan on Rb atoms, with a ramp of 160 mG toward a lower Z-offset field. Even after numerous iterations, the maximum number of atoms transferred to the dark state is at a different field with respect to the minimum of the cloud size, the latter providing an indirect measurement of the temperature. The offset between the maximum number of atoms and the minimum temperature does not disappear even when removing the magnetic field ramp.

The optimal intensity for the OL for both species is strongly correlated to the Z-offset field, due to the necessity to match the level spacing. Therefore the intensity of the OL is typically scanned next and it can be done simultaneously for Rb and Cs. For both species, we could identify a clear maximum in the atom number and a minimum in the cloud size, although the two features are not found at the same intensity even after several rounds of optimization, similar to what we observed for the Z-offset field. Loading into the reservoir improved when optimizing dRSC for the lower

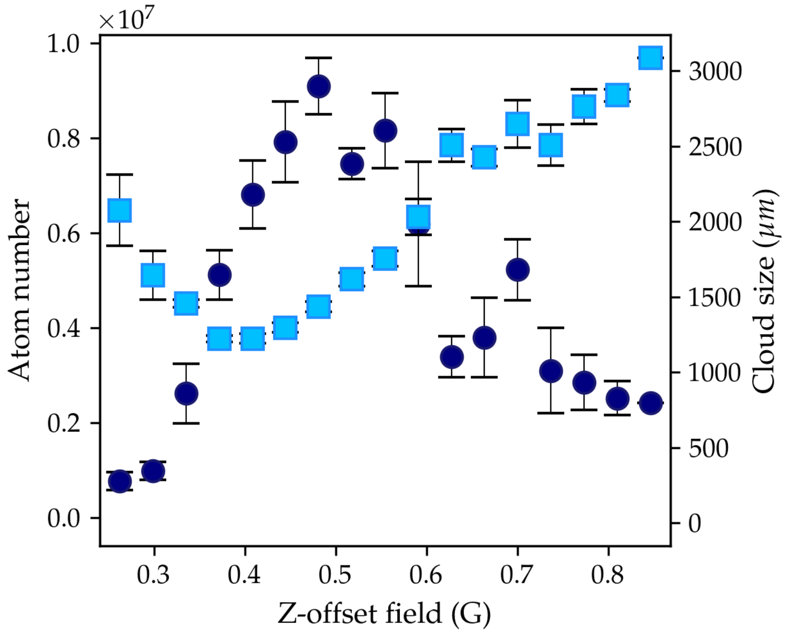

Figure 6.5: Optimization run for Z-offset field during dRSC. Rb atom number (navy circle) and cloud size (light-blue squares) after dRSC as a function of the Z-offset field. The cloud size is estimated as the average between the rms-radius along the x- and z-direction after 50 ms levitated expansion and is used as a relative measurement of the cloud temperature during the scan. The errorbars are the standard deviations over three repetitions.

temperature. The polarization of the lattice beams is set to linear and optimized by looking at atom numbers and temperatures, its optimization starts only after a few iterations where the other parameters are optimized.

The polarizer frequency should be resonant with the transition from the higher hyperfine state, after accounting for the Zeeman and Stark shift. However, we do not observe a strong dependence of the atom number on this parameter, when changing the polarizer frequency within 2Γ from the resonance condition. The number of atoms in the cloud saturates as a function of the polarizer intensity, but for intensities that lead to the same atom number a significant decrease of the temperature can still be observed. This behavior becomes more and more pronounced as all the parameters approach their optimum value over multiple iterations of the optimization loop. The evolution of the Rb atom number as a function of the polarizer intensity is shown in Fig. 6.6, over four iterations. As the optimization proceeds, the atom number increases, and the saturation behavior becomes more pronounced. At the same time, the cloud size in the saturated regime decreases, indicating a decrease of the temperature.

The polarization of the polarizer beam is set to be σ^+. The polarizer enters the cell at a small angle with respect to the magnetic field, due to this angle the projection of the polarization on the quantization axis should have the right amount of π-polarization (see Sec. 3.7). However, it is possible to fine-tune this angle, by adding a small transversal field with the X- and Y-offset coils to

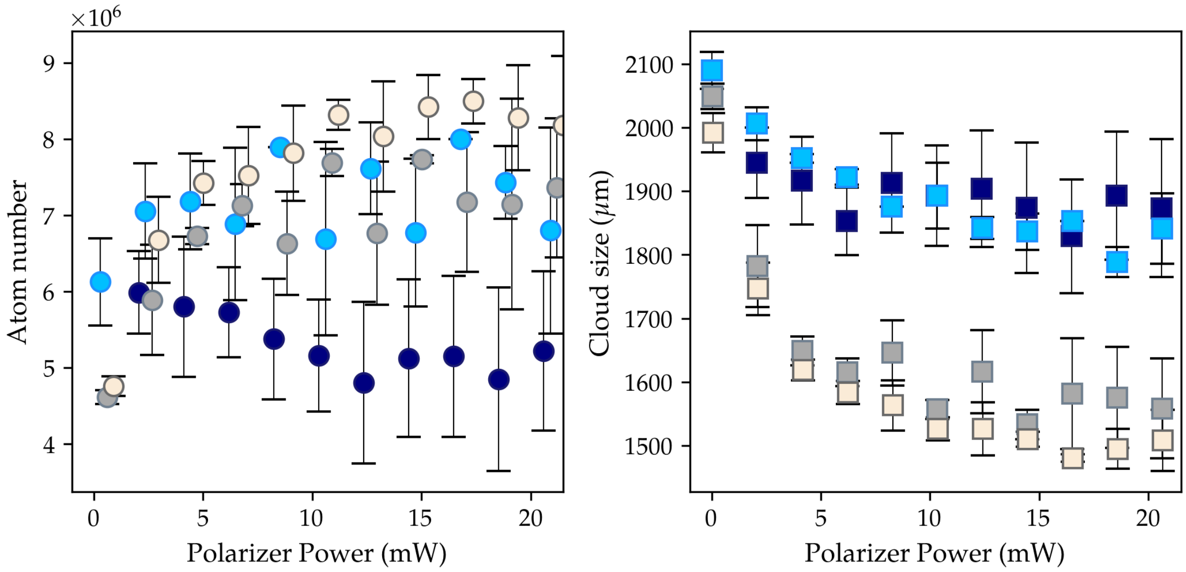

Figure 6.6: Trends of the characteristics of Rb cloud with the polarizer power for dRSC over multiple optimization loops. Left: Atom number after dRSC as a function of the polarizer intensity. Right: Average cloud size as a function of the polarizer intensity. In order, the 1^{st}, 2^{nd}, 3^{rd}, and 4^{th} iterations of the optimization loop are represented in navy, cyan, grey, and cream.

tilt the quantization axis. When scanning the X- and Y- offset fields, we observe a clear maximum of the atom number and a minimum of the cloud temperature for the current applied to each offset coil. The two features coincide within the resolution of the measurement. For both the OL and polarizer beams, the final intensity and frequency are not the only important parameters, but the way these beams are switched on and off also plays a role. We observed that ramping up and down the OL and the polarizer intensities with a quick linear ramp of $1-2$ ms helps to lower the temperatures, with respect to an abrupt on/off switching at the final power. This is related to the atoms following more adiabatically the changes of the potential landscape.

The final parameter under exam in the optimization of dRSC is the duration of the pulse. The number of atoms in the dark state saturates for pulses longer than 2 ms after the optimization is completed. On the contrary, the cloud size for both species has a minimum around a pulse duration of 5 ms. When the system is still far from the optimum condition in the parameter space, the minima of the temperature for the two species can be at quite different pulse durations with respect to each other, but it converges to similar values over multiple iterations of the optimization loop.

The optimization of dRSC is done, without and with the presence of the reservoir ODT. As the presence of the ODT changes the potential landscape and introduces an additional Stark shift to the hyperfine states, it is necessary to adjust the parameters. Small changes can be seen in all parameters discussed above, but the bigger change is an increase in the polarizer intensity, probably being the polarizer closer to resonance, its optimization is more sensitive to the Stark shift of the involved levels. Very different from what was discussed in Sec. 3.9, we did not see a significative improvement

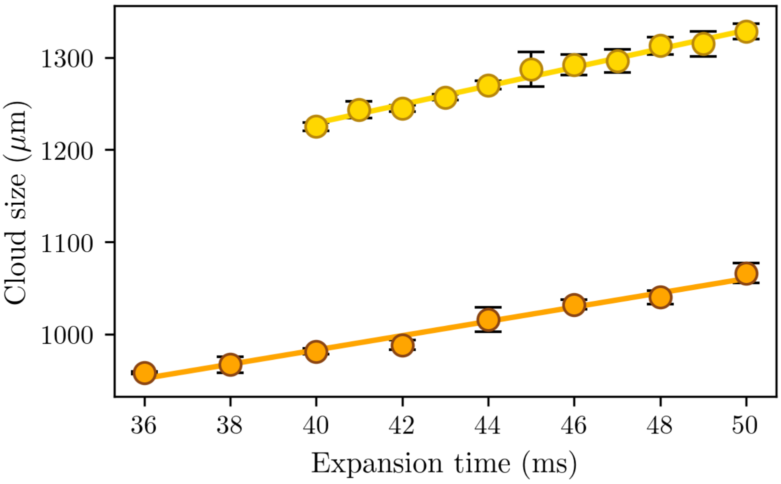

Figure 6.7: Temperature measurements for Cs after dRSCwith and without the reservoir trap on. The size of the cloud averaged over two directions is recorded as a function of the time of levitated expansion, in orange after only dRSC, and in yellow when the reservoir beam is on at the same time as dRSC. The solid lines are linear fits, $\langle v \rangle$ extracted from the fit are used to retrieve the temperatures. In the specific case, $0.51(4)\,\mu$K and $1.6(1)\,\mu$K, respectively without and with the reservoir beam.

when applying three independent pulses and letting the atoms relax in the reservoir, therefore the current experimental sequence uses a single pulse to simplify the experimental sequence.

In general, the optimization of the cloud after dRSC when this cooling step is applied without the presence of the ODT can reach temperatures around $0.5\,\mu$K the atom number is typically around 5×10^6 atoms for Rb and 1×10^7 atoms for Cs. On the contrary, when the dRSC is applied in the presence of the reservoir trap, the minimum temperatures of the clouds we achieve in the optimization are about $1\,\mu$K for Cs and $4\,\mu$K for Rb. A comparison of the temperature in the two cases for Cs is shown in Fig. 6.7. The atoms are released from the OL for dRSC by ramping it down in 1 ms the polarizer and the reservoir beam (when present), are switched off instantaneously. The levitation gradient is switched on in 2 ms to separate the atoms in the dark state, from the atoms that have not been transferred. The cloud size is recorded as a function of the time of levitated expansion, the size is assumed to be directly proportional to the root of the mean squared velocity $\sqrt{\langle v^2 \rangle}$ of the atoms, for a Maxwell-Boltzmann velocity distribution. The temperature is estimated as $T = m\langle v^2 \rangle / k_B$. The temperatures reached when switching on the reservoir during dRSC are lower than those reached by switching on the reservoir ODT after dRSC. In addition, switching on earlier the reservoir ODT has the technical advantage of giving the optical setup of the reservoir enough time to thermalize. Therefore it minimizes thermal drifts during the dimple loading, which might otherwise lead to intensity drifts and beam-pointing instabilities.

6.4.5 Dipole traps

In this section, I discuss the partial optimization of the cooling in the ODTs and in particular of the implementation of the dimple trick (Sec. 2.6.1), starting with the loading of the atoms into the reservoir and then the transfer of the atoms from the reservoir into the dimples (see Sec. 3.10). Despite I worked for some time on evaporative cooling in the dimples, especially with Cs, it had been found that evaporation was severely limited by background collision, and never led to the realization of BECs, therefore I will not discuss it here in detail. As described in Sec. 2.6.1, the dimple trick requires a delicate equilibrium: on one side, it needs fast thermalization, i.e., high elastic scattering rates, to load the dimples, on the other it needs small three-body loss rates to curb losses in the dimples. As discussed in the previous Subsection 6.4.4, the reservoir is switched on before dRSC to help stability, the optimization leads to anticipate it by 100 ms with respect to dRSC. The parameters of the reservoir after dRSChave been estimated by measuring the number of trapped atoms, their temperature (with measurements analogous to Fig. 6.7) and the trap frequency. The latter has been measured by measuring the frequency of the harmonic oscillations in the vertical directions. The oscillations have been excited by decreasing the levitation field in 3 ms from 31 G/cm to 25 G/cm and then bringing the field back to the initial value. An example of such measurement is provided in Fig. 6.8, for a power of the first pass of the reservoir trap of 35 W. The measurement has been done with $2.91(5) \times 10^6$ atoms at a temperature of $1.6\,\mu$K. The cloud has been recorded for different hold times in the ODT after sudden release 5 ms of levitated expansion plus 15 ms of TOF have been applied. The position has been fitted by a cosine oscillation with an exponential decay of the amplitude described by the equation:

$$y(t) = c + A\cos(\omega_\mathrm{t} t + \phi)\exp(-t/\tau) \tag{6.1}$$

where c is a constant offset, A is the amplitude, $\omega_\mathrm{t}/(2\pi)$ is the trap frequency, ϕ is the initial phase, and τ is the decay time. The trap frequency along the vertical direction $\nu_\mathrm{t,z}$ has been measured with Cs and it is $\nu_\mathrm{t,z} = 16.2(1)\,\mathrm{Hz}$, the oscillations decay in $2.0(3) \times 10^2$ ms.In the hypothesis that the two beams of the reservoir are providing the same trapping (which implies that the angular trap frequencies along the other two directions are $\omega_\mathrm{t,x} = \omega_\mathrm{t,y} = \omega_\mathrm{t,z}/\sqrt{2}$), the trap frequencies, number of atoms, and temperature have been used to calculate all the other trap parameters as described in Sec. 2.4. For a magnetic field of $\sim 40\,\mathrm{G}$ as switched on after dRSC, which gives $a_\mathrm{Cs} = 870\,\mathrm{a}_0$, the atoms have a peak density $n_0 = 2.4(4) \times 10^{10}\,\mathrm{atoms/cm}^3$ and peak elastic scattering rate $\Gamma_\mathrm{el} = 26.35(2)\,\mathrm{Hz}$, the three-body rate is here negligible. In the sequence, we hold the atoms in the reservoir for 500 ms to allow them to thermalize in the trap, before switching on the dimples. Based on the elastic scattering rate and the approximation of three scattering events per atom for thermalization, the thermalization time can be estimated to be ~ 115 ms.

In typical conditions for the experimental sequence, the atoms in the reservoir are almost levitated for the full time, with a magnetic field gradient along the vertical direction that compromises between Cs ($\nabla B = 31\,\mathrm{G/cm}$) and Rb ($\nabla B = 30.2\,\mathrm{G/cm}$) perfect levitation values. After thermalization, when the loading of the dimples starts, there are 1.8×10^6 atoms for Rb and 3.3×10^6 atoms for Cs in the reservoir. The number of Rb atoms held in the reservoir is improved by more than 30% with respect to the previous sequence, while Cs is similar to the previous value, confirming once more that the new laser setup can simplify the experimental setup without compromising on the performances. After holding the atoms in the reservoir for 500 ms, the intensities of the dimples

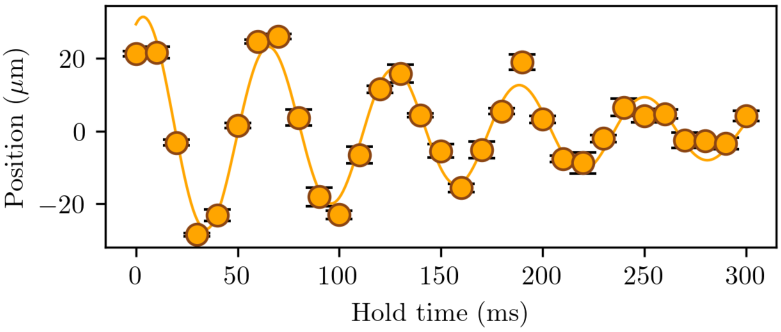

Figure 6.8: Measurement of the vertical trap frequency for the reservoir trap measured with Cs atoms. The position of the cloud is plotted as a function of the hold time in the dimple after the initial excitation of the dipole mode. For imaging 5 ms of levitated expansion and 15 ms of TOF have been applied.The solid lines are fits of the decaying oscillation returning an oscillation frequency of 16.3(1) Hz.

beams are ramped up in 500 ms while the reservoir beams are kept at constant intensities, thus the reservoir maintains the same depth and frequency. At the end of the dimples ramp-up time, the reservoir is switched off instantaneously and the field is changed quickly in 1 ms from 40 G to 21 G, where the conditions are suitable for Cs condensation [156]. At the same time, the intensity of the dimples is decreased to reduce their trap depth and to start the first ramp of evaporative cooling.

Initially, the second pass of the reservoir provided a much weaker confinement. To increase the density and the scattering rate in these conditions I tried introducing a step of forced evaporative cooling in the reservoir. This was implemented by using the magnetic field gradient to tilt the potential of the reservoir trap in the vertical direction and reduce its effective depth, similar to the technique applied in Ref. [107], which had shown accelerating evaporative cooling of Cs. With respect to the technique applied in the RbCs project for evaporative cooling in the dimples that reduces the power of the beams, the tilting has the advantage of preserving the trap frequencies, which helps to keep higher scattering rates and peak densities during evaporation.

When changing the field to $\nabla B \sim 26\,\mathrm{G/cm}$ in 3 s. I achieved for Cs about 3×10^4 atoms at 340 nK with an estimated phase-space density of 1.12×10^{-4}. For Rb 3.5×10^5 atoms at 720 nK with an estimated phase-space density of 6.8×10^{-5}. Thanks to this improvement it was possible to load 8-20% of the atoms from the reservoir in the dimples, in line with the typical 10% observed in the past on the RbCs project and other projects in Innsbruck for similar reservoir-to-dimple volume ratios.

Although the total atom number is too low to continue with forced evaporative cooling in the dimples, this technique could be further optimized to achieve suitable conditions for the Feshbach association non-degenerate clouds, in view of STIRAP tests and further for evaporative cooling of molecules with electric field or microwave shielding. The procedure could be similar to Ref. [31] that used initial temperatures of $\sim 200\,\mathrm{nK}$ for both species when performing Feshbach association and further transferred the molecules to the ground state via STIRAP.

As for the achievement of large BECs, it was more beneficial to increase the density of the atoms by changing the size of the second pass of the reservoir. The current sizes of the beams at the atom location[6] for typical working conditions measured with a CCD camera[7] are for the first pass $w_{1,x} = 1165$ μm, $w_{1,x} = 1487$ μm, and for the second $w_{2,x} = 981$ μm and $w_{2,y} = 1253$ μm, x and y here represent the main axis of the beam transversal section. The original size of the second pass at the beginning of the optimization was $w_x^1 = 1468$ μm and $w_y^1 = 1805$ μm. As discussed in the next Section (Sec. 6.4.6), with a bigger size of the reservoir the effective trap depth decreases not only because of the lower local intensity but also because an anti-trapping effect in the horizontal plane (Sec 6.4.6), that increases with the distance from the center of the quadrupole field, tilts the potential in the horizontal plane. The values provided in this section for atom number, timings, *etc.*, have been obtained with the tighter reservoir trap, with the exception of the forced evaporative cooling in the reservoir.

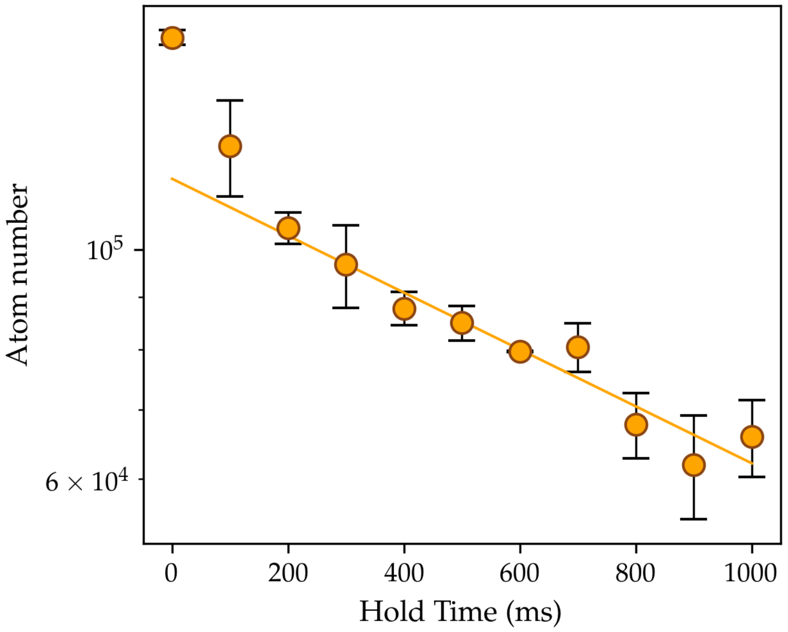

Figure 6.9: Measurement of the lifetime of Cs atoms in the dimples. Atom number as a function of the hold time in the crossing of the Cs dimple and shared dimple. The fit is an exponential decay and is applied for $t > 200$ ms and gives a characteristic time of 1.6 s.

I will not go into details about the attempts at evaporative cooling in the dimples, as it was observed that the effort in that direction has been limited by high vacuum pressures. In particular, the evaporation rate which should be a two-body process was competing with the one-body losses due to background collisions. In Fig. 6.9, I show a lifetime measurement for Cs in the crossed dimple trap, starting with 1×10^5 atoms at 0.49(2) μK. The initial decay is attributed to plain evaporation.

---

[6] This was reproduced by reflecting the beams away before crossing the cell and measuring at the expected distance of the atoms from the mirror.

[7] Thorlabs - BC106N-VIS/M CCD Camera Beam Profiler

	T (nK)	N	PSD	γ_3 (Hz)	Γ_{el} (Hz)	n (atoms/cm^3)	V_T (μK)	$\bar{\omega}_T$ (Hz)
New	180	85e3	0.22e-1	6e-3	94	4.9e12	1.84	52
Old [151]	150	70e3	0.5	0.01	89.6	7.10e12	1.5	57

Table 6.2: Cs cloud characteristics in the dimples. Temperature (T), atom number (N), phase-space density (PSD), three-body scattering rate (γ_3), elastic scattering rate (Γ_{el}), Peak density (n), algebraic average of the trapping potential (V_T), geometric average of the trap frequencies ($\bar{\omega}_T$). The values are presented for the attempted evaporation sequence realized during the work of this thesis and the corresponding original optimization from Ref. [151] when available.

The remaining atom number as a function of time has been fitted for a hold time greater than 200 ms with an exponential decay. This returned a lifetime of 1.6(1) s. For comparison, the lifetime was measured in a magnetic trap after MOT and compression. In this case, the atoms at about 130 μK had a lifetime of 2.3 s, this value is assumed to be the vacuum-limited lifetime. Given the two numbers, it is safe to conclude that the lifetime in the dimple is strongly limited by the collisions with the background gas.

I would just mention here the best result, which was achieved for Cs with two evaporation ramps (Rb laser for dRSC OL was under maintenance at the time), both cutting the trap depth by $\sim 75\%$. Each ramp has a duration of 200 ms. The cloud conditions after the two ramps are shown in Tab. 6.2, as done for the reservoir, the atom number, temperature, and frequencies are used to calculate the peak values for density, elastic and inelastic scattering rates, and phase-space density. The values measured here are compatible with the third evaporation ramps, as reported in Ref. [151] for the original characterization of evaporative cooling in the RbCs project. In both cases, the magnetic field is 21 G.

The duration of the ramps I found during the optimization is shorter than typical values, which are up to a few seconds (the sequence reported in Ref. [151] used in total 1.75 s to the step discussed in Tab. 6.2), and the evaporation efficiency in this optimization was found to be $\eta = 1$–2, against typical efficiency $\eta > 2-3$. The optimal duration is most likely strongly affected by the competition between the evaporative cooling and the one-body losses, due to the poor vacuum conditions, the fast ramps in turn limit the efficiency of the evaporative cooling.

6.4.6 Anti-trapping

During levitation, the gradient from the quadrupole field compensates for the gravitational pull in the vertical direction, but in the horizontal plane, it gives rise to an anti-trapping term that pushes the atoms away from the center. Such anti-trapping is small and it is typically negligible when working with clouds that are aligned with the center of the quadrupole field in the horizontal plane. However, the immiscibility of the two BECs implies that at least one of the two species is not aligned with the center of the quadrupole, during the evaporative cooling therefore part of those atoms experiences this anti-trapping potential. During the old evaporation sequence, the two clouds were displaced up to 400 μm [151]. To estimate the anti-trapping potential, we measured the acceleration of the atoms in the horizontal plane for different values of the quadrupole field. The dimple intensities for the Cs dimple and the shared dimple are ramped up in 500 ms, and the atoms are held in the dimples for additional 500 ms after the intensities have reached the final value. Afterward, the dimples are

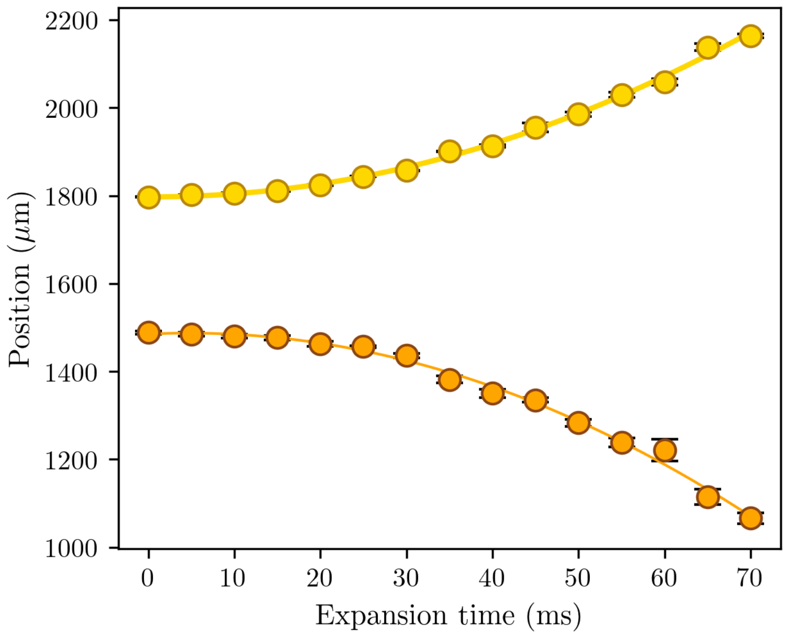

Figure 6.10: Estimation of the anti-trapping potential. Position of the Cs cloud in the horizontal plane as a function of time. The orange and yellow data refer to the x and $y-$axis of the camera. The solid lines are second-order polynomial fits.

removed and the atoms are levitated. To trace the movement of the atoms in the horizontal plane, the image is acquired from the bottom of the cell at different times after the removal of the dimples. Fig. 6.10 shows an example of such measurement at $\nabla B_z = 31\,\mathrm{G/cm}$ with $B = 46\,\mathrm{G}$. The cloud trajectory is fitted with a second-order polynomial for each direction. The acceleration in the two directions a_x, a_y is approximated to be constant over the observed distance of about $500\,\mu$m, and the gradient is estimated as $dU/dx = ma_x$, respectively, $dU/dy = ma_y$. For extreme quadrupole gradients, the atoms experience a force up to $\sim 1.79 \times 10^{-23}\,\mathrm{N} \sim 2 \times 10^{-3}\,(\mathrm{J/k_B})/\mathrm{m}$, to compare it with V^{lat}. In the optimization of the sequence, the anti-trapping hindered the loading of the reservoir and the dimples (Sec. 6.4.5) for the larger beam waist of the reservoir, as it reduced the trap depth of the reservoir by about 30%, and it affected Rb superfluid transport as seen in Sec. 5.5.

6.4.7 General results

I would like now to take a general look at the results of the optimization, to discuss the role of the new laser setups and the changes in the sequence. The new laser system addresses Zeeman slowing, MOT, and dRSC. I will start here to discuss the results obtained via absorption imaging after the MOT compression. In Fig. 6.11, I show the number of atoms as a function of the average intensity of the MOT beams. For every data point, the MOT was loaded for 4 s, and then it was compressed. In total three repetitions were taken, the standard deviation is indicated by the errorbars. First, the saturation of the intensity, already discussed in Sec. 6.4.3, is here well visible. This regime sets in for intensities about twice the saturation intensity ($I_{\mathrm{sat}}^{\mathrm{Rb}} = 1.67$ mW/cm^2 [157], $I_{\mathrm{sat}}^{\mathrm{Cs}} = 1.102$ mW/cm^2 [158]). Reaching such a regime with the old laser system would have required changing the beam sizes, or changing the beam configuration, e.g. retroreflecting the beams. The maximum intensity of the old setup for the same beam configuration is also shown in Fig. 6.11 for reference, it barely reached saturation for Rb and it was around 30% below saturation for Cs. The importance of being in the saturated regime can be understood by considering the fact that small fluctuations in the beam power will have no effect on the final number of atoms. Fig. 6.11 shows the stability of the atom number in the MOT after compression in the saturated regime on a shot-to-shot base over about one hour. In total, more than 670 repetitions were executed. The average number for Rb during this measurement is $N^{\mathrm{Rb}} = 1.560 \times 10^7$ with standard deviation only $\sigma_{\mathrm{N}}^{\mathrm{Rb}} = 1.2 \times 10^5$ (about 1%), for Cs it is $N^{\mathrm{Cs}} = 1.855 \times 10^7$ with standard deviation $\sigma_{\mathrm{N}}^{\mathrm{Rb}} = 8.3 \times 10^5$ (about 4%). The fluctuations in the measured atom number for Cs are partly due to absorption imaging, because the two pulses of absorption imaging light, that acquire the images with and without the atoms are not perfectly identical, indeed small intensity fluctuations between the two are present, most likely due to the quality of the fiber delivering the beam to the main table. While Rb intensity has fewer fluctuations. Having a stable and reproducible atom number in the MOT after compression is a requisite to have a stable atom number in the rest of the sequence.

The next question is what happens to the atoms loaded in the MOT when moving to the next steps of the sequence? Would increasing the number of atoms in the MOT through different means (e.g. loading times, atomic flows, *etc.*) increase the number of atoms in the BEC, or is the bottleneck at a different step? Does the interplay of the two species play a role in the topic? To answer these questions I performed a comparative analysis of the number of atoms at three different steps in the sequences: in the compressed MOT, after dRSC, and in the reservoir ODT. For this analysis I vary the number of atoms in the MOT by changing the loading time of the MOT, then the experimental sequence is carried out as usual until the step under exams. Benchmarks are taken as follows:

- $\mathcal{M}$ is the atom number measured in situ after releasing the atoms from the compressed MOT as a function of the MOT loading time.
- $\mathcal{D}$ is the atom number measured following dRSC after levitated expansion and contains only the atoms in the dark state of dRSC, the atom number is taken as a function of the MOT loading time.
- $\mathcal{R}$ is the atom number measured in situ after holding the atoms in the reservoir trap for 500 ms (typical conditions for starting the loading of the dimples), as a function of the MOT loading time.

Note that due to the different conditions in which the benchmarks are done after each curve, the saturation values reported do not account for the absolute efficiency of the cooling and trapping steps but only for the relative efficiency. The three curves $\mathcal{M}$, $\mathcal{D}$, and $\mathcal{R}$ are acquired for each species when cooling down the RbCs mixture and then when loading and cooling only one species (the other is removed by not switching on Zeeman and MOT light). Each curve is fit with the function used for the MOT loading rate (Appendix C) to obtain the saturation number N_{s} and a saturation time τ_{s}. The results of the individual fits are listed in Tab. 6.3. τ_{s} is given with respect to the MOT loading time, therefore it represents indirectly the atom number in the MOT. If the number of atoms in

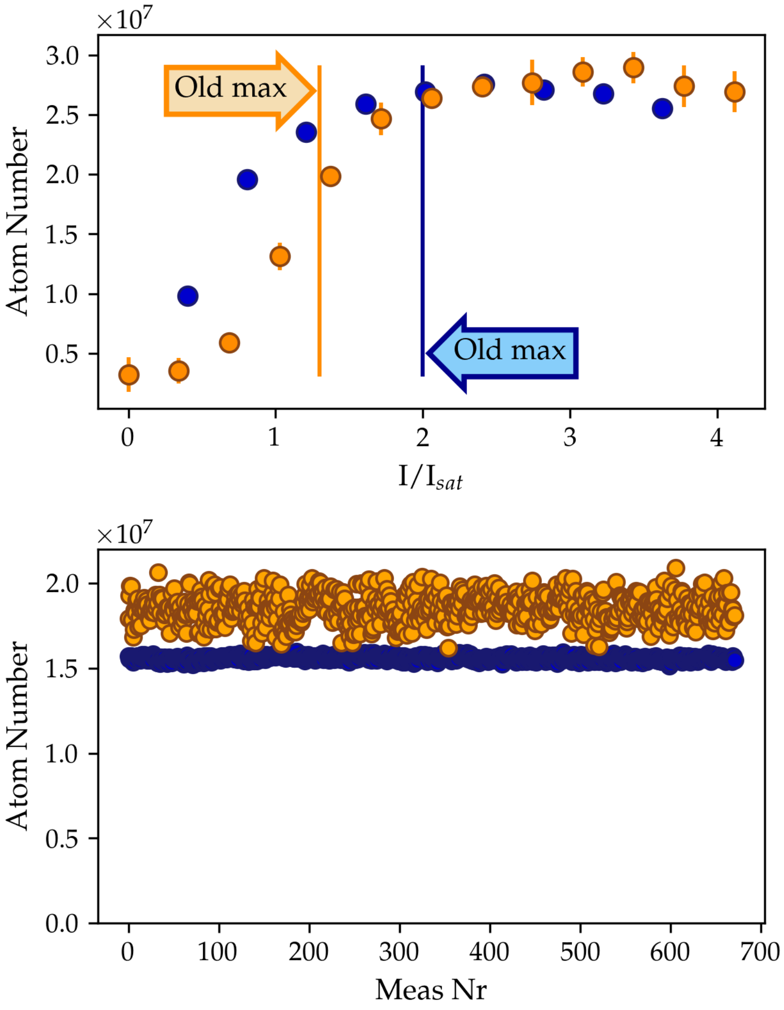

Figure 6.11: MOT saturation regime. Top: Number of atoms in the compressed MOT as a function of the average intensity of the MOT beams for the new laser setup. In blue Rb in orange Cs. The loading time is 4 s. The solid vertical lines represent the maximum power available from the old setups, respectively orange for Cs MOT and blue for Rb MOT. Bottom: Number of atoms in the compressed MOT over more than 600 repetitions (about 1 hour), in blue for Rb and in orange for Cs.

the MOT is limiting the atom number after dRSC or in the reservoir, the curves will have the same trend and in particular, the τ_s for $\mathcal{D}$ or $\mathcal{R}$ would be equal to τ_s for $\mathcal{M}$. Fig. 6.12 reports $\mathcal{M}$, $\mathcal{D}$, and $\mathcal{R}$ with their respective fits, for an easier comparison, each curve and its fit have been normalized to their N_s.

Quantity	Curve	Rb with Cs	Rb alone	Cs with Rb	Cs alone
N_s	$\mathcal{M}$	3.69(4)e7	3.68(8)e7	1.01(1)e8	1.60(4)e8
	$\mathcal{D}$	3.64(7)e6	4.54(7)e6	9.4(1)e6	1.52(3)e7
	$\mathcal{R}$	1.86(2)e6	2.74(5)e6	3.38(4)e6	4.45(5)e6
τ_s(ms)	$\mathcal{M}$	2.05(9)e3	2.3(2)e3	2.2(1)e3	5.9(3)e3
	$\mathcal{D}$	1.7(1)e3	2.1(1)e3	3.4(1)e3	5.0(2)e3
	$\mathcal{R}$	1.33(9)e3	1.8(2)e3	3.9(1)e3	2.6(1)e3

Table 6.3: Saturation values used for the normalization of the curves reported in Fig. 6.12.

Case 1 Rb loaded alone

When Rb is loaded alone, the difference between the normalized $\mathcal{M}$, $\mathcal{D}$, and $\mathcal{R}$ is minimal. The three curves collapse on a single one within the errorbars, as confirmed by the τ_ss. This can be interpreted as the transfer efficiency being the same independently of the initial atom number, therefore it suggests that the number of atoms in the reservoir can be improved by further improving the number of atoms in the Rb MOT.

Case 2 Rb loaded at the same time as Cs

When Rb and Cs are loaded together $\mathcal{R}$ saturates at shorter τ_s than $\mathcal{M}$ and $\mathcal{D}$, i.e., the transfer efficiency changes with the atom number. As a consequence an increase in the atom number in the MOT should not be expected to convert proportionally to an increase in the atom number in the reservoir nor consequently in the BEC. In addition, when loading the Rb atoms in the presence of Cs atoms there is a drop in the saturation number of $\mathcal{D}$ and $\mathcal{R}$ of 20% and 30%, respectively, this is most likely due to interaction between the two species even if the gases are fairly dilute at this stages.

Case 3 Cs loaded alone

Cs has the opposite behavior to Rb. For Cs loaded alone, there is a well-pronounced difference in the saturation times of $\mathcal{R}$ with respect to $\mathcal{M}$ and $\mathcal{D}$. Similarly to case 2, this leads to the interpretation that there is likely a bottleneck past the MOT for the atom number.

Case 4 Cs loaded at the same time as Rb

When Cs is loaded with Rb the difference of the saturation times of $\mathcal{R}$ with respect to $\mathcal{M}$ and $\mathcal{D}$ reduces. Therefore the presence of Rb is helping the loading of Cs atoms in the reservoir ODT. On the other hand, the number of atoms at which $\mathcal{M}$ saturates is smaller by about 37% when Cs is loaded with Rb, but the difference in N_{s} for Cs for the two cases is only 25% in $\mathcal{R}$.

For $\mathcal{R}$ the different behavior between the two species could be explained by the temperature of the cloud with respect to the trap depth of the reservoir. If Cs is too hot, during the 500 ms hold time, plain evaporation will lead to large losses of Cs. In the presence of Rb, interspecies thermalization is possible as already observed in other instances. Since Rb is lighter and sees a shallower trap thanks to the different polarizability, when colliding with Cs it takes more kinetic energy and escape the trap more easily, therefore it sympathetically cools down Cs. Therefore for Cs, the number of atoms in $\mathcal{R}$ increases due to the faster cooling and lower losses. Instead, for Rb, the atom number reduces due to the collisions with Cs that increase the losses. In both cases, the number at which $\mathcal{R}$ saturates depends on the density of the other species and a_{Cs}. Finally, for the loading of the dimples, although the results were not conclusive due to vacuum problems, I would like to stress again that the number, phase-space density, and temperature achieved with Cs atoms after two evaporation ramps were consistent with the results from the third evaporation ramp as reported in Ref. [151].

6.5 Implementation of live data analyses

In the mindset of an overall streamlining of the day-to-day operation in the labs, a new data analysis tool has been introduced. Before discussing which benefits it brings, I will go here briefly through the general process of data acquisition and analysis, to help fix the lexicon. Typically each execution of the experimental sequence, a shot, is concluded with the acquisition of the absorption pictures. The pictures show the optical density of the cloud, from there it is possible to retrieve the atom number, the size, and, when necessary, the shape of the cloud. A run is composed of multiple shots that differ by the value of one or more parameters. In the following, I refer to the parameter changed during the run as scan parameter. For a run, the data retrieved from the individual shots are compared to identify their possible trends as a function of the scan parameter. During the optimization presented in the previous sections up to 20-40 runs per day have been taken, typically they are composed of 11-21 data points each of them acquired with at least three identical shots. To deal with the large mole of data it is important then to automatize as much as possible the process and to have a way to index properly the data upon storage.

The new data analysis and storage is based on Lyse. Lyse is part of the Labscript suite, a series of Python-based open-source tools designed specifically to run and manage cold atoms experiments [201, 202, 203]. Thanks to this addition, it becomes possible to perform live analysis of the data as they come, saving the large amount of time that was previously spent on post-processing the data. I restructured the data analysis system around Lyse's potential, with attention also to the storage and indexing of the data.

6.5.1 Limitations of the old analysis tools

The data analysis in the experiment was modular with all custom scripts. The picture acquisition for each shot is controlled in MATLAB, while the analysis of the pictures from the shot is based on C++ and works on a shot-to-shot base with no long-term memory. The MATLAB and C++ scripts work

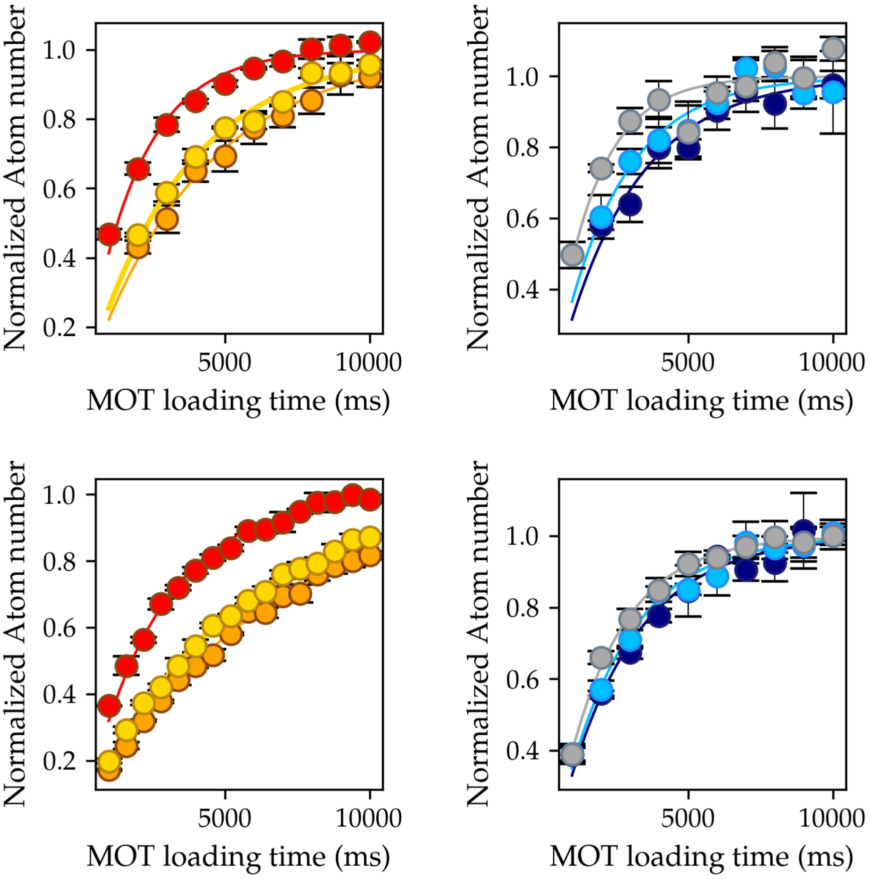

Figure 6.12: Comparison of cloud saturation for different steps. Left: Cs. Right: Rb. Top: In the RbCs mixture. Bottom: One species is loaded and cool individually. Each plot reports the normalized atom number after MOT compression, curve $\mathcal{M}$ in dark blue for Rb and orange for Cs. Normalized atom number at the end of dRSC curve $\mathcal{D}$ in yellow for Rb and in light blue for Cs. Normalized atom number after holding the atoms in the reservoir trap for 500 ms, curve $\mathcal{R}$ in red for Rb and in grey for Cs. The solid lines are fit for exponential growth similar to the MOT loading rates (Appendix C). N_s from the fits are used to normalize the data.

quite reliable and efficiently together. The data from a measurement are visualized in LabVIEW, this script does not perform the analysis. The data visualized in LabVIEW can be saved and/or sent to Origin on demand for further analysis.

The problems observed with the LabVIEW interface are multiple:

- It only has memory of the current measurement and it is impossible to compare multiple curves from multiple runs.
- Data are stored only if explicitly asked, and if they are not saved immediately there is no way to later identify which shots belonged to the run.
- When visualizing the results of a run, fitting is only implemented for temperature measurement, and adding more fitting functions is cumbersome.
- The use of different tools for visualizing the data live and postprocessing them for the analysis increases the complexity of the analysis system and the time consumption
- In Origin, all the plots need to be treated separately, which is time-consuming when dealing with large amounts of data.
- The parameter file is not user-friendly and the only way to retrieve any relevant parameter is to reload the entire experimental sequence.
- There is almost no way to reproduce which parameter is scanned during a run, if not explicitly mentioned in the labbook or renamed promptly in LabVIEW.

With this structure, the analysis often took almost as much time as the data acquisition itself, and a lot of information was lost.

6.5.2 Data analysis with Lyse

Lyse has a modular approach to data analysis, with two kinds of routines: single-shot routines and multi-shot routines. The single-shot as defined above corresponds to a single execution of the sequence, multi-shot can include one or several runs. The data from a shot are passed to Lyse in the form of a .h5 file. The information of the .h5 file is treated as pandas dataframe entries [204, 205], and it can be visualized in the Lyse interface. Multi-shot routines extract information from multiple .h5 files. Each routine, either single-shot or multi-shot, consists of an arbitrary custom-written Python script and, in principle, an arbitrary number of routines with arbitrary complexity can be performed by Lyse on the data from the shots and runs.

The creation of the .h5 file in Labscript is done by Runmanager and automatically passed to Lyse. For the RbCs the creation of the .h5 file was implemented by Dimitrios Trypogeorgos [8], starting from the data produced by C++ script described above. The start of a shot in the custom control software[9] triggers the creation of a new .h5 file. The file stores the shot number, the numeric

---

[8] Institute of Nanotechnology, Consiglio Nazionale delle Ricerche (CNR-NANOTEC), Via Monteroni, I-73100 Lecce, Italy

[9] This is a custom LabVIEW program not discussed in this thesis, not to be confused with the LabVIEW script used to visualize the data

value of the scan parameter (if any, and without an indication over which parameter is scanned), the time at which the shot is taken, and the data produced by the C++ software analyzing the pictures.

I wrote the custom routines for Lyse that are currently used in the lab for data analysis, including fitting procedures, and indexing and storage of the analyzed data with the run parameters. In addition, I created routines for measuring and plotting vacuum pressures to correlate them with the data, when the first vacuum problem arose. I will give here an overview of the main routines that are used in the day-to-day operation and provide a more detailed description of some of them in Appendix B. Initially, the routines have the purpose of covering the functions of the LabVIEW interface and addressing its limitations. I tried to keep the structure modular, but at the same time tried to limit the number of files that needed changing, to reduce the possibility of human errors. The core of the analysis is composed of a single-shot routine, a multi-shot routine, and a Python dictionary that communicates with both:

- **Params** is a Python dictionary, i.e., an associative array of the type *key*:*value*, that stores the information relevant to classify the shot and to speed up live and post-processing analysis. This is not a Lyse routine, but an auxiliary file used in multiple routines. The first and most important key of the dictionary is an alpha-numeric identifier 'Meas Nr' that allows bunching together the shots, and it is used across the RbCs project's internal documentation to refer to the run, e.g. in the labbook, in the naming of the plots, fits, *etc.* The other important key of Params is the indication of the scan parameter that is changed during the run. In addition to these two entries, Params stores the numerical values of additional parameters that might be changed on the same day on different runs to be able to do additional comparisons in multi-shot routines covering multiple runs or post-processing. Params stores also the folder where the data analyzed during the day are stored (pictures from absorption imaging and raw data are also saved separately outside of Lyse). All the key-value pairs contained in Params, with the exception of the saving folder, are written on the .h5 by the routine Add Meas Nr.

- **Add Meas Nr** is a single-shot routine consisting of a single `for` loop to write the information from Params on the .h5 file. Add Meas Nr does not need changes, therefore it limits the insurgence of errors due to the writing of the file.

- **Plot with average** is a multi-shot routine that performs the analysis on the run. It collects the .h5 files sharing the identifier Meas Nr from Params, i.e. the files that belong to the same run. It plots the atom number and the size of the cloud against the scan parameter during the run, labeling the scan parameter according to its definition in Params. The data and plots are saved in the folder containing the results for the day, also specified in Params. A series of True and False in the beginning provides the possibility to use the raw or averaged data (in the latter case errorbars representing the standard deviation are added), to select which species to plot, to decide if a fit should be done or not, and apply a calibration to the X-axis. The type of fit can be selected directly from a list on a run-by-run basis, while the calibration is stored in a separate file for each variable and is applied automatically based on the variable name. In addition, there is the possibility to set one or more arbitrary conditions to remove data from the plot and/or the fit. Plot with average returns a .txt file with the data, two .png high-resolution plots, one for the atom number and one for the cloud size, and a file with the fitting results (if a fit is performed). This routine was written when I had a limited knowledge of Python and edited considering that the next user could also have little to no knowledge of the programming language, for this reason, it doesn't use high-level Python built-in functions. To keep Plot with average readable, three auxiliary files are used. **Function file** contains auxiliary functions, like ordering of 2D arrays, averages, and cuts out for the arrays, *etc.*[10]. **Function dictionary** contains the definition of the implemented fitting models, including the fitting function and a function to calculate the initial guess for the fits, and the calculation of the interesting parameters, e.g., expansion fits return directly the temperature in addition to the mean velocity. The functions defined within Function dictionary are listed in Appendix C. **Calibration** is a Python dictionary that, as mentioned earlier, contains the calibration for most variables scanned in the experiment. The relevant calibration is found automatically by Plot with average, on request, when the name of the scan parameter matches a key in Calibration.

Simpler analysis scripts are also realized ad-hoc for different situations, e.g. multi-shot routines for plotting together several runs either as separated scatter plots or as a 2D color plot, for plotting and fitting the position of the cloud (e.g. trap frequencies measurement, levitation calibration), *etc.*

The monitoring of the vacuum pressures instead is based on one single-shot and one multi-shot routine:

- **Lyse pressures** is a single-shot routine that opens a serial communication with the ultra-high vacuum (UHV) gauge controller to read and save the pressure readings to the .h5 file. The time of the reading is stored together with the reading, to account for possible delays or overwrites.
- **Plot pressures:** plots the pressure data from Lyse pressure as a function of either, shot number or absolute time. This helped for example to acquire data about an ion pump failure and correlate it with a drop in the atom number.

I wrote also a similar version of the *Lyse pressures*, independent of Lyse to help monitor the bake-out and detect early faults. In this case, the UHV gauges are read at regular intervals in time and the readings are stored in a log. A separate script can monitor the log from the gauge and from the ion pump (usually created through the Agilent Aplus software) and send out acoustic alarms based on the latest reading.

6.6 Additional remarks

For the sake of completeness, it is necessary to note that these changes took a really long time, almost one year was spent initially on the oven refurbishment and replacement, three years on rebuilding the laser setup and optimizing the sequence, and due to the successive vacuum problems the experiment is not yet up to its standards. The work presented in this section, with the exception of the oven replacement, and the optimization of evaporative cooling, has been carried out most

---

[10] These functions are defined on the basis of simple structures common to most high-level programming languages. This file could be largely replaced by introducing Python Numpy built-in functions but on the base of personal experience, I fear that doing so, and in general nesting specific built-in functions, would make the code more obscure for users that are not familiar with said functions.

of the time with only two Ph. D. students working on it, and what sums up to months of only a single person working in the lab, due to COVID-prevention measures and personal holidays. In these conditions, and despite weekly meetings with the full team working under the guidance of Prof. Nägerl, we incurred several difficulties.

For once, previous parameters and setup, which led to successful experiments and fundamental results for the ultracold molecules community such as Ref. [63, 31], were not sufficiently questioned. It is clear from the previous success of the project that the parameters and setup were good enough to make the experiment work, during the optimization we assumed they were also optimal. Under this premise, we worked from the perspective of only minor adjustments. An example of such behavior is what happened with the Zeeman slower, as mentioned in Sec. 6.4.2, where the detuning of the light was scanned in a small region around the previous value, not addressing that the final value is significantly smaller than in similar experiments. Similarly, the frequency of the repumper light for Zeeman has not been adjusted independently of the frequency of the MOT repumper light. Both topics have only in recent days become the object of further investigation.

A similar problem arose also regarding the calibration techniques. Such an example is represented anecdotally by the calibration of the homogeneous magnetic field. In the past microwave transfer between hyperfine states has been routinely used for calibrating the magnetic field as a function of the control software parameter in volts 3.5. The technique was typically applied to a BEC in the lattice. During rebuilding, after the failure and replacement of the driver for the coils generating said field, the same technique was applied to atoms in the reservoir trap since BECs were not available. On the hotter atoms, Stern-Gerlach separation yielded limited resolution. The calibration results were misinterpreted by observing the wrong atomic transition and consequently associating the control software parameters with the wrong field. This led us to underestimate for months the homogeneous magnetic field by a factor of 3. The impossibility of quickly finding a calibration of the field as a function of the current in the coils contributed to the error, typical past calibrations on the RbCs experiment only reported the field as a function of the software parameters. In this case, some checks were also disregarded too quickly, like the erroneous interpretation of a Cs FR at 120-G in place of the 48-G resonance. In the end, the mistake was solved by calculating anew the expected field, switching to radiofrequency calibration, after building an ad-hoc antenna, and cross-checking the calibration with detailed scans of four Feshbach resonances.

The difficulty in finding proper documentation made it necessary sometimes to reconstruct well-known information from first principles, like in the above-mentioned field calibration as a function of the current or the use of the fluorescence photodiodes.

Finally, another obstacle was the use of complex hand-soldered electronic devices that were near-impossible to debug (the coil driver mentioned above was one of them), and hand-modified electronic devices with insufficient documentation of the changes.

6.7 Conclusion

The changes in the infrastructure for the experiment, with the introduction of high-power lasers for the cooling transition of Rb and Cs, helped to reduce the complexity of the experimental setup and the maintenance time. In addition, the new laser system made available a small but relevant amount of extra power available for the individual cooling steps, that would have otherwise required sacrificing the beam size or beam independence, e.g. retroreflecting MOT beams. The new conditions triggered the revisitation and optimization of the full experimental sequence. The optimization, facilitated by the introduction of real-time analysis through a series of dedicated scripts, led to the creation of very stable MOTs of Rb and Cs, both with slightly larger atom numbers than provided by the previous setup. The revisitation of the experimental sequence confirmed the known interplay between the different cooling and trapping steps, and it highlighted once more that the simultaneous cooling of Rb and Cs requires a delicate equilibrium. The comparison of the cloud properties at different steps shows that while Rb, if loaded alone, could still be improved by improving the MOT, this is not straightforward when loaded in the presence of Cs, with the number being limited in the reservoir trap. On the contrary, Cs cooling is improved by the presence of Rb, but due to saturation effects in the reservoir it appears unlikely it would be improved proportionally to an improvement in the number in the MOT. Although it was not possible to finalize the optimization with the creation of BECs or molecules due to vacuum problems, I am confident that the detailed work done on controlling all the experimental parameters will lead to a successful continuation of the experiment. As a note to future students I would encourage them when embarking on such an effort to distribute the work with one person constantly monitoring the conditions of the old setup, one person working on the new setup, and one person assisting on either side. The most difficult part is certainly to find the right balance between questioning the previous parameters, and at the same time not reinventing the wheel at every step. This requires a great deal of experience in the field, especially in the case previous parameters were good enough to make the experiment work and lead to spectacular results. In addition, it will not be stressed enough that whenever such an effort is taken, or a new technique is introduced in the lab, it is also necessary to take the time to properly document it. I have seen this task sometimes pushed on the youngest students because as everything is new to them they will eagerly get into a great length of details, it would be appropriate that in a second step, someone with experience also goes through it to make sure that no important information or more subtle, but crucial, detail has been omitted.

Chapter 7

Conclusions and outlook

7.1 Conclusions

During the course of this thesis, the discussion took two main directions, on one hand, great attention has been given to the protocol for mixing Rb and Cs in the optical lattice, which makes use of superfluid transport of Rb, while Cs is held in a Mott insulator to suppress interactions. On the other hand, the experimental apparatus and data analysis have been made significantly simpler thanks to several targeted interventions.

I investigated in detail the stability of the Mott insulator of Cs, focusing on the regime where the scattering length is comparable to the harmonic oscillator length, and I showed the emergence of inelastic confinement-induced resonances due to the confinement from the lattice. These are due to the coupling between the relative motion and center-of-mass motions. The identification of the exact relative motion and center-of-mass motion states involved in the resonances led to the observation of excitation in the Mott-insulator including the presence of atoms in excited bands and possibly doubly occupied sites. The presence of excitations can explain the short lifetime of the Mott insulator, and the considerable losses observed during the time it takes to transport Rb. Part of these results led to the work of Ref. [74].

The efficiency of Rb transport has been reviewed, with particular attention again to the role of the confinement. In this case, I focused on the confinement from the transport trap and its interplay with the lattice depth. The data showed the presence of a lower and maximum trap frequency for transport. Contrary to the interpretation of Ref. [124], I did not identify an optimum transport regime, but just an optimum frequency with respect to the number of transported atoms. The analysis used a numerical simulation of the one-dimensional time-dependent Gross-Pitaevskii equation to introduce some experimental conditions. Although on a fairly qualitative level, this analysis showed that the emergence of a lower critical trap frequency could be attributed to at least two possible causes: the presence of an energy gradient along the transport direction, and the possibility of an inhomogeneity of the lattice, the latter was simulated with the addition of a modulation on the lattice amplitude.

During my Ph.D. work, the experimental apparatus has been largely revisited. The oven has been replaced with a temporary design that grants a higher flux of atoms. Two high-power lasers have been introduced that emit at the atomic D2 cooling transition for both Rb and Cs. These lasers helped to greatly simplify the experimental setup by allowing the removal from the experiment of one master laser, four slave lasers, and a tapered amplifier. Consequently, a large number of optical elements and electronic devices have also been removed. The introduction of real-time data analysis, in contrast to post-processing, sped up daily operations and allowed for an in-depth characterization of the experimental sequence. The changes to the experimental setup and sequence led to stable experimental conditions in the stages investigated (up to the loading of the dimples) and the maintenance time was reduced significantly. The change highlighted a few problems with previous documentation and the definition of lab procedures. These have been addressed by revising entirely the documentation of the measurement and with new calibrations, in particular, the data storage system has been reviewed contextually to the introduction of the live data analysis. The atom number and atomic temperatures in the cooling stages investigated, although worse than in other similar experiments, are comparable to or slightly better than what was achieved in the same project with the previous setup. In addition, the reproducibility of the experimental conditions has improved on a shot-to-shot basis. The improved stability together with the better understanding of the confinement creates a strong basis for the future investigation of dipolar physics with RbCs molecules.

7.2 Outlook

7.2.1 Dynamics of atoms and molecules association on ICIR

In Chapter 4, I showed that inelastic confinement-induced resonances in a Mott insulator with predominant single occupancy of the lattice sites match energetically the case of doubly occupied sites. This energy mismatch opens a lot of questions on the underlying dynamics and the presence of defects and excitations in the Mott insulator. Repeating the measurements with different initial conditions and comparing the dynamical loss and heating rate can help to elucidate the kind of excitations that lead to the detection of the resonances and improve the understanding of the dynamics in the optical lattice. Among the excitations detected in the ICIRs measurements is the presence of atoms in excited lattice bands. This could be particularly crucial for the RbCs project. The higher the band of the optical lattice the atoms are in, the higher the mobility of the atoms, hence the frequency of three-body recombination events can increase significantly. A better understanding of the excitations of the atoms to higher optical lattice bands can be beneficial both for improving the stability of the Mott insulator and lowering the overall entropy of both the Cs sample and the molecular RbCs sample in the optical lattice. Understanding and controlling the excitations in the lattice is also crucial to the work with the molecules in view of the additional complexity deriving from the dipolar interaction term.

In general, inelastic confinement-induced resonances offer the possibility to engineer both the resonance position and the resonance strength. In this regard it would be interesting to probe in detail the coupling strength of these resonances and the possibility of tuning the scattering length, one way would be to investigate that through second-order processes in the lattice similar to Ref. [172].

The results presented here are for Cs only and the coupling between center-of-mass and relative motion comes only from the anharmonicity of the lattice. In the presence of heteronuclear scattering the coupling strength between center-of-mass and relative motion is further enhanced by the mass imbalance and the different polarizabilities. Thanks to this, ICIRs can open a new way to form heteronuclear molecules in the optical lattice and hold great promise for the formation of molecules in optical tweezers in processes like mergoassociation [170].

7.2.2 Improving the efficiency of superfluid transport

In Chapter 5, I showed the presence of a lower and upper critical trap frequency for coherent transport of Rb atoms. The identification of the possible reasons behind the limitation of transport at low trap frequencies, achieved through the numerical simulations, provides an immediate way to improve the performance of the transport. The magnetic anti-trapping potential, which is the more likely cause of inefficient transport at low trap frequencies, can be compensated with the introduction of an optical potential. Alternatively, the tracking coils can be used to move the center of the quadrupole field in the horizontal plane in such a way that it follows the Rb dimple, this will require a characterization of the effect of the deriving tilting on Cs atoms. The homogeneity of the depth of the OL can be improved by ensuring the mechanical stability of the system and by reducing the interference between orthogonal beams.

The upper trapping frequency for transport is significantly lower than the predictions. A possible candidate to explain it is the dimensionality of the system. A systematic study of transport efficiency as a function of the angle between the transport direction and lattice axes, or of transport in anisotropic lattices can be the key to understanding the role of dimensionality and second-order tunneling processes that allow the atoms to move diagonally in the lattice. It would also be interesting to repeat the experiment with Cs to investigate experimentally the role of interactions on the transport properties and to repeat the experiments with different condensate fractions.

However, improving the lower or upper critical trapping frequency for the superfluid transport only leads to a limited gain in transport efficiency. A much bigger improvement can be achieved with the introduction of the short-cut-to-adiabaticity methods that have been proposed in recent years for both atoms and ions [206, 207]. These methods find the shorter trajectory between the initial and final state without the constraint of remaining in a well-defined eigenstate of the systems. Such methods, not only can improve the efficiency of transport of Rb but they would also cut down significantly the transport time, therefore only limited losses in the Cs Mott-insulator would take place during the transport. A detailed understanding of the potential landscape is instrumental to short-cut-to-adiabaticity techniques and the results of this thesis constitute the first step in that direction.

7.2.3 Additional upgrades stemming from the new laser system

The introduction of the new high-power lasers presented in Chapter 6 improved significantly the stability and reduced the maintenance time on a daily basis. However, the number of atoms in the MOT is smaller than in other experiments, in the case of Rb by almost an order of magnitude). As mentioned in Sec. 6.6, the frequencies of the beams for Zeeman cooling and repumper might be sub-optimal. Revising this step could potentially lead to an increase in the atom numbers in the

MOT, although at this stage it is unclear how much of such improvement would transfer to the next cooling steps.

An important feature of the new Rb laser system that has not been used is that it also outputs the residual light that has not been doubled in frequency. As a matter of fact, the laser emits up to 15 W at 1560 nm, in addition to the 780-nm output discussed in Chapter 6. Such light could be used for an additional dipole trap or optical lattice beams. A few applications would be the creation of an optical potential to compensate for the magnetic gradients as discussed in the previous subsection. A two-dimensional optical dipole trap that enables evaporation and condensation of polarized molecules similar to the procedure of Ref. [29]. The formation of a one-dimensional or two-dimensional lattice for the realization of new quantum phases [20].

7.2.4 One-dimensional samples and alternative mixing schemes

One of the possible directions for future research in the RbCs project is the confinement of the molecules in one-dimensional tubes, rather than a cubic lattice. Experimentally this could be achieved by reducing the power of one of the lattice beams while increasing the power of the other beams to increase the perpendicular confinement. In such a way, a trap depth $> 30\,\mathrm{E}_{\mathrm{rec}}^{\mathrm{Cs}}$ could be achieved in the transversal direction. In the one-dimensional confinement, a dipolar gas at zero temperature is expected to enter different regimes including the formation of a Tonks Girardeau gas and crystal phase [208], which has not yet been investigated with dipolar heteronuclear molecules. In addition, the presence of dipolar interactions modifies the position of confinement-induced resonances enriching the scattering properties of the sample [209, 139]. Even more interesting in the one-dimensional geometry is the possibility of the formation of clusters between tubes due to the long-range character of the dipolar interactions, this possibility has no analog with alkali atoms in typical optical lattices [210].

7.2.5 Ultracold dipolar molecules as a playground

The changes to the experimental apparatus and data analysis, which enhance the stability of the experiment, should culminate with the possibility of having samples of Feshbach molecules reliably on a daily basis. After the experiment has undergone the necessary vacuum maintenance, the immediate next step would then be combining the mixing in the optical lattice with the application of STIRAP to achieve ground-state molecules. These steps seem easily within reach, considering that STIRAP was previously tested in the RbCs project (when associating the molecules in the bulk close to the 190-G resonance) and held transfer efficiencies of the Feshbach molecules to the rovibrational ground state above 90% [31]. In addition, STIRAP had been applied to molecules formed on the 355-G resonance [169]. Polarization of the ground state molecules in the laboratory frame can be achieved by the use of electrodes, which are already installed around the cell. The installation of an appropriate microwave source is also in the plans.

The big missing milestone in the field of ultracold dipolar molecules is without a doubt a Bose-Einstein condensate of dipolar molecules. So far two experiments have shown the possibility to reach a degenerate Fermi gas of molecules, through the employment of shielding techniques [29, 46, 30]. Very recently evaporative cooling of dipolar molecules with microwave shielding has been successfully applied to bosonic molecules as well [49, 50]. In the RbCs project, the most obvious pathway to the formation of a BEC would be to form the molecules in the lattice and then remove the lattice adiabatically, to release the atoms to a ODT. A proper choice of the ODT geometry could lead directly to condensation. Alternatively, electric field or microwave shielding can be used to perform evaporative cooling in the ODT until degeneracy is reached. In particular, the parameters for microwave shielding for RbCs ground state molecules have already been calculated in Ref. [211].

The stronger point of the RbCs project in Innsbruck remains undoubtedly the possibility of forming molecular samples directly in the optical lattice, with very low entropy. This is well suited for the investigation of new quantum phases [20, 212, 213, 214] quantum magnetism phenomena [58] and for the implementation of quantum simulations [54].

Appendices

Appendix A

Optimal parameters

This appendix summarizes the value obtained in the optimization of the experimental sequence described in Chapter 6 and updated to March 2023. The appendix composes of two tables, one for the magnetic fields and one with the light intensities and oven temperatures. The parameters extend only up to the loading in the reservoir trap, as the loading of the dimples needs revision.

Parameter	Optimal
Zeeman	
Zeeman coils current 1,6	2.5 A
Zeeman coils current 2-5	2 A
MOT	
Homogeneous field MOT	0 G
Quadrupole field MOT	5.77 G/cm
Compression	
Quadrupole compression MOT	18.32 G/cm
Raman	
Z-offset field initial	0.48 G
Z-offset field final	0.32 G
Reservoir	
Homogeneous field reservoir	42 G

Table A.1: Magnetic field for the sequence steps, following the optimization of the sequence (Updated to February 2022).

Parameter	Rb	Cs
Ovens		
T Oven	$60\,^{\circ}C$	$60\,^{\circ}C$
T Mixing chamber	$100\,^{\circ}C$	
Zeeman		
Zeeman intensity	14.3 mW	5.29 mW
Zeeman frequency	-22 MHz	-20 MHz
Zeeman repumper intensity	1.3 mW	2.55 mW
Zeeman repumper detuning	-21 MHz	$+12$ MHz
MOT		
MOT intensity (overall)	143 mW	92 mW
MOT frequency	-24 MHz	-6.5 MHz
MOT repumper intensity	20 mW	16.5 W
MOT repumper detuning	-21 MHz	$+12$ MHz
Compression		
Compression intensity (overall)	143 mW	92 mW
Compression frequency	68 MHz	-26 MHz
dRSC		
Lattice intensity	199 mW	80 mW
Lattice frequency	-21 GHz	9 GHz
Polarizer intensity		$164\,\mu$W
Polarizer frequency	0 MHz	$+14$ MHz
Depumper intensity	$370\,\mu$W	—
Depumper frequency	-330 MHz	—
Pulse duration	10 ms	
Ramp-up time	0.1 ms	
Ramp down time	0.3 ms	
Reservoir		
Reservoir initial power	35 W	

Table A.2: Parameters for Rb and Cs following the optimization of the sequence (Updated to February 2022)

Appendix **B**

Scripts

B.1 Pressure monitors

In response to the numerous problems with the vacuum system on the oven side and the malfunctioning of the ion pump on that section, I develop a few tools to monitor pressures. One set of scripts works in conjuction with the agilent softare 'Aplus' and has the ability to monitor the pressure remotely and set up alarms. A separate script records the pressures from the gauge through lyse and allows correlating the reading with the data acquisition.

The remote monitoring splits uses four parts.

- A log file for the ion pump, created through the software 'Aplus' for the ion pump controller
- A log file for the independent vacuum gauges, I create by serial communication with the gauge reader
- Two periodic check, one for each of the log files with the ability to trigger alarms.

The log files are saved on the shared folder in the ZID Server, so that through a VPN connection they can be easily read from outside the university. The alarm works better if located on the remote computer as it uses bash commands on the operative system. Here, I will discuss the log file from the gauge reading and the alarm based on that. The alarm based on the ion pump log is fairly similar.

B.1.1 Gauge reading and log file

The idea is to set up a serial communication with the gauge reader, for that the Python library `serial` is used. In order to set up the communication it is necessary to know the COM port number on which the gauge reader is connected, when in doubt the list of ports can be obtained in Python with the following lines:

```
from serial.tools import list_ports as pl

ports=list(pl.comports())
```

```
for p in ports:
        print(p)
```

Serial communication works in two steps; First a message is output from the computer on the COM, this is the command to be executed by the instrument in this case 'read gauge filament'. Then the computer waits for an input from the COM port, in this case, the pressure value. In the script for the log, the two commands are sent in a while loop broken only by a keyboard interrupt. I show here the full code, and below is a breakdown of the main parts.

```
import serial
from datetime import datetime
import time
path='//zidshare/rbcs/Exp_Data/IonPumps/22-05-05_Pressure_logs/'
filename='Pressure_gauge_Log_1.txt'
now = datetime.now() # current date and time
year = now.strftime("%Y")
month = now.strftime("%m")
day = now.strftime("%d")
filename=filename+'_'+day+'-'+month+'-'+year

log_file=open(path+filename,'w')
log_file.write('Log␣Journal␣for␣pressure␣gauge␣\n␣HFIG1\t␣HFIG2\t␣datetime\n')
print('program␣running,␣press␣Ctrl+C␣to␣terminate')
try:
    while True:

        with serial.Serial(port='COM3',baudrate=9600,bytesize=8,timeout=1,
        stopbits=serial.STOPBITS_ONE) as ser:
        #    print(ser)
            ser.write('#0002UHFIG1\r'.encode('ascii'))
            HFIG1=ser.read(1000)
            ser.write('#0002UHFIG2\r'.encode('ascii'))
            HFIG2=ser.read(1000)
            ser.close()

            log_file = open(path+filename,'a+')
            log_file.write(str(HFIG1)+'\t'+str(HFIG2)+'\t'+
            datetime.now().strftime("%Y-%m-%d␣%H:%M:%S")+'\n')
            log_file.close()
            time.sleep(5)
except KeyboardInterrupt:
    log_file.close()
    pass
```

Libraries

```
import serial
from datetime import datetime
import time
```

- **Serial** for serial communication through the COM port with protocol RS-232.
- **Datetime** to record the current time for the log file
- **Time** to delay the next log entry.

Creation of the log file

```
path='//zidshare/rbcs/Exp_Data/IonPumps/22-05-05_Pressure_logs/'
filename='Pressure_gauge_Log_1.txt'
now = datetime.now() # current date and time
year = now.strftime("%Y")
month = now.strftime("%m")
day = now.strftime("%d")
filename=filename+'_'+day+'-'+month+'-'+year
log_file=open(path+filename,'w')
log_file.write('Log␣Journal␣for␣pressure␣gauge␣\n␣HFIG1\t␣HFIG2\t␣datetime\n')
print('program␣running,␣press␣Ctrl+C␣to␣terminate')
```

Path and filename select the location and name of the destination file. When the program starts, the name of the file is modified to incorporate the current date, this is a precaution to avoid overwriting the same log file. A title line and the three columns identifier are added at the top of the log file. A reminder is shown in the terminal on how to terminate the log with the keyboard interrupt.

The while loop

```
    while True:

        with serial.Serial(port='COM3',baudrate=9600,bytesize=8,timeout=1,
        stopbits=serial.STOPBITS_ONE) as ser:
            ser.write('#0002UHFIG1\r'.encode('ascii'))
            HFIG1=ser.read(1000)
            ser.write('#0002UHFIG2\r'.encode('ascii'))
            HFIG2=ser.read(1000)
            ser.close()

            log_file = open(path+filename,'a+')
            log_file.write(str(HFIG1)+'\t'+str(HFIG2)+'\t'+
            datetime.now().strftime("%Y-%m-%d␣%H:%M:%S")+'\n')
            log_file.close()
            time.sleep(5)
```

Serial.Serial sets up the properties of the communication, all the necessary parameters can be found on the manual of gauge reader [1]. The commands are also reported on the manual.

In turn, filament 2 of gauge 1 (UHFIG1) and gauge 2 (UHFIG2) are read. After writing each request through ser.write, the program waits for the answer from the gauge reader and stores the answer on the respective variable. The reading is in a string form with special characters for the beginning and the end of the string. After receiving the two values, the program opens the log file and updates it with the two strings containing the pressure values and the current time. The file is closed, to be accessible from the alarm program discussed below. Through time.sleep it is possible to select the time (in seconds) before the subsequent execution of the while loop.

Terminating the log file

---

[1] `https://www.agilent.com/cs/library/usermanuals/public/Copy%20of%20XGS-600%20Gauge%20Controller.pdf`

```
    except KeyboardInterrupt:
    log_file.close()
    pass
```

In the case of a keyboard interrupt (Ctrl+C), the while loop is broken and the closing instruction for the log file is sent again for safety.

Gauge reading in Lyse

The gauge reading for Lyse works in a similar way, with the main difference being that instead of a continuous reading through the while loop, there is a single iteration of the reading. Therefore I will not discuss the detailed code breakdown, but just give a quick overview of the parts. First, the program ensures that Lyse is running. Then it communicates with the gauge reader, storing temporarily the results in Data1 and Data2. Next, the reading is converted to a float, after removing the special characters. The floats corresponding to the pressures are written in Lyse pandas dataframe. Finally, the time of the reading is added to the dataframe.

```
import lyse
from pathlib import Path
import serial
import h5py
import numpy as np
import time
from datetime import datetime
start=time.time()
if lyse.spinning_top:
     # If so, use the filepath of the current shot
     h5_path = lyse.path
else:
     # If not, get the filepath of the last shot of the lyse DataFrame
     df = lyse.data()
     h5_path = df.filepath.iloc[-1]
run = lyse.Run(h5_path)
# try:
#     glob=run.get_results('Lyse_pressures')
#     print(glob[:])

# except:
#     print('It did not work')
with serial.Serial(port='COM3',baudrate=9600,bytesize=8,timeout=1,
stopbits=serial.STOPBITS_ONE) as ser:
        #    print(ser)
            ser.write('#0002UHFIG1\r'.encode('ascii'))
            Data1=ser.read(1000)
            ser.write('#0002UHFIG2\r'.encode('ascii'))
            Data2=ser.read(1000)
            ser.close()
print(type(Data1))
D1=str(Data1)
D1=D1.strip('b\'>')
D1=D1.strip('>')
D1=D1.strip('\\r\'')
HFIG1=float(D1)
D2=str(Data2)
D2=D2.strip("b\'>")
D2=D2.strip('/r\'')
D2=D2.strip('\\')
```

```
HFIG2=float(D2)
run.save_results('HFIG1',HFIG1)
run.save_results('HFIG2',HFIG2)

# run.save_results('HFIG1',1e-9)
# run.save_results('HFIG2',1e-11)


now=datetime.now()
#ts=datetime.timestamp(now)
run.save_results('Reading',now.isoformat())
```

B.1.2 Copy log and Alarm

In addition to logging the pressure, it might be necessary to keep a close eye on it and be ready to intervene on the system, e.g. during baking. In this case, it is useful to have an alarm set up if a parameter exceeds a safety value or when a certain benchmark has been achieved. The copy and log alarm does exactly this job. I wrote two very similar versions, one for the log file from the gauge and one for the log file from the ion pump. I describe here only the version used to monitor the gauge. The general idea of the code is quite simple. It makes a copy of the log file generated by the gauge reading, such that the original file can keep being updated live. If the copied file is read correctly the last line of the file is acquired and an alarm is triggered if at least one of the two pressures is too high. An alarm also goes off if it is not possible to read the original file or if the file has not been updated when it was supposed to. The alarms based on the reading and update are triggered by comparing the relative value to a typed in value. The alarm generated by a failed reading is triggered through a try-except structure.

```
import os
import time
i=0
import pathlib

from datetime import datetime as dt



import shutil
try:
    while True:
        try:
            original=pathlib.Path('Pressure_gauge_Log_1.txt')
            mtime = dt.fromtimestamp(original.stat().st_mtime)
            J=dt.now()-mtime
            #make copy
            target1='Gauge_Copy1.txt'
            target2='Gauge_Copy2.txt'
            shutil.copyfile(original,target1)
            shutil.copyfile(original,target2)

            #read last line
            os.system('cls')
            f=open(target1)
            Lines=f.readlines()
            A=Lines[-1]
            print(A)
```

```
            B=A.split('\t')
            D=B[0].strip("b>'")
            D=D.strip('/r')
            D=D.strip('\\')
            HFIG1=float(D)
            C=B[1].strip("b>'")
            C=C.strip('/r')
            C=C.strip('\\')
            HFIG2=float(C)

            #generate alarms
            print(J.total_seconds())
            if J.total_seconds()>60:
                print('Gauge␣Reading␣Stopped␣Running')
                os.system("start␣Alarm2.mp3")
            if HFIG1>3e-9 or HFIG2>1e-9:
                print('Highpressure␣in␣the␣main␣chamber!!!')
                os.system("start␣Alarm3.mp3")
            f.close()
            time.sleep(180)
        except OSError:
            print('Check␣Internet␣connection')
            os.system("start␣Alarm1.mp3")
            time.sleep(180)
except KeyboardInterrupt:
    pass
```

Libraries:

```
import os
import time
i=0
import pathlib

from datetime import datetime as dt
```

- **Os** is the library that helps to interface with the operative system of the computer, here it is used to call the shell terminal of the operative system and to run a command that corresponds to the alarm.
- **Time** contains time-related functions, here it is used to pause in between readings
- **Shutil** is a library that allows high-end operation on files or group of files, here it is used to make a copy of the original log file
- **Datetime.datetime** deals with dates, time stamps and time intervals, here it is used to check the file update

The try-except constructs

```
try:
    while True:
        try:
            original=pathlib.Path('Pressure_gauge_Log_1.txt')
...
         except OSError:
            print('Check␣Internet␣connection')
```

```
            os.system("start␣Alarm1.mp3")
            time.sleep(180)
except KeyboardInterrupt:
    pass
```

The outer try-except is used to introduce a keyboard interrupt from the user to break the while loop and terminate the program execution.

The inner try-except instead is used to trigger the alarm relative to problems with the reading of the original log file. This kind of problem generates an OS error in Python. Being the original log file located on the server, this alarm is typically triggered by problems relative to the VPN connection, the internet connection, or more rarely by problems of the server itself. The alarm itself is written on an operative system shell through `os.system()` method. In the example, it opens `Alarm1.mp3` with the default player.

Copy the file

```
            original=pathlib.Path(’Pressure_gauge_Log_1.txt’)
            mtime = dt.fromtimestamp(original.stat().st_mtime)
            J=dt.now()-mtime
            #make copy
            target1=’Gauge_Copy1.txt’
            target2=’Gauge_Copy2.txt’
            shutil.copyfile(original,target1)
            shutil.copyfile(original,target2)
```

The location of the original file is stored in `original`. To check that the file is being updated correctly, the timestamp from the last update is also acquired and stored as `mtime`. As seen in the previous section, the file content has four columns: one for each filament to show the reading, one with the date, and one with the time of the reading. An additional timestamp with the current time at which the loop is executed is also taken, to compare it with `mtime`. This is later used to trigger an alarm. The program creates two copies with destination `target1` and `target2`, through the `shutil.copyfile`. The redundancy is thought such that multiple people can also access the data and perform additional analysis without interfering with the original log file or with each other. The copies are overwritten at every execution of the while loop.

Read the pressure value

```
 #read last line
            os.system(’cls’)
            f=open(target1)
            Lines=f.readlines()
            A=Lines[-1]
            print(A)
            B=A.split(’\t’)
            D=B[0].strip("b>’")
            D=D.strip(’/r’)
            D=D.strip(’\\’)
            HFIG1=float(D)
            C=B[1].strip("b>’")
            C=C.strip(’/r’)
            C=C.strip(’\\’)
            HFIG2=float(C)
```

```
            print(J.total_seconds())
```

The program opens one copy to read the last line. The line acquired as a single string contains the reading from the gauge with the special character for start and stop from the COM port, the date and the time of the reading. The string is split in an array `B` of four strings. The strings corresponding to the pressure reading are stripped of the special characters and converted to float through the string method `strip`. The final float value is stored in `HFIG1` and `HFIG2` I start by clearing the shell of the terminal to prepare it to send messages if needed.

Alarms

```
  #generate alarms
            if J.total_seconds()>60:
                print('Gauge␣reading␣stopped␣running')
                os.system("start␣Alarm2.mp3")
            if HFIG1>3e-9 or HFIG2>1e-9:
                print('Highpressure␣in␣the␣main␣chamber!!!')
                os.system("start␣Alarm3.mp3")
            f.close()
            time.sleep(180)
```

The final part of the code generates the other two alarms. The first alarm, corresponding to the first `if`, is triggered if the last update of the original file was too old, in the example older than 60 s. This time should be adjusted to be reasonable with respect to the time intervals in the logging, at least 2-3 times the time interval. If the time interval between in the file log is short, it is necessary to remember that the gauge reading takes a finite time typically of the order of a second. Similar to the alarm for the OS Error, a missed update in the original file triggers an action specified through the `os.system()` method.

The second `if` corresponds to the alarm triggered by the pressure values. The reading stored in `HFIG1` and `HFIG2` are compared to threshold values. The thresholds should be adjusted according to the need of the application. If the values exceed the thresholds, a new instance of `os.system()` method is open.

For all the alarms in the example, different .mp3 files are started. This was quite convenient when moving away from the laptop and when it was necessary to monitor the parameters at night.

B.2 Plot with Average

Plot with average is a script to use in everyday live analysis of the data that does exactly what the name suggests, it takes the data for either species relative to atom number or cloud size, it optionally averages them over multiple repetitions, plots them, and on request fits them with one out of several options. As a general remark, the parameters in Plot with average are set in such a way that they do not need to be changed at every run, but just when different kinds of analysis are performed, since the run details are imported from an external parameter file.

The output consists of:

- two figures, one with the plot of the atom number for both species, one with two plots side by side reporting the x and y size of the cloud respectively for Rb and Cs.
- a text file containing the raw data or the average data with their standard deviations.
- a text file containing the fit results if a fit was applied.

B.2.1 Libraries

```
import sys
sys.path.insert(1,'//zidshare/rbcs/Lab/scripts/Python/plot_wAverage')
import functionfile as fl #contains auxiliary functions
import function_dictionary as my_dict #contains the definition of the
fitting models
import Param
from datetime import datetime
from scipy import optimize as ft #for fitting
import numpy as np
import matplotlib.pyplot as plt
```

The script uses:

- **sys** to add a path the list of directory where Python scans for files. This is used to import the auxiliary files:
  - **functionfile** contains auxiliary custom functions for sorting and averaging the data.
  - **function dictionary** contains the custom defined fitting models.
  - **Params** contains the parameters for the current measurement, this file is updated for every experimental run.
- **datetime** is used for the current date
- **scipy.optimize** is a standard Python package for fitting
- **numpy** is the standard Python package for array manipulations and mathematical functions
- **matplotlib.pyplot** is the standard Python package for plotting.

Parameters

The initial part of the code, contains all the variable relative to the data selection and the kind of analysis to perform. This is the only part that need to be changed on a day-to-day bases.

```
    ###Parameters###
#data source
Loading_from_Lyse=True
#when loading from Lyse
select_by_sequence=False
select_by_measnr=True #possible only when working in combination with
add measnr script
SequenceStart=10
SequenceEnd=np.inf
```

```
ParDict=Param.ParDict
if select_by_measnr==True:
    MeasNr=’M’+str(ParDict[’MeasNr’])
    #MeasNr=’M2’
else: MeasNr=’_’
#MeasNr=’M13’

#Measurement details
scan_variable=True
scanned_variable=ParDict[’Scan_variable’]
#scanned_variable=’Rb polarizer detuning (V)’
Title=’Temperature’
```

The program asks to confirm Lyse as the source of the data (a different version can take as input previous data from file). Within Lyse it can select data based on the shot number `select_by_sequence` or by the run identifier `select_by_meas_nr`. In the first case, the initial and the final shot number can be chosen and all data in that interval are plotted. For constantly updating data it is possible to set the end point to infinity (`np.inf`). This option is useful for stability checks, warm-up of the experiment, or when scanning manually a variable which is not controlled from the control software.

The second option allows to crop the data according to a run identifier `Meas_Nr`. This identifier is typically associated with the experimental run, the current run can be selected by reading the number directly from the parameter file or a previous run can be reloaded for the analysis by typing in the identifier, to change between the two it is necessary to comment uncomment the relative line. Analogously the name of the variable scanned during the run can be read from the parameter file for the current run or typed in manually for previous runs.

```

#Analysis
Rb_on=True
Cs_on=True
PlotNsum=True
Plotrms=True
```

Successively a series of boolean variables select the species to plot, Rb and or Cs, and the variable to plot for each species selected between atom number and cloud size.

```
Average=True
FitModel=False
Model=1
        #0=Loadingrate
        #1=Temperature
        #2=Lorentzian
        #3=Expdec1
        #4=Linear_Temp
ExcludePoints_From_plot=[’CsNROISum␣<␣0’] # ,’CsyRMS_radius_um > 3000’
ExcludePoints_From_Rb_plot=[’None’] # CsNROISum ’X > 3’ #works but slow
ExcludePoints_From_Cs_plot=[’None’] # CsNROISum ’X > 3’ #works but slow
ExcludePoints_From_Rb_fit=[’None’]# spaces are important!!!
ExcludePoints_From_Cs_fit=[’None’]
```

Boolean variables are also used to indicate if the data should be averaged, in which case the plot will show directly the mean and standard deviation of the data, and if the data should be fitted. A numerical value selects the fitting model. Currently, five models have been implemented as shown in the commented list, the definition of the corresponding fitting functions can be found in Appendix C. It is possible to exclude some data from the plot or the fit, if it is easier to identify wrong shots or if it is expected that the model would be appropriate only in a certain interval. The exclusion condition, e.g. ExcludePoints_From_Cs_fit, should be written as ‘variable’ ‘criterion’ ‘threshold’, always including the space between each element, e.g., CsNROISum $<$ 0 will exclude all Cs points for which the estimated atom number is negative, which are clearly unphysical and derive typically from imaging problems.

```
#saving options
Save=True
Save_data_to_file=True #use only one time per measurement
Save_path=Param.Folder
#Save_path='//zidshare/rbcs/Exp_Data/Homogeneous field Coils
/21-02-19_Calibration_with_Imaging/'
Save_filename=str(MeasNr)+scanned_variable
```

Finally, there are the saving options, booleans specify if the plots should be saved and if a text file with the data should be saved. The output path can be read from the parameter file, which is set to the folder for the current day or alternatively it can be typed in manually. The file name is generated automatically as the run number followed by the scanned variable. Later in the code, to the file name are added suffixes for average or raw data, for the species if only one species is selected, and the current date.

Safety checks

```
    ndefinedmodel=5
#########################################
#%%


#verify that only one option is selected
Check_loading=Loading_from_Lyse+Loading_from_file
if Check_loading==0:
    sys.exit('No␣data␣source␣selected')
if Check_loading>1:
    sys.exit('Multiple␣data␣sources␣selected')

#verify if fitting that the model is known
if FitModel==True:
    ModelKnown=False
    for i in range (0,ndefinedmodel):
        if Model==i:
            ModelKnown=True
    if ModelKnown==False:
        sys.exit('Fitting␣model␣not␣defined')

Check_data=Rb_on+Cs_on
if Check_data==0:
    sys.exit('No␣species␣selected')

#Add details and date to filenames
if Rb_on==False:
    Save_filename=Save_filename+'_Cs_Only'
if Cs_on==False:
    Save_filename=Save_filename+'_Rb_Only'

now = datetime.now() # current date and time
year = now.strftime("%Y")
```

```
month = now.strftime("%m")
day = now.strftime("%d")
Save_filename=Save_filename+'_'+day+'_'+month+'_'+year
```

There are a few safety checks used to prevent the program from running into errors and to output appropriate warnings. If a check fails the program stops running.

The checks are meant to ensure that a proper source is selected for the data (Check_loading, check that the selected fitting model is defined (ndefinedmodel and ModelKnown), check that at least one species is selected for display (Check_data). The filename is modified to specify the species if only one species is selected, this is usefull in the rare occasion that the number data needs to be displayed separately, the same run will keep exactly the same designation but a different suffix indicating the species. The current date is added to the name of the plots, this is done to prevent accidental overwriting if the user forgot to change the folder in Params.

Loading and selecting the data from Lyse

```

#loading from lyse
if Loading_from_Lyse==True:
    import lyse

    df=lyse.data()
        Check_select=select_by_sequence+select_by_measnr
    if Check_select==0:
        sys.exit('No␣criteria␣for␣data␣selection␣in␣Lyse␣Matrix')
    if Check_select>1:
        sys.exit('Multiple␣criteria␣for␣data␣selection␣in␣Lyse␣Matrix')


    if select_by_sequence==True:
        df = df[df['sequence_index']>SequenceStart]
        df = df[df['sequence_index']<SequenceEnd]
    if select_by_measnr==True:
        df = df[df['Add_MeasNr_beta']['MeasNr']==MeasNr]
        #df2=df[df['Add_MeasNr_beta']['MeasNr']=='M3']
        #df=np.append(df1,df2,axis=0)
    sz=np.shape(df)
    if scan_variable ==True:
        Data=np.append(np.reshape(df['X'].values,(sz[0],1)),
        np.reshape(df['CsNfit'].values,(sz[0],1)),axis=1)

    else :
        Data=np.append(np.reshape(df['sequence_index'].values,(sz[0],1)),
        np.reshape(df['CsNfit'].values,(sz[0],1)),axis=1)
    Data=np.append(Data,
    np.reshape(df['RbNfit'].values,(sz[0],1)),axis=1)

    Data=np.append(Data,
    np.reshape(df['CsxRMS_radius_um'].values,(sz[0],1)),axis=1)
    Data=np.append(Data,
    np.reshape(df['CsyRMS_radius_um'].values,(sz[0],1)),axis=1)
    Data=np.append(Data,
    np.reshape(df['RbxRMS_radius_um'].values,(sz[0],1)),axis=1)
    Data=np.append(Data,
    np.reshape(df['RbyRMS_radius_um'].values,(sz[0],1)),axis=1)
```

In the case that the data are loaded from Lyse. The Lyse library is imported. This contains the methods to read the dataframe from lyse. The whole Lyse dataframe is initially stored in df. An additional safety check is performed here to ensure either select_by_sequence or select_by_measnr is selected, but not both. The dataframe is then cropped according to the chosen criterion, starting from the data an array Data is built adding the columns one by one. Typically, the atom number is associated with the result from the fitting in the image evaluation program XXNfit where XX stands here for Rb and Cs. If the cloud is not fitted properly it might be convenient to swap this parameter with the direct sum over the pixels XXNROISum.

```
if Average==True:
    mat=fl.average_data(Data)
    suffix='av'
else:
    mat=Data
    suffix='raw'
```

If the average is selected the data are averaged, through fl.average_data contained in the function file. The corresponding suffix is attached to the filename.

```
    if Loading_from_Lyse==True:
    if PlotNsum==True:
        if Rb_on==True:
            N_Rb=mat[:,2]
        if Cs_on==True:
            N_Cs=mat[:,1]
    if Plotrms==True:
        if Rb_on==True:
            rx_Rb=mat[:,5]
            ry_Rb=mat[:,6]
        if Cs_on==True:
            rx_Cs=mat[:,3]
            ry_Cs=mat[:,4]
if Average==True:
    if Rb_on==True:
        N_Rb_err=mat[:,9]
    if Cs_on==True:
        N_Cs_err=mat[:,8]

if Average==True:
    if Rb_on==True:
        rx_Rb_err=mat[:,12]
        ry_Rb_err=mat[:,13]
    if Cs_on==True:
        rx_Cs_err=mat[:,10]
        ry_Cs_err=mat[:,11]
x1=mat[:,0]
```

To make the code consistent with different data sources, here not discussed, after the average the columns are split into separate arrays and named accordingly to the content. The names for the standard deviation are added within the if, this a simple way to acknowledge that the Data array has a different number of columns if the average and standard deviation are calculated.

Number plot

```
    if PlotNsum==True:
```

```
fig1, axN = plt.subplots(1,1)

if Average==True:
    if Cs_on==True:
        if Loading_from_Lyse==True:
            axN.errorbar(x1,N_Cs,yerr=N_Cs_err,marker=’o’,
            linestyle=’None’,label=’Cs’,markerfacecolor=’coral’,
            markeredgecolor=’saddlebrown’,ecolor=’saddlebrown’,capsize=2)

    if Rb_on==True:
        if Loading_from_Lyse==True:
            axN.errorbar(x1,N_Rb,yerr=N_Rb_err,marker=’o’,
            linestyle=’None’,label=’Rb’,markerfacecolor=’dodgerblue’,
            markeredgecolor=’midnightblue’,ecolor=’midnightblue’,
            capsize=5)
else:
    if Cs_on==True:
        axN.scatter(x1,N_Cs, marker=’o’,linestyle=’None’,label=’Cs’,
        color=’coral’,edgecolor=’saddlebrown’)
    if Rb_on==True:
        axN.scatter(x1,N_Rb, marker=’o’,linestyle=’None’,label=’Rb’,
        color=’dodgerblue’,edgecolor=’midnightblue’)
```

A plot of the atom number is created at this point, if it has been selected in the parameters section. The plot is based either on `plt.scatter` or `plt.errorbar` depending if the data are raw or averaged. Which species is plotted is also decided according to the data selection parameter, it could be Rb or Cs or both. The colors are assigned by default according to the usual laboratory color scheme: blue shades for Rb and orange shades for Cs.

```
scanned_variable=scanned_variable[::-1].replace(’_’,’)’,1)
scanned_variable=scanned_variable.replace(’_’,’(’,1)
scanned_variable=scanned_variable[::-1].replace(’_’,’␣’)

axN.set_xlabel(scanned_variable)
axN.set_ylabel(r’Atom␣number␣(fit)’)
axN.legend(loc=’upper␣right’)
plt.show()
```

The label for the horizontal axis is derived from the ’scanned variable’ if assigned, as mention in the beginning the last two underscores ’_’ are replaced with round brackets, and should be placed around the units for the axis, all other underscores are interpreted as space. So for example: `Repumper_power__mW_` becomes "Repumper power (mW)". The label for the vertical axis is always "Atom number".

Cloud size plot

```
if Plotrms==True:
fig2, axs = plt.subplots(1,2,gridspec_kw={’width_ratios’: [5, 5]})
if Cs_on==True:
    if Average==True:

        axs[0].errorbar(x1,rx_Cs,yerr=rx_Cs_err,marker=’o’, label=’Cs␣x’,
        linestyle=’None’, markerfacecolor=’orangered’,
        markeredgecolor=’saddlebrown’,ecolor=’saddlebrown’,capsize=2)
        axs[0].errorbar(x1,ry_Cs,yerr=ry_Cs_err,marker=’o’,
        linestyle=’None’, label=’Cs␣y’, markerfacecolor=’orange’,
```

```
            markeredgecolor='saddlebrown', ecolor='saddlebrown', capsize=2)

        else:
            axs[0].scatter(x1,rx_Cs,marker='o',label='Cs␣x',linestyle='None',
            color='orangered',edgecolor='saddlebrown')
            axs[0].scatter(x1,ry_Cs,marker='o',linestyle='None',
            label='Cs␣y',color='orange',edgecolor='saddlebrown')

        axs[0].set_xlabel(scanned_variable)
        axs[0].set_ylabel(r'rms␣radius␣($\mu␣m$)' )
        axs[0].legend(loc='upper␣left')

    # axs[2].plot(x1,RbN_x_fit,label='Rb x fit',color='darkblue')
    if Rb_on==True:
        if Average==True:
            axs[1].errorbar(x1, rx_Rb,yerr=rx_Rb_err,label='Rb␣x␣fit',
            marker='o',linestyle='None',markerfacecolor='darkblue',
            markeredgecolor='midnightblue',ecolor='midnightblue',capsize=2)
            axs[1].errorbar(x1,ry_Rb,yerr=ry_Rb_err,marker='o',
            linestyle='None', label='Rb␣y', markerfacecolor='dodgerblue',
            markeredgecolor='midnightblue',
            ecolor='midnightblue',capsize=2)
        else:
            axs[1].scatter(x1, rx_Rb, label='Rb␣x␣fit',marker='o',
            linestyle='None', color='darkblue', edgecolor='midnightblue')
            axs[1].scatter(x1, ry_Rb, marker='o',linestyle='None',
            label='Rb␣y',color='dodgerblue',edgecolor='midnightblue')


        axs[1].set_xlabel(scanned_variable)
        axs[1].set_ylabel(r'rms␣radius␣($\mu␣m$)' )
        axs[1].legend(loc='upper␣left')
        plt.show
```

The plot of the cloud size is realized in a similar way. The main difference is that two plots are created side by side in the same figure: one for Cs and one for Rb, for that the method *plt.subplots*() is used. Each plot has two curves corresponding to the size in the x- and y- directions of the imaging plane in μm. Analogously to the atom number plot, it is possible to plot either the averaged data over multiple shots or the raw data. It is not yet possible to select this option independently for number and size. The axis labeling uses the scan_variable for the x-axis and "rms-radius (μm)" for the y-axis.

B.2.2 Fits

```
if FitModel==True:
    if Data.shape[0]>3:
        x_fit=np.linspace(min(x1),max(x1),1000)
        #assign dictionary
        if Model==0:
            fit_model=my_dict.dict_loading
        if Model==1:
            fit_model=my_dict.dict_expansion
        if Model==2:
            fit_model=my_dict.dict_lorentzian
...
```

The fits section begins by loading the right fit model from function_dictionary. The model is a dictionary containing:

- The fitting function as from Appendix C.
- The variable to be fit (atom number or cloud size)
- A function for the evaluation of the initial guess for the fit from the data
- A function for the annotation of the fit results on the plot
- A function for the annotation of the fit results on the plot

While inserting the variable to be fit in the model, might seem as a limit on the generality, it saves a lot of time on the day-to-day operation.

An array for the $x-variable$, used later to evaluate and plot the fitted function, is also calculated here. The array runs between the minimum and the maximum of the X1 data, and it consists of 1000 points. This is sufficiently smooth for typical applications.

```
    #check validity of model with respect to data
        if PlotNsum==False and fit_model['fit_atom_number']==True:
            fit_model['fit_atom_number']=False
            print('Impossible␣to␣fit␣atom␣number:␣atom␣number␣not␣present.
␣␣␣␣␣␣␣␣␣␣␣␣\n␣The␣model␣choice␣might␣be␣wrong.
␣␣␣␣␣␣␣␣␣␣␣␣\n␣Current␣model␣'+fit_model['ModName'])
        if Plotrms==False and fit_model['fit_radius']==True:
            fit_model['fit_radius']=False
            print('Impossible␣to␣fit␣rms-radius:␣rms-radius␣not␣present.
␣␣␣␣␣␣␣␣␣␣␣␣\n␣The␣model␣choice␣might␣be␣wrong.
␣␣␣␣␣␣␣␣␣␣␣␣\n␣Current␣model␣'+fit_model['ModName'])
```

Safety checks to ensure that the right variable is being plotted with respect to the selected model are executed before fitting.

```
        Rb_fit_mat=mat
        Cs_fit_mat=mat
        for cond in ExcludePoints_From_Rb_fit:
            Rb_fit_mat=fl.exclude_points_by_condition(Rb_fit_mat,cond)
        for cond in ExcludePoints_From_Cs_fit:
            Cs_fit_mat=fl.exclude_points_by_condition(mat,cond)

        if PlotNsum==True:
            if Rb_on==True:
                N_Rb=Rb_fit_mat[:,2]
            if Cs_on==True:
                N_Cs=Cs_fit_mat[:,1]
            if Average==True:
                if Rb_on==True:
                    N_Rb_err=Rb_fit_mat[:,9]
                if Cs_on==True:
                    N_Cs_err=Cs_fit_mat[:,8]
        if Plotrms==True:
            if Rb_on==True:
                rx_Rb=Rb_fit_mat[:,5]
                ry_Rb=Rb_fit_mat[:,6]
            if Cs_on==True:
                rx_Cs=Cs_fit_mat[:,3]
```

```
                ry_Cs=Cs_fit_mat[:,4]
            if Average==True:
                if Rb_on==True:
                    rx_Rb_err=Rb_fit_mat[:,12]
                    ry_Rb_err=Rb_fit_mat[:,13]
                if Cs_on==True:
                    rx_Cs_err=Cs_fit_mat[:,10]
                    ry_Cs_err=Cs_fit_mat[:,11]
        x1_Rb=Rb_fit_mat[:,0]
        x1_Cs=Cs_fit_mat[:,0]
```

A copy of the initial data set is created. This allow to crop the data according to the Exclude_from_fit condition (among the parameters at the beginning of the file), without affecting the global array to be saved at the end. For simplicity, a copy of the individual variables composing the matrices, in agreement with the user selection, is taken.

```
            if fit_model['fit_atom_number']==True:
            text='Fit␣Results'
            if Rb_on==True:
                Fitfile.write('Fit␣on␣Rb␣N:\n')
                Fitfile.write('Excluded␣points␣from␣fit\t')
                for cond in ExcludePoints_From_Rb_fit:
                    Fitfile.write(cond+'\t')
                Fitfile.write('\n')
                try:
                    RbN_pars,RbN_cov=ft.curve_fit(f=fit_model['fit_function'],
                    p0=fit_model['startingpoints'](x1,N_Rb))
                    RbN_y_fit=fit_model['fit_function'](x_fit,RbN_pars[0],
                    RbN_pars[1]), RbN_pars[2],
                    axN.plot(x_fit,RbN_y_fit,color='midnightblue'),
                    label=(),)
                    text=text+'\n␣Rb'
                    text=text+'\n'+fit_model['annotation']
                    (RbN_pars,'Rb')
                    Fitfile.write(fit_model['Fit_text']
                    (RbN_pars,RbN_cov,'Rb'))
                except RuntimeError:
                    print("Error␣-␣curve_fit␣failed")
                    Fitfile.write('Fit_failed')
```

The full fitting procedure is wrapped in a try-except structure, that highlights the insurgence of problems with the fitting and returns an error message if the fit failed. It first calculates the initial guess with the starting points from the model definition, then it executes the fit, plots the evaluation of the fitted function over X with the fit parameters on top of the data, adds the annotation with the fit results to the plot according to the model definition, and adds the results to the output file. Results and uncertainties are reported in scientific notation, with three significant digits for the results and two for the uncertainty. I reported above only the structure for Rb atom number. The other fits are performed in the same way.

```

if Save_data_to_file==True:
        file_new = open(Save_path+Save_filename+'_'+suffix+'.txt', 'w')
        if Loading_from_Lyse==True:

            file_new.write('Idx␣'+str(min(df['sequence_index']))+'_'
            +str(max(df['sequence_index']))+'\n')
            file_new.write('Scanning␣'+scanned_variable)
```

```
            for key in ParDict:
                #file_new.write('%s %e \n' % (key,ParDict[key]))
                file_new.write(key+'␣'+str(ParDict[key])+'\n')

        file_new.write('X\t␣NCs\t␣NRb\t␣rms_Cs_x\t␣rms_Cs_y\t␣rms_Rb_x
␣␣␣␣␣␣␣␣\t␣rms_Rb_y\t␣(+SDs␣in␣same␣order)\n')
        np.savetxt(file_new, mat )
        file_new.close
if Save==True:
    if PlotNsum==True:
        fig1.savefig((Save_path+Save_filename+('_N_%s.png' % suffix)),
        dpi=300)
    if Plotrms==True:
        fig2.savefig((Save_path+Save_filename+('_rms_%s.png' % suffix)),
        dpi=300)
```

Finally, the results are saved. The output consists of a text file with the data, the plots, the fit results. The fit results are saved contextually to the fitting procedure above. The output file contains the initial and final shot number of the data analyzed, for easy tracing of the pictures and sequence files. The file reports also all the variables specified in the ’Params’ file. Following there’s a row with the naming of the variables and the data themselves and the data by columns, with tab delimiters. The figures are saved as high-resolution .png files. No output goes back to Lyse.

Appendix C

Fitting functions

In the laboratory meeting when discussing external literature or very old literature from our lab, we often incur long discussions over the definition of fitting parameters, e.g., is the gaussian radius here defined as $1/e$ or $1/e^2$? To avoid future confusion, I want here to summarize the functions used throughout the text and their definition. The same definition is coded in the scripts developed for Lyse.

Gaussian	$y(x) = d + a\ exp\left(-2\frac{(x-x_c)^2}{\sigma_0^2}\right)$
Loading rates	$N(t) = N_s(1 - e^{-t/\tau})$
Thermal expansion (with initial size)	$\sigma(t) = \sqrt{\sigma_0^2 + (vt)^2}$
(without initial size)	$r(t) = r_0 + vt$
Exponential decay	$N(t) = N_0 e^{-t/\tau}$

Acknowledgements

The work presented in this thesis represented one of the bigger adventures of my life and I will be forever grateful to the people that crossed my path in these years and contributed to it. They made me a better scientist, but most of all they helped me become a better person.

I would like to start by thanking Hanns-Christoph Nägerl for giving me the opportunity to work in his laboratory. The faith he had in my skills and the independence that he allowed me in my work since my very early days in Innsbruck boosted my confidence and helped me become a stronger person. I wish to thank my second supervisor Tracy Northup who helped me navigate through some tricky parts of my Ph.D. work, and showed me how to find the right balance.

Manuele Landini joined the Nägerl group as a senior scientist a few years after I started my Ph.D. work, it would never cease to amaze me the way he takes a personal interest in every single topic we throw at him and mostly how he finds the time for all of it. The way he tremendously improved the workflow in the group will forever mark a line for my generation of Ph.D. students in the group: before and after Manuele.

In the laboratory, I had the opportunity to overlap with a large number of people. Mostly and foremost I want to thank Camilo for having my back, always, no matter what. We learned and grew together. Ideas bounced back and forth constantly evolving and improving to the point that is hard to say which one belonged to whom in the end (except technical stuff, when it works, it is likely his). He invested a lot in helping me refine the ICIR project and together we rebuilt and rethought half the experiment. I can never repay him for his unwavering support as a colleague and as a friend.

In order of appearance I would like to thank Lukas and Andreas for introducing me to the laboratory, the technology we use more often, and more in general to all the resources that professor Nägerl, the Department of Experimental Physics, and the university generously put at our disposal for the research work. I started in the laboratory almost at the same time as Erich, we had such different approaches that it was one year of constantly debating each step before our methodologies evolved and finally converged. My way of doing science improved drastically from it. His determination and support are one of the main reasons the work on ICIRs ever got out of the laboratory. Toward the end of my time in the group, Zekai Chen joined the group and he brought new energy and new ideas to the team. His enthusiasm about SF transport kept me going and improved my work on the topic. I would also like to thank all the other members of the RbCs team that I have overlapped with for longer or shorter time: Karthik, Arpita, Silva, Elisabeth, Beatrix, Younes, Tao

"Paul", Luisa.

A special thanks goes to Dimitris Trypogeorgos, he joined the RbCs project for a very short but very critical time. His experience, knowledge, and character made a huge difference: in the project, in the work style, and in the well-being of the people in the lab. On top of making me addicted to Python. I look forward to collaborating with him again.

My experience as a scientist in Innsbruck was bigger than the RbCs project, I would like to thank everyone in the Strongly correlated quantum matter group for the constant exchange of ideas, materials, and time. It helped better build my research and gave me the opportunity to learn in depth about their project broadening my knowledge of the field and its technical struggles.

More in general I would like to thank all the members of the ultracold community in Innsbruck, which over the years became way too many to name. Was it hiking, climbing, over a beer, or watching a movie, not only I had a really great time, but between an 'how are you?' and 'How is the lab going?' I also learned from them how to better present my research, and what people in the field would be interested about. Talking with them also taught me about different ways of structuring the workflow, the groups, and the leadership. A special mention to Rianne, who was my unofficial tutor in Innsbruck, from research and university structure to shopping and slopes.

The last seven years in Innsbruck were not just partying and research. Life, real life, became complicated and some days grew darker than others. There are no words to thank the people who helped me go through those days: Elisa, Cosetta, Cornee, Milena, Camilo. I could never express how much what they would just claim 'it's nothing' made all the difference in the world.

I am lucky enough to have a large support outside of Innsbruck as well. People that might not be part of everyday life but are every day in my heart. People, who are always there no matter what, just one phone call away, at any crazy time: Irene, Serena, Andrea, Peter, Niccolò, Consuelo, Alessandro.

Finally, I would like to thank my family, my big patchwork family with its ups and downs. I have a half little brother, who is almost as old as this thesis work, bouncing up and down with energy and amazing me with his discoveries of the world. I have grandparents who learned how to use Facebook for me and that alone should say everything about their love, and I have grandparents who may be watching over me from a better place and make me feel safe. I have an entire stepfamily, with a stepbrother, a stepgrandmother, and mostly a stepfather who is there for me, and who almost adopted me.

Mostly I have two amazing Parents, who, each in their own way, despite their differences and their struggles, are always on my side. Their unwavering love brought me up from my early steps to the person I am today, teaching me that for every fall there is the chance to stand up again. They showed me with their lives, before their words, that there exists no closed door on someone's dreams and wills.

Symbols and abbreviations

V^{lat} Depth of the optical lattice.

V_{t} Depth of the dipole trap.

CM Center-of-mass motion.

RM Relative motion.

μ Chemical potential.

$\omega_{\mathrm{Rb,x}}$ Rb trapping frequency along x (transport direction).

$\overline{m}$ Reduced mass.

τ_{h} Hold time in the lattice.

a_{h} Harmonic oscillator length: $a_{\mathrm{h}} = \sqrt{\frac{\hbar}{m_{\mathrm{Cs}}\omega(V_0)}}$.

a_{s} s-wave scattering length.

AOM Acousto-optic modulators.

BEC Bose-Einstein condensate.

dRSC Degenerate Raman Side-band cooling.

ECIR Elastic confinement-induced resonance.

FR Feschbach resonance.

GPE Gross Pitaevskii equation.

ICIR Inelastic confinement-induced resonance.

MI Mott Insulator.

MOT Magneto optical trap.

ODT Optical dipole trap.

OL Optical lattice.

PBS Polarizing beam splitters.

PSD Phase-space density.

SF Superfluid.

TA Tapered amplifier.

TOF Time of flight.

List of Figures

Bibliography

[1] M. H. Anderson, J. R. Ensher, M. R. Matthews, C. E. Wieman, and E. A. Cornell, "Observation of Bose-Einstein condensation in a dilute atomic vapor," *Science*, vol. 269, no. 5221, pp. 198–201, 1995.

[2] K. B. Davis, M. O. Mewes, M. R. Andrews, N. J. van Druten, D. S. Durfee, D. M. Kurn, and W. Ketterle, "Bose-Einstein condensation in a gas of sodium atoms," *Phys. Rev. Lett.*, vol. 75, pp. 3969–3973, 1995.

[3] L. Pitaevskii and S. Stringari, *Bose-Einstein condensation and superfluidity*, vol. 164. Oxford University Press, 2016.

[4] C. Chin, R. Grimm, P. Julienne, and E. Tiesinga, "Feshbach resonances in ultracold gases," *Rev. Mod. Phys.*, vol. 82, pp. 1225–1286, 2010.

[5] G. C. Strinati, P. Pieri, G. Röpke, P. Schuck, and M. Urban, "The BCS–BEC crossover: From ultra-cold Fermi gases to nuclear systems," *Phys. Rep.*, vol. 738, pp. 1–76, 2018.

[6] L. N. Cooper, "Bound electron pairs in a degenerate Fermi gas," *Phys. Rev.*, vol. 104, pp. 1189–1190, 1956.

[7] M. Greiner, O. Mandel, T. Esslinger, T. W. Hänsch, and I. Bloch, "Quantum phase transition from a superfluid to a Mott insulator in a gas of ultracold atoms," *Nature*, vol. 415, no. 6867, pp. 39–44, 2002.

[8] O. Morsch and M. Oberthaler, "Dynamics of Bose-Einstein condensates in optical lattices," *Rev. Mod. Phys.*, vol. 78, no. 1, p. 179, 2006.

[9] T. Kinoshita, T. Wenger, and D. S. Weiss, "Observation of a one-dimensional Tonks-Girardeau gas," *Science*, vol. 305, no. 5687, pp. 1125–1128, 2004.

[10] E. Haller, M. Gustavsson, M. J. Mark, J. G. Danzl, R. Hart, G. Pupillo, and H.-C. Nägerl, "Realization of an excited, strongly correlated quantum gas phase," *Science*, vol. 325, no. 5945, pp. 1224–1227, 2009.

[11] H. Ritsch, P. Domokos, F. Brennecke, and T. Esslinger, “Cold atoms in cavity-generated dynamical optical potentials,” *Rev. Mod. Phys.*, vol. 85, pp. 553–601, 2013.

[12] A. Browaeys and T. Lahaye, “Many-body physics with individually controlled Rydberg atoms,” *Nat. Phys.*, vol. 16, no. 2, pp. 132–142, 2020.

[13] L. Chomaz, I. Ferrier-Barbut, F. Ferlaino, B. Laburthe-Tolra, B. L. Lev, and T. Pfau, “Dipolar physics: A review of experiments with magnetic quantum gases,” *Rep. Prog. Phys.*, 2022.

[14] J. L. Bohn, A. M. Rey, and J. Ye, “Cold molecules: Progress in quantum engineering of chemistry and quantum matter,” *Science*, vol. 357, no. 6355, pp. 1002–1010, 2017.

[15] G. Pupillo, A. Micheli, H. P. Büchler, and P. Zoller, “Condensed matter physics with cold polar molecules,” *10.48550/arXiv.0805.1896*, 2008.

[16] L. Tanzi, E. Lucioni, F. Famà, J. Catani, A. Fioretti, C. Gabbanini, R. N. Bisset, L. Santos, and G. Modugno, “Observation of a dipolar quantum gas with metastable supersolid properties,” *Phys. Rev. Lett.*, vol. 122, p. 130405, 2019.

[17] F. Böttcher, J.-N. Schmidt, M. Wenzel, J. Hertkorn, M. Guo, T. Langen, and T. Pfau, “Transient supersolid properties in an array of dipolar quantum droplets,” *Phys. Rev. X*, vol. 9, p. 011051, 2019.

[18] L. Chomaz, D. Petter, P. Ilzhöfer, G. Natale, A. Trautmann, C. Politi, G. Durastante, R. M. W. van Bijnen, A. Patscheider, M. Sohmen, M. J. Mark, and F. Ferlaino, “Long-lived and transient supersolid behaviors in dipolar quantum gases,” *Phys. Rev. X*, vol. 9, p. 021012, 2019.

[19] M. Schmidt, L. Lassablière, G. Quéméner, and T. Langen, “Self-bound dipolar droplets and supersolids in molecular Bose-Einstein condensates,” *Phys. Rev. Res.*, vol. 4, no. 1, p. 013235, 2022.

[20] B. Capogrosso-Sansone, C. Trefzger, M. Lewenstein, P. Zoller, and G. Pupillo, “Quantum phases of cold polar molecules in 2D optical lattices,” *Phys. Rev. Lett.*, vol. 104, p. 125301, 2010.

[21] T. Sowiński, O. Dutta, P. Hauke, L. Tagliacozzo, and M. Lewenstein, “Dipolar molecules in optical lattices,” *Phys. Rev. Lett.*, vol. 108, p. 115301, 2012.

[22] M. Mayle, B. P. Ruzic, and J. L. Bohn, “Statistical aspects of ultracold resonant scattering,” *Phys. Rev. A*, vol. 85, p. 062712, 2012.

[23] M. Mayle, G. Quéméner, B. P. Ruzic, and J. L. Bohn, “Scattering of ultracold molecules in the highly resonant regime,” *Phys. Rev. A*, vol. 87, p. 012709, 2013.

[24] T. Langen, G. Valtolina, D. Wang, and J. Ye, “Quantum state manipulation and science of ultracold molecules,” *arXiv:2305.13445*, 2023.

[25] N. J. Fitch and M. R. Tarbutt, *From hot beams to trapped ultracold molecules: motivations, methods and future directions*, pp. 491–516. Cham: Springer International Publishing, 2021.

[26] L. Anderegg, B. L. Augenbraun, Y. Bao, S. Burchesky, L. W. Cheuk, W. Ketterle, and J. M. Doyle, "Laser cooling of optically trapped molecules," *Nat. Phys.*, vol. 14, no. 9, pp. 890–893, 2018.

[27] ACME Collaboration, "Order of magnitude smaller limit on the electric dipole moment of the electron," *Science*, vol. 343, no. 6168, pp. 269–272, 2014.

[28] ACME Collaboration, "Improved limit on the electric dipole moment of the electron," *Nature*, vol. 562, no. 7727, pp. 355–360, 2018.

[29] G. Valtolina, K. Matsuda, W. G. Tobias, J.-R. Li, L. De Marco, and J. Ye, "Dipolar evaporation of reactive molecules to below the Fermi temperature," *Nature*, vol. 588, no. 7837, pp. 239–243, 2020.

[30] R. Bause, A. Schindewolf, R. Tao, M. Duda, X.-Y. Chen, G. Quéméner, T. Karman, A. Christianen, I. Bloch, and X.-Y. Luo, "Collisions of ultracold molecules in bright and dark optical dipole traps," *Phys. Rev. Res.*, vol. 3, p. 033013, 2021.

[31] T. Takekoshi, L. Reichsöllner, A. Schindewolf, J. M. Hutson, C. R. Le Sueur, O. Dulieu, F. Ferlaino, R. Grimm, and H.-C. Nägerl, "Ultracold dense samples of dipolar RbCs molecules in the rovibrational and hyperfine ground state," *Phys. Rev. Lett.*, vol. 113, p. 205301, 2014.

[32] R. Bause, A. Christianen, A. Schindewolf, I. Bloch, and X.-Y. Luo, "Ultracold sticky collisions: Theoretical and experimental status," *J. Phys. Chem. A*, vol. 127, no. 3, pp. 729–741, 2023. PMID: 36624934.

[33] M. A. Nichols, Y.-X. Liu, L. Zhu, M.-G. Hu, Y. Liu, and K.-K. Ni, "Detection of long-lived complexes in ultracold atom-molecule collisions," *Phys. Rev. X*, vol. 12, p. 011049, 2022.

[34] P. D. Gregory, M. D. Frye, J. A. Blackmore, E. M. Bridge, R. Sawant, J. M. Hutson, and S. L. Cornish, "Sticky collisions of ultracold RbCs molecules.," *Nat. Comm.*, vol. 10, no. 1, p. 3104, 2019.

[35] P. D. Gregory, J. A. Blackmore, S. L. Bromley, and S. L. Cornish, "Loss of ultracold ^{87}Rb and ^{133}Cs molecules via optical excitation of long-lived two-body collision complexes," *Phys. Rev. Lett.*, vol. 124, no. 16, p. 163402, 2020.

[36] P. Gersema, K. K. Voges, M. Meyer zum Alten Borgloh, L. Koch, T. Hartmann, A. Zenesini, S. Ospelkaus, J. Lin, J. He, and D. Wang, "Probing photoinduced two-body loss of ultracold nonreactive bosonic ^{23}Na^{87}Rb and ^{23}Na^{39}K molecules," *Phys. Rev. Lett.*, vol. 127, p. 163401, 2021.

[37] A. Christianen, M. W. Zwierlein, G. C. Groenenboom, and T. Karman, "Photoinduced two-body loss of ultracold molecules," *Phys. Rev. Lett.*, vol. 123, p. 123402, 2019.

[38] P. Gregory, J. Blackmore, M. Frye, L. Fernley, S. Bromley, J. Hutson, and S. Cornish, "Molecule-molecule and atom-molecule collisions with ultracold RbCs molecules," *New J. Phys.*, vol. 23, p. 125004, 2021.

[39] K. K. Voges, P. Gersema, T. Hartmann, S. Ospelkaus, and A. Zenesini, “Hyperfine dependent atom-molecule loss analyzed by the analytic solution of few-body loss equations,” *Phys. Rev. Res.*, vol. 4, p. 023184, 2022.

[40] A. V. Avdeenkov, M. Kajita, and J. L. Bohn, “Suppression of inelastic collisions of polar $^{1}\sigma$ state molecules in an electrostatic field,” *Phys. Rev. A*, vol. 73, no. 2, p. 022707, 2006.

[41] G. Wang and G. Quéméner, “Tuning ultracold collisions of excited rotational dipolar molecules,” *New J. Phys.*, vol. 17, no. 3, p. 035015, 2015.

[42] G. Quéméner and J. L. Bohn, “Shielding $^{2}\sigma$ ultracold dipolar molecular collisions with electric fields,” *Phys. Rev. A*, vol. 93, no. 1, p. 012704, 2016.

[43] M. L. González-Martínez, J. L. Bohn, and G. Quéméner, “Adimensional theory of shielding in ultracold collisions of dipolar rotors,” *Phys. Rev. A*, vol. 96, no. 3, p. 032718, 2017.

[44] Z. Z. Yan, J. W. Park, Y. Ni, H. Loh, S. Will, T. Karman, and M. Zwierlein, “Resonant dipolar collisions of ultracold molecules induced by microwave dressing,” *Phys. Rev. Lett.*, vol. 125, p. 063401, 2020.

[45] K. Matsuda, L. D. Marco, J.-R. Li, W. G. Tobias, G. Valtolina, G. Quéméner, and J. Ye, “Resonant collisional shielding of reactive molecules using electric fields,” *Science*, vol. 370, no. 6522, pp. 1324–1327, 2020.

[46] J.-R. Li, W. G. Tobias, K. Matsuda, C. Miller, G. Valtolina, L. De Marco, R. R. Wang, L. Lassablière, G. Quéméner, J. L. Bohn, *et al.*, “Tuning of dipolar interactions and evaporative cooling in a three-dimensional molecular quantum gas,” *Nat. Phys.*, vol. 17, no. 10, pp. 1144–1148, 2021.

[47] L. Anderegg, S. Burchesky, Y. Bao, S. S. Yu, T. Karman, E. Chae, K.-K. Ni, W. Ketterle, and J. M. Doyle, “Observation of microwave shielding of ultracold molecules,” *Science*, vol. 373, no. 6556, pp. 779–782, 2021.

[48] A. Schindewolf, R. Bause, X.-Y. Chen, M. Duda, T. Karman, I. Bloch, and X.-Y. Luo, “Evaporation of microwave-shielded polar molecules to quantum degeneracy,” *Nature*, vol. 607, no. 7920, pp. 677–681, 2022.

[49] N. Bigagli, C. Warner, W. Yuan, S. Zhang, I. Stevenson, T. Karman, and S. Will, “Collisionally stable gas of bosonic dipolar ground state molecules,” *arXiv/2303.16845*, 2023.

[50] J. Lin, G. Chen, M. Jin, Z. Shi, F. Deng, W. Zhang, G. Quéméner, T. Shi, S. Yi, and D. Wang, “Microwave shielding of bosonic NaRb molecules,” *arXiv/2304.08312*, 2023.

[51] J. G. Danzl, M. J. Mark, E. Haller, M. Gustavsson, R. Hart, J. Aldegunde, J. M. Hutson, and H.-C. Nägerl, “An ultracold high-density sample of rovibronic ground-state molecules in an optical lattice,” *Nat. Phys.*, vol. 6, no. 4, pp. 265–270, 2010.

[52] A. Chotia, B. Neyenhuis, S. A. Moses, B. Yan, J. P. Covey, M. Foss-Feig, A. M. Rey, D. S. Jin, and J. Ye, “Long-lived dipolar molecules and Feshbach molecules in a 3D optical lattice,” *Phys. Rev. Lett.*, vol. 108, p. 080405, 2012.

[53] J. Lin, J. He, M. Jin, G. Chen, and D. Wang, “Seconds-scale coherence on nuclear spin transitions of ultracold polar molecules in 3D optical lattices,” *Phys. Rev. Lett.*, vol. 128, p. 223201, 2022.

[54] A. Micheli, G. Brennen, and P. Zoller, “A toolbox for lattice-spin models with polar molecules,” *Nat. Phys.*, vol. 2, no. 5, pp. 341–347, 2006.

[55] H. P. Büchler, E. Demler, M. Lukin, A. Micheli, N. Prokof’ev, G. Pupillo, and P. Zoller, “Strongly correlated 2D quantum phases with cold polar molecules: Controlling the shape of the interaction potential,” *Phys. Rev. Lett.*, vol. 98, p. 060404, 2007.

[56] N. Y. Yao, M. P. Zaletel, D. M. Stamper-Kurn, and A. Vishwanath, “A quantum dipolar spin liquid,” *Nat. Phys.*, vol. 14, no. 4, pp. 405–410, 2018.

[57] S. V. Syzranov, M. L. Wall, V. Gurarie, and A. M. Rey, “Spin–orbital dynamics in a system of polar molecules,” *Nat. Comm.*, vol. 5, no. 1, p. 5391, 2014.

[58] A. V. Gorshkov, S. R. Manmana, G. Chen, J. Ye, E. Demler, M. D. Lukin, and A. M. Rey, “Tunable superfluidity and quantum magnetism with ultracold polar molecules,” *Phys. Rev. Lett.*, vol. 107, p. 115301, 2011.

[59] B. Yan, S. A. Moses, B. Gadway, J. P. Covey, K. R. Hazzard, A. Rey, D. S. Jin, and J. Ye, “Observation of dipolar spin-exchange interactions with lattice-confined polar molecules,” *Nature*, vol. 501, no. 7468, pp. 521–525, 2013.

[60] W. G. Tobias, K. Matsuda, J.-R. Li, C. Miller, A. N. Carroll, T. Bilitewski, A. M. Rey, and J. Ye, “Reactions between layer-resolved molecules mediated by dipolar spin exchange,” *Science*, vol. 375, no. 6586, pp. 1299–1303, 2022.

[61] J.-R. Li, K. Matsuda, C. Miller, A. N. Carroll, W. G. Tobias, J. S. Higgins, and J. Ye, “Tunable itinerant spin dynamics with polar molecules,” *Nature*, vol. 614, no. 7946, pp. 70–74, 2023.

[62] S. A. Moses, J. P. Covey, M. T. Miecnikowski, B. Yan, B. Gadway, J. Ye, and D. S. Jin, “Creation of a low-entropy quantum gas of polar molecules in an optical lattice,” *Science*, vol. 350, no. 6261, pp. 659–662, 2015.

[63] L. Reichsöllner, A. Schindewolf, T. Takekoshi, R. Grimm, and H.-C. Nägerl, “Quantum engineering of a low-entropy gas of heteronuclear bosonic molecules in an optical lattice,” *Phys. Rev. Lett.*, vol. 118, p. 073201, 2017.

[64] I. Bloch, J. Dalibard, and W. Zwerger, “Many-body physics with ultracold gases,” *Rev. Mod. Phys.*, vol. 80, pp. 885–964, 2008.

[65] S. I. Mistakidis, A. G. Volosniev, R. E. Barfknecht, T. Fogarty, T. Busch, A. Foerster, P. Schmelcher, and N. T. Zinner, "Cold atoms in low dimensions – a laboratory for quantum dynamics," *arXiv:2202.11071*, 2022.

[66] Z. Hadzibabic, P. Krüger, M. Cheneau, B. Battelier, and J. Dalibard, "Berezinskii–Kosterlitz–Thouless crossover in a trapped atomic gas," *Nature*, vol. 441, no. 7097, pp. 1118–1121, 2006.

[67] B. Paredes, A. Widera, V. Murg, O. Mandel, S. Fölling, I. Cirac, G. V. Shlyapnikov, T. W. Hänsch, and I. Bloch, "Tonks–Girardeau gas of ultracold atoms in an optical lattice," *Nature*, vol. 429, no. 6989, pp. 277–281, 2004.

[68] D. S. Petrov, M. Holzmann, and G. V. Shlyapnikov, "Bose-Einstein condensation in quasi-2D trapped gases," *Phys. Rev. Lett.*, vol. 84, pp. 2551–2555, 2000.

[69] B. Fröhlich, M. Feld, E. Vogt, M. Koschorreck, W. Zwerger, and M. Köhl, "Radio-frequency spectroscopy of a strongly interacting two-dimensional Fermi gas," *Phys. Rev. Lett.*, vol. 106, p. 105301, 2011.

[70] M. Olshanii, "Atomic scattering in the presence of an external confinement and a gas of impenetrable bosons," *Phys. Rev. Lett.*, vol. 81, pp. 938–941, 1998.

[71] E. Haller, M. J. Mark, R. Hart, J. G. Danzl, L. Reichsöllner, V. Melezhik, P. Schmelcher, and H.-C. Nägerl, "Confinement-induced resonances in low-dimensional quantum systems," *Phys. Rev. Lett.*, vol. 104, p. 153203, 2010.

[72] S. Sala, P.-I. Schneider, and A. Saenz, "Inelastic confinement-induced resonances in low-dimensional quantum systems," *Phys. Rev. Lett.*, vol. 109, p. 073201, 2012.

[73] M. Troppenz, S. Sala, P.-I. Schneider, and A. Saenz, "Inelastic confinement-induced resonances in quantum dots," *arXiv/1509.01159*, 2015.

[74] D. Capecchi, C. Cantillano, M. J. Mark, F. Meinert, A. Schindewolf, M. Landini, A. Saenz, F. Revuelta, and H.-C. Nägerl, "Observation of confinement-induced resonances in a 3D lattice," *Phys. Rev. Lett.*, vol. 131, p. 213002, 2023.

[75] C. Cohen-Tannoudji and D. Guéry-Odelin, *Advances in atomic physics: an overview.* World scientific, 2011.

[76] H. J. Metcalf and P. Van der Straten, *Laser cooling and trapping of neutral atoms.* Wiley Online Library, 2007.

[77] C. Cohen-Tannoudji, J. Dupont-Roc, and G. Grynberg, *Atom-photon interactions: basic processes and applications.* John Wiley & Sons, 1998.

[78] R. Grimm, M. Weidemüller, and Y. B. Ovchinnikov, "Optical dipole traps for neutral atoms," 2000.

[79] D. J. Griffiths and D. F. Schroeter, *Introduction to quantum mechanics.* Cambridge University Press, 2018.

[80] W. Gerlach and O. Stern, "Der experimentelle Nachweis der Richtungsquantelung im Magnetfeld," *Zeitschrift für Physik*, vol. 9, no. 1, pp. 349–352, 1922.

[81] P. O. Fedichev, M. W. Reynolds, and G. V. Shlyapnikov, "Three-body recombination of ultracold atoms to a weakly bound s level," *Phys. Rev. Lett.*, vol. 77, pp. 2921–2924, 1996.

[82] E. Nielsen and J. H. Macek, "Low-energy recombination of identical bosons by three-body collisions," *Phys. Rev. Lett.*, vol. 83, pp. 1566–1569, 1999.

[83] B. D. Esry, C. H. Greene, and J. P. Burke, "Recombination of three atoms in the ultracold limit," *Phys. Rev. Lett.*, vol. 83, pp. 1751–1754, 1999.

[84] P. F. Bedaque, E. Braaten, and H.-W. Hammer, "Three-body recombination in Bose gases with large scattering length," *Phys. Rev. Lett.*, vol. 85, pp. 908–911, 2000.

[85] W. D. Phillips and H. Metcalf, "Laser deceleration of an atomic beam," *Phys. Rev. Lett.*, vol. 48, pp. 596–599, 1982.

[86] A. Camara, R. Kaiser, and G. Labeyrie, "Scaling behavior of a very large magneto-optical trap," *Phys. Rev. A*, vol. 90, no. 6, p. 063404, 2014.

[87] E. S. Shuman, J. F. Barry, D. R. Glenn, and D. DeMille, "Radiative force from optical cycling on a diatomic molecule," *Phys. Rev. Lett.*, vol. 103, p. 223001, 2009.

[88] E. S. Shuman, J. F. Barry, and D. DeMille, "Laser cooling of a diatomic molecule," *Nature*, vol. 467, no. 7317, pp. 820–823, 2010.

[89] J. Barry, D. McCarron, E. Norrgard, M. Steinecker, and D. DeMille, "Magneto-optical trapping of a diatomic molecule," *Nature*, vol. 512, no. 7514, pp. 286–289, 2014.

[90] M. R. Tarbutt, "Laser cooling of molecules," *Contemporary Physics*, vol. 59, no. 4, pp. 356–376, 2018.

[91] J. Walraven, "Quantum gases lectures," *https://staff.fnwi.uva.nl/j.t.m.walraven/walraven/Publications_files/ Quantum-Gases.pdf*, 2019.

[92] O. J. Luiten, M. W. Reynolds, and J. T. M. Walraven, "Kinetic theory of the evaporative cooling of a trapped gas," *Phys. Rev. A*, vol. 53, pp. 381–389, 1996.

[93] L. D. Landau and E. M. Lifshitz, *Quantum mechanics: non-relativistic theory*, vol. 3. Elsevier, 2013.

[94] T. Weber, J. Herbig, M. Mark, H.-C. Nägerl, and R. Grimm, "Three-body recombination at large scattering lengths in an ultracold atomic gas," *Phys. Rev. Lett.*, vol. 91, p. 123201, 2003.

[95] B. S. Rem, A. T. Grier, I. Ferrier-Barbut, U. Eismann, T. Langen, N. Navon, L. Khaykovich, F. Werner, D. S. Petrov, F. Chevy, and C. Salomon, "Lifetime of the Bose gas with resonant interactions," *Phys. Rev. Lett.*, vol. 110, p. 163202, 2013.

[96] R. J. Fletcher, A. L. Gaunt, N. Navon, R. P. Smith, and Z. Hadzibabic, "Stability of a unitary Bose gas," *Phys. Rev. Lett.*, vol. 111, p. 125303, 2013.

[97] U. Eismann, L. Khaykovich, S. Laurent, I. Ferrier-Barbut, B. S. Rem, A. T. Grier, M. Delehaye, F. Chevy, C. Salomon, L.-C. Ha, and C. Chin, "Universal loss dynamics in a unitary Bose gas," *Phys. Rev. X*, vol. 6, p. 021025, 2016.

[98] Bose, "Plancks Gesetz und Lichtquantenhypothese," *Zeitschrift für Physik*, vol. 26, no. 1, pp. 178–181, 1924.

[99] A. Einstein, "Quantentheorie des einatomigen idealen Gases.," *Albert Einstein: Akademie-Vorträge: Sitzungsberichte der Preußischen Akademie der Wissenschaften 1914–1932*, pp. 245–257, 1924.

[100] N. Bogoliubov, "On the theory of superfluidity," *J. Phys*, vol. 11, no. 1, p. 23, 1947.

[101] F. London, "The λ-phenomenon of liquid helium and the Bose-Einstein degeneracy," *Nature*, vol. 141, no. 3571, pp. 643–644, 1938.

[102] L. Landau, "Theory of the superfluidity of helium II (english translation)," *Phys. Rev.*, vol. 60, no. 4, p. 356, 1941.

[103] P. W. H. Pinkse, A. Mosk, M. Weidemüller, M. W. Reynolds, T. W. Hijmans, and J. T. M. Walraven, "Adiabatically changing the phase-space density of a trapped Bose gas," *Phys. Rev. Lett.*, vol. 78, pp. 990–993, 1997.

[104] D. M. Stamper-Kurn, H.-J. Miesner, A. P. Chikkatur, S. Inouye, J. Stenger, and W. Ketterle, "Reversible formation of a Bose-Einstein condensate," *Phys. Rev. Lett.*, vol. 81, pp. 2194–2197, 1998.

[105] C. S. Adams, H. J. Lee, N. Davidson, M. Kasevich, and S. Chu, "Evaporative cooling in a crossed dipole trap," *Phys. Rev. Lett.*, vol. 74, pp. 3577–3580, 1995.

[106] W. Ketterle, D. S. Durfee, and D. M. Stamper-Kurn, "Making, probing and understanding Bose-Einstein condensates," *arXiv/cond-mat/9904034*, 1999.

[107] C.-L. Hung, X. Zhang, N. Gemelke, and C. Chin, "Accelerating evaporative cooling of atoms into Bose-Einstein condensation in optical traps," *Phys. Rev. A*, vol. 78, p. 011604, 2008.

[108] V. Vuletić, C. Chin, A. J. Kerman, and S. Chu, "Degenerate Raman sideband cooling of trapped cesium atoms at very high atomic densities," *Phys. Rev. Lett.*, vol. 81, pp. 5768–5771, 1998.

[109] A. J. Kerman, *Raman sideband cooling and cold atomic collisions in optical lattices.* PhD thesis, Stanford University, California, 2002.

[110] P. Solano, Y. Duan, Y.-T. Chen, A. Rudelis, C. Chin, and V. Vuletić, "Strongly correlated quantum gas prepared by direct laser cooling," *Phys. Rev. Lett.*, vol. 123, p. 173401, 2019.

[111] D. Jaksch, C. Bruder, J. I. Cirac, C. W. Gardiner, and P. Zoller, "Cold bosonic atoms in optical lattices," *Phys. Rev. Lett.*, vol. 81, pp. 3108–3111, 1998.

[112] M. P. A. Fisher, P. B. Weichman, G. Grinstein, and D. S. Fisher, "Boson localization and the superfluid-insulator transition," *Phys. Rev. B*, vol. 40, pp. 546–570, 1989.

[113] M. P. Kennett, "Out-of-equilibrium dynamics of the Bose-Hubbard model," *International Scholarly Research Notices*, vol. 2013, 2013.

[114] G. Grosso and G. P. Parravicini, *Solid state physics.* Academic press, 2013.

[115] Q. Niu, X.-G. Zhao, G. A. Georgakis, and M. G. Raizen, "Atomic Landau-Zener tunneling and Wannier-Stark ladders in optical potentials," *Phys. Rev. Lett.*, vol. 76, pp. 4504–4507, 1996.

[116] M. Cristiani, O. Morsch, J. H. Müller, D. Ciampini, and E. Arimondo, "Experimental properties of Bose-Einstein condensates in one-dimensional optical lattices: Bloch oscillations, Landau-Zener tunneling, and mean-field effects," *Phys. Rev. A*, vol. 65, p. 063612, 2002.

[117] F. Bloch, "Über die Quantenmechanik der Elektronen in Kristallgittern," *Zeitschrift für Physik*, vol. 52, no. 7-8, pp. 555–600, 1929.

[118] M. B. Dahan, E. Peik, J. Reichel, Y. Castin, and C. Salomon, "Bloch oscillations of atoms in an optical potential," *Phys. Rev. Lett.*, vol. 76, no. 24, p. 4508, 1996.

[119] O. Morsch, J. H. Müller, M. Cristiani, D. Ciampini, and E. Arimondo, "Bloch oscillations and mean-field effects of Bose-Einstein condensates in 1D optical lattices," *Phys. Rev. Lett.*, vol. 87, p. 140402, 2001.

[120] M. Gustavsson, E. Haller, M. J. Mark, J. G. Danzl, R. Hart, A. J. Daley, and H.-C. Nägerl, "Interference of interacting matter waves," *New J. Phys.*, vol. 12, no. 6, p. 065029, 2010.

[121] F. Meinert, M. J. Mark, E. Kirilov, K. Lauber, P. Weinmann, M. Gröbner, and H.-C. Nägerl, "Interaction-induced quantum phase revivals and evidence for the transition to the quantum chaotic regime in 1D atomic Bloch oscillations," *Phys. Rev. Lett.*, vol. 112, p. 193003, 2014.

[122] J. Mun, P. Medley, G. K. Campbell, L. G. Marcassa, D. E. Pritchard, and W. Ketterle, "Phase diagram for a Bose-Einstein Condensate moving in an optical lattice," *Phys. Rev. Lett.*, vol. 99, p. 150604, 2007.

[123] F. Cataliotti, L. Fallani, F. Ferlaino, C. Fort, P. Maddaloni, and M. Inguscio, "Superfluid current disruption in a chain of weakly coupled Bose–Einstein condensates," *New J. Phys.*, vol. 5, no. 1, p. 71, 2003.

[124] A. Schindewolf, *Quantum engineering of a low-entropy Sample of RbCs molecules in an optical lattice.* PhD thesis, University of Innsbruck, 2018.

[125] C. Trefzger, C. Menotti, B. Capogrosso-Sansone, and M. Lewenstein, "Ultracold dipolar gases in optical lattices," *J. Phys. B*, vol. 44, no. 19, p. 193001, 2011.

[126] N. Y. Yao, A. V. Gorshkov, C. R. Laumann, A. M. Läuchli, J. Ye, and M. D. Lukin, "Realizing fractional Chern insulators in dipolar spin systems," *Phys. Rev. Lett.*, vol. 110, no. 18, p. 185302, 2013.

[127] V. Dunjko, M. G. Moore, T. Bergeman, and M. Olshanii, "Confinement-induced resonances," vol. 60, pp. 461–510, 2011.

[128] K.Huang, *Statistical Mechanics, 2nd edn.* New York: Wiley, 1987.

[129] T. Bergeman, M. G. Moore, and M. Olshanii, "Atom-atom scattering under cylindrical harmonic confinement: Numerical and analytic studies of the confinement-induced resonance," *Phys. Rev. Lett.*, vol. 91, p. 163201, 2003.

[130] S. Sala and A. Saenz, "Theory of inelastic confinement-induced resonances due to the coupling of center-of-mass and relative motion," *Phys. Rev. A*, vol. 94, p. 022713, 2016.

[131] G. Zürn, F. Serwane, T. Lompe, A. N. Wenz, M. G. Ries, J. E. Bohn, and S. Jochim, "Fermionization of two distinguishable fermions," *Phys. Rev. Lett.*, vol. 108, p. 075303, 2012.

[132] L. Riegger, N. Darkwah Oppong, M. Höfer, D. R. Fernandes, I. Bloch, and S. Fölling, "Localized magnetic moments with tunable spin exchange in a gas of ultracold fermions," *Phys. Rev. Lett.*, vol. 120, p. 143601, 2018.

[133] W. Kao, K.-Y. Li, K.-Y. Lin, S. Gopalakrishnan, and B. L. Lev, "Topological pumping of a 1D dipolar gas into strongly correlated prethermal states," *Science*, vol. 371, no. 6526, pp. 296–300, 2021.

[134] H. Moritz, T. Stöferle, K. Günter, M. Köhl, and T. Esslinger, "Confinement induced molecules in a 1D Fermi gas," *Phys. Rev. Lett.*, vol. 94, p. 210401, 2005.

[135] T. Kraemer, J. Herbig, M. Mark, T. Weber, C. Chin, H.-C. Nägerl, and R. Grimm, "Optimized production of a cesium Bose–Einstein condensate," *Appl. Phys. B*, vol. 79, p. 1013–1019, 2004.

[136] S.-G. Peng, H. Hu, X.-J. Liu, and P. D. Drummond, "Confinement-induced resonances in anharmonic waveguides," *Phys. Rev. A*, vol. 84, p. 043619, 2011.

[137] S. Sala, G. Zürn, T. Lompe, A. N. Wenz, S. Murmann, F. Serwane, S. Jochim, and A. Saenz, "Coherent molecule formation in anharmonic potentials near confinement-induced resonances," *Phys. Rev. Lett.*, vol. 110, p. 203202, 2013.

[138] D. Xiao, R. Zhang, and P. Zhang, "Confinement induced resonance with weak bare interaction in a quasi 3+0 dimensional ultracold gas," *Few-Body Systems*, vol. 60, p. 63, 2019.

[139] B. Schulz, S. Sala, and A. Saenz, "Resonances in ultracold dipolar atomic and molecular gases," *New J. Phys.*, vol. 17, no. 6, p. 065002, 2015.

[140] E. Fermi, "Sul moto dei neutroni nelle sostanze idrogenate," *La Ricerca Scientifica*, vol. 7, p. 13, 1936.

[141] T. Busch, B.-G. Englert, K. Rzazewski, and M. Wilkens, “Two cold atoms in a harmonic trap,” *Found. of Phys.*, vol. 28, 1998.

[142] E. L. Bolda, E. Tiesinga, and P. S. Julienne, “Effective-scattering-length model of ultracold atomic collisions and Feshbach resonances in tight harmonic traps,” *Phys. Rev. A*, vol. 66, p. 013403, 2002.

[143] E. Mathieu, “Mémoire sur le mouvement vibratoire d’une membrane de forme elliptique,” *J. Math. Pures Appl.*, vol. 13, pp. 137–203, 1868.

[144] H. Buchholz, *The confluent hypergeometric function: with special emphasis on its applications*, vol. 15. Springer Science & Business Media, 2013.

[145] S. Grishkevich and A. Saenz, “Theoretical description of two ultracold atoms in a single site of a three-dimensional optical lattice using realistic interatomic interaction potentials,” *Phys. Rev. A*, vol. 80, p. 013403, 2009.

[146] S. I. J., *Cardinal Spline Interpolation.* Society for Industrial and Applied Mathematics, 1973.

[147] K. Pilch, *Optical trapping and Feshbach spectroscopy of an ultracold Rb-Cs mixture.* PhD thesis, University of Innsbruck, 2009.

[148] B. Engeser, *A novel surface trapping apparatus for ultracold cesium atoms and the investigation of an Efimov resonance.* PhD thesis, University of Innsbruck, 2006.

[149] A. D. Lercher, *Doppel-Spezies Bose-Einstein-Kondensat von Rubidium und Cäsium Atomen in räumlich getrennten optischen Fallen.* PhD thesis, "University of Innsbruck", 2002.

[150] M. Debatin, *Creation of Ultracold RbCs Ground-State Molecules.* PhD thesis, University of Innsbruck, 2013.

[151] L. Reichsöllner, *A general quantum-engineering technique for efficient production of ultracold dipolar molecules.* PhD thesis, University of Innsbruck, 2018.

[152] C. Ospelkaus, S. Ospelkaus, L. Humbert, P. Ernst, K. Sengstock, and K. Bongs, “Ultracold heteronuclear molecules in a 3D optical lattice,” *Phys. Rev. Lett.*, vol. 97, p. 120402, 2006.

[153] K.-K. Ni, S. Ospelkaus, M. H. G. de Miranda, A. Pe’er, B. Neyenhuis, J. J. Zirbel, S. Kotochigova, P. S. Julienne, D. S. Jin, and J. Ye, “A high phase-space-density gas of polar molecules,” *Science*, vol. 322, no. 5899, pp. 231–235, 2008.

[154] P. K. Molony, P. D. Gregory, Z. Ji, B. Lu, M. P. Köppinger, C. R. Le Sueur, C. L. Blackley, J. M. Hutson, and S. L. Cornish, “Creation of ultracold ^{87}Rb^{133}Cs molecules in the rovibrational ground state,” *Phys. Rev. Lett.*, vol. 113, p. 255301, 2014.

[155] M. P. Köppinger, D. J. McCarron, D. L. Jenkin, P. K. Molony, H.-W. Cho, S. L. Cornish, C. R. Le Sueur, C. L. Blackley, and J. M. Hutson, “Production of optically trapped ^{8}7RbCs Feshbach molecules,” *Phys. Rev. A*, vol. 89, no. 3, p. 033604, 2014.

[156] T. Weber, *Bose-Einstein Condensation of Optically Trapped Cesium.* PhD thesis, University of Innsbruck, 2003.

[157] D. A. Steck, “Rubidium 87 D line data.”

[158] D. A. Steck, “Cesium D line data.”

[159] A. E. Siegman, *Lasers.* University science books, 1986.

[160] J. C. Kangara, A. J. Hachtel, M. C. Gillette, J. T. Barkeloo, E. R. Clements, S. Bali, B. E. Unks, N. A. Proite, D. D. Yavuz, P. J. Martin, *et al.*, “Design and construction of cost-effective tapered amplifier systems for laser cooling and trapping experiments,” *American J. Phys.*, vol. 82, no. 8, pp. 805–817, 2014.

[161] Z. Liu and R. Slavík, “Optical injection locking: From principle to applications,” *J. of Lightwave Tech.*, vol. 38, no. 1, pp. 43–59, 2020.

[162] W. Demtröder, “Laser spectroscopy 2,” *Experimental techniques*, vol. 5, 2014.

[163] C. Hippler, “Ein selbstgebauter ytterbium-Faserverstärker mit 25 W Ausgangsleistung bei 1064 nm zur Realisierung eines optischen Gitters für ultrakalte RbCs-Moleküle,” Master’s thesis, Technischen Universität München, 2013.

[164] E. Wille, *Preparation of an optically trapped Fermi-Fermi mixture of* ^{6}Li *and* ^{40}K *atoms and characterization of the interspecies interaction by Feshbach spectroscopy.* PhD thesis, University of Innsbruck, 2009.

[165] H. Ammann and N. Christensen, “Delta kick cooling: A new method for cooling atoms,” *Phys. Rev. Lett.*, vol. 78, pp. 2088–2091, 1997.

[166] M. F. Sykes and J. W. Essam, “Critical percolation probabilities by series methods,” *Phys. Rev.*, vol. 133, pp. A310–A315, 1964.

[167] N. V. Vitanov, A. A. Rangelov, B. W. Shore, and K. Bergmann, “Stimulated Raman adiabatic passage in physics, chemistry, and beyond,” *Rev. Mod. Phys.*, vol. 89, p. 015006, 2017.

[168] K. Bergmann, H.-C. Nägerl, C. Panda, G. Gabrielse, E. Miloglyadov, M. Quack, G. Seyfang, G. Wichmann, S. Ospelkaus, A. Kuhn, *et al.*, “Roadmap on STIRAP applications,” *J. Phys. B*, vol. 52, no. 20, p. 202001, 2019.

[169] A. Das, P. D. Gregory, T. Takekoshi, L. Fernley, M. Landini, J. M. Hutson, S. L. Cornish, and H.-C. Nägerl, “An association sequence suitable for producing ground-state RbCs molecules in optical lattices,” *arXiv:2303.16144*, 2023.

[170] D. K. Ruttley, A. Guttridge, S. Spence, R. C. Bird, C. R. Le Sueur, J. M. Hutson, and S. L. Cornish, “Formation of ultracold molecules by merging optical tweezers,” *Phys. Rev. Lett.*, vol. 130, p. 223401, 2023.

[171] M. Berninger, A. Zenesini, B. Huang, W. Harm, H.-C. Nägerl, F. Ferlaino, R. Grimm, P. S. Julienne, and J. M. Hutson, "Feshbach resonances, weakly bound molecular states, and coupled-channel potentials for cesium at high magnetic fields," *Phys. Rev. A*, vol. 87, p. 032517, 2013.

[172] Y. K. Lee, H. Lin, and W. Ketterle, "Spin dynamics dominated by resonant tunneling into molecular states," *Phys. Rev. Lett.*, vol. 131, p. 213001, Nov 2023.

[173] O. Jürgensen, F. Meinert, M. J. Mark, H.-C. Nägerl, and D.-S. Lühmann, "Observation of density-induced tunneling," *Phys. Rev. Lett.*, vol. 113, p. 193003, 2014.

[174] S. Trotzky, P. Cheinet, S. Fölling, M. Feld, U. Schnorrberger, A. M. Rey, A. Polkovnikov, E. A. Demler, M. D. Lukin, and I. Bloch, "Time-resolved observation and control of superexchange interactions with ultracold atoms in optical lattices," *Science*, vol. 319, no. 5861, pp. 295–299, 2008.

[175] F. Revuelta and A. Saenz, "Inelastic confinement-induced resonances in multiwell potentials," *In preparation.*

[176] H. P. Büchler, "Microscopic derivation of Hubbard parameters for cold atomic gases," *Phys. Rev. Lett.*, vol. 104, p. 090402, 2010.

[177] A. Patscheider, B. Zhu, L. Chomaz, D. Petter, S. Baier, A.-M. Rey, F. Ferlaino, and M. J. Mark, "Controlling dipolar exchange interactions in a dense three-dimensional array of large-spin fermions," *Phys. Rev. Res.*, vol. 2, p. 023050, 2020.

[178] G. Natale, T. Bland, S. Gschwendtner, L. Lafforgue, D. S. Grün, A. Patscheider, M. J. Mark, and F. Ferlaino, "Strongly dipolar gases in a one-dimensional lattice: Bloch oscillations and matter-wave localization," *10.48550/arXiv.2205.03280*, 2022.

[179] M. Rispoli, A. Lukin, R. Schittko, S. Kim, M. E. Tai, J. Léonard, and M. Greiner, "Quantum critical behaviour at the many-body localization transition," *Nature*, vol. 573, p. 385, 2019.

[180] E. Haller, J. Hudson, A. Kelly, D. A. Cotta, B. Peaudecerf, and S. Bruce, Graham D.and Kuhr, "Single-atom imaging of fermions in a quantum-gas microscope," *Nat. Phys.*, vol. 11, pp. 738–742, 2015.

[181] Y. Wang, S. Subhankar, P. Bienias, M. Łącki, T.-C. Tsui, M. A. Baranov, A. V. Gorshkov, P. Zoller, J. V. Porto, and S. L. Rolston, "Dark state optical lattice with a subwavelength spatial structure," *Phys. Rev. Lett.*, vol. 120, p. 083601, 2018.

[182] L. Amico, M. Boshier, G. Birkl, A. Minguzzi, C. Miniatura, L.-C. Kwek, D. Aghamalyan, V. Ahufinger, D. Anderson, N. Andrei, A. S. Arnold, M. Baker, T. A. Bell, T. Bland, J. P. Brantut, D. Cassettari, W. J. Chetcuti, F. Chevy, R. Citro, S. De Palo, R. Dumke, M. Edwards, R. Folman, J. Fortagh, S. A. Gardiner, B. M. Garraway, G. Gauthier, A. Günther, T. Haug, C. Hufnagel, M. Keil, P. Ireland, M. Lebrat, W. Li, L. Longchambon, J. Mompart, O. Morsch, P. Naldesi, T. W. Neely, M. Olshanii, E. Orignac, S. Pandey, A. Pérez-Obiol, H. Perrin,

L. Piroli, J. Polo, A. L. Pritchard, N. P. Proukakis, C. Rylands, H. Rubinsztein-Dunlop, F. Scazza, S. Stringari, F. Tosto, A. Trombettoni, N. Victorin, W. v. Klitzing, D. Wilkowski, K. Xhani, and A. Yakimenko, “Roadmap on atomtronics: State of the art and perspective,” *AVS Quantum Science*, vol. 3, no. 3, p. 039201, 2021.

[183] M. Kliesch, C. Gogolin, and J. Eisert, “Lieb-Robinson bounds and the simulation of time-evolution of local observables in lattice systems,” *Many-Electron Approaches in Physics, Chemistry and Mathematics: A Multidisciplinary View*, pp. 301–318, 2014.

[184] T. L. Gustavson, A. P. Chikkatur, A. E. Leanhardt, A. Görlitz, S. Gupta, D. E. Pritchard, and W. Ketterle, “Transport of Bose-Einstein condensates with optical tweezers,” *Phys. Rev. Lett.*, vol. 88, p. 020401, 2001.

[185] J. H. Denschlag, J. E. Simsarian, H. Häffner, C. McKenzie, A. Browaeys, D. Cho, K. Helmerson, S. L. Rolston, and W. D. Phillips, “A Bose-Einstein condensate in an optical lattice,” *J. Phys. B*, vol. 35, no. 14, p. 3095, 2002.

[186] A. Dhar, C. Baals, B. Santra, A. Müllers, R. Labouvie, T. Mertz, I. Vasic, A. Cichy, H. Ott, and W. Hofstetter, “Transport of strongly correlated bosons in an optical lattice,” *Physica status solidi (b)*, vol. 256, no. 9, p. 1800752, 2019.

[187] E. Torrontegui, S. Ibáñez, S. Martínez-Garaot, M. Modugno, A. del Campo, D. Guéry-Odelin, A. Ruschhaupt, X. Chen, and J. G. Muga, “Shortcuts to adiabaticity,” in *Advances in atomic, molecular, and optical physics*, vol. 62, pp. 117–169, Elsevier, 2013.

[188] M. Greiner, *Ultracold quantum gases in three-dimensional optical lattice potentials*. PhD thesis, Ludwig-Maximilians-Universität München, 2003.

[189] M. Feit, J. Fleck, and A. Steiger, “Solution of the Schrödinger equation by a spectral method,” *J. Comp. Phys.*, vol. 47, no. 3, pp. 412–433, 1982.

[190] The Matplotlib development team, “Interpolations for imshow.” https://matplotlib.org/stable/gallery/images_contours_and_fields/interpolation_methods.html.

[191] W. T. Vetterling and W. H. Press, *Numerical recipes: example book C*. Cambridge University Press, 1992.

[192] S. Aubry and G. André, “Analyticity breaking and Anderson localization in incommensurate lattices,” *Ann. Israel Phys. Soc*, vol. 3, no. 133, p. 18, 1980.

[193] C. P. Koch, U. Boscain, T. Calarco, G. Dirr, S. Filipp, S. J. Glaser, R. Kosloff, S. Montangero, T. Schulte-Herbrüggen, D. Sugny, *et al.*, “Quantum optimal control in quantum technologies. strategic report on current status, visions and goals for research in Europe,” *EPJ Quantum Technology*, vol. 9, no. 1, p. 19, 2022.

[194] *VacIon Plus 20 pumps User Manual.*

[195] Thorlabs, "Choosing a wave plate." `https://www.thorlabs.com/newgrouppage9.cfm?objectgroup_id=10777#:~:text=Compared%20to%20their%20zero%2Dorder,sensitivities%20are%20not%20an%20issue.`

[196] E. Optics, "Understanding waveplates and retarders." `https://www.edmundoptics.eu/knowledge-center/application-notes/optics/understanding-waveplates/`.

[197] A. Pini, "The basics of voltage controlled oscillators (VCOs) and how to select and use them." `https://www.digikey.at/en/articles/the-basics-of-voltage-controlled-oscillators-vcos`.

[198] E. Murphy and C. Slattery, "Ask the application engineer—33: All about direct digital synthesis." `https://www.analog.com/en/analog-dialogue/articles/all-about-direct-digital-synthesis.html#:~:text=Direct%20digital%20synthesis%20(DDS)%20is,digital%2Dto%2Danalog%20conversion.`

[199] D. J. Thompson and S. Robert, "Narrow linewidth tunable external cavity diode laser using wide bandwidth filter," *Rev. Sci. Inst.*, vol. 83, p. 023107, 2012.

[200] P. Tierney, *State-dependent forces in cold quantum gases.* PhD thesis, Durham University, 2009.

[201] P. T. Starkey, *A software framework for control and automation of precisely timed experiments.* PhD thesis, Monash University, 2019.

[202] C. J. Billington, *State-dependent forces in cold quantum gases.* PhD thesis, Monash University, 2018.

[203] P. T. Starkey, C. J. Billington, S. P. Johnstone, M. Jasperse, K. Helmerson, L. D. Turner, and R. P. Anderson, "A scripted control system for autonomous hardware-timed experiments," *Rev. Sci. Inst.*, vol. 84, no. 8, p. 085111, 2013.

[204] The pandas development team, "pandas-dev/pandas: Pandas," 2020.

[205] Wes McKinney, "Data Structures for Statistical Computing in Python," in *Proceedings of the 9th Python in Science Conference* (Stéfan van der Walt and Jarrod Millman, eds.), pp. 56 – 61, 2010.

[206] D. Guéry-Odelin and J. Muga, "Transport in a harmonic trap: Shortcuts to adiabaticity and robust protocols," *Phys. Rev. A*, vol. 90, no. 6, p. 063425, 2014.

[207] S. An, D. Lv, A. Del Campo, and K. Kim, "Shortcuts to adiabaticity by counterdiabatic driving for trapped-ion displacement in phase space," *Nat. Comm.*, vol. 7, no. 1, p. 12999, 2016.

[208] B. Chatterjee, M. C. Tsatsos, and A. U. Lode, "Correlations of strongly interacting one-dimensional ultracold dipolar few-boson systems in optical lattices," *New J. Phys.*, vol. 21, no. 3, p. 033030, 2019.

[209] S. Sinha and L. Santos, “Cold dipolar gases in quasi-one-dimensional geometries,” *Phys. Rev. Lett.*, vol. 99, p. 140406, 2007.

[210] J. R. Armstrong, A. S. Jensen, A. G. Volosniev, and N. T. Zinner, “Clusters in separated tubes of tilted dipoles,” *Mathematics*, vol. 8, no. 4, 2020.

[211] T. Karman and J. M. Hutson, “Microwave shielding of ultracold polar molecules with imperfectly circular polarization,” *Phys. Rev. A*, vol. 100, p. 052704, 2019.

[212] W. Lechner and P. Zoller, “From classical to quantum glasses with ultracold polar molecules,” *Phys. Rev. Lett.*, vol. 111, p. 185306, 2013.

[213] A. W. Glaetzle, M. Dalmonte, R. Nath, I. Rousochatzakis, R. Moessner, and P. Zoller, “Quantum spin-ice and dimer models with Rydberg atoms,” *Phys. Rev. X*, vol. 4, p. 041037, 2014.

[214] F. Cinti, T. Macrì, W. Lechner, G. Pupillo, and T. Pohl, “Defect-induced supersolidity with soft-core bosons,” *Nat. Comm.*, vol. 5, no. 1, p. 3235, 2014.